Corrosion Studies of Advanced Gas-cooled Reactor (AGR) Spent Nuclear Fuel

Yifeng (Nigel) Huang,

MChem (Hons.)

Submitted to Lancaster University in partial fulfilment for the requirements for the degree of **Doctor of Philosophy**

March 2025

Acknowledgements

First and foremost, I owe my sincerest gratitude and appreciation to my supervisor, Professor Colin Boxall, for his unwavering and dedicated support throughout my PhD journey. Colin has played a huge role in my personal and professional development, and most importantly, he has supported me through my long and arduous journey through the dark and mysterious world of research academia.

I would like to thank Richard Wilbraham, the ‘Wizard of UTGARD’, for providing a wealth of knowledge and guidance throughout my research and laboratory journey. I am very grateful for his kindness and generosity, he has shared his experiences and taught me everything I ever needed to know about all sorts of practical work, without which I would not have been able to carry out my studies.

I would also like to express my deepest thanks to my industrial supervisor David Hambley, at the National Nuclear Laboratory, for providing all the industrial knowledge and insights into the UK’s nuclear legacy, and most importantly, for his support in gaining access to NNL Windscale labs to conduct the first ever electrochemistry experiments on legacy AGR spent nuclear fuel, and of course to all the NNL technicians who made the experiments possible. I would also like to acknowledge the EPSRC and their Next Generation Nuclear Centre for Doctoral Training (NGN CDT) for their funding of this PhD studentship; the relationships and network opportunities have been invaluable.

I am grateful for the unconditional support of my family, and I am very thankful for all the great friends I have made along the way, and thankful for all the shared experiences of the joys and challenges of a PhD.

Most importantly and above all else, I dedicate my thesis to my dearest, Penny, for her infinite care and affection, without which I would have quit already by week two. Penny has been by my side throughout every step of this journey, and seven years later it has become a part of me as much as it has become a part of her. For that, I am forever grateful to have shared this experience together.

Abstract

The UK's nuclear fleet primarily comprises Advanced Gas-cooled Reactors (AGRs), utilising UO_2 as the fuel source. As of 2019, the UK's inventory of AGR Spent Nuclear Fuel (SNF) was approximately 2200 tHM (tonnes of Heavy Metal), with projections exceeding 4000 tHM by 2030, destined for disposal in a Geological Disposal Facility (GDF). Interim storage of AGR SNF takes place in wet storage ponds containing caustic demineralised water (pH 11.4, chloride <1 ppm) to mitigate corrosion. However, in cases of fuel pin / cladding failure, water ingress may lead to fuel corrosion, the implications of which remain insufficiently understood.

This study investigates the electrochemical corrosion behaviour of AGR SNF under conditions relevant to UK wet storage. A series of experiments were conducted to characterise the corrosion mechanisms of UO_2, AGR SIMFUELs, and AGR cladding materials, including coupled-electrode systems simulating cladding-fuel interactions in real AGR SNF. These baseline studies enabled direct comparison with the first-ever electrochemical investigation of legacy AGR SNF under hot-cell conditions. This two-part study examined electrochemical behaviour in Simplified Simulant Pond Water (SSPW) at various pH levels, followed by an assessment of chloride ion concentration effects.

These preliminary results indicate that the electrochemical behaviour of legacy AGR SNF closely aligns with that of AGR SIMFUELs, validating their use as SNF simulants. Furthermore, findings confirm that current AGR wet storage conditions effectively suppress and prevent further corrosion of SNF during interim pond storage. These insights contribute to the fundamental understanding of AGR SNF corrosion and inform the long-term management of AGR SNF in the UK.

Declaration

I, Yifeng (Nigel) Huang, declare that the work presented in this thesis has been conducted by myself and has not been submitted elsewhere for the award of any other degree unless stated otherwise. The work presented in this thesis was conducted at Lancaster University between August 2018 and March 2025.

Signature: _____

Yifeng (Nigel) Huang

Table of Contents

List of Figures

List of Tables

List of Key Terms and Abbreviations

Term	Definition
25-SIMF	25 GWd/tU AGR SIMFUEL
43-hiLn	43 GWd/tU AGR SIMFUEL with higher lanthanide doping
43-hiLnCr	43 GWd/tU AGR SIMFUEL with higher lanthanide and chromium-doped
43-SIMF	43 GWd/tU AGR SIMFUEL
AGR	Advanced Gas-cooled Reactors
CV	Cyclic Voltammetry
EBR-1	Experimental Breeder Reactor
EDX	Energy Dispersive X-ray
EEC	Equivalent Electrochemical Circuit
EIS	Electrochemical Impedance Spectroscopy
FPs	Fission Products
GDF	Geological Disposal Facility
GWd/tHM	Gigawatt-days per Tonne of Heavy Metal
HLW	High Level Waste
IGA	Intergranular Corrosion Attack
IGSCC	Intergranular Stress Corrosion Cracking
LO	Longitudinal Optical
LSV	Linear Sweep Voltammetry
LWR	Light Water Reactor
MSM	Master-Slave Manipulators
OCP	Open Circuit Potential
PTFE	Polytetrafluoroethylene
PZC	Potential of Zero Current
RIS	Radiation Induced Segregation
SEM	Scanning Electron Microscopy
SIMFUEL	Simulant Spent Nuclear Fuel
SNF	Spent Nuclear Fuel
SPW	Simulant Pond Water
SSPW	Simplified Simulant Pond Water
THORP	Thermal Oxide Reprocessing Plant
TRS	THORP Receipt and Storage
UK NNL	United Kingdom National Nuclear Laboratory
XPS	X-ray Photoelectron Spectroscopy
XRD	X-ray Diffraction

List of Publications

1. *AGR fuel corrosion: SIMFUEL-based method development in preparation for electrochemical studies of real spent AGR nuclear fuel electrode* – Yifeng Huang, Colin Boxall, David Hambley, Richard Wilbraham, MRS Advances, Volume 8, pages 7–13. Published: 13 October 2022.

1 Introduction and Background

1.1 Research Motivations and Objectives

The majority of the UK's operating nuclear fleet are Advanced Gas-cooled Reactors (AGR), which use annular ceramic UO_2 fuel pellets encased in a 20/25/Nb austenitic stainless-steel cladding to make up the fuel pins; the stainless-steel cladding is a niobium-stabilised low-carbon steel containing 20% chromium and 25% nickel.

Since 2022, the UK is no longer reprocessing spent nuclear fuel (SNF), instead moving towards an open fuel cycle, involving interim pond storage of SNF, with an aim for final disposal in a geological disposal facility (GDF).

As of 2019, the UK's holdings of AGR SNF stood at ~2200 tHM (tonnes of Heavy Metal) with an estimated eventual inventory of >4000 tHM by 2030, all ultimately destined for geological disposal. However, since GDF site construction has not started and with only rough estimates for planning purposes for waste package receipt by 2070s, is it likely that the UK's SNF holdings will remain in interim storage ponds for decades to come [1, 2].

Currently, the UK's AGR SNF is stored in wet ponds in demineralised water dosed with caustic to a pH of 11.4, with chloride concentrations kept to < 1 ppm [3]. The caustic dosing is intended to inhibit the corrosion of the fuel pin cladding and thus maintain its structural integrity during the storage period. However, in the case of any fuel pins in which the integrity of the cladding has been compromised during its time in pond storage, water ingress may occur through cladding wall breaches to contact the UO_2.

This may lead to the formation of a corrosion cell at the interface between the pond water and the physically coupled fuel pellet and cladding. The consequences of this remain to be fully understood, thus, it is necessary to investigate the electrochemical corrosion processes taking place at this interface under relevant wet storage conditions.

This research project aims to carry out electrochemical studies across a number of experimental campaigns, to study the corrosion behaviour of AGR SNF

materials. The main experimental campaign will involve the first-ever electrochemical study of legacy AGR SNF, conducted at the UK's National Nuclear Laboratory at the Windscale Laboratory, under hot-cell conditions.

Additionally, the use of non-active and lower-activity spent fuel simulants will also be explored to assist in the interpretation of the real-fuel study. Specifically, the study of AGR simulant spent fuels (SIMFUELs) and 20/25/Nb stainless-steel AGR cladding, under conditions relevant to UK AGR wet pond storage. A summary of the chapter contents is listed below:

- **Chapter 1**: A brief introduction to the history of nuclear power and general overview of the nuclear fuel cycle, with an overview of the UK's nuclear fuel cycle and describes aspects of UK's Advanced Gas-cooled Reactors.
- **Chapter 2**: A brief literature review of the supporting background electrochemistry theories and concepts and a summary of the literature studies that are relevant to the electrochemical corrosion studies of UO_2/AGR SIMFUELs and 20/25/Nb stainless steel AGR cladding.
- **Chapter 3**: Presents details of the experimental techniques, methods and materials used.
- **Chapter 4**: Presents the results and discussions of the corrosion studies of UO_2 and AGR SIMFUELs under baseline measurement conditions and conditions relevant to AGR wet pond storage.
- **Chapter 5**: Presents the results and discussions of the coupled/composite electrode studies of AGR cladding and 25 GWd/tU SIMFUEL under conditions relevant to AGR wet pond storage.
- **Chapter 6**: Presents the results and discussions from the experimental campaign conducting the first-ever electrochemical corrosion studies of legacy AGR SNF.
- **Chapter 7**: Presents the results and discussions from the experimental campaign investigating the method development for electrochemical surface oxidation studies of AGR SIMFUELs with in-situ μ-Raman spectroscopy.
- **Chapter 8**: Presents the summaries of the main conclusions from each chapter and further work.

1.2 The Nuclear Fuel Cycle

Otto Hahn and Fritz Strassman's discovery of nuclear fission in 1938 was a monumental milestone [4]. These findings would later be theorised by Lise Meitner and Otto Frisch, in which the phenomenon was described as the capture of a neutron by a nucleus, leading to the nucleus splitting into two non-equal parts [5]. Such reactions link together to form a sustained fission chain reaction and thus generate extreme magnitudes of energy. Subsequently, in 1939, Niels Bohr summarised that fission was more likely to occur in U-235 than in U-238, with slow-moving neutrons as opposed to fast neutrons. During this time, the concept of 'moderators' was proposed by Leó Szilárd and Enrico Fermi [6], which would slow down neutrons to an energetically favourable state for fission. Together, these ideas would eventually become a staple for our understanding of a classical nuclear fission reaction and enable a new era of science and engineering.

Civil nuclear programmes began to gather momentum at the start of the 1950s. Argonne National Laboratory in Idaho USA demonstrated the first ever electricity producing nuclear reactor, an Experimental Breeder Reactor (EBR-1), in December 1951. Five years later, in October 1956, the UK opened its first ever commercial nuclear power station, Calder Hall at Windscale, which operated four Magnox reactors, serving as dual purpose reactors to produce power and weapons grade plutonium.

A typical nuclear fuel cycle involves a series of connected industrial processes to produce electricity from uranium using nuclear power reactors. The main processes can be organised into three categories: the 'front-end' consisting of the fuel fabrication pipeline, the 'service period' during which the reactor is in operation, and the 'back-end' which refers to the management of waste and spent fuel.

The first stage of the cycle begins with the acquisition of uranium, via mining and extraction from uranium ore, the uranium content in the mined ore is very low and thus requires further processing. The process in which the uranium is extracted is known as milling; this process outputs a uranium oxide concentrate, typically known as 'yellowcake' and contains ~80% uranium. This large-scale

extraction is done via chemical leaching of the crushed ore (with sulphuric acid or strong alkaline), the extractant solution is further separated and precipitated to give U_3O_8.

Naturally, the uranium oxide from the mill contains only 0.7% of fissile U-235. Further treatment is required, in a process known as conversion and enrichment, to increase the percentage of U-235 to roughly 3.5% - 5%, which is the amount required for fuel in UK AGRs [7]. In the UK, the enrichment process starts with the import of UF_6 which is processed and enriched at Urenco, Capenhurst.

Oxide based fuel fabrication is the broader term which covers: the manufacture of the ceramic UO_2 fuel pellets, the encapsulation of the fuel pellets into steel tubes to give fuel rods, and the assembly of the fuel rods into a larger container suitable for placement inside a reactor. The specifics of the fuel pellet and fuel assembly design will vary depending on the type of reactor.

Typically, the ceramic fuel pellets are formed by pressing UO_2 powder into a pellet form and sintered at 1400°C to densify. In the case of an AGR, the pellets are then stacked inside stainless steel tubes and grouped together in a graphite 'sleeve' to form a 'fuel assembly'. Each AGR assembly contains 36 steel tubes, each with 64 pellets [8]. In the UK, fuel fabrication is carried out by Westinghouse Springfields Fuel Ltd.

During the service period, fuel is used in a reactor to produce electricity. Depending on the reactor type, the core can contain up to 75 tonnes of low-enriched uranium. Fuel assemblies in the core will be replaced with fresh fuel periodically to maintain reactor efficiency. During operation, the operators of the reactors will be concerned with fuel burn-up (or fuel utilisation), defined as the fission energy produced per unit mass of fuel and measured in gigawatt-days per tonne of heavy metal (GWd/tHM), hence, is equivalent to the atomic percentage of the total uranium content fissioned.

The back-end processes of the fuel cycle begin once the spent fuel is removed from the reactor. Upon its removal from a reactor, it is thermally hot and highly radioactive due to in-reactor-generated fission and activation products. Consequently, the spent fuel is placed into storage ponds at reactor sites to

cool down and allow radiation levels to decrease; for AGR SNF this period of storage typically lasts for ~100 days. Once it is safe for handling and transport, the SNF will be moved to an interim storage facility where it will be further cooled. The method of interim storage can be dry or wet and will vary depending on the national policy. Policy will also dictate the two possible fuel cycle routes:

- **Closed fuel cycle**: The SNF can be reprocessed to recover the usable uranium, which is recycled to form new fuel that subsequently re-enters the fuel cycle.
- **Open fuel cycle**: The SNF can be placed into interim wet or dry storage and eventually disposed of in a repository.

1.3 Spent Nuclear Fuel Management in the UK

Until November 2018, UK AGR SNF was reprocessed at the Thermal Oxide Reprocessing Plant (THORP) at Sellafield. However, due to the change in the UK's energy policy, SNF reprocessing operations at THORP have now ceased [9]. Future plans for all UK SNF will involve final disposal in a GDF.

The GDF may not be open for receipt of spent fuel until at least ~2075 and until then AGR SNF will be kept in interim storage ponds at Sellafield. These ponds are dosed with NaOH (to pH 11.4) which acts as a corrosion inhibitor for the stainless steel cladding [10]. Interim storage periods for SNF may now be extended by up to 100 years following the adoption of an open fuel cycle [11].

1.3.1 Interim Storage and Spent Fuel Disposal

The end of SNF reprocessing means the extension of the length of time at which SNF is stored in interim storage, potentially beyond the original design life of the interim storage facility. The UK currently operates under a 'storage and disposal' option for the backend of an open fuel cycle. This is the holding case for nations that do not yet have a disposal facility but have the need for SNF and high-level waste (HLW) management. This interim approach is a result of difficulties in locating and licensing an appropriate repository site. In the UK the availability of a disposal facility is planned for 2075 at the earliest. The current approach follows the preferred option to manage SNF via interim wet storage in

the THORP Receipt and Storage (TR&S). This would mean an extension of the expected lifetime of the current wet storage ponds to accommodate spent fuel for up to 25 years or even longer [12] [13].

The UK has over 25 years of experience in wet-storing SNF. A recent post-storage examination study of AGR spent fuel showed that 25+ year old spent fuel exhibited minimal deterioration of the fuel pellet or cladding after being stored in caustic ponds. During storage, the spent fuel is fully submerged underwater, the outer steel cladding is in direct contact with the water and the fuel pellets are sealed inside the cladding. Thus, the main risk associated with this storage is the potential for cladding corrosion, a process that may be promoted by sensitisation of stainless-steel cladding caused by Radiation Induced Segregation (RIS), a phenomenon discussed later in this thesis.

Since 1986, the risk of corrosion has generally been minimised via alkaline dosing of the storage pond waters with NaOH to a pH of ~11.4 [14]. However, there are other scenarios where the steel cladding may be compromised, exposing the fuel pellets to the pond waters, for example: mechanical damage to the fuel pins during handling or failure of fuel pins during burn-up in the reactor.

If a breach were to occur during pond storage, fission gases within the fuel pin would be released, along with soluble fission products from the boundary between the fuel and the cladding. Contact with water could also establish an oxidative environment between the cladding, fuel pellet and water, by the formation of a corrosion cell with the surrounding water acting as an electrolyte which may contain chemical species that could promote corrosion of the cladding, fuel pellet, or both.

As well as dosing to pH 11.4 to inhibit corrosion, the in-pond conditions at TRS are kept to a low chloride concentration of <0.1 ppm to prevent chloride-accelerated corrosion processes and at a temperature of 24°C. However, following the closure of THORP and the end of reprocessing, changes have been proposed to increase the loading of spent fuel to accommodate future SNF. To facilitate this, a new racking system has been proposed which would mean closer packing of the fuel and thus an increase in storage pond water

temperatures [15]. This may affect the extent of protection afforded by the current caustic dosing.

The UK government has set out to build a GDF with initial actions laid out in a 2014 White Paper [9]. These actions were to establish the start of land-use planning process, community engagement and national screening of geological locations suitable for a GDF. A GDF itself is a site for storing and isolating radioactive waste deep inside a suitable rock formation, approximately between 200 m and 1000 m underground and involves a highly engineered multi-barrier concept. The idea is to isolate and contain the waste as it decays naturally over time and prevent radioactivity from reaching the surface at harmful levels over the disposal lifetime [9].

The use of a multi-barrier approach is one of the main defences in a GDF, which is a system of multiple layers of protection surrounding the wasteform, with each layer designed to stop or slow down the leaching of radioactivity over geological timescales. Current operations for the UK government involve searching for a suitable site with a willing community, and it is expected the planning of this will take 15-20 years with approval from the regulators and stakeholders (Office for Nuclear Regulation, Nuclear Waste Services, Environmental Agency, Natural Resources Wales, and Scottish Environment Protection Agency) before any construction can begin.

1.4 Advanced Gas-cooled Reactors and Fuel Design

The UK's nuclear power comes from its fleet of 9 reactors, 8 of which are Advanced Gas-Cooled Reactors (AGR). These are spread over England and Scotland, generating power through 470-610 MW turbine-generator units. The AGR was designed in the UK and developed as part of the generation II British Gas-Cooled Reactors following on from the Magnox reactor design.

AGR reactors are graphite moderated and cooled with CO_2. The heat generated within the core is transferred to the pressurised CO_2 gas in the reactor's primary coolant circuit, which transfers its heat to a secondary water cooling circuit.

This water boils to produce superheated steam for turning the turbine-generators [16]. The AGR fuel assembly consists of low-enriched cylindrical

annular UO_2 pellets (typically between 2.5 – 3.5% enrichment), with dimensions of: 14.6 mm length, 6.4 mm ID and 14.6 mm OD [17], stacked vertically inside 20/25/Nb stainless-steel cladding tubes and sealed and back-filled with helium to form fuel pins.

Each element contains 36 fuel pins surrounded by two concentric graphite sleeves. These are stacked vertically to form a fuel assembly or ‘stringer’ (Figure 1-2). The 20/25/Nb stainless steel cladding tubing has helical machined ribbed fins on the outer surface (Figure 1-1) to improve heat transfer between the cladding and the CO_2 gas coolant.

Figure 1-1: Multi-start ribbed AGR 20/25/Nb stainless steel cladding.

Figure 1-2: AGR Fuel element (This figure is released under a CC BY-NC-SA 4.0 Licence from Science Museum Group. AGR Fuel Element, c 1982. 1982-1575 Science Museum Group Collection Online [18])

1.4.1 UO_2 and Spent Fuel Simulants

The crystal structure of UO_2 is cubic fluorite, as shown in Figure 1-3, consists of a uranium U^{4+} face-centred cubic lattice, which occupies the octahedral sites, coordinated to eight other uranium atoms. Together with oxygen O^{2-} forming a cubic sublattice, which occupies the tetrahedral sites [19].

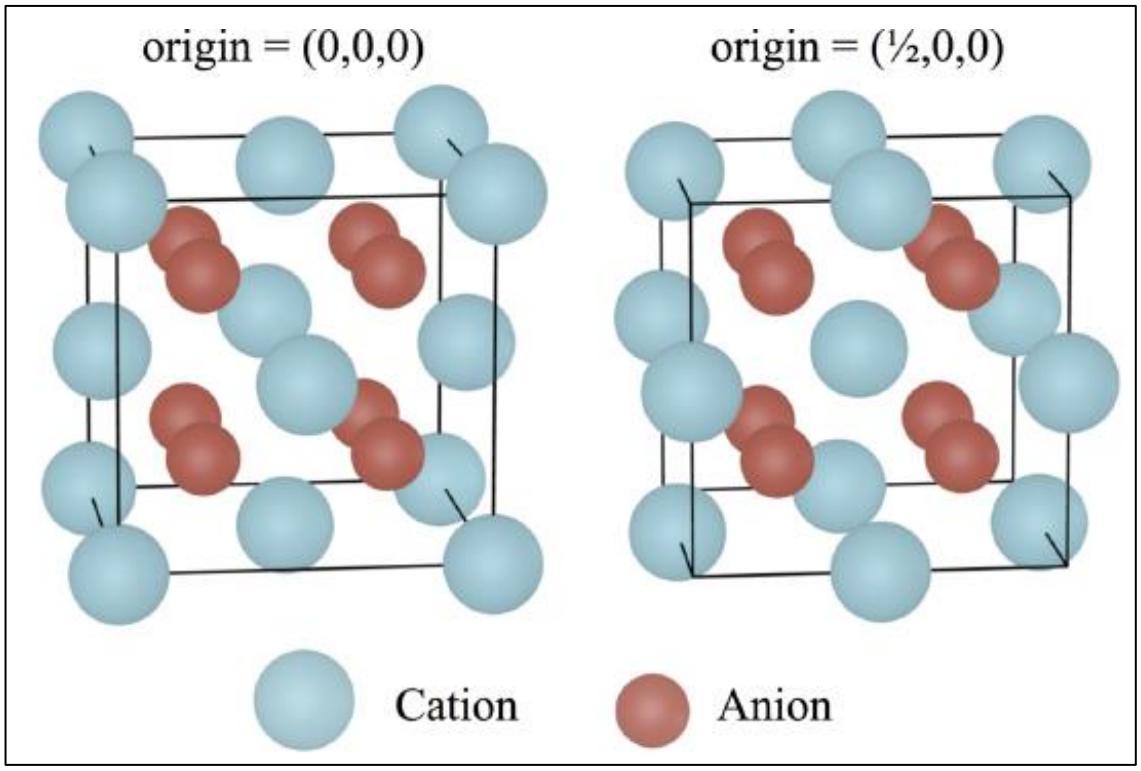

Figure 1-3: Cubic fluorite unit cell of illustrating the uranium (cation) FCC lattice and the oxygen (anion) cubic sublattice (This figure is released under a CC BY-NC-SA 4.0 Licence from LibreTexts libraries [20]).

Such a lattice presents an abundance of empty interstitial sites located within the oxygen sublattice, which can accommodate interstitial oxygen ions (O_i). This process leads to slight distortions in the oxygen cubic sublattice which introduces random point defects. It also results in the material being rendered hyperstoichiometric, in the form of UO_{2+x}, where the degree of hyperstoichiometry changes with the amount of incorporated oxygen.

High degrees of hyperstoichiometry results in the formation of extended defect clusters, such as Willis and cuboctahedral clusters and ultimately the onset of the transition from cubic to tetragonal structure [21-23]. Incorporation of oxygen atoms into the U-O cubic fluorite lattice would require oxidation of the uranium atoms to U(V)/U(VI).

The process of UO_2 oxidation to higher oxides has been widely accepted in literature as a two-stage process involving the initial oxidation of UO_2 to U_3O_7/U_4O_9, followed by further oxidation to U_3O_8 [24-27]:

$$UO_2 \longrightarrow U_3O_7/U_4O_9 \longrightarrow U_3O_8$$

Equation 1-1

The formation of these main oxides of uranium is strongly dependent upon conditions of temperature and pressure. U_3O_7 forms at 150°C as a phase transformation and further oxides to U_3O_8 at 375°C. Upon further heating, U_3O_8 will convert back to UO_2 [28].

From the above, it can be seen that in its dioxide form, the UO_2 lattice can readily accept new oxygen atoms, this deviation from its stoichiometric composition can arise in the reactor during irradiation or during manufacture of the fuel pellets. This may lead to unfavourable changes to the properties of the fuel such as the melting temperature and creep rates [29].

Although much of the existing fuel research is carried out on pure UO_2, as a basic analogue to real spent fuel, these results cannot be considered a true representation of in-reactor irradiated fuels. Simple UO_2 lacks the chemistry associated with the wide range of fission products present in spent fuel. However, due to its high radioactivity, the handling of real irradiated spent fuel poses a limiting step towards scientific research, thus a more practical analogue is needed.

An alternative to pure UO_2 would be to use simulated spent fuels also known as SIMFUELs. These materials aim to simulate the composition of real SNF using a majority composition of UO_2 (>90% wt.), doped with a variety of non-radioactive elements to simulate the fission product composition, depending on the degree of burn-up.

Another advantage to using custom-made simulant fuel pellets is the ability to fine-tune what goes into the simulated spent fuel matrix; this allows for a bottom-up approach that enables the effects of single fuel dopants to be studied in so-called split-SIMFUELs.

The majority of published studies on uranium oxide fuels and associated spent fuel simulants are relevant to Light Water Reactor (LWR) and CANDU Pressurised Heavy Water Reactor fuels [17, 30-37]. The exact composition of dopants and burn-ups simulated will differ from AGR SIMFUELs, due to differences in fuel cladding material, disposal containment systems, pre-disposal interim storage and geological disposal environments. Thus, bespoke AGR SIMFUELs have been created and studied by a number of authors [38-42], and will be discussed further in Section 1.4.3.

1.4.2 Composition of Spent Fuel

Post irradiation, UO_2 fuel properties will change. In particular, the fission products will result in the formation of new species and chemical compositional changes in the spent fuel matrix. This will affect how the spent fuel behaves in its storage environment through the different stages of interim pond storage.

There are three main categories of radionuclide inventory that occur in the spent fuel matrix which have been identified as: (i) at the fuel-cladding gap, (ii) at the fuel grain boundaries, and (iii) at the intra-grain fuel matrix [43].

Each of the three main inventories, identified above, will have differing amounts of the four main categories of fission products (FPs) associated with them. These four groups of fission products found within a typical UO_2 spent fuel can be summarised as follows [44]:

- **Gaseous/volatile species** (He, Kr, Cs, I) which can migrate easily within the fuel matrix. A small percentage can migrate to the fuel sheath gap, and some that migrate to the grain boundaries. But the majority is trapped in the form of fission gas bubbles.
- **Non-volatile fission products** but unstable as oxides (Mo, Ru, Pd), small amounts of these can form noble metal (ε) particles at grain boundaries.
- **Fission products which are stable as oxides** but incompatible with UO_2 matrix (Rb, Cs, Ba, Zn, Nb, Mo, Te, Sr), these can separate into precipitates to form secondary phases such as perovskites, also known as ‘grey-phases’.

- **Elements retained by the fuel matrix**, actinides (Np, Pu, Am, Cm) and lanthanides (La, Ce, Pr, Nd, Pm, Sm, Eu, Gd, Y). The incorporation of lanthanides and other rare earth elements will also enhance the electrical conductivity of the UO_2 SIMFUELs. This has implications for the electrochemical behaviour of the SIMFUELs [34, 45].

1.4.3 AGR SIMFUELs

The first UK AGR-specific spent fuel simulants were processed, characterised and reported by Hiezl et al. [46]. These SIMFUELs were made to simulate SNF which have been cooled for 100 years, at 25 GWd/tU and 43 GWd/tU burn-up.

Table 1-1 shows the at.% of the oxides present in each of the SIMFUEL simulated burn-ups. The microstructure measurements of the SIMFUEL pellet average grain sizes (4.2 ± 0.6 μm for low burn-up and 3.0 ± 1.3 μm for high burn-up) were reported to be comparable to the lower end of the average grain sizes for real SNF (3 - 30 μm).

The manufactured SIMFUELs were also able to simulate a variety of secondary phases such as metallic and oxide precipitates, which are present in real spent fuel.

The SIMFUELs used in this study have been obtained from this batch of manufactured pellets and will therefore be of the same composition and material specifications and produced using the manufacturing processes outlined in Hiezl et. al [46, 47].

SIMFUEL Compounds		100 years cooling time	
Oxides	**Powder d(0.5)/μm**	**25 GWd/t U**	**43 GWd/t U**
UO_2	3.80 ± 0.25	97.587	95.87
Nd_2O_3	21.68 + 0.32	0.483	0.827
ZrO_2	15.24 ± 0.01	0.369	0.602
MoO_3	21.42 ± 0.34	0.334	0.566
RuO_2	3.88 ± 0.07	0.257	0.454
$BaCO_3$	-	0.244	0.435
CeO_2	22.87 ± 0.11	0.193	0.329
PdO	46.12 ± 0.24	0.09	0.199
Rh_2O_3	0.70 + 0.25	0.038	0.056
La_2O_3	6.54 ± 0.12	0.096	0.16
SrO	-	0.032	0.05
Y_2O_3	10.17 ± 0.19	0.041	0.064
Cs_2CO_3	-	0.191	0.309
TeO_2	-	0.044	0.079

Table 1-1: AGR SIMFUEL compositions calculated by FISPIN in at.% [46].

1.4.4 20/25/Nb Stainless Steel Cladding

20/25/Nb austenitic stainless steel was chosen as the cladding material for AGR fuel pins due to its favourable high temperature resistance to withstand in-reactor gas temperatures, thus, providing longevity within the reactor core. Table 1-2 shows the composition of the 20/25/Nb stainless steel.

Component	Cr	Ni	Nb	Mn	Si	C	N	Fe
% wt.	20.12	24.75	0.70	0.62	0.57	0.049	0.016	balance

Table 1-2: Chemical composition of 20/25/Nb stainless steel obtained from manufacturer (refer to Section 3).

The presence of 0.7 % wt. niobium alloy acts to protect the steel against corrosion susceptibility associated with chromium carbide formation, facilitated by the presence of dissolved carbon in the steel matrix.

The formation of chromium carbides decreases the concentration of chromium at the grain boundaries, thus negatively impacting the corrosion protection derived from chromium oxide formation.

The niobium protects against chromium carbide formation through the competing formation of niobium carbide nanoparticles throughout the steel matrix, thus preventing the carbon from participating in chromium carbide formation [48, 49].

1.5 Research Objectives

As noted earlier in Section 1.1, this research project aims to carry out electrochemical studies across a number of experimental campaigns, to study the corrosion behaviour of AGR SNF materials, under conditions relevant to UK AGR wet pond storage. This includes experimental studies on real legacy AGR SNF, AGR SIMFUELs, and 20/25/Nb stainless-steel AGR cladding. The following thesis chapters will present and discuss these studies.

2 Background and Literature Review

This chapter introduces the supporting background and literature relevant to the electrochemical corrosion studies of UO_2/AGR SIMFUELs and 20/25/Nb stainless steel AGR cladding.

Section 2.1 describes the relevant background concepts, theories and processes associated with electrochemical corrosion studies.

Section 2.2 presents a brief literature review summarising the properties of UO_2/SIMFUELs and the relevant studies of the factors influencing its corrosion behaviour.

Section 2.3 presents a brief literature review summarising the general corrosion processes of stainless steels and the relevant studies of the factors influencing the corrosion behaviour of typical stainless steels and 20/25/Nb stainless steel AGR cladding.

2.1 General Electrochemical Concepts

Electrochemistry is the study of the relationship between a chemical process and its associated electrical changes. These processes can be either destructive, constructive, or both simultaneously. In a typical electrochemical process, a chemical reaction takes place consisting of a reduction and oxidation reaction, in which the transfer of electrons between the reactive species is mediated by the passage of these electrons through an external circuit.

Corrosion processes are also electrochemical reactions. These naturally occurring processes can cause destruction to the material of interest, for example, the rusting of iron.

In an electrochemical redox reaction, the use of an externally applied potential through an electrode can generate a thermodynamically favourable state for electron transfer processes to take place. The driving force behind such a reaction comes from the ability to control and alter the voltage and thus the energy of the electrons.

Electrochemistry is therefore a useful tool for probing corrosion processes; the techniques used can be categorised as ‘dynamic methods’ since these methods

investigate reactions where the position of electrochemical equilibrium deviates depending on the type of external influence [50].

The following sections will detail a typical electrochemical corrosion process and the underlying theory which describes the behaviour and relationships within the mechanism of such processes.

2.1.1 Corrosion as an Electrochemical Process

In the first instance, it is useful to consider a basic corrosion reaction in which a metal is being destructively transformed by interactions with its surrounding environment, as seen in Figure 2-1.

In such a process, the metal is undergoing oxidation and entering the solution/environment in the form of its metal ions; this reaction involves the loss of electrons (i.e. $M \rightarrow M^{m+} + me^{-}$) and is referred to as the anodic reaction site. To accompany the loss of electrons, a reduction reaction must also be taking place simultaneously, in the form of $X^{x+} + xe^{-} \rightarrow X$; this reaction involves the gain of electrons and is referred to as the cathodic reaction site.

These two half-cell reactions must complement each other via the exchange of electrons to give a full cell or redox reaction.

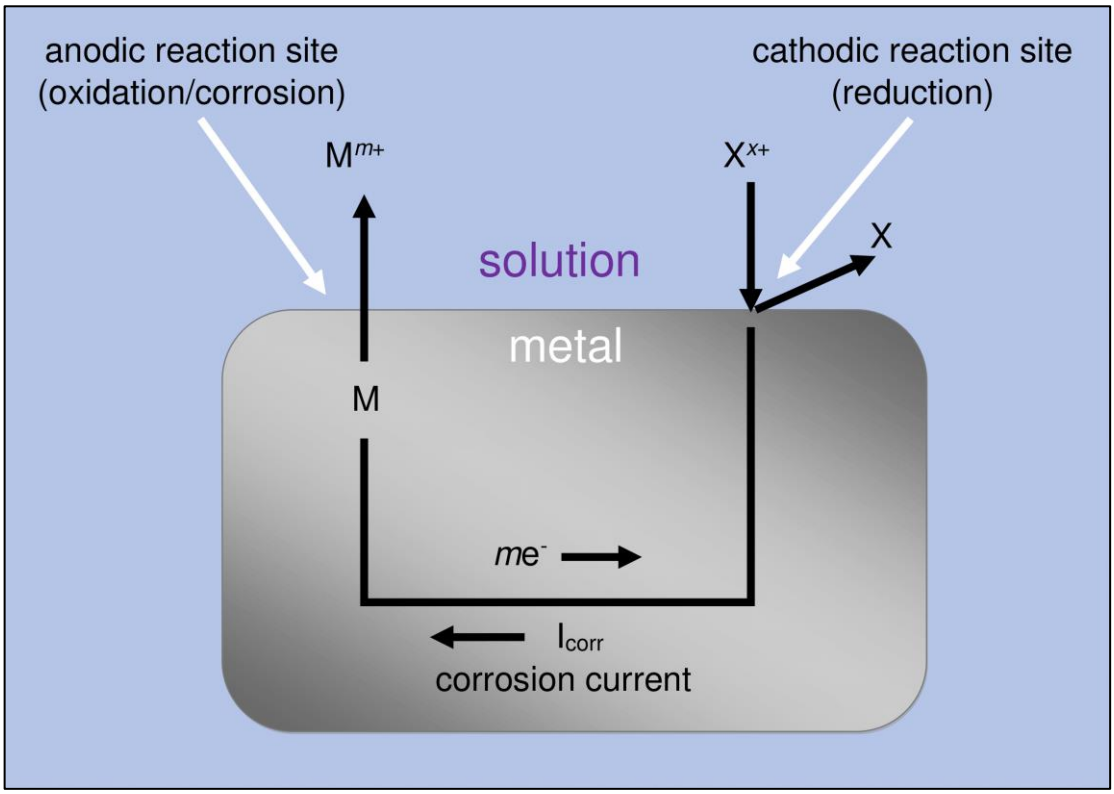

Figure 2-1: Schematic of a basic corrosion reaction represented as an electrochemical process [51].

Several general forms of corrosion exist. In its simplest interpretation, uniform corrosion occurs when anodic and cathodic sites are near-coincident and uniformly spread over the corroding surface. Localised corrosion is said to occur when the opposite is true, i.e., when the anodic and cathodic sites are spatially separate and do not change over time, with corrosion then considered to occur only at the anodic site [51]. This interpretation will depend greatly on the specific systems of interest and on the scale and magnitude of the observation.

For example, when a piece of iron exposed to the natural environment is in direct contact with water, the surface of the iron acts as the anodic site, where the iron itself is oxidised:

$$Fe(s) \rightarrow Fe^{2+}(aq) + 2e^-$$

Equation 2-1

The free electrons released by the iron oxidation reaction are then consumed by the cathodic process also occurring at the surface of the iron. However, in this

case the iron is acting an electrode that transfers electrons to the oxygen in the air and the adjacent water:

$$O_2(g) + 2H_2O(l) + 4e^- \rightarrow 4OH^-(aq)$$

Equation 2-2

For each overall electrochemical process, the separate anodic and cathodic reactions – in this instance iron oxidation and oxygen reduction, respectively – are referred to as half-cell reactions.

In the example considered here the hydroxide ions produced within the solution adjacent to the iron surface may react with the Fe(II) at the iron surface to produce an iron hydroxide precipitate at the iron surface which is oxidised further to produce iron oxide. The net result is the pitting of the iron surface as a result of the iron dissolution process and correlated deposit of rust, as illustrated in Figure 2-2:

$$\text{(a)} \qquad Fe^{2+}(aq) + 2OH^-(aq) \rightarrow Fe(OH)_2(s)$$

$$\text{(b)} \qquad 4Fe(OH)_2(s) + O_2(g) \rightarrow 2Fe_2O_3 \cdot H_2O(s) + 2H_2O(l)$$

Equation 2-3(a) and (b)

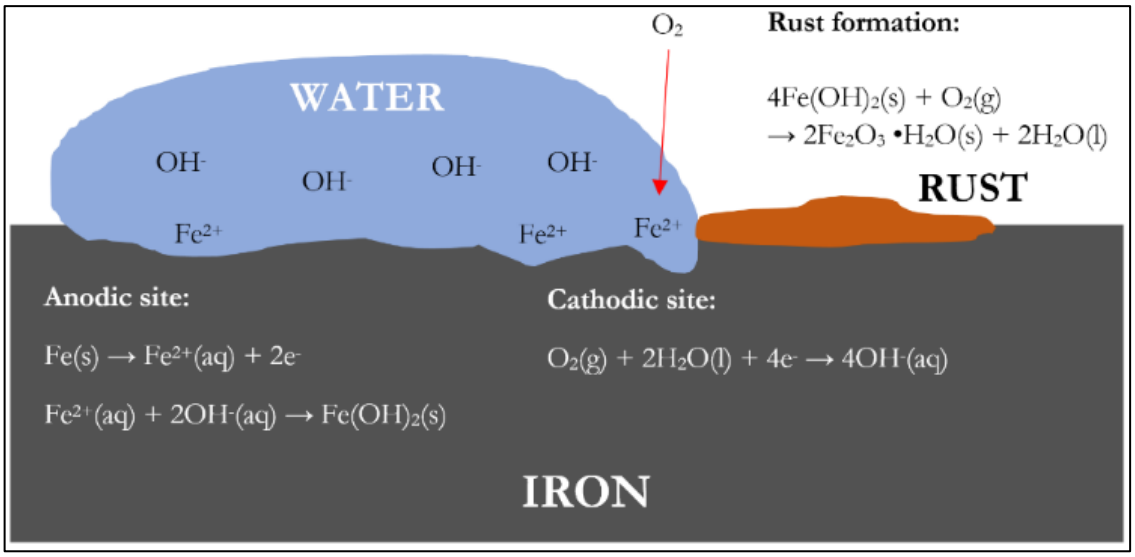

Figure 2-2: Schematic of rust formation, showing the coupled redox reactions between iron, water, and air.

The movement of electrons in these reactions, produces a flow of current known as ‘Faradaic current’ because the overall process involves the interfacial transfer of electrons. The progress of Faradaic processes is described by Faraday’s first law of electrolysis:

$$Q = nFm$$

Equation 2-4

Where n is the number of electrons participating in the reaction/equation, F is the Faraday constant, and m is the number of moles of substance produced or consumed during the reaction, which is proportional to the total electrical charge, Q, passed through the electrode.

2.1.2 Reference Electrodes

An important quantity that can be measured between the anode and the cathode is the potential difference. This is derived from the difference in redox potentials between the anodic and cathodic half-cell reactions and is a direct measure of the thermodynamic driving force of the process under steady state conditions, the redox reactions between metal and the solution are at equilibrium.

The absolute values of the potential at either the anode or cathode cannot be directly measured, although the potential of either electrode can be measured against a known standard reference electrode system. Such reference electrodes behave as the baseline for the measured potential difference across an electrochemical cell.

A reference electrode system is constructed from a half-cell reaction which produces a known constant potential and passes virtually no current. A common reference electrode system is the Ag/AgCl electrode [52] (measured at ~-209 mV vs. the Standard Hydrogen Electrode and ~-35 mV vs the Saturated Calomel Electrode), shown in Figure 2-3, which consists of a silver chloride coated silver wire submerged in an electrolyte solution of concentrated chloride. The overall cell reaction is $Ag^0 + Cl^- \rightleftharpoons AgCl + e^-$.

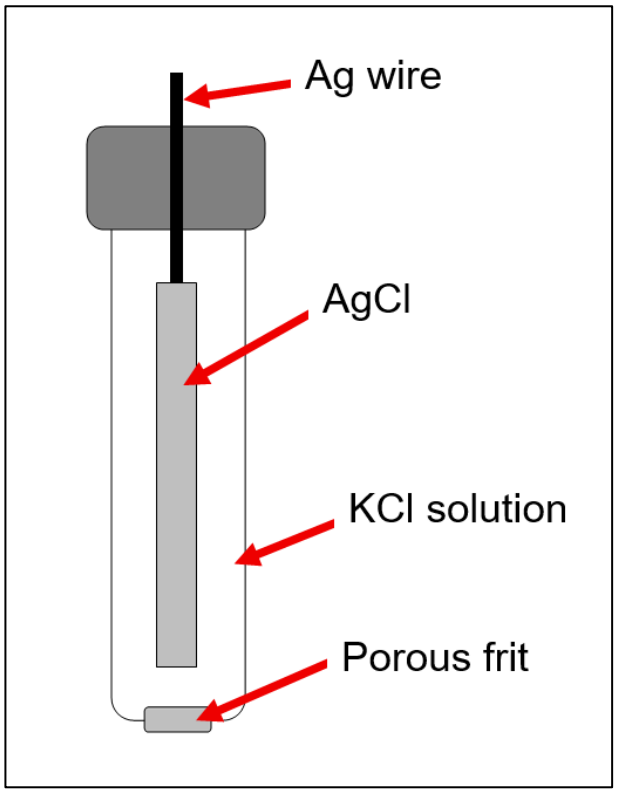

Figure 2-3: Schematic of an Ag/AgCl reference electrode.

2.1.3 Voltammetry

The term voltammetry applies to a family of techniques used for studying electrochemical systems, all of which involve the application of an external potential (E) through an electrode and recording of the resultant current (i) flow generated in the cell, over time (t).

According to Faraday's first Law and as may be inferred from above Equation 2-4, the passage of current through the system will cause the concentration of the active species in the cell to increase or decrease due to simultaneous oxidation and reduction reactions.

Measurement of the current, and thus change of cell composition, as a function of the applied external potential allows for the probing of materials and their oxidative and reductive process in various electrolyte media and under different conditions.

To carry out voltammetry, an electrochemical cell setup is required, as shown in Figure 2-4, typically consisting of a three-electrode system: a working electrode

(WE), a reference electrode (RE), and a counter/auxiliary (CE) electrode, all submerged in an electrolyte.

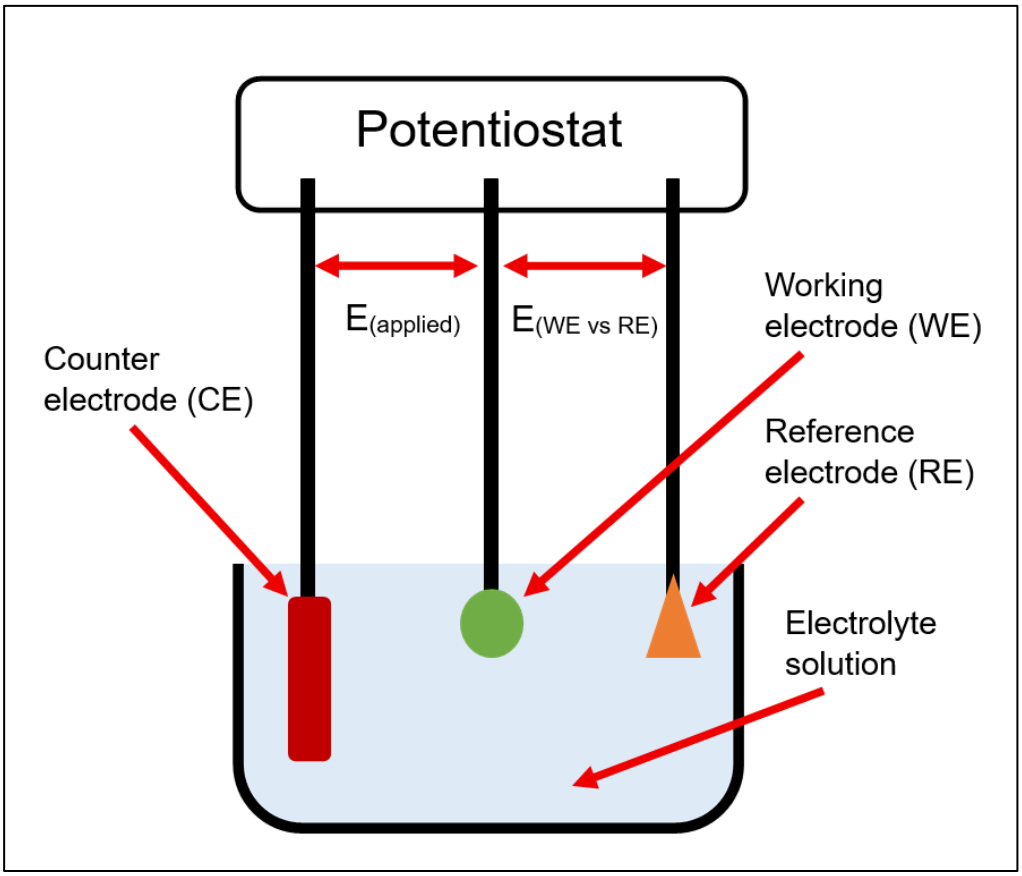

Figure 2-4: Schematic of a simple three electrode electrochemical cell connected to a potentiostat showing the connections of the electrodes to the potentiostat. $E_{(applied)}$ indicates the applied potential between the CE and WE and $E_{(WE\ vs\ RE)}$ indicates the potential recorded between the WE and RE.

These are all connected to a potentiostat which serves to either apply an external voltage and measure the generated current (potentiostatic mode) or apply an external current and measure the resultant voltage (galvanostatic mode). Under convention, a working electrode is where the redox process of interest occurs.

During voltammetry, such electrolytic cells require the application of an external potential that is different to the Open Circuit Potential (OCP), to drive the electrochemical reaction. OCP is a measure of the system's resting potential over time at steady state equilibrium.

In summary, we have discussed the background electrochemical concepts which are to support the corrosion studies of UO_2, SIMFUELs and 20/25/Nb stainless steel, presented later in this thesis.

We now move onto the literature review section of Section 2.2 which supports the understanding of the corrosion behaviour of UO_2 and SIMFUELs.

Section 2.3 supports the understanding of the corrosion behaviour of 20/25/Nb stainless steel relevant to the studies of AGR cladding.

2.2 Corrosion Behaviour of UO_2 and SIMFUELs

UO_2 is the main fuel type choice for the majority of nuclear reactors, including UK-specific AGRs. Prior to irradiation in a reactor, uranium dioxide fuels typically exhibit a near stoichiometric composition of UO_2.

As described in Chapter 1 Section 1.4.1, pure undoped-UO_2 has a perfect cubic fluorite crystal structure, see Figure 1-3 for the unit cell. This unit cell contains empty interstitial sites that are capable of accommodating additional oxygen atoms which can lead to a distortion of the lattice and induce hyperstoichiometry in the form of UO_{2+x}. Further incorporation of oxygen atoms into the lattice is accompanied by the oxidation of the uranium atoms, which leads to the formation of higher oxides of UO_2, such as U_3O_7, U_4O_9 and U_3O_8.

Sections 2.1.1, 2.1.2, and 2.1.3 provides an overview of the background theory on the structure, stoichiometry and voltammetric behaviour of undoped-UO_2, relevant to its oxidation/corrosion behaviour. In addition to the oxidation of the UO_2, the in-reactor irradiation of UO_2 fuel will also result in the formation of new fission product species in the lattice, known as the spent fuel matrix.

As described in Chapter 1 Section 1.4.2, SIMFUELs can serve as experimental analogues to real irradiated SNF, which aim to simulate the matrix composition of real spent fuel. These SIMFUEL materials can be doped with a variety of non-radioactive elements to simulate different fission product compositions, including those specific to UK AGR spent fuels, as described in Chapter 1 Section 1.4.3. Section 2.2 presents a literature review of the studies of the factors that affect the oxidation/corrosion of undoped-UO_2 and doped-UO_2/SIMFUELs and specifically studies relevant to AGR SIMFUELs.

2.2.1 Structure and Stoichiometry

Pure undoped-UO_2 is near stoichiometric and adopts a cubic fluorite lattice, as discussed in Chapter 1 Section 1.4.1. Due to the vacant octahedral site at the centre of its unit cell, in the oxygen sub-lattice, see Figure 1-3 for unit cell, it can easily accommodate additional oxygen interstitial anions.

As a result of this, the cubic fluorite lattice is considered to be more flexible and capable of generating derivatives compared to other basic lattice structures [23, 53]. Such flexibility is advantageous in the context of UO_2-based nuclear fuels as the structure and composition of the fuel material is subject to many changes during reactor irradiation, due to the formation of activation and fission products.

Due to the flexibility of the cubic fluorite lattice, many of these activation and fission products may be readily incorporated into the UO_2 matrix as a solid solution, producing a doped UO_2 lattice. Those activation and fission products that are not accommodated in the solid solution, either for crystallographic or thermodynamic reasons, may instead form solid precipitates such as nanoparticulate deposits of noble metals [53].

The introduction of fission products into the UO_2 matrix inevitably makes the material inherently non-stoichiometric, tending towards either the hypo- or hyperstoichiometric forms of UO_{2-x} or UO_{2+x}, respectively depending upon the local oxidative stress. However, such changes are again readily accommodated by the flexibility of the cubic fluorite structure.

Such deviations from stoichiometric UO_2 can also occur during the fuel fabrication stage, for example, hyperstoichiometry can also occur due to incomplete sintering during the fabrication and due to oxidation caused by accidental exposure to air [53].

Many of these structural changes can be most easily and safely explored using spent fuel simulants or SIMFUELs. Two experimental methods with which to study the morphological and structural changes that occur as a result of the presence of activation and fission products in spent fuel matrices are: Scanning Electron Microscopy (SEM) and μ-Raman spectroscopy.

In the case of μ-Raman spectroscopy, this technique enables the analysis of the surface structure, the effects of dopants on the UO_2/SIMFUEL structure, and the characterisation of stoichiometric and hyper-stoichiometric UO_2 phases and their relation to defect structures and surface reactivity. Chapter 3 details the experimental methods used for μ-Raman spectroscopy.

The Raman spectra of a perfect cubic fluorite structure of undoped stoichiometric UO_2, shown in Figure 2-5, exhibits an intense vibration at 445 cm^{-1}, typically associated with the fundamental U-O stretch [54].

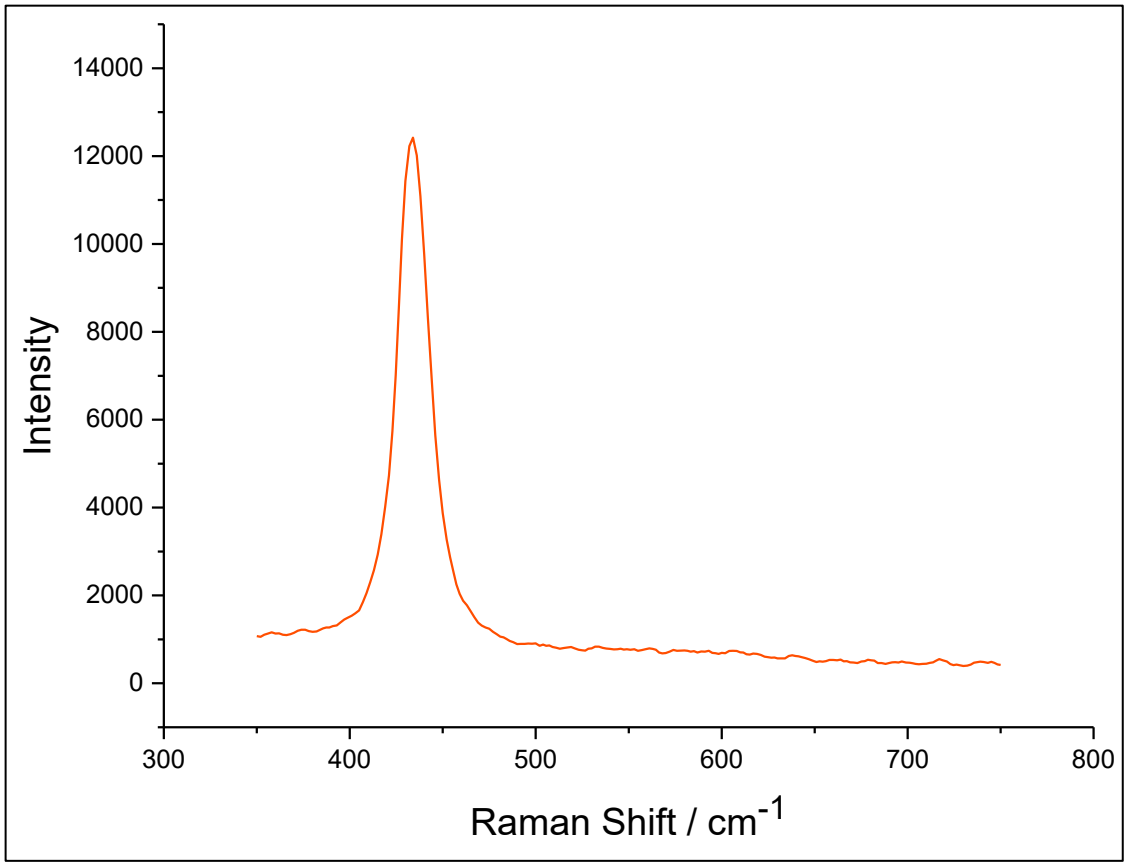

Figure 2-5: Raman spectra of undoped UO_2 showing the intense fundamental U-O stretch at 445 cm^{-1}.

In contrast, the Raman spectra acquired from a sample of non-stoichiometric $UO_{2.1}$, Figure 2-6(B)/(C)/(D), shows varying degrees of hyperstoichiometry in the form of deviations from the spectra of the cubic fluorite stoichiometric UO_2. As a result of the lattice distortions, the fundamental U-O stretch shows a decrease in the relative peak intensity which is also accompanied by the

appearance of a new adjacent broad band, typically associated with UO_2 lattice defects.

In this example the defected UO_2 lattice is a result of hyperstoichiometry caused by oxygen incorporation into the matrix, this specific scenario is further discussed in the text below.

Similar changes to the pure UO_2 Raman spectra are also observed in the spectra of doped-UO_2 or SIMFUELs materials. In these materials, the lattice defects are mainly associated with the incorporation of dopants into the UO_2 matrix but can also additionally be associated with the aforementioned hyperstoichiometry, depending on the conditions and characteristics of the material under study.

Further discussions on the effects of dopants on the UO_2 matrix of undoped-UO_2 and SIMFUELs are presented in Sections 2.2.4.4 and 2.2.5, respectively.

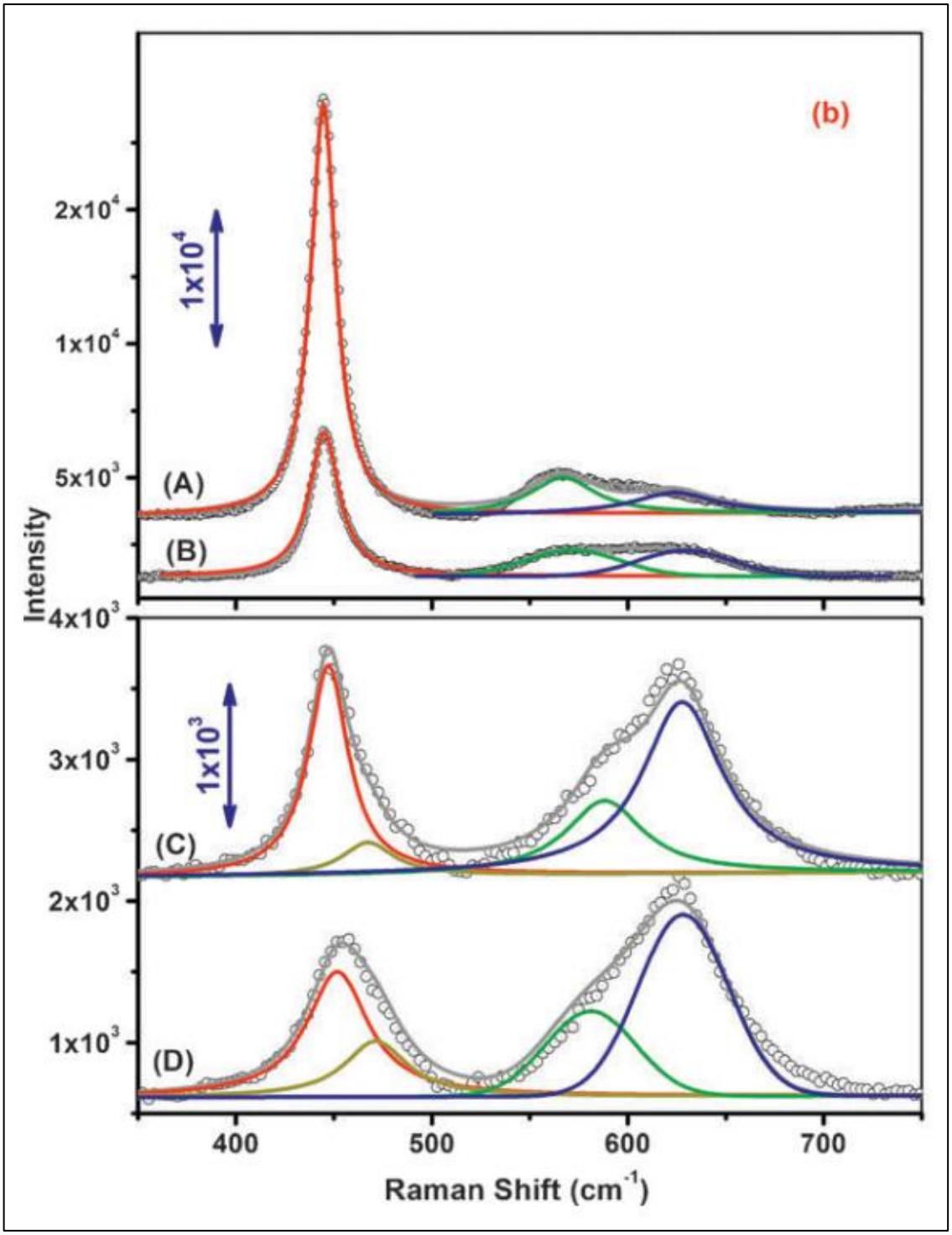

Figure 2-6: Raman spectra recorded on different grain types with varying degrees of UO hyper-stoichiometries: (A) smooth grain type, near stoichiometric, (B) very shallow horizontal stepped patterns, slightly hyper-stoichiometric, with $x \leq 0.13$, (C) pronounced horizontal stepped pattern, non-stoichiometric, with $0.13 \leq x \leq 0.24$, (D) vertical terraced stepped pattern, highly non-stoichiometric, with $0.25 \leq x \leq 0.33$. The Raman spectra shows the deviation from a stoichiometric UO_2 spectra (see Figure 2-5), this is shown as a decrease in the relative peak intensity of the fundamental U-O stretch and accompanied by the appearance of a new adjacent broad band, typically associated with UO_2 lattice defects (Figure taken with permission from [23, 55]).

Using a combination of μ-Raman spectroscopy and SEM, it has been possible to characterise the different UO_2 surface grain stoichiometries and thus determine and correlate four distinct defect structure phases as a function of UO_2 hyperstoichiometry.

In studies by He et al., it was reported that the degree of non-stoichiometry can be related to the surface grain morphology, as shown by the comparison of the Raman spectra of Figure 2-6 with the surface SEM image of the $UO_{2.1}$ surface of Figure 2-7 from which they were recorded from [23, 55].

Figure 2-7 also includes stoichiometry data measured by EDX (Energy-Dispersive X-ray) spectroscopy, showing that the smooth grains, type (A), indicate a near stoichiometric composition of $UO_{2.01}$ and the rough/spiralled grains, type (B), (C) and (D), indicate a non-stoichiometric composition of $UO_{2.15}$, $UO_{2.22}$ and $UO_{2.31}$, respectively.

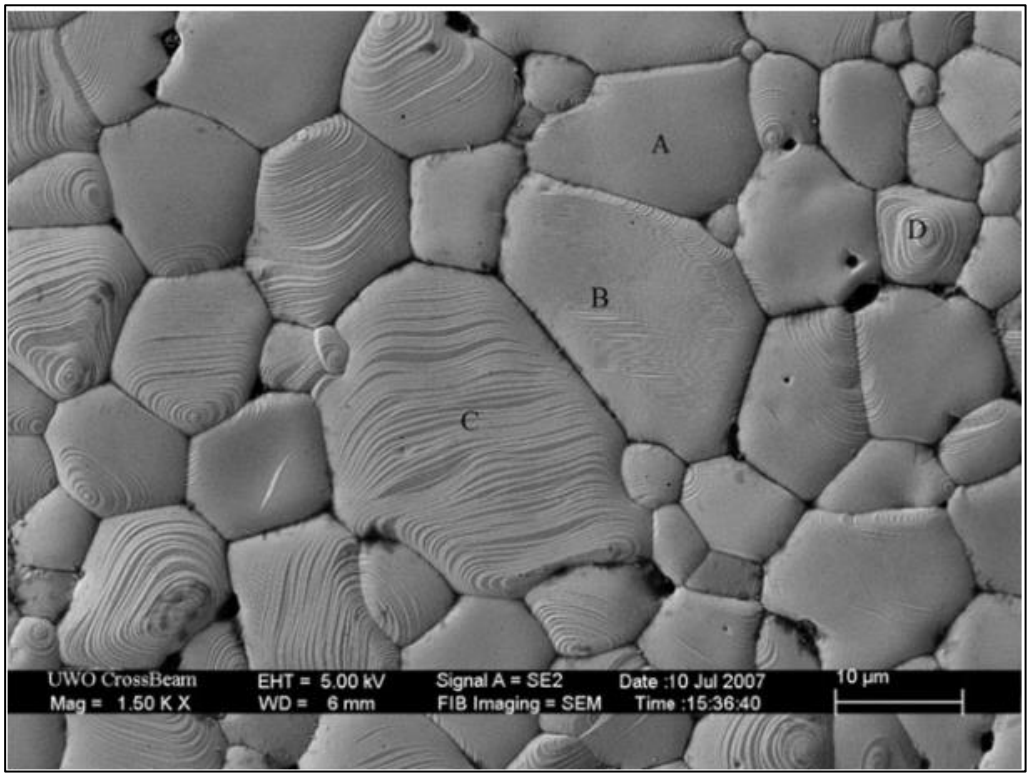

Figure 2-7: SEM image of $UO_{2.1}$ showing different grains: (A) smooth grain, approximately x = ~0.01 (B) slightly hyper-stoichiometric, x = ~0.15 (C) rough grain, x = ~0.22 (D) highly non-stoichiometric, x = ~0.31. This figure corresponds to the Raman spectra presented in Figure 2-6 (Figure taken with permission from [23, 55]).

Specifically, μ-Raman spectra acquired at the four different grain morphologies reveal differing spectra; the smooth grains of type (A) produce spectra, seen in Figure 2-6, with a single intense vibration at ~445 cm^{-1} associated with the fundamental U-O stretch, and an accompanying broad peak at ~1150 cm^{-1} (not shown here in this spectra) known as the 2LO phonon. This 2LO phonon is due to the first overtone of a selection rule forbidden longitudinal optical phonon at ~575 cm^{-1}.

Both are indicative of a well-ordered cubic fluorite lattice structure. In contrast to the Raman spectra of Figure 2-6 (C)/(D), as introduced above, which have been acquired from the surface of the rough stepped/spiralled grains of type (C) and (D), exhibits less intense broader peaks and the additional formation of a broad band between ~520 and ~700 cm^{-1}.

The introduction of these hyperstoichiometry derived lattice defects causes distortion to the cubic symmetry, resulting in local relaxations of the selection rule, and thus allowing a number of normally dipole-forbidden transitions to occur.

As a result of these lattice distortions, the fundamental U-O stretch at ~445 cm^{-1} decreases in intensity, along with its accompanying 2LO phonon peak at ~1150 cm^{-1}.

This is accompanied by the relative increase in a broad region of peaks associated with lattice damage, also known as the “defect band”, between ~520 to ~700 cm^{-1}, these peaks can be attributed to the lattice transition from a perfect cubic symmetry to a tetragonal structure.

The spectra belonging to the non-stoichiometric grain morphologies of type (B)/(C)/(D) in Figure 2-6, can be further deconvoluted and used to interpret the Raman spectral changes that are associated with the increasing degree of UO_2 hyperstoichiometry, as it deviates from the cubic fluorite lattice of stoichiometric UO_2.

Other studies on the characterisation of hyperstoichiometric UO_2 have also been reported in the literature. In a study by Elorrieta et al., [56] samples of

UO_{2+x} with different degrees of hyperstoichiometry were prepared and analysed by a range of techniques including μ-Raman spectroscopy.

By using thermogravimetric analysis, it was possible to determine the exact hyperstoichiometric composition of the oxide samples which further enabled the correlation between hyperstoichiometry and the measured Raman spectra. This enabled the values of x at which key structural transitions occurred at, to be determined.

Figure 2-8 shows a compilation of Raman spectra acquired from different hyperstoichiometric UO_2 samples at x values between 0.03 and 0.24. All samples demonstrated similar UO_2-like Raman spectra and upon increasing the stoichiometry, a broad band of peaks appeared in the region of ~500-700 cm^{-1}.

As above, this broad band was interpreted as being a combination of features at approximately 560 cm^{-1} and 630 cm^{-1}. The evolution of this broad band region of peaks can be seen in Figure 2-8 which shows, with increasing hyperstoichiometry: (i) a broadening and up-shifting of the ~445 cm^{-1} fundamental U-O stretch, (ii) a decrease in intensity of the 2LO band at ~1150 cm^{-1}, and (iii) a continuous increase in the ~630 cm^{-1} band.

Increases in the degree of hyperstoichiometry as described here are said to enhance the galvanic coupling at anodic and cathodic sites, promoting corrosion, see Section 2.1.1 and Figure 2-1 for the discussion of corrosion reactions as electrochemical processes.

This property is a consequence of oxygen interstitial incorporation into the cubic fluorite lattice which in turn converts UO_2 to a p-type semiconductor as UO_{2+x}, due to the necessary oxidation of U(IV) to U(V) and/or U(VI) in order to maintain charge balance within the matrix.

As a result, this process generates holes in a 5f sub-band in the UO_2 electronic structure giving rise to increased electrical conductivity [32]. Additionally, the presence of these newly formed U(V)/U(VI) donor-acceptor sites can also catalyse the reduction of oxidants such as O_2 and H_2O_2, leading to accelerated corrosion.

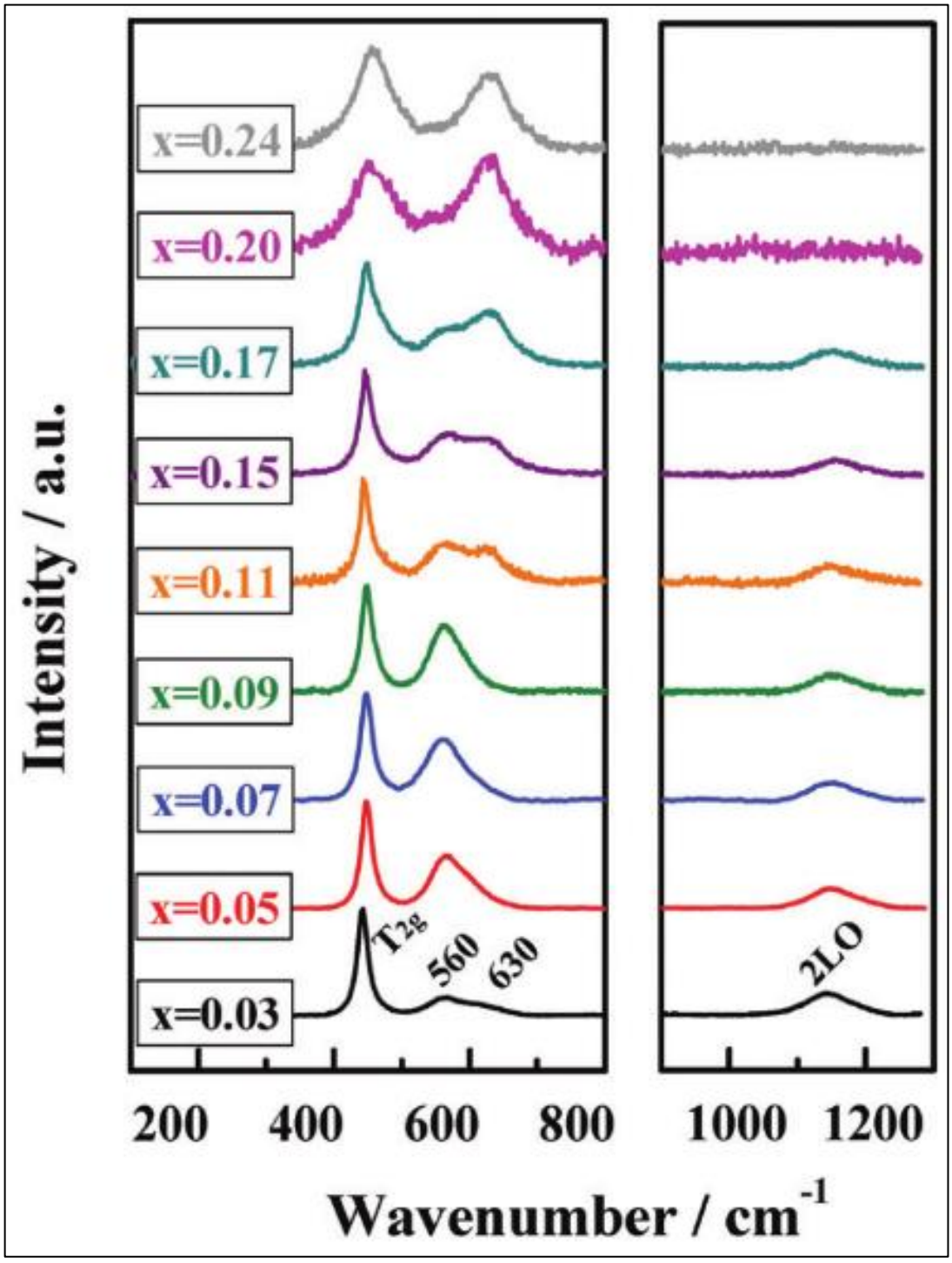

Figure 2-8: A compilation of Raman spectra acquired from different hyperstoichiometric UO_2 samples at x values between 0.03 and 0.24. All samples demonstrated similar UO_2-like Raman spectra and upon increasing the stoichiometry, a broad band of peaks appeared in the region of ~500-700 cm^{-1} (Figure taken with permission from [56]).

2.2.2 Thermodynamics of the UO_2-H_2O System

The thermodynamics of the UO_2 system in water is most readily visualised through the use of Pourbaix diagrams, named after its inventor Marcel Pourbaix [57]. As such, Pourbaix diagrams are an additional resource that can assist in the investigation of the redox behaviour of UO_2/SIMFUELs and thus assist in understanding the results of corrosion studies of such materials.

Pourbaix diagrams can help predict the thermodynamic stability of an element under study – in this case U – as a function of the redox stress of the system, most readily expressed as an electrode potential E, and the pH of the medium in which the element is immersed.

They are thus constructed in terms of the potential applied to a metal/metal-alloy and the solution pH. They can therefore be used to predict the dominant thermodynamically stable species/favourable oxidation state, at a given potential and pH.

To demonstrate, we first consider the equilibrium Pourbaix diagram of the water system, shown in Figure 2-9. The region bound by the two diagonal lines represents the region of water stability. The two diagonal lines, (b) and (a), represent respectively the equilibrium potentials for water oxidation and reduction as a function of pH. At potentials above line (b) water is oxidised to oxygen whilst at potentials below line (a) water is reduced to hydrogen.

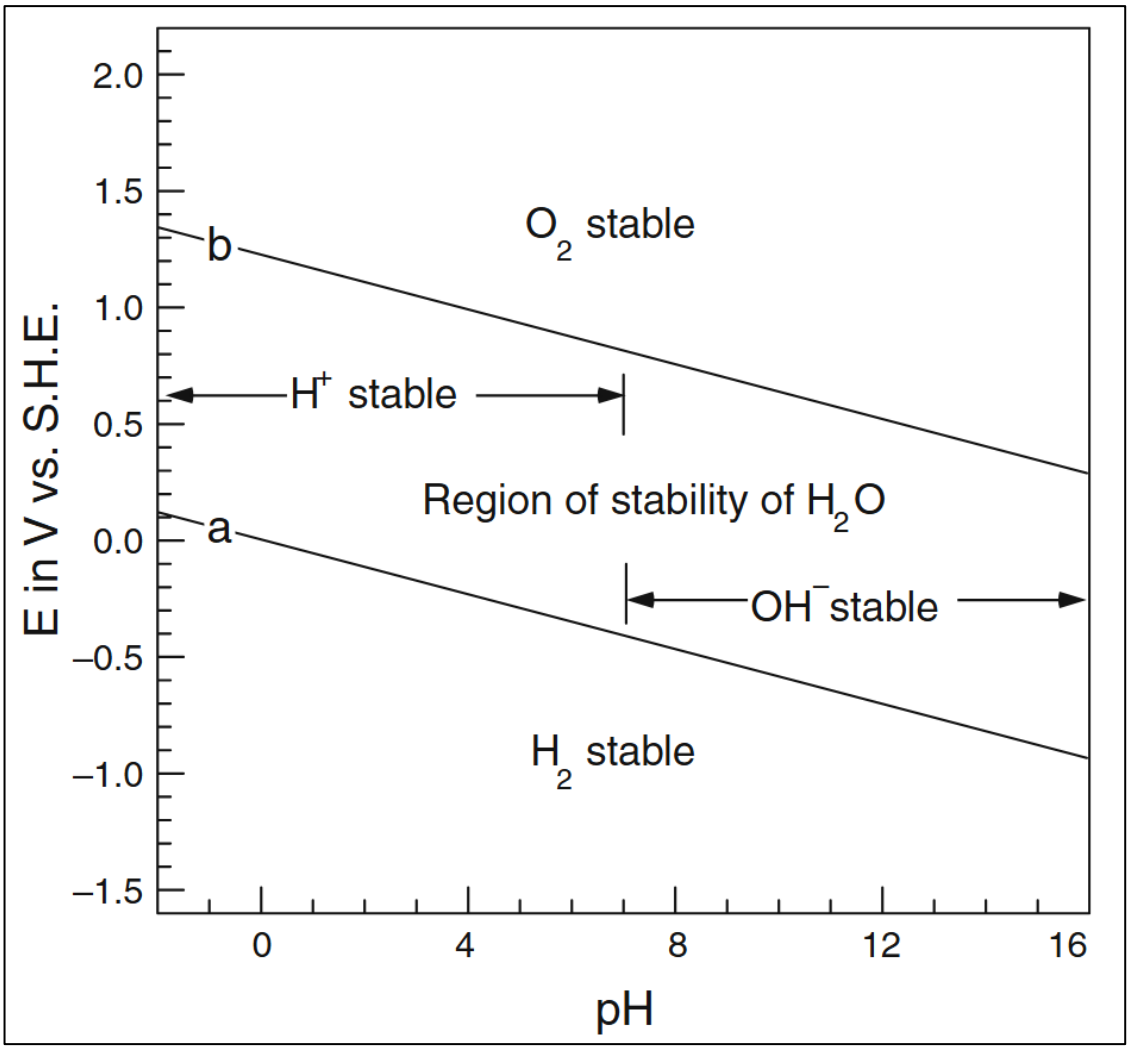

Figure 2-9: Pourbaix diagram of water equilibria system showing the regions of water stability with respect to the region of oxygen liberation and region of hydrogen liberation (This figure is taken with permission from [58]).

Figure 2-10 shows a uranium-water Pourbaix diagram at 25°C reported by Paquette et al., again, the diagram gives an indication of the uranium species that are thermodynamically stable as a function of equilibrium potential and water pH [59].

This diagram tells us that the uranium is predominantly stable in the form of solid UO_2 at neutral pH, but under oxidising conditions the stable form is dominated by the soluble oxidised UO_2^{2+} species, especially at pH < 6. Different Pourbaix diagrams of this similar system can be found in literature with different diagrams depending on the conditions explored such as pressure, temperature, solution concentration, and especially activities of the dissolved species in the solution [59-63].

However, there are limitations which must be considered when using Pourbaix diagrams: (i) Pourbaix diagrams only represent the thermodynamic equilibrium and do not provide information regarding kinetics of the system, (ii) Pourbaix diagrams are constructed only for the given conditions of the system being modelled (e.g. temperature, pressure, solution etc.) and (iii) Pourbaix diagrams represent only the thermodynamic stabilities of the dominating species and does not account for non-dominating/meta-stable species that may also be present.

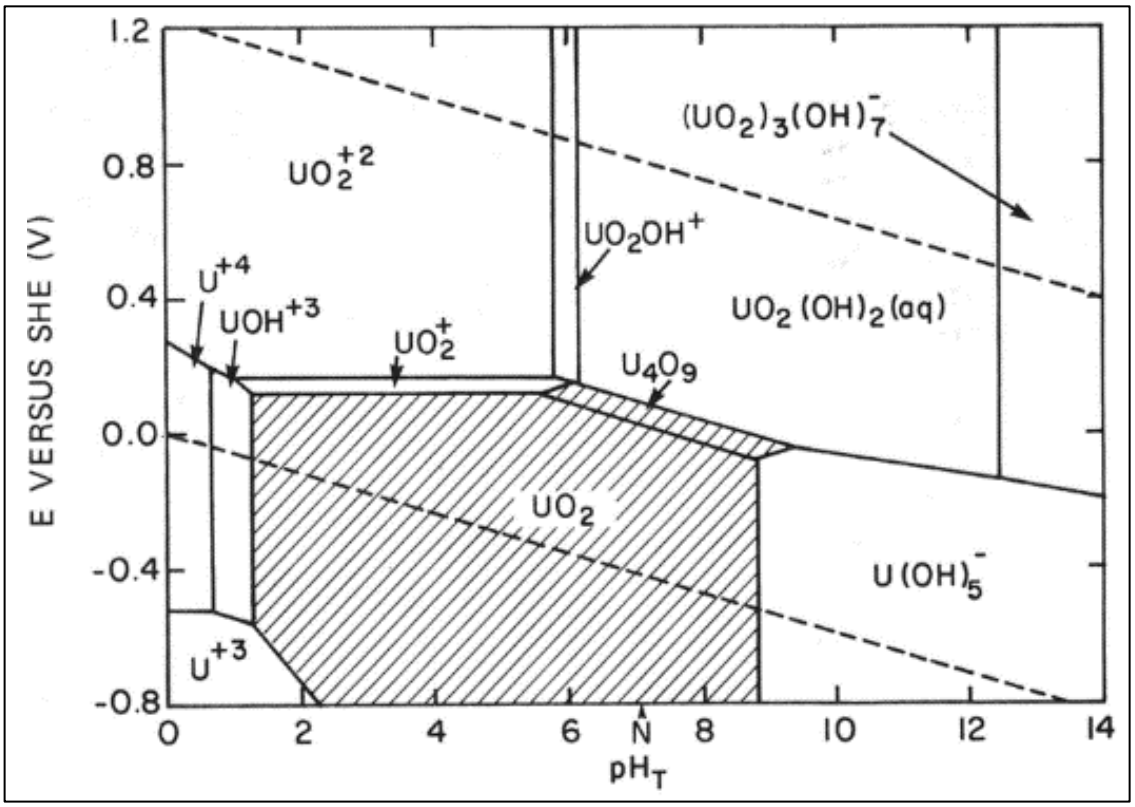

Figure 2-10: Pourbaix diagram of uranium-water system at 25°C (Figure taken with permission of Informa UK Limited, trading as Taylor & Francis Group, https://www.tandfonline.com, from [59], © copyright 2017).

2.2.3 Voltammetric Behaviour of UO_2

The dependence of the corrosion of UO_2 on redox conditions is well reported in literature as it concerns the SNF wet storage and disposal scenarios post reactor irradiation, as discussed in Chapter 1 Section 1.3.1. These scenarios may involve situations in which the UO_2 fuel pellet component of the SNF becomes in direct contact with storage pond waters or environmental ground waters, creating opportunity for the development of a corrosion cell between the UO_2 and its surrounding aqueous solutions and thus promoting redox processes, as previously described in Sections 2.1.1 and 2.1.3 and described in Section 2.2.2 on UO_2 thermodynamics. Therefore, it is crucial to understand how redox conditions can affect the corrosion behaviour of UO_2.

These redox processes can be influenced and controlled by the UO_2's surrounding chemistry such as the presence of radiolytic and/or non-radiolytic oxidising species, the solution pH, and the chemical composition of species at the surface of the UO_2, discussion of these factors and influences are presented in Section 2.2.4.

A powerful technique for exploring the redox/corrosion behaviour of UO_2 is the electrochemical technique of cyclic voltammetry (CV), further described in Chapter 3 Section 3.2.5. This technique can be employed to study the oxidation and reduction reactions taking place at the surface of a UO_2 electrode.

Figure 2-11 shows the typical form of a Cyclic Voltammogram (CV) recorded on UO_2 in 0.01 mol/dm^3 NaCl at pH 5.3, by Seibert et al., [64]. The CV exhibits oxidation and reduction current features in the voltage regions labelled I to V. The current behaviour in these regions is described and interpreted in detail in Siebert et al., [64], and summarised below:

- Region I, the current is attributed to the reversible oxidation of nonstoichiometric surface UO_{2+x} at the grain boundaries to form hyperstoichiometric $UO_{2.33}$ species.
- Region II, the current is attributed to the partially reversible oxidation of the bulk UO_2 to UO_{2+x} involving the O^{2-} incorporation into the lattice until a limiting stoichiometry of $UO_{2.33}$ and is accompanied by the oxidation of adjacent U(IV) to U(V)/U(VI) for charge balance.

- Region III, the current is attributed to the further oxidation of the surface UO_2 generating soluble U(VI) via dissolution as UO_2^{2+}, at acidic pHs. Whereas at high pHs, the UO_2^{2+} species may re-precipitate as U(VI) hydrated species at the surface.
- Region IV, the current is attributed to the reduction of adsorbed surface U(VI) species upon application of cathodic potentials, the U(VI) and surface oxide layer is reduced, and peak height is said to be influenced by the surface layer thickness.
- Region V, the current is attributed to the reduction of the $UO_{2.33}/UO_{2+x}$ oxide layers previously generated in Region II or reduction of the higher oxides of $UO_{2.5}/UO_{2.6}$ previously generated in Region III from recrystallisation processes.

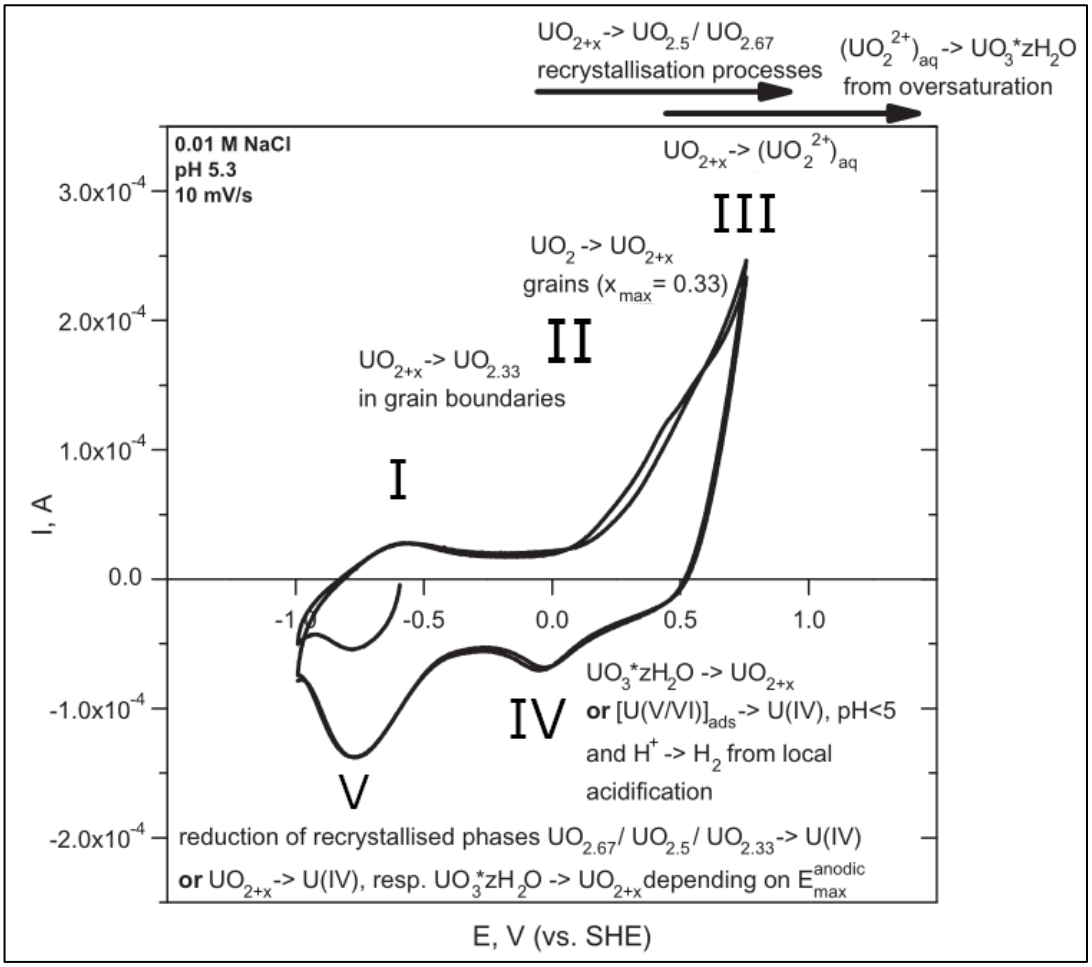

Figure 2-11: Cyclic voltammogram of a UO_2 electrode recorded in 0.01 mol/dm^3 NaCl at pH 5.3 with a scan rate of 10 mV/s (Figure taken and adapted with permission from [64]).

2.2.4 Factors Affecting Corrosion

Corrosion studies of UO_2 are important over the whole nuclear life-cycle, especially in the context of the corrosion/dissolution behaviour of SNF post-irradiation.

Various factors can influence SNF corrosion/dissolution such as solution pH, temperature, pond/ground water chemistry, fuel matrix dopants/fission products and the influence of products derived from water radiolysis.

A brief literature review of the key factors that can influence SNF corrosion/dissolution will be discussed in this section.

A further review of literature studies that are specific to AGR SIMFUELs is presented later in Section 2.2.5.

2.2.4.1 Influence of Oxygen

Depending on the local environment of the SNF, the atmosphere surrounding the UO_2 may contain oxygen. This can lead to the presence of dissolved oxygen in any aqueous medium with which the UO_2 is in contact. In addition to atmospheric oxygen, the dissolved oxygen may also come from the processes associated with water radiolysis.

This section briefly summarises the key findings from a selection of literature studies on the influence of O_2 on the corrosion behaviour of UO_2 and SIMFUELs.

Section 2.1.1 describes the model of corrosion as two coupled half-cell reactions – an anodic metal oxidation process, see Equation 2-1, and a coupled cathodic process, such as the reduction of oxygen, see Equation 2-2.

The rate of the cathodic reduction of oxygen has widely been reported in the literature as a slow process due to the breaking of strong O-O bonds. In the case of UO_2 this process is catalysed by the mixed oxidation state surface sites, U(VI)/U(V) or U(V)/U(IV) donor-acceptor sites [32, 65].

The proposed mechanism suggests a four-electron transfer process for the reduction of O_2, counter intuitively, involving the oxidised U(V) species and the adsorbed O_2 species; the mechanism ends with the subsequent reduction of the

adsorbed superoxide ion to hydroxide ion and oxidation of the UO_2 matrix. However, extensive oxidation of the fuel surface can also lead to the accumulation of corrosion products which can block the donor-acceptor sites and suppress O_2 reduction.

Stoichiometry of the UO_2 surface can also affect O_2 reduction since the surface composition of the UO_2 can change depending on the amount of oxidation, leading to a range of non-stoichiometric UO_{2+x} sites which can act as donor-acceptor sites at the surface, as previously discussed in Section 2.2.1. Thus under oxidising conditions, an increase in hyperstoichiometry can be correlated with an increase in the rate of UO_2 oxidation overall.

Fission product dopants can also affect O_2 reduction, for example rare earth elements in the 3+ oxidation state (RE^{3+}) which can exist in solid solution with the UO_2 matrix, or noble metals which can precipitate as so-called ε-particles. The presence of RE^{3+} species promotes the conversion of U(IV) to U(V) thus generating more donor-acceptor sites which can enhance the reduction of oxygen. In contrast, the presence of ε-particles, catalytically enhances O_2 reduction in a manner similar to that which occurs during the electrochemical reduction of O_2 to water at noble metal electrodes [32, 33].

Torrero et al., [66] have reported on a study of UO_2 dissolution rates as a function of pH and $[O_2]$, shown in Figure 2-12. The data showed that between the pH range of ~3 to 6.5, the dissolution rates increased with decreasing pH and increasing $[O_2]$.

However, above pH ~6.5 this dependence was no longer observed, as the dissolution rates reached a low level that was near independent of pH and O_2 concentration. It was suggested that the behaviour observed at lower pH was due to the competing adsorption between protons and oxygen at U(IV) surface sites which in turn promoted the dissolution of U(VI).

In contrast, it was proposed that the observed behaviour at higher pH was attributable to the reduced rate of proton-driven dissolution. As a result, the oxygen dissolution proceeded primarily via diffusion into the solid structure, leading to the accumulation of an oxidised surface layer, further blocking dissolution.

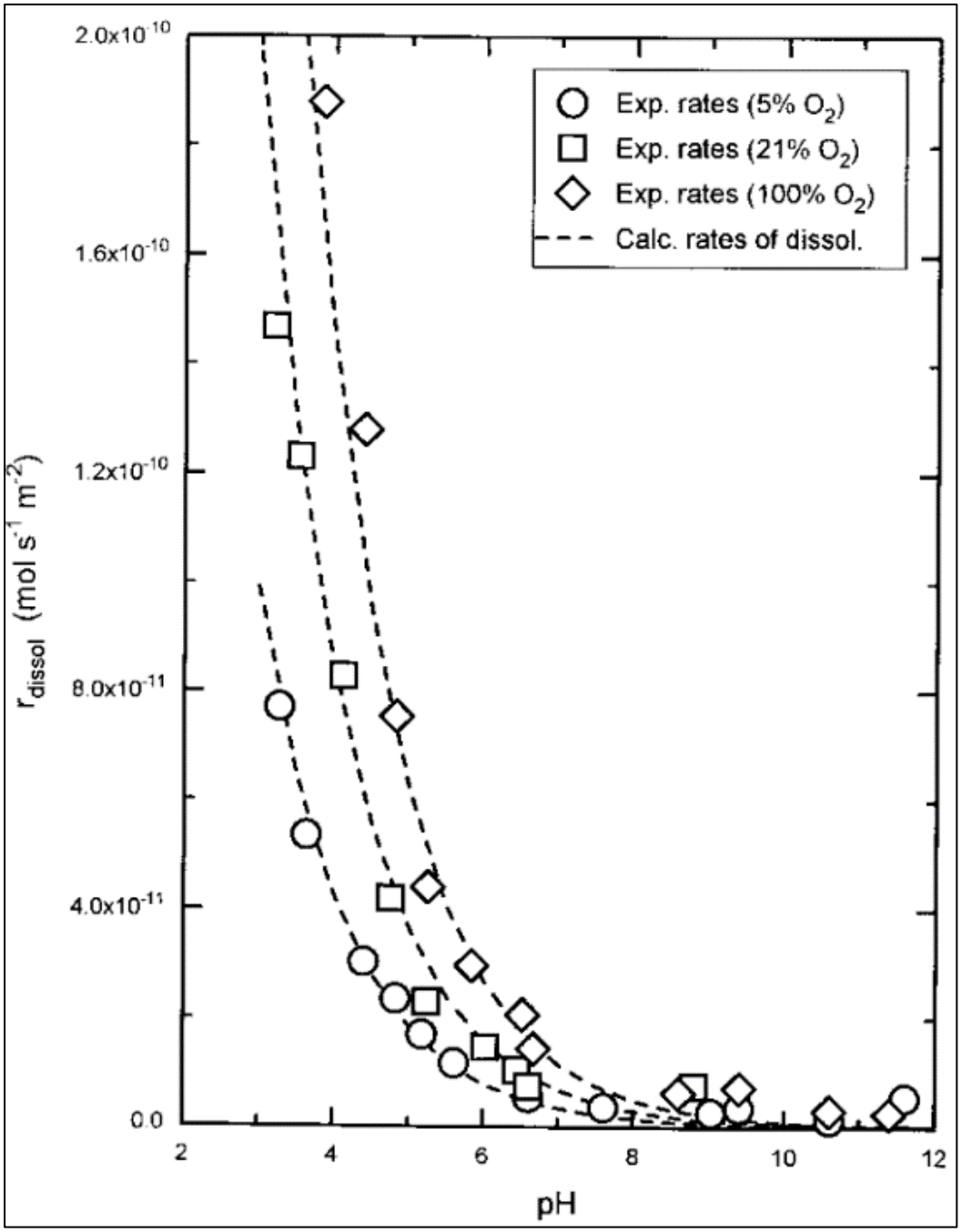

Figure 2-12: UO_2 dissolution rates as a function of pH and oxygen concentration (Figure taken with permission from [66]).

2.2.4.2 Influence of Radiolysis Products

The type of radiation field surrounding the spent fuel will depend on the time since discharge. For typical oxide fuels, the alpha field dose rates will be maintained for the longest period, up to ~10,000 years, whereas the beta and gamma fields will have decayed significantly by ~1,000 years [33].

Over the lifetime of the SNF containment, the dominant radiation field present at any one time will induce radiolysis of the surrounding water external to the fuel containment, in the case of gamma radiation, and any water that has come into contact with the spent fuel, in the case of all radiation types, generating molecular and radical species. This section briefly summarises the key literature on the influence of radiolytic oxidants on the corrosion behaviour of UO_2 and SIMFUELs.

The majority of water radiolysis at the fuel/water interface will be caused by the short penetration range of alpha particles [67]. This radiolysis can produce both oxidants such as, OH• and H_2O_2, and reductants such as H• and H_2, with H_2O_2 being one of the major products of water radiolysis and contributes to the dissolution of UO_2 [68, 69]. The decomposition of H_2O_2 also produces O_2 as a secondary oxidant that can also drive oxidation/dissolution of the UO_2 surface [68, 69].
In a study by Shoesmith et al., results from electrochemical measurements conducted on UO_2 electrodes, showed faster oxidation rates of UO_2 to $UO_{2.33}$, when in the presence of hydrogen peroxide compared to oxygenated solutions [32].

Similar observations were also reported by Eke Roth and Jonsson, [69]. In both these studies, the H_2O_2 reduction process was thought to occur on the UO_2 surface via a coupled electrochemical process, catalysed by the formation of its own U(IV)/U(V) donor acceptor sites [70]. This catalytic process has been discussed previously in the above sections.

Clarens et al., studied the relationship between pH and the oxidative dissolution of UO_2 in 10^{-5} mol/dm^3 hydrogen peroxide [71]. Their plot of dissolution rate as a function of pH can be seen in Figure 2-13. From this it can be seen that the rate of dissolution decreased linearly with pH until a plateau at pH 7; this

plateau maintains up to pH 9, above which the rate of dissolution then increased linearly.

This linear increase in the alkaline region was attributed to the decomposition of H_2O_2 in alkaline media due to its acidity and thus forming HO_2^- anions. The perhydroxy anions then becomes the predominant reductant species involved in the oxidation mechanism of UO_2.

However, at peroxide concentrations greater than 10^{-5} mol/dm^3, the dissolution rates were much lower, likely attributed to the precipitation of secondary phases such as studtite and increased rate of hydrogen peroxide decomposition.

Overall, it was concluded that dissolution rates were generally higher in the presence of hydrogen peroxide than in the presence of oxygen, between the pH range of 3 to 10.5.

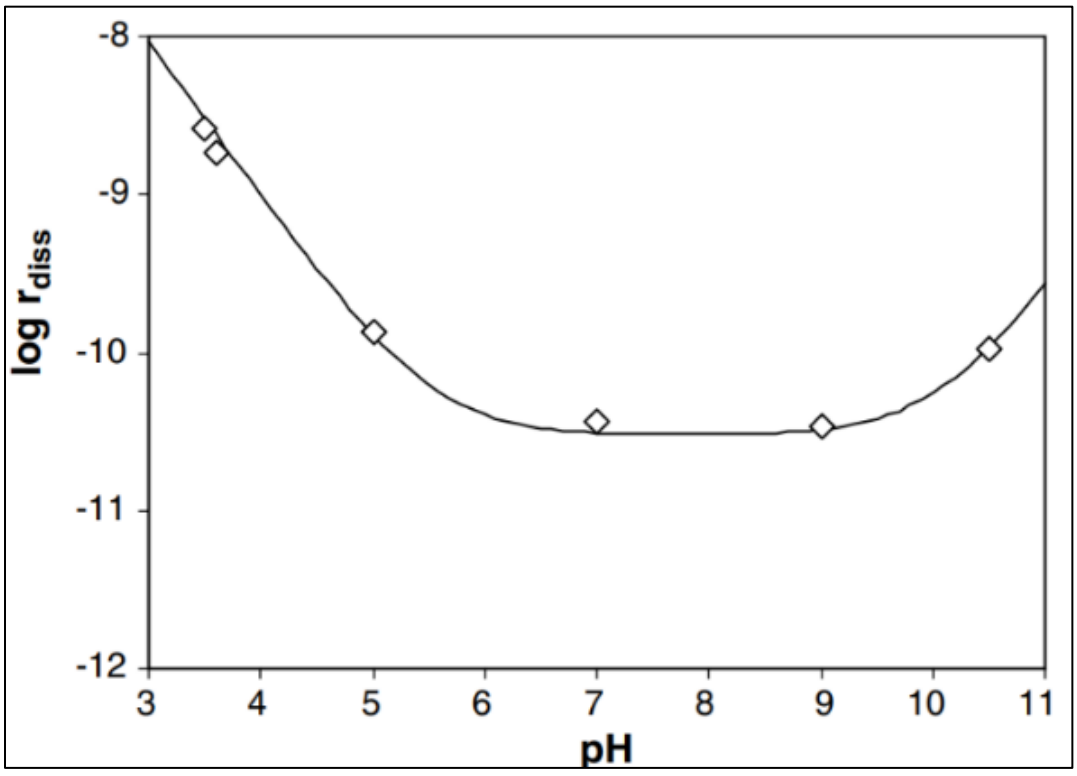

Figure 2-13: UO_2 dissolution rates as a function of pH recorded in 10^{-5} M H_2O_2 (Figure taken with permission from [71]).

For doped-UO_2 and SIMFUELs, the introduction of dopants into the matrix can affect the local reduction of H_2O_2. Betteridge et al., and Goldik et al., have

shown that the presence of noble metal particles (ε-particles) significantly enhance the H_2O_2 decomposition at the SIMFUEL surface, compared to the modest influence of rare-earth dopants on the same process [72, 73].

Goldik et al., have conducted electrochemical studies on CANDU SIMFUELs at three different simulated burn-ups at 1.5 at.%, 6 at.%, both including ε-particles in their matrix, and a split-SIMFUEL at 1.5 at.% with no ε-particles [73].

Cyclic voltammetry of the SIMFUELs in 0.1 mol/dm^3 NaCl electrolytes at pH 9.5 containing H_2O_2, showed that H_2O_2 reduction rates, even at relatively low overpotentials of -0.3 V, increased with the number density of ε-particles. But at larger overpotentials of -0.8 V the dependence on ε-particle population was much weaker as the higher currents lead to more vigorous H_2O_2 reduction via the whole UO_2 surface.

This suggests that H_2O_2 reduction via the ε-particles is the dominant cathodic process during the natural corrosion process of UO_2 – which are typically characterised by low overpotentials – and implies that reactor burn-up could influence the corrosion rates of SNF.

Another important aspect on the reduction H_2O_2 is its interactions with H_2. The production of H_2 can occur during the anaerobic corrosion of iron. This mechanism is relevant to SNF wet storage or disposal scenarios where SNF may be in the vicinity of iron, especially under anoxic conditions.

Importantly, it has been reported that the presence of hydrogen can inhibit oxidation and thus dissolution of UO_2 [74-77]. The process of inhibition can occur via the H_2-driven consumption of oxidants in competition with that by UO_2, shown in the general mechanism of Equation 2-5. H_2 suppression of UO_2 dissolution can also proceed by direct reduction of UO_2^{2+}, shown in the general mechanism of Equation 2-6 [75].

$$Ox + H_2 \rightarrow red + 2H^+$$

Equation 2-5

$$UO_2^{2+} + H_2 \rightarrow UO_2 + 2H^+$$

Equation 2-6

In a study by Razdan and Shoesmith, two possible pathways by which dissolved H_2 could consume the products of H_2O_2 decomposition [77].

Both mechanisms involved the catalytic support of ε-particles and the consumption of OH• radicals as follow: (i) by direct scavenging of OH• on e-particles, as shown in Figure 2-14(a); or (ii) via the oxidation of H_2 directly on the ε-particles, which is coupled galvanically with H_2O_2 oxidation on the fuel surface as shown in Figure 2-14(b), thus preventing the reaction of OH• with UO_2.

However, it was found that at sufficiently large [H_2O_2], the hydrogen suppression effect was overwhelmed and the irreversible dissolution of the surface to U(VI) dominated.

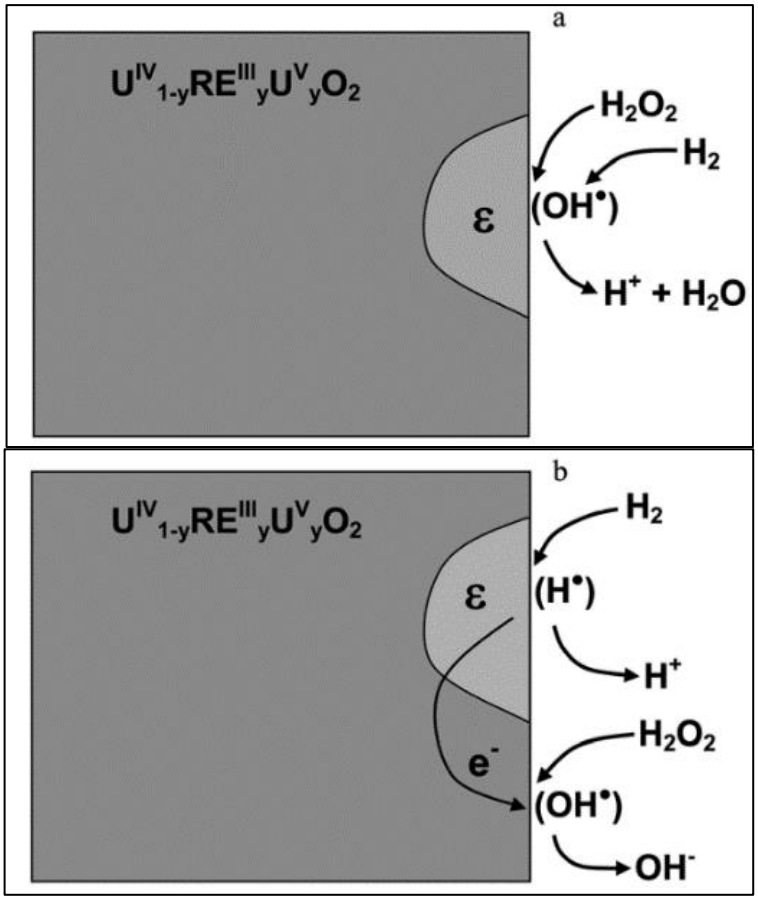

Figure 2-14: Schematic of two possible pathways for the consumption of hydroxyl radicals by hydrogen: (a) direct scavenging and (b) indirectly via the oxidation of H_2O_2 (Figure taken and adapted with permission from [77]).

2.2.4.3 Influence of pH

As previously discussed in Chapter 1 Section 1.3, the UK currently operates under a ‘storage and disposal’ strategy for SNF management and will be repurposing the THORP spent fuel storage ponds into an interim storage site for future SNF.

Currently, the interim storage ponds at Sellafield are dosed with NaOH (to pH≈11.4) which acts as a corrosion inhibitor for, *inter alia*, the stainless steel from which the fuel cladding is comprised of.

Indeed, this pH has already been deemed safe and capable of inhibiting corrosion of that 20/25/Nb stainless steel AGR cladding. However, in addition to protecting the stainless steel cladding from corrosion during wet interim storage, it is also important to understand the implications of solution pH on the wet storage of the UO_2/fuel pellet component of spent fuel pins.

This section briefly summarises key literature on the influence of pH on the corrosion behaviour of UO_2, SIMFUELs and uranium-based SNF. Given the radiological difficulties associated with the study of real SNF, most literature focuses on UO_2 and SIMFUEL materials [78-80].

In a report by D.W. Shoesmith, a discussion of UO_2 solubilities as a function of pH was presented [32] Figure 2-15 summarises their findings and shows the dependence of pH on the solubility of UO_2 under oxidising and reducing conditions. In the case of the former, the most significant trend was observed at below pH 5 where the rate of dissolution increased with decreasing pH.

In contrast, the neutral to alkaline region between pH 5 to 10 expressed no significant pH dependence. In the region above pH 10, the rate of dissolution increased with increasing pH.

This result is also consistent with the studies presented by Torrero et al., which was described earlier in Figure 2-12 of Section 2.2.4.1, which shows a similar dependence of UO_2 dissolution rates on pH in the presence of 10^{-5} mol/dm^3 H_2O_2 [66].

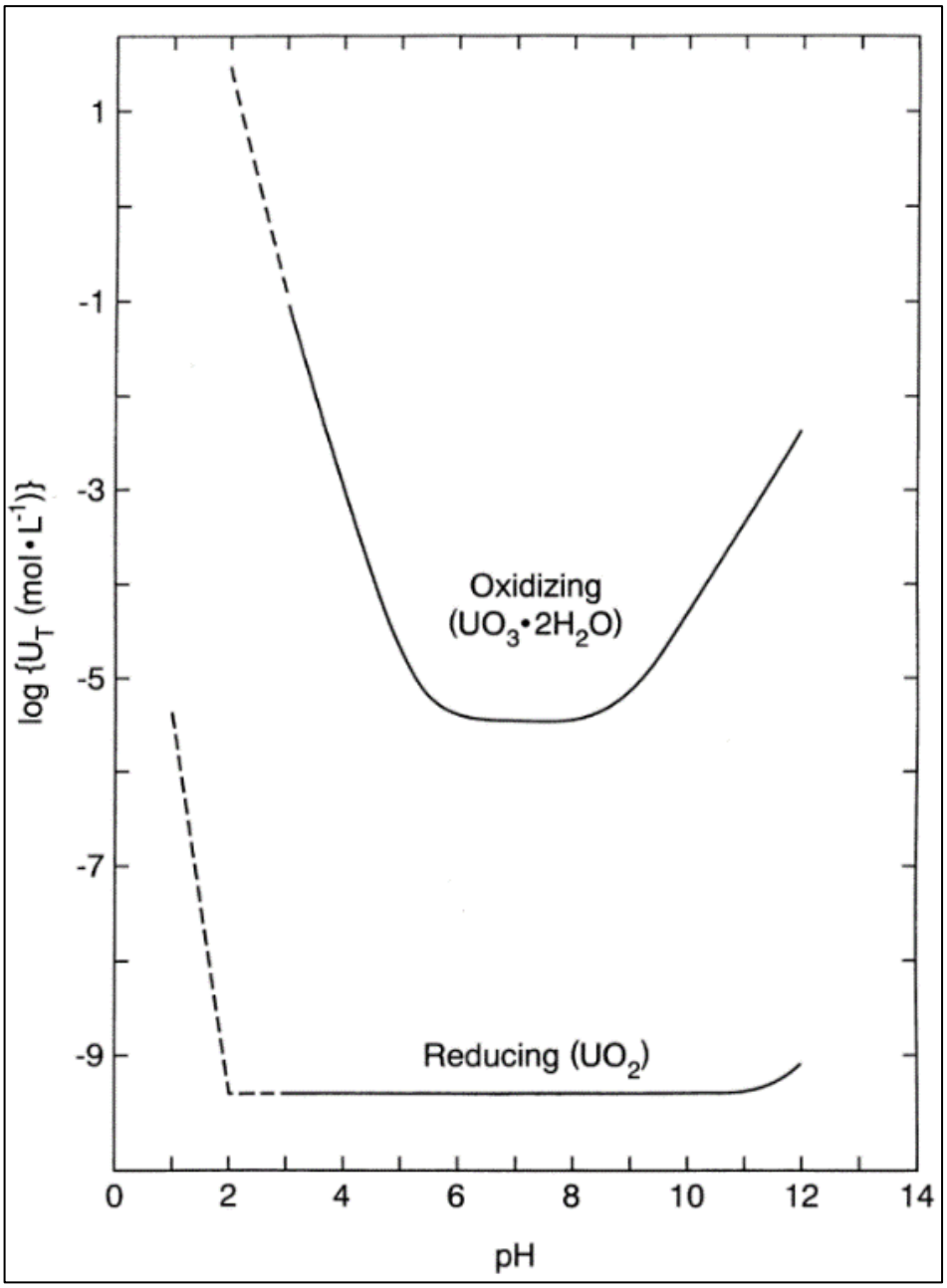

Figure 2-15: Solubilities of UO_2 and schoepite as a function of pH at 25°C (Figure taken with permission from [32]).

Santos, Noël, and Shoesmith, have studied the surface reactivity of SIMFUELs using cyclic voltammetry and XPS in acidic, neutral and alkaline solutions [81].

Under acidic conditions it was observed that dissolution of U(VI) species occurred via the surface-adsorbed hydrolysed U(V) species, with the mechanism proceeding via the extraction of a U atom from the oxide lattice to form a surface-adsorbed hydrolysed species. Which is then further hydrolysed and converted to a U(VI) species before dissolution as UO_2^{2+}.

Under neutral to alkaline conditions the dissolution proceeds via a strongly coordinated U(V) intermediate which involves the incorporation of O^{2-} interstitials.

As pH becomes more alkaline, pH > 10, the mechanism proceeds via a similar route as observed in neutral solutions, but the dissolution of the U(VI) species into the solution is further enhanced by uranyl hydrolysis reactions.

Similarly, in a report by Sunder et al., the pH dependence of UO_2 dissolution in oxygenated solutions was studied using electrochemical techniques and XPS [82]. In general it was found that corrosion potentials and dissolution rates were greater at acidic conditions than in neutral to alkaline conditions. The observations are described as follows:

- Over the pH range of 5 to 12, the initial surface layer formed during the oxidation of the UO_2 surface is the UO_{2+x}, where $0 < x \leq 0.33$, which reaches a maximum stoichiometry of $UO_{2.33}$ (U_3O_7) before further oxidation to a hydrated U(VI) species.
- The thickening of this $UO_{2.33}$ film was also found to increase with pH. Over time, the growth and build-up of the $UO_{2.33}$ film blocks the UO_2 surface from further oxidation and decreases the rate of surface oxidation.
- The solubility and dissolution rates were also simultaneously at their lowest whilst in the pH region of ~ 7 to ~ 10.
- At the higher alkaline regions of pH 10 to 12, a large increase in solubility of U(VI) was observed, but with only a small increase in dissolution rate; this rate increase was attributed to the stabilisation of the predominant $UO_2(OH)_4^{2-}$ species in solution and/or by reaction with OH^- ions.
- At acidic pH conditions the dissolution was found to proceed directly via the oxidation to the U(VI) state and not via the formation of the $UO_{2.33}$ surface layer.

2.2.4.4 Influence of Dopants

As previously discussed in Section 2.2.1, the incorporation of dopant species into the UO_2 matrix can cause lattice defects and distort the cubic fluorite lattice, thus changing its structural properties and influencing its corrosion behaviour.

In the case of SNF, the presence of dopants can occur in the UO_2 matrix due to the formation of activation and fission products during reactor irradiation. In the case of doped-UO_2/SIMFUELs, they can also be artificially incorporated into the UO_2 matrix for research purposes.

This section briefly summarises key literature on the influence of dopants on the corrosion behaviour of UO_2 and SIMFUELs.

In a study by Shoesmith et al., Raman spectroscopy was used to characterise CANDU (Canada Deuterium Uranium, pressurized heavy-water reactor) SIMFUELs [83]. From the Raman spectra analysis of Figure 2-16, it was reported that the characteristic Raman UO_2 peaks, the fundamental U-O stretch at ~445 cm^{-1} and the 2LO phonon at ~1150 cm^{-1}, decreased in intensity with increasing amounts of dopants. There were also changes to the ~575 cm^{-1} and ~640 cm^{-1} peak intensities which are associated with lattice distortions as a result of the introduction of defects due to the incorporation of the rare earth dopants.

Although the presence of the ~530 cm^{-1} peak can be observed in the ‘defect band” of the spectra in Figure 2-16, its associated changes with dopant introduction were not discussed in the above-mentioned review by Shoesmith et al. However, this ~530 cm^{-1} peak has previously been characterised and assigned by Wilbraham et al. – in a Raman study of AGR SIMFUELs – as a dopant-related peak, found to increase with dopant introduction [38].

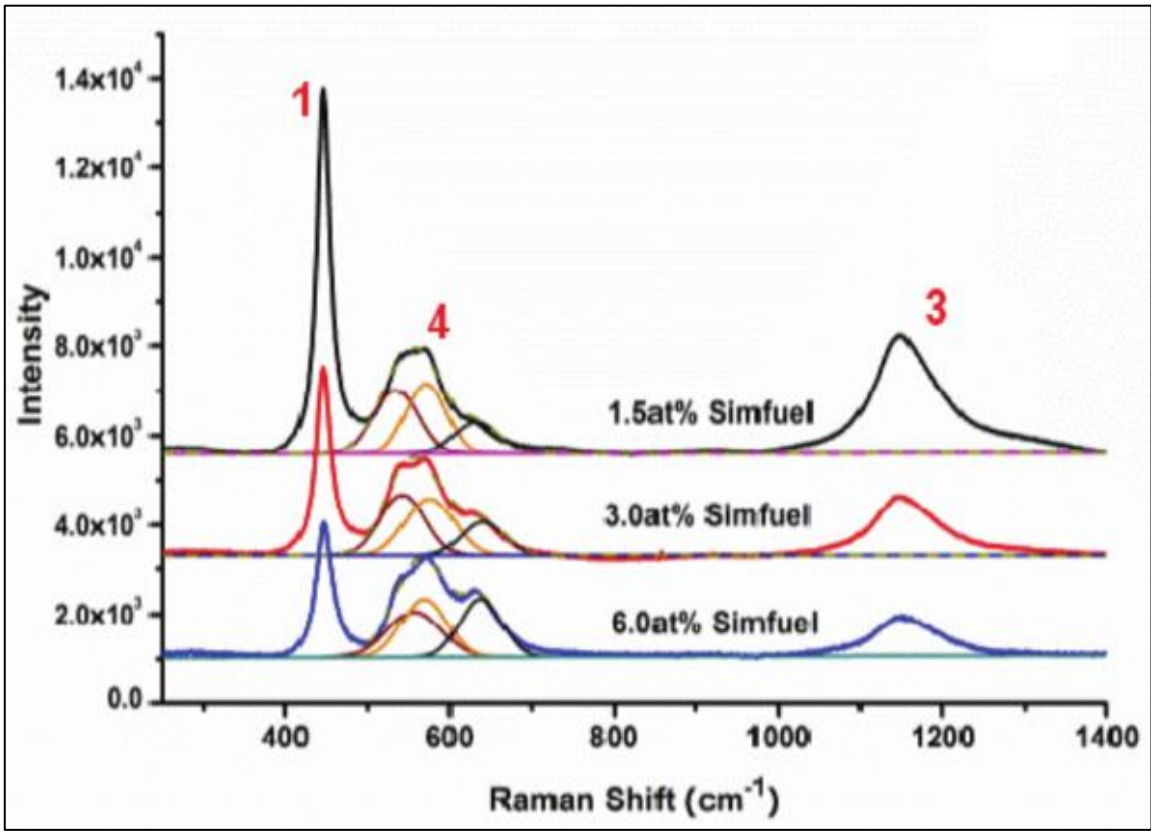

Figure 2-16: Raman spectra for CANDU SIMFUEL at different levels of simulated burn-up (Figure taken adapted with permission from [83].

The study presents a detailed characterisation of the three “defect band” peak contributions. The assignments of the three main contributing peaks can be summarised as follows:

- ~533 cm^{-1} peak: A dopant-related peak, also seen in other doped-UO_2 and SIMFUEL materials, found to increase with increasing lanthanide (III) doping. It is associated with oxygen-vacancy-induced lattice distortions, due to the creation of oxygen vacancies from the incorporation of lanthanide (III) dopants.
- ~575 cm^{-1} peak: This peak was assigned to the LO (Longitudinal Optical) phonon that is usually selection rule forbidden in pure UO_2. It is associated with the loss of translational symmetry and UO_2 lattice distortion which can be due to: (i) the addition of oxygen-interstitials due to oxidation/hyperstoichiometry or (ii) oxygen-vacancy-induced lattice distortion from the incorporation of dopants.

It appears in the SIMFUEL samples and increases in intensity with level of doping which is contrary to the behaviour observed in undoped-UO_2, as described above in Section 2.2.1. This contrary behaviour was tentatively attributed to behaviour seen only in lanthanide-doped materials, likely a combination of selection rule relaxation and phonon scattering upon dopant incorporation.

At the lower lanthanide doped SIMFUEL, the phonon scattering effect on the ~575 cm^{-1} peak is masked by the relaxation of selection rules, resulting in an overall increase in the LO phonon. This explanation can similarly be used to explain the observed increase in the LO phonon of the higher lanthanide doped SIMFUEL.

However, it was suggested that a dopant concentration 'tipping point' exists such that the relaxation of selection rules is no longer masking the phonon scattering effect, resulting in the decrease of the ~575 $^{cm-1}$ peak, in line with the decrease in intensity of the 2LO peak at ~1150 cm^{-1}, as previously described in Section 2.2.1.

- ~624 cm^{-1} peak: This peak is present across the undoped and doped samples, however, the intensity does not change much between them. This peak is associated with the clustering of oxygen interstitials to form cuboctahedrons, equivalent to U_4O_9, thus this peak can indicate the degree of oxidation/hyperstoichiometry as UO_2 oxidises to UO_{2+x} and U_4O_9.

As described earlier in Section 2.2.1, the dopants in SIMFUELs can be used to simulate features such as noble metal ε-particles (namely Rh, Pd and Ru), which are sites that can catalyse oxidation/reduction reactions.

The ε-particles can cathodically catalyse the reduction of H_2O_2 oxidant species, in a manner analogous to the catalytic reduction of O_2. The ε-particles can also anodically catalyse the oxidation of H_2 reductant species [73].

Additionally, the dopants in SIMFUELs can also be used to simulate secondary phases and precipitates formed within the UO_2 matrix, also known as 'grey-phases', as previously described in Chapter 1 Section 1.4.2 [37].

In a study by Hiezl et al., it was reported that (Ba, Sr)(Zr, RE)O_3 oxide precipitates were formed and characterised during the preparation of AGR SIMFUELs, to simulate such grey-phases, similar to those found in real SNF [46].

In a voltammetry study of CANDU SIMFUELs by He et al., it was again found that there was a suppression of anodic reactivity with increasing doping level [83]. Although, when compared with undoped-UO_2 it marked a significant increase in current response.

The cyclic voltammograms showed a decrease in current density for the initial oxidation steps as the level of dopants increased. This observation was explained as the possibility of the fluorite lattice stabilising against anodic oxidation and dissolution, caused by the formation of dopant-vacancy clusters and the decrease in the number of oxygen vacancies available for oxidation.

2.2.5 Review of AGR SIMFUEL Studies

As previously discussed in Chapter 1 Section 1.4.1, the majority of published studies on uranium oxide fuels and associated spent fuel simulants are based on the research of materials related to Light Water Reactor fuels and CANDU Pressurised Heavy Water Reactor fuels.

Thus, in support of the AGR SIMFUEL and real SNF studies of this thesis, the following section summarises the key literature on AGR-specific SIMFUEL studies. This area of research is not in abundance due to the limited availability and accessibility of AGR-specific SIMFUELs [46, 84]. Electrochemical and μ-Raman spectroscopic studies on AGR SIMFUELs have been reported in literature by Rauff-Nisthar et al., Howett et al., and Wilbraham et al., [15, 38, 39, 41, 42, 85, 86].

In a study by Rauff-Nisthar et al., μ-Raman spectroscopy was used to characterise two AGR SIMFUELs with simulated burn-ups of 25 and 43 GWd/tU [42].

The resultant Raman spectra as shown in Figure 2-17 from which it can be seen that all contain the characteristic UO_2 fundamental U-O stretch, at ~445 cm^{-1} and the adjacent broad “defect band” between ~500 to 700 cm^{-1}.

From these studies, it was observed that as the simulated burn-up of the SIMFUEL increased, i.e., the density of dopants in the SIMFUEL matrix was increased, the “defect band” also increased in intensity, relative to the fundamental U-O stretch.

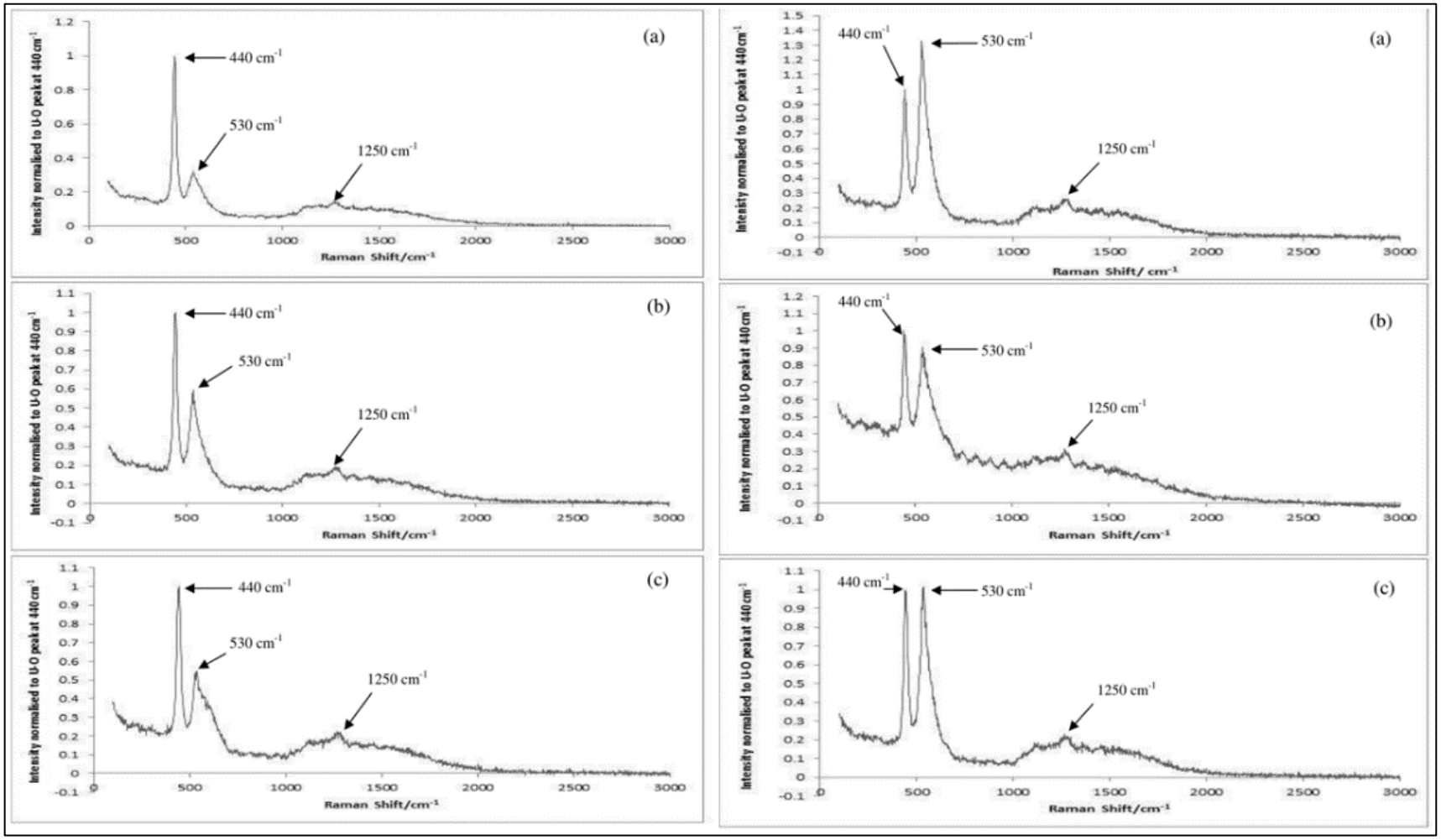

Figure 2-17: μ-Raman spectra of (left) 25 GWd/tU AGR SIMFUEL and (right) 43 GWd/tU AGR SIMFUEL, recorded in (a) as-received sample, (b) 1 hour exposure in oxygenated water, and (c) 1 hour exposure in 100 μmol/dm^3 H_2O_2 (Figure taken and adapted with permission from [42]).

Rauff-Nisthar et al., also presented a cyclic voltammetry and OCP study of the same SIMFUELs in a range of electrolyte systems, including 0.1 mol/dm^3 Na_2SO_4 pH 5 solution and modified simplified groundwater solution (containing 10 mmol/dm^3 NaCl and 2 mmol/dm^3 $NaHCO_3$ at pH 8.2) [41, 85].

CVs from the sulphate study are shown in Figure 2-18, from which it can be seen that the current response from the SIMFUELs was significantly higher than that of the undoped-UO_2, suggesting that susceptibility to anodic corrosion was increased with the degree of simulated burn-up.

This high current response was particularly noticeable at ~-0.1 V which, as discussed in Section 2.2.3, corresponds to the in-grain oxidation of UO_2 to UO_{2+x} and at ~0.4 V which corresponds to the oxidative dissolution of UO_2^{2+}.

OCP measurements from the same sulphate study were also compared with the respective CV of each material, the recorded OCPs we found to be in the region where in-grain oxidation of UO_2 to UO_{2+x} is taking place, indicating that the SIMFUELs were not undergoing dissolution under the sulphate conditions.

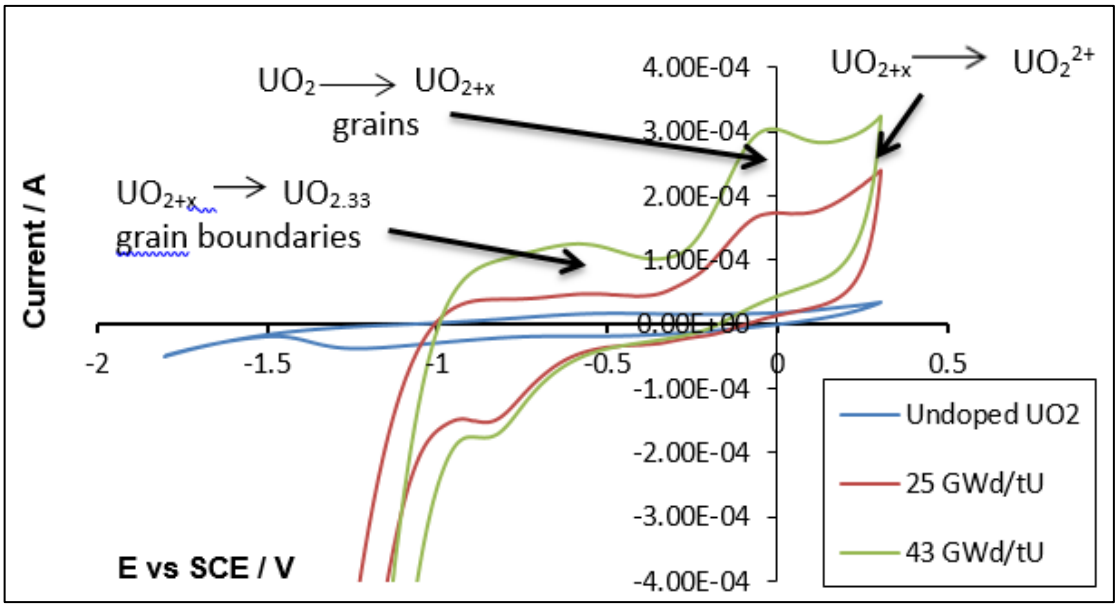

Figure 2-18: Cyclic voltammograms showing the electrochemical response of undoped-UO_2, 25 GWd/tU and 43 GWd/tU, recorded in 0.1 M Na_2SO_4 (Figure taken and adapted with permission from [41]).

Additionally, Rauff-Nisthar et al., also conducted H_2O_2 voltammetry studies in modified simplified groundwater electrolytes. It was reported that extended exposure in H_2O_2 led to an increase in open circuit potentials, observed at both the low and high simulated burn-up SIMFUELs.

This was hypothesised as the possibility of increased corrosion susceptibility due to peroxide-driven surface oxidation and the formation of the readily seen peroxide mineral, metastudtite.

The effect of H_2O_2 on the UO_2 and SIMFUEL matrix was also investigated using μ-Raman spectroscopy, it was found that stoichiometric undoped-UO_2 samples exhibited a near perfect cubic fluorite structure after exposure to oxygenated water containing 100 mmol/dm^3 H_2O_2. The ~ 445 cm^{-1} U-O stretch showed no formation of a shoulder, suggesting the absence of a transition towards a tetragonal structure.

Howett et al., presented preliminary corrosion studies of AGR SIMFUELs in simulant AGR SNF storage pond waters were conducted to investigate the effect of pH on the voltammetry behaviour of UO_2 and SIMFUELs [15].

Voltammetric and OCP data from this study are shown in Figure 2-19 and demonstrates that dosing pond waters to pH 11.4 could provide protection against corrosion. This is evidenced by the lower corrosion currents observed in the CV measurements of Figure 2-19(B) recorded in pH 11.4 electrolytes, than those recorded in non-caustic-dosed electrolytes, seen in Figure 2-19(A).

It is also evidenced by the reduction in OCPs for all samples recorded in pH 11.4 electrolytes, as seen in Figure 2-19(D) versus Figure 2-19(C), which suggests a transition of the materials from an OCP region of active dissolution to a region of surface oxide layer formation.

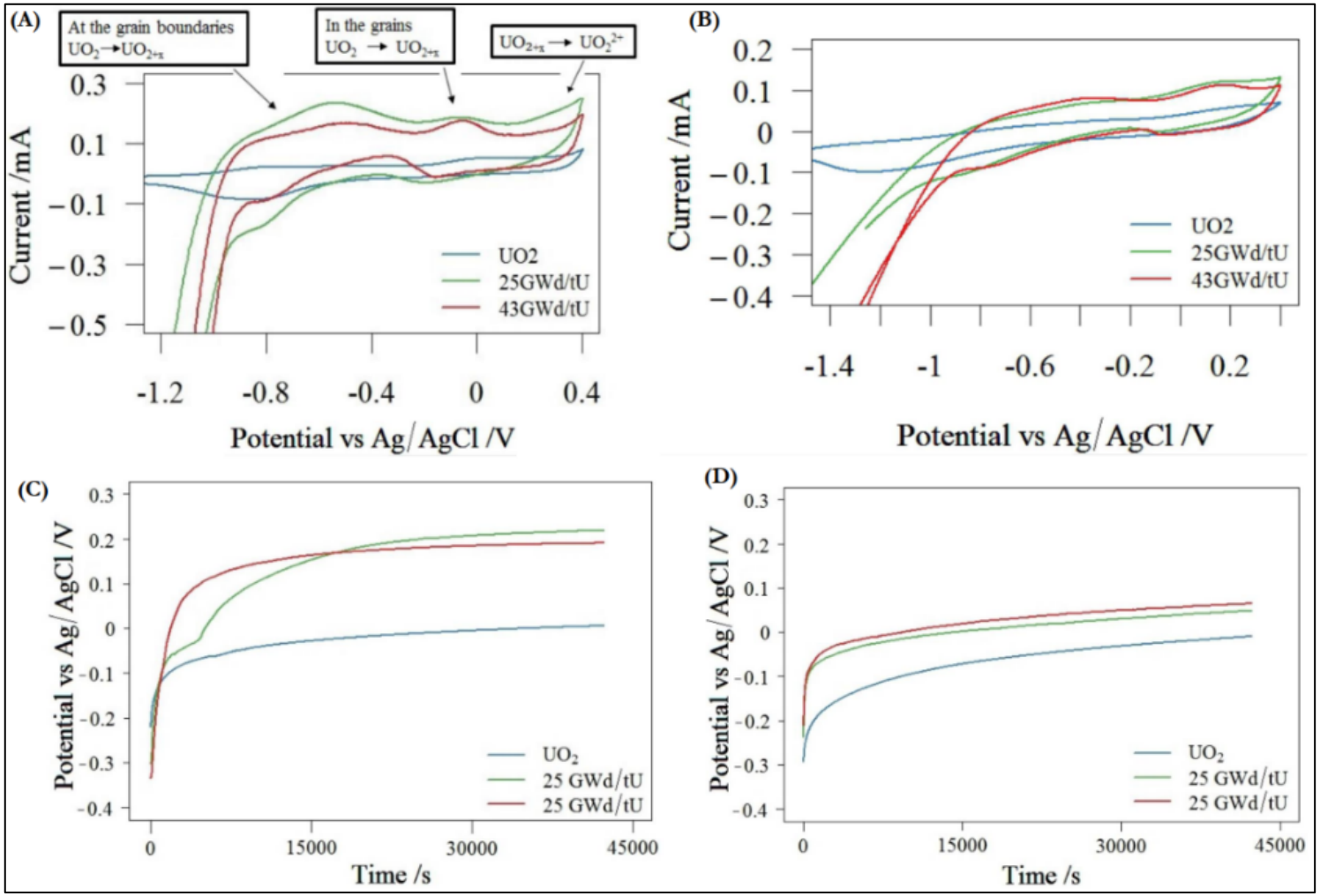

Figure 2-19: Cyclic voltammogram of UO_2, 25 and 43 GWd/tU SIMFUELs in (A) 0.5 M Na_2SO_4, pH ~5.6 (B) simulant pond water pH ~11.4. And open circuit potentials of UO_2, 25 and 43 GWd/tU SIMFUELs in (C) 0.5 M Na_2SO_4, pH ~5.6 (D) simulant pond water pH ~11.4 (Figure taken and adapted with permission from [15]).

In a study by Wilbraham et al., μ-Raman spectroscopy was conducted on AGR SIMFUELs to characterise the structure of the same SIMFUEL materials [86]. The results reinforced the findings of earlier SIMFUEL Raman studies, specifically the effects of dopants on the UO_2 fuel matrix as a function of simulated burn-up, see Figure 2-20.

Similar conclusions were also made regarding the bulk structural changes as a function of increasing doping levels. These can be summarised as (i) the decrease in the fundamental U-O stretch at ~445 cm^{-1}, indicative of lattice distortions and transition away from a perfect cubic fluorite lattice structure due to hyperstoichiometry or dopant incorporation, and (ii) the development of a broad brand at ~500 – 650 cm^{-1} indicative of lattice distortions due to dopant incorporation.

The broad band was fitted and deconvoluted to three peak contributions. Most notably from this study, the ~534 cm^{-1} peak was assigned to a local phonon mode associated with oxygen-vacancy-induced lattice distortions from lanthanide(III) incorporation. A detailed summary of the other two peak assignments can be found in the above Section 2.2.4.4.

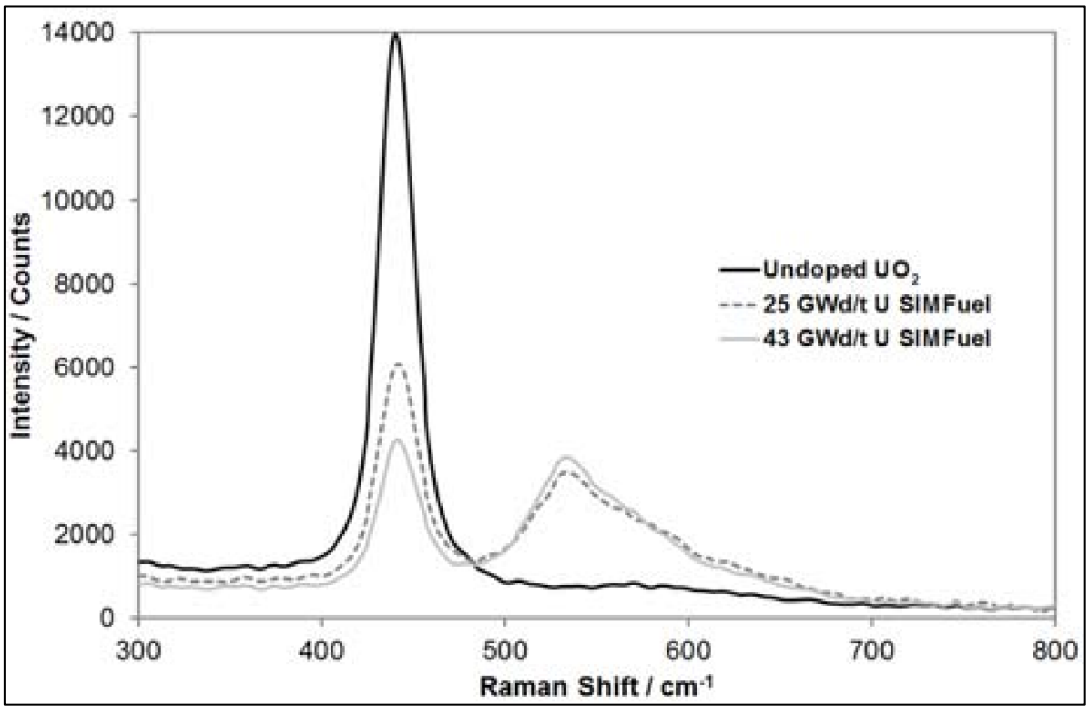

Figure 2-20: Raman spectra of undoped UO_2, 25 GWd/tU and 43 GWd/tU SIMFUEL samples (Figure taken with permission from [86]).

In a further study by Wilbraham et al., XPS, μ-Raman spectroscopy and XRD was used to investigate and determine the O/U ratios in undoped-UO_2 and AGR SIMFUELs – with the XPS and Raman techniques being found to be the most optimal for U/O ratio determination [38].

The UO_2 and SIMFUELs were determined to be stoichiometric, and possibly slightly hyperstoichiometric. Deconvolution of the broad "defect band", between ~500 and 700 cm^{-1} of Figure 2-21, revealed three main contributions, the same as those reported in the earlier study by Wilbraham et al., discussed above.

In this study, Wilbraham et al., also presents a detailed assignment of the three main contributing peaks of the "defect band". A summary of the assignments of the three main contributing peaks, seen in Figure 2-21, can be found in the above Section 2.2.4.4.

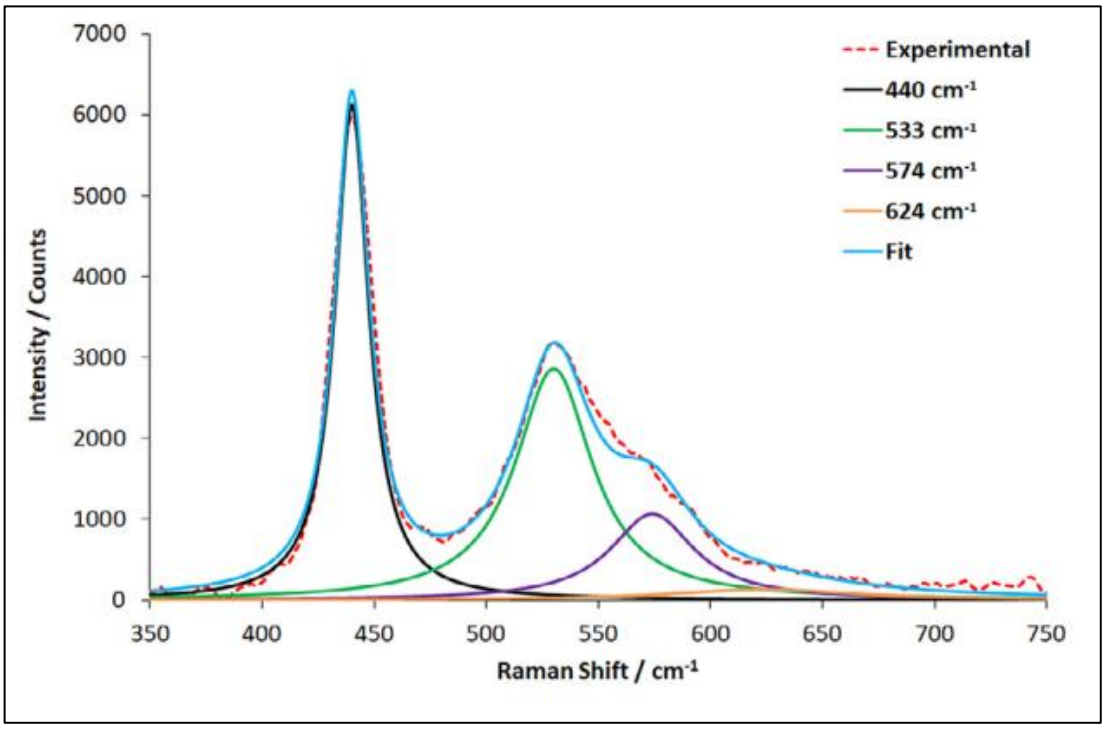

Figure 2-21: Example of Raman spectra peak fitting of a single spectra from the 25 GWd/tU SIMFUEL sample (Figure is release under Creative Commons CC-BY license from [38]).

2.3 Corrosion Behaviour of 20/25/Nb Stainless Steel

20/25/Nb austenitic stainless steel is the cladding material of choice for AGR fuel pins, due to its favourable in-reactor operation properties, as previously described in Chapter 1 Section 1.2.

The specific composition of this steel enables corrosion protection via the presence of 0.7 wt. % Nb in the alloy, as seen in Table 1-2. This protection is derived from Nb acting as a carbon sink – forming Nb carbides – thus preventing the formation of Cr carbides and loss of the protective Cr oxide layer.

Corrosion susceptibility of the cladding material is an important aspect during the lifetime of the spent fuel following removal from the reactor core, as it must be addressed during SNF wet storage and disposal scenarios post reactor irradiation, as discussed in Chapter 1 Section 1.3.1.

During wet storage, the cladding material will be the main component of the fuel pin that is exposed to the pond waters, creating opportunity for the development of a corrosion cell between the stainless steel cladding and its surrounding aqueous solutions and thus promoting a redox process, as previously described in Sections 2.1.1 and 2.1.3. Therefore, it is crucial to understand how redox conditions can affect the corrosion behaviour of stainless steels and more specifically, 20/25/Nb stainless steel.

Corrosion of stainless steels can occur via a number of different physical processes and can be categorised by the method and location of attack. The chemical composition, structure and its local environment can also influence its corrosion behaviour.

The general corrosion process for stainless steel can be explained and expressed as an electrochemical process, similar to that of the iron oxidation/corrosion process described in Section 2.1.1, Equation 2-1 and Equation 2-2.

This section is organised as follows: Section 2.3.1 presents a general overview of the fundamental mechanisms of stainless steel corrosion. Section 2.3.2 briefly describes the thermodynamic Pourbaix diagrams relevant to the common stainless steels and especially to the corrosion studies of 20/25/Nb stainless

steel AGR cladding presented later in this thesis. Section 2.3.3 briefly describes the key literature of the factors that affect the oxidation and corrosion of 20/25/Nb stainless steel AGR cladding.

2.3.1 Stainless Steel Corrosion Processes

As mentioned above, the stainless steel corrosion process can be described similarly to that of the iron oxidation/corrosion process shown in Section 2.1.1, Equation 2-1 and Equation 2-2. The general electrochemistry theory and concepts are also presented in Section 2.1.

This section will discuss the common corrosion mechanism types for stainless steels in order to provide a baseline understanding of how each mechanism can be relevant when studying the corrosion behaviour of 20/25/Nb stainless steel. The common corrosion mechanism types as summarised as follows:

Uniform Corrosion: This corrosion mechanism type tends to occur evenly or uniformly across the whole surface of the material, resulting in a thinning of the material from the exposed surface area. This process occurs in such a way due to the randomness in occurrence of multiple anodic and cathodic reaction sites across the affected area. This type of corrosion is not as prominent on stainless steel due to the protection offered by the presence of a passive film [87].

Pitting Corrosion: A highly localised form of corrosion that is destructive and produces distinctive pits on the surface of the material; these pits can adopt a variety of shapes and sizes and be difficult to detect.

This mechanism occurs when the material is exposed to corrosive environments and can be affected by the chemical composition of the surrounding electrolyte, pH, temperature and microstructure of the steel. For example, the presence of chloride ions in an aerobic atmosphere can promote pitting corrosion [87].

Using chloride and stainless steel as an example we can describe the autocatalytic process that takes place when a pit is formed and develops further. This rapid autocatalytic process is what drives the dissolution of the material and the distinct growth of the pits via penetration through the steel. In an aerated aqueous chloride environment, the presence of Cl^- ions can initiate

the propagation of pitting corrosion by competing with the oxide and hydroxide ions in the passivation of the steel surface layer by forming metal-chloride adsorbed complexes.

This forces local depassivation and increases the likelihood of further pitting corrosion, depending on the stability of the initial pit. If the pit is metastable, then it may become inactive shortly after formation as the surrounding convection current may reduce the concentration of oxidising anions surrounding the pit, allowing for re-passivation to occur.

However, if left to stabilise, the rapid autocatalytic oxidation of the metal via the chloride ions takes place as a result of coupling with the adjacent oxygen reduction. Metal dissolution takes place inside the pit, generating an excess of local positive charge and thus drawing in more Cl^- ions, further increasing the vulnerability of the passive layer and preventing passive layer formation and so propagating the pit.

Crevice Corrosion: Similar to pitting corrosion, this type of oxidisation mechanism has an affinity for localised areas of attack on the surface of steels, by preferentially targeting small tight crevices with limited access to a supply of oxygen.

Thus, bypassing any passivating effects afforded from the oxide surface layer on the steel, leaving it vulnerable to attack, via the same method as a pit. This leads to the development of a concentration cell between the oxygen-starved environment inside the crevice (anode) and the highly oxidative electrolyte outside the crevice (cathode) [87].

Severity of the corrosion can depend on the localised concentration of chloride present and the size and depth of the crevice; the deeper and narrower, the more severe.

Intergranular Corrosion: This form of corrosion mechanism takes place selectively at or near the grain boundaries but with no significant dissolution of the grains themselves.

It is associated with the potential differences between the grains and precipitates, impurities, or other metallic phases formed at the grain boundaries, and therefore, the mechanism will differ depending on the steel alloy.

In austenitic stainless steel, a common mechanism of intergranular corrosion is derived from the formation of chromium carbide precipitates at grain boundaries. This is known to take place when austenitic stainless steels undergo sensitisation when they are reheated to a temperature between 400 – 800 °C [87].

This precipitation process creates zones at the boundaries where the chromium has been depleted as a result of a reaction with carbon impurities within the steel to form the aforementioned Cr carbides. This process of Cr depletion results in less passivation in relation to the rest of the surface, resulting in a corrosion cell forming between the depleted zone (anode) and the adjacent grains (cathode) [88].

Stress Corrosion Cracking: This mechanism requires a combination of tensile stress and corrosion. The tensile stress can arise from externally applied forces or residual stresses due to heat or mechanical treatment.

The resulting cracks can then develop further as they become subjected to a corrosive environment and oxidise via a corrosion cell similar to pitting corrosion and then further propagates through the material. In austenitic stainless steels, this can be caused by a combination of material under tensile stress in an environment of oxygen, chloride and high temperature [89, 90].

2.3.2 Pourbaix Diagrams of Stainless Steel

Pourbaix diagrams are plots of electrode potential E of the system vs. pH. Section 2.2.2 describes the construction, interpretation and purpose of Pourbaix diagrams and their use as a tool for predicting the dominant thermodynamically stable species/favourable oxidation state at a solid surface or in solution, at a given potential and pH.

This section presents the common Pourbaix diagrams associated with stainless steels and especially those relevant to the studies of 20/25/Nb stainless steel AGR cladding. Pourbaix diagrams for the main elemental components of 20/25/Nb stainless steel, Fe, Ni, and Cr, are presented below.

Typical Pourbaix diagrams for the iron-H_2O system, nickel-H_2O system, chromium-H_2O system, along with simplified versions which show the approximate respective regions of passivity, corrosion and immunity, are predicted in Figure 2-22, Figure 2-23 and Figure 2-24, respectively. These diagrams can be used to interpret and describe each alloying metal's ability to influence the passivity, immunity and corrosivity of typical stainless steels.

At alkaline pH, the Fe-H_2O system exhibits passivation at potentials between roughly -0.5 V to 1.0 V, derived predominantly from the oxide form of Fe_2O_3. At this potential range, stainless steel will sit comfortably under passivation, with the addition of Ni and Cr alloying metals providing further enhancements not only to the chemical stability but also to the mechanical properties.

By overlaying the simplified Pourbaix diagrams of each major contributing alloy we can thermodynamically predict how each alloy contributes to the passivation of a typical stainless steel, as shown in Figure 2-25.

The overlapping coloured regions of each contributing metal alloy gives an indication of the expected region of passivation for a typical stainless steel [39, 91, 92].

It can be seen from Figure 2-25, the iron and chromium contribute the majority of the passivation effects in the neutral to alkaline regions of water stability, and the addition of chromium helps to enhance the corrosion resistance in reducing environments compared with just pure iron [91].

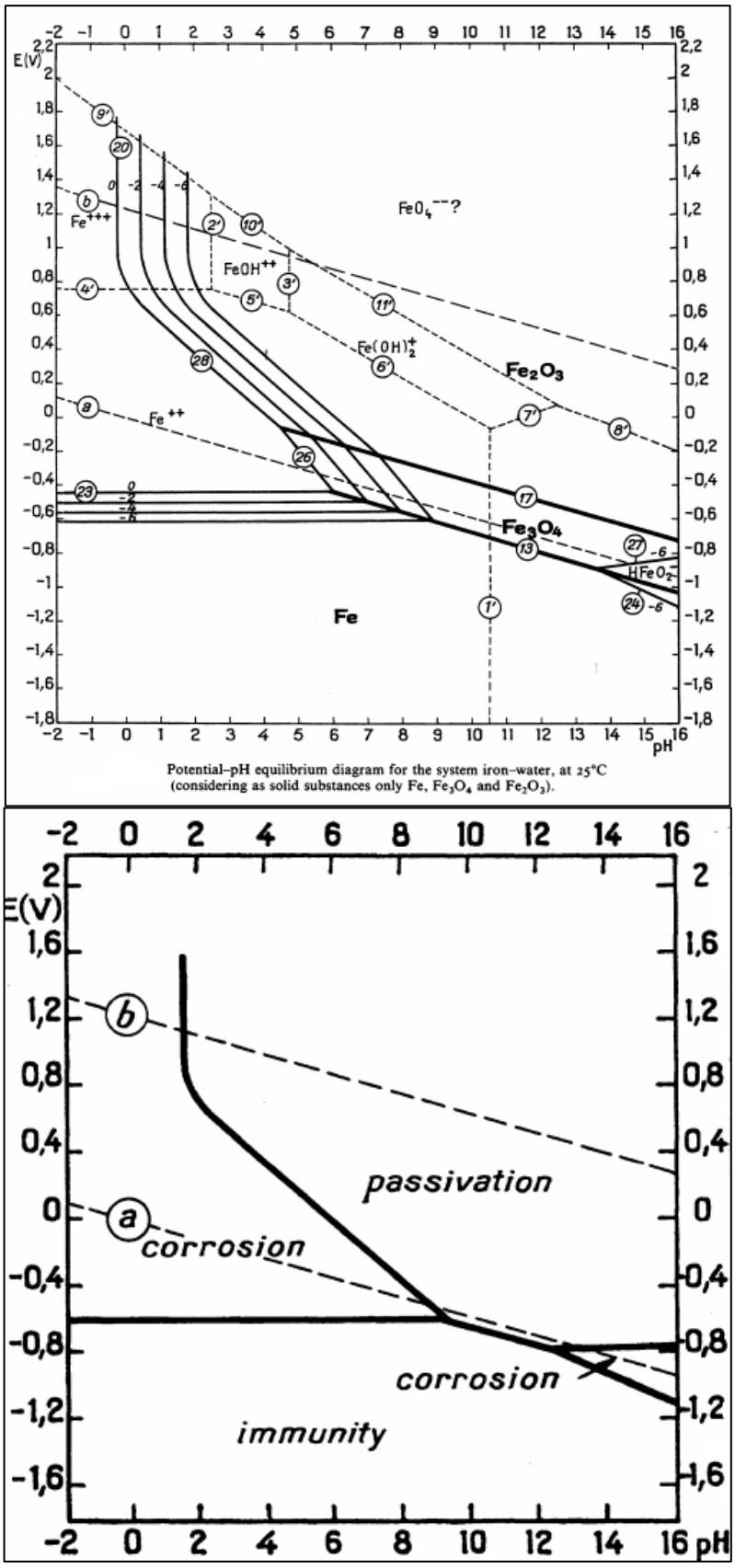

Potential–pH equilibrium diagram for the system iron–water, at 25°C (considering as solid substances only Fe, Fe_3O_4 and Fe_2O_3).

Figure 2-22: Pourbaix diagram of (top) Fe/H_2O system at 25 °C, and (bottom) simplified Pourbaix diagram of the same system (Figure taken and adapted with permission from [57]).

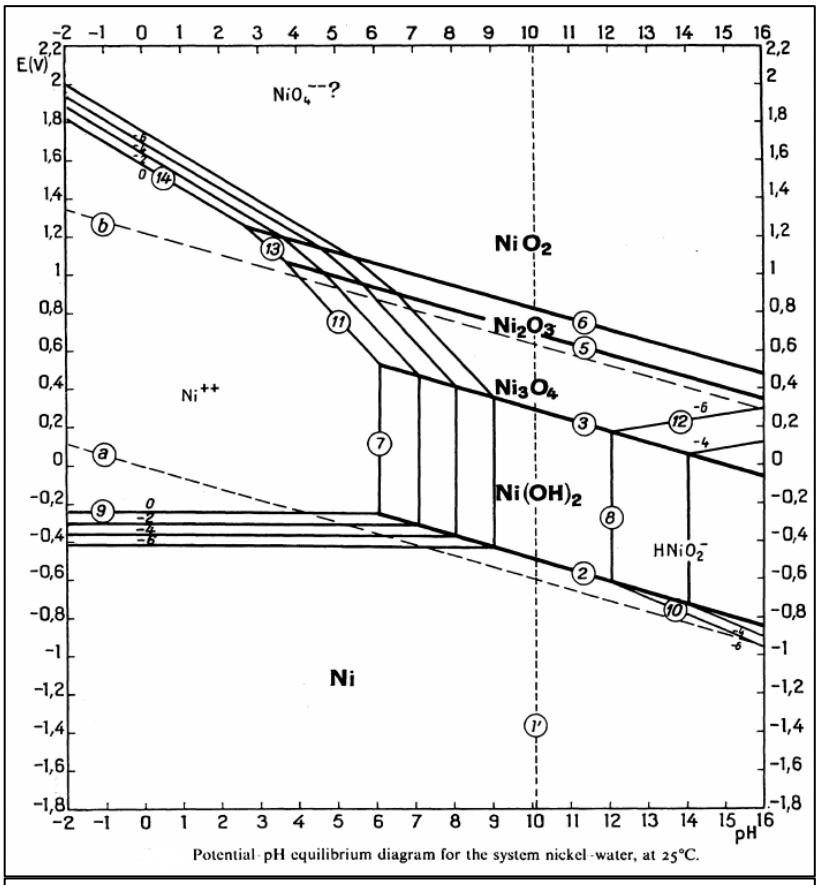

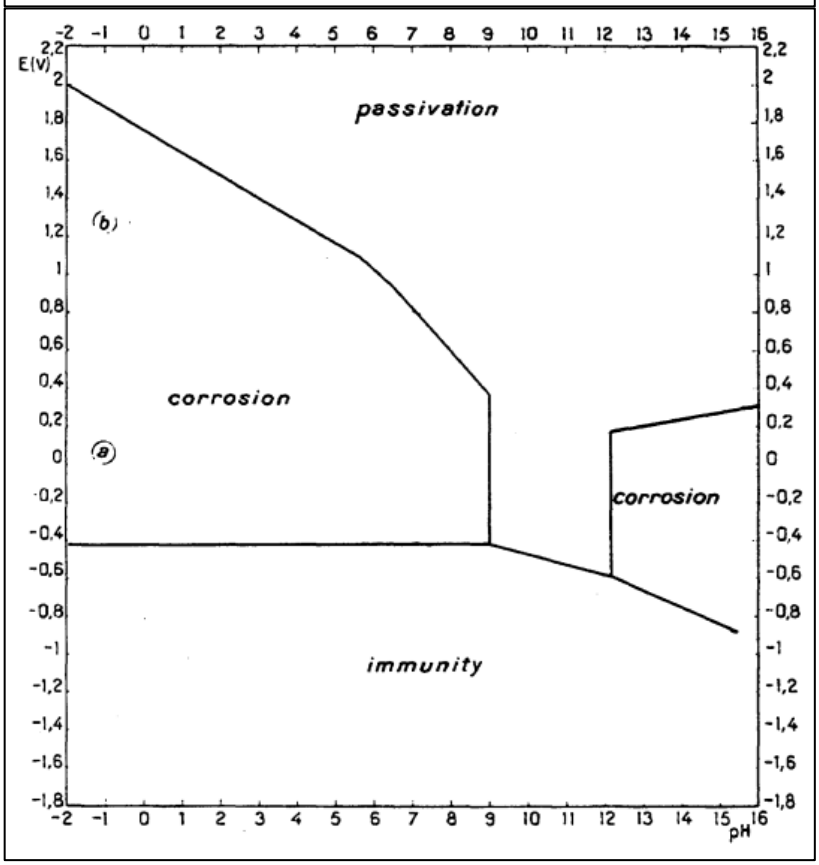

Figure 2-23: Pourbaix diagram of (top) Ni/H_2O system at 25 °C, and (bottom) simplified Pourbaix diagram of the same system (Figure taken and adapted with permission from [57]).

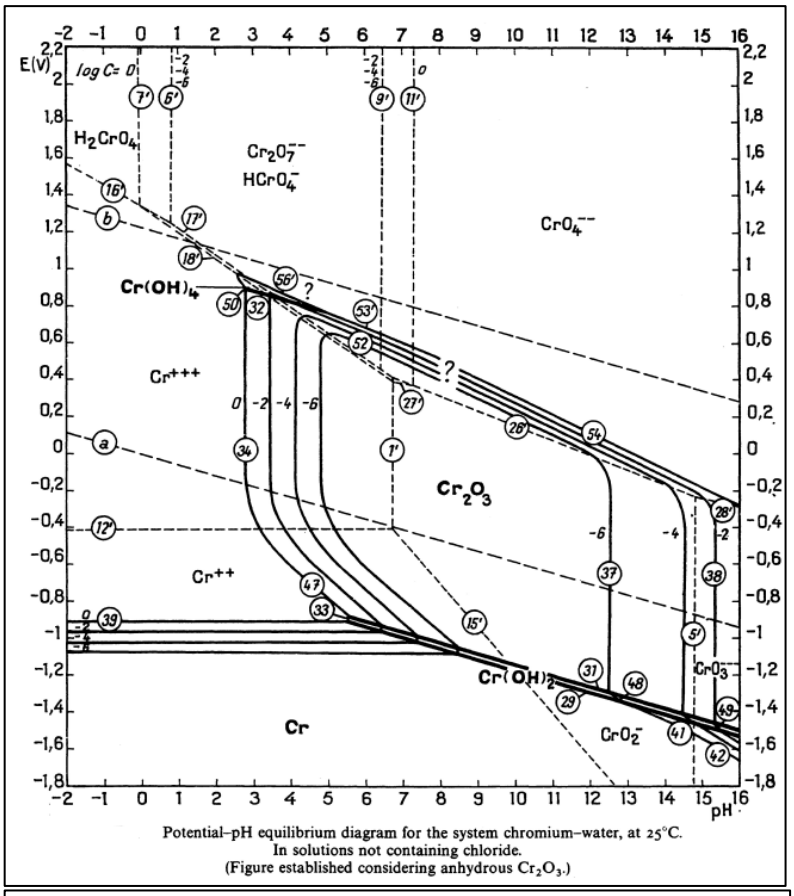

Potential–pH equilibrium diagram for the system chromium–water, at 25°C.
In solutions not containing chloride.
(Figure established considering anhydrous Cr_2O_3.)

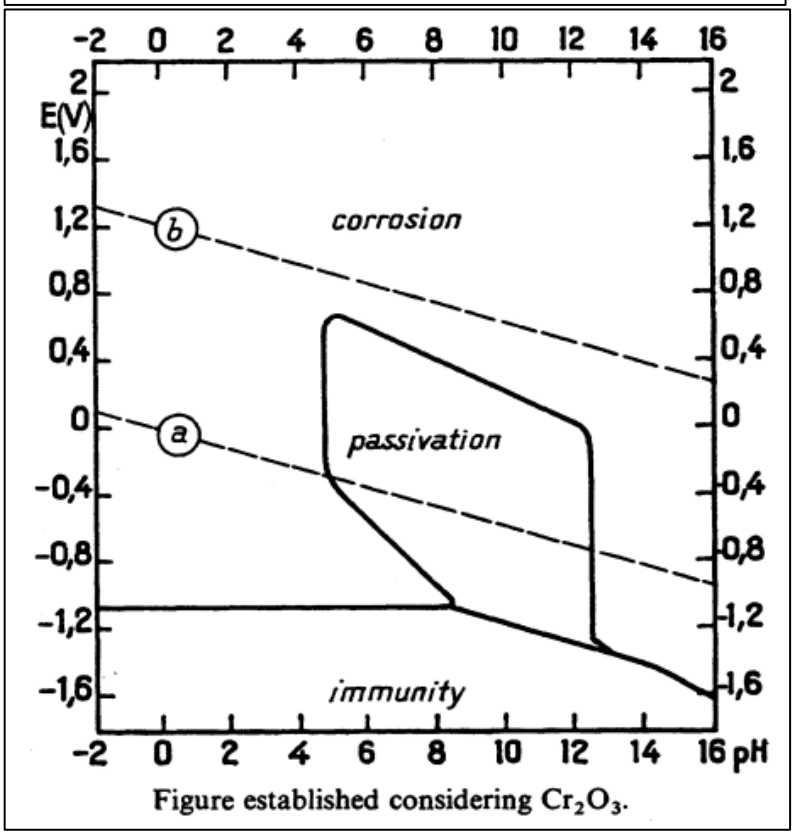

Figure established considering Cr_2O_3.

Figure 2-24: Pourbaix diagram of (top) Cr/H_2O system at 25 °C, and (bottom) simplified Pourbaix diagram of the same system (Figure taken and adapted with permission from [57]).

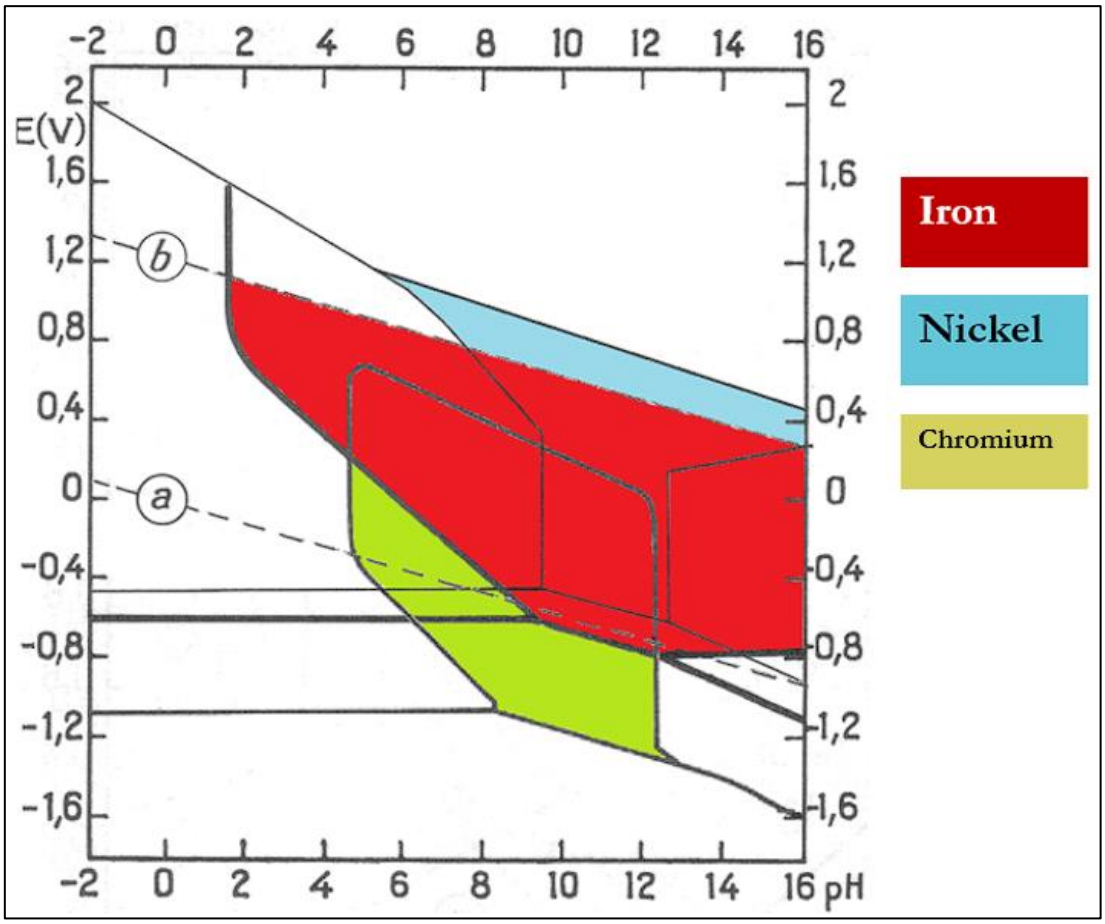

Figure 2-25: Simplified Pourbaix diagram of the combined simplified Pourbaix diagrams of iron, nickel and chromium at 25 °C (Figure taken and adapted with permission from [91]).

2.3.3 Factors Affecting Corrosion

Corrosion research of 20/25/Nb stainless steel AGR cladding is an important area as it concerns the behaviour of the SNF post-reactor removal.

Understanding the corrosion behaviour of AGR cladding under different conditions and the factors that can influence its corrosion is important as the cladding material is the final barrier between the UO_2 spent fuel pellets and its surrounding environment. Various factors can influence corrosion such as pH, pond/ground water chemistry, radiolysis, and Radiation-Induced Segregation (RIS).

This section briefly summarises the key literature of the factors that can influence the corrosion of typical stainless steels and 20/25/Nb stainless steel AGR cladding.

2.3.3.1 Influence of Chloride

The presence of Cl^- around steel can cause competition for the passivation of the surface oxide layer by formation of metal-chloride complexes. As described in Section 2.3.1, this will lead to localised forms of corrosion such as pitting, crevice corrosion and stress corrosion cracking.

During these processes, the oxidation of Fe^{2+} to Fe^{3+} is accelerated and solubilisation of iron occurs, compounding the effect of the initial chloride attack. This is further enhanced if the chemical environment is acidic and the concentration of chloride is high [93].

Anwyl et al., reports on electrochemical polarisation studies of 20/25/Nb AGR cladding as a function of chloride concentration in the electrolyte [48]. The polarisation curves of Figure 2-26 confirms the above-described enhancement in corrosion susceptibility, as a function of increasing chloride concentration.

The critical pitting potential, at ~ 0.4 V in 50 – 500 mM NaCl, was observed shifting to lower potentials with increasing [Cl^-], at ~0.2 V, reaching a state where initiation of pitting can occur, thus reducing the region of passivity for the steel. This effect also simultaneously shifts the onset of transpassivity towards lower potentials.

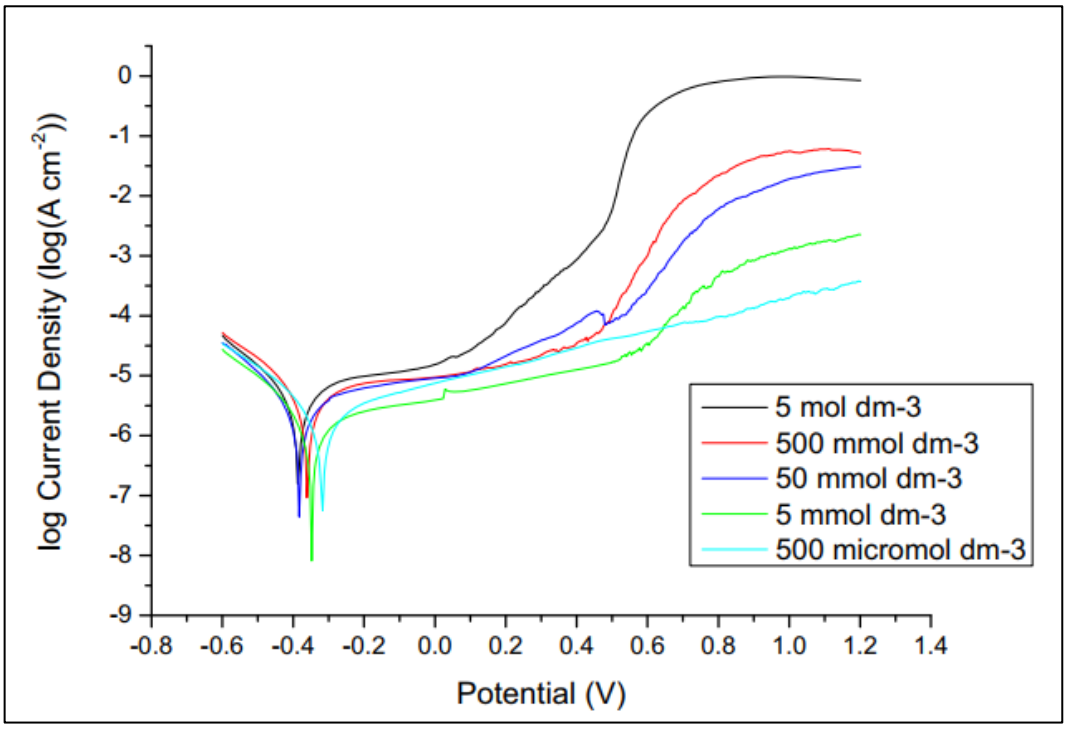

Figure 2-26: Polarisation curves of AGR cladding in different concentrations of NaCl at pH 5.5 (Figure released under Creative Commons license from [48]).

2.3.3.2 Influence of Radiolysis Products

The products of water radiolysis can contain both oxidising and reducing species. Amongst the radiolysis products, H_2O_2 is the most long-lived oxidising agent generated during the radiolysis of water and thus plays a major role in any radiolysis-enhanced corrosion process.

In a report by Makjan et al., voltammetry studies were carried out on 304 stainless steel in peroxide under high-temperature water, up to 80 °C [94]. The results showed pitting corrosion as the dominant form of corrosion and with the acceleration of such events with increasing [H_2O_2] and temperature. SEM-EDX was also used to determine preferential depletion of Fe and Ni over Cr, due to the formation of stable Cr oxides [95-97].

The influence of pH plays a role on the effect of H_2O_2. In early electrochemical studies on 304L stainless steel by Song et al., it was reported that changes to the OCPs induced by each of the H_2O_2 concentrations were least prominent at very alkaline and very acidic pHs [98].

It was hypothesised that at extreme acidic conditions, the cathodic reaction rate for reduction of H^+ was greater than that of H_2O_2, i.e., H^+ becomes the stronger oxidising agent. Similarly, at higher alkaline pH, the competing cathodic reaction is that of OH^- reduction. However, in neutral pH solutions, the pitting potential is shifted to less positive potentials and a decrease in the passive potential range is observed.

Anwyl et al., studied the effect of 10 $\mu mol/dm^3$ H_2O_2, on 20/25/Nb AGR cladding using linear sweep voltammetry, in a pH 6.8 simulant groundwater electrolyte [48]. The specific peroxide concentration was chosen to mimic the predicted near-field H_2O_2 concentrations for a scenario of spent nuclear fuel stored in a repository, surrounded by groundwater [99].

The presence of H_2O_2 caused an increase in the OCP of the steel cladding and a decrease in the passive range, as shown in the polarisation curves of Figure 2-27. The decrease in current densities over the passive potential range was also attributed to the faster growth of the passive oxide layer resulting from higher oxidative stress caused by the presence of H_2O_2. It was suggested that

this effect could potentially afford greater protection to the steel surface than a thinner oxide layer, if uncompromised.

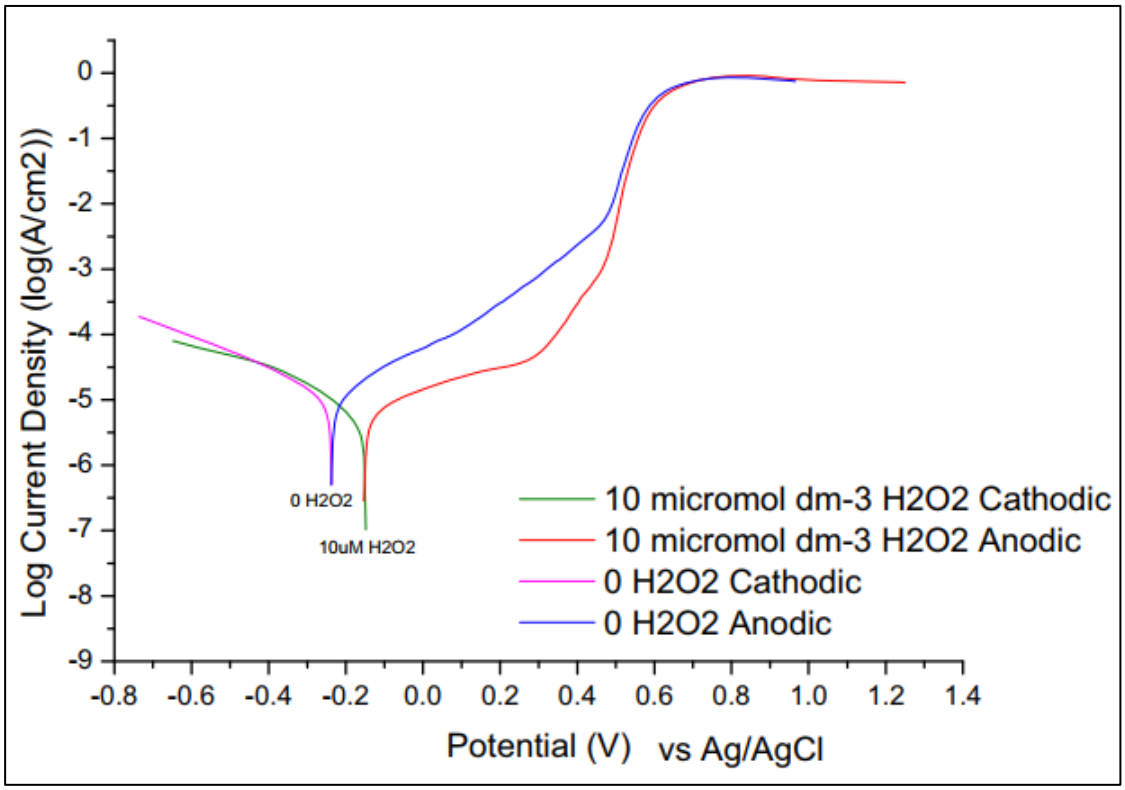

Figure 2-27: Polarisation curves of 20/25/Nb in evaporite simulant groundwater at pH 6.8 (Figure released under Creative Commons license from [48]).

2.3.3.3 Influence of pH

According to the stainless steel Pourbaix diagrams presented and discussed in Section 2.3.2, we can predict the type of stable oxide formations that may occur at different combinations of E and pH.

From Figure 2-28, it can be inferred that stainless steels will remain passive under alkaline conditions, protected from dissolution by the process surface oxide layer formation. This is in contrast with acidic conditions, where increased oxidation/corrosion is expected to occur due to the dissolution of iron and the more favourable formation of chromium-oxide surface layers [3].

In studies by Fattah-Alhosseini et al., a series of voltammetry studies were conducted on stainless steels under concentrated acidic conditions and supported by EIS [100, 101].

The voltammetry data showed increased corrosion current densities as a function of decreasing pH. This observation was further supported by passive film resistance and capacitance data from additional EIS measurements, seen in Figure 2-29, which suggests a decreasing oxide layer with decreasing pH as shown by the decreasing passive film resistance. In contrast, increasing the pH resulted in the formation of thicker and less defective oxide layers, offering better corrosion protection [101, 102].

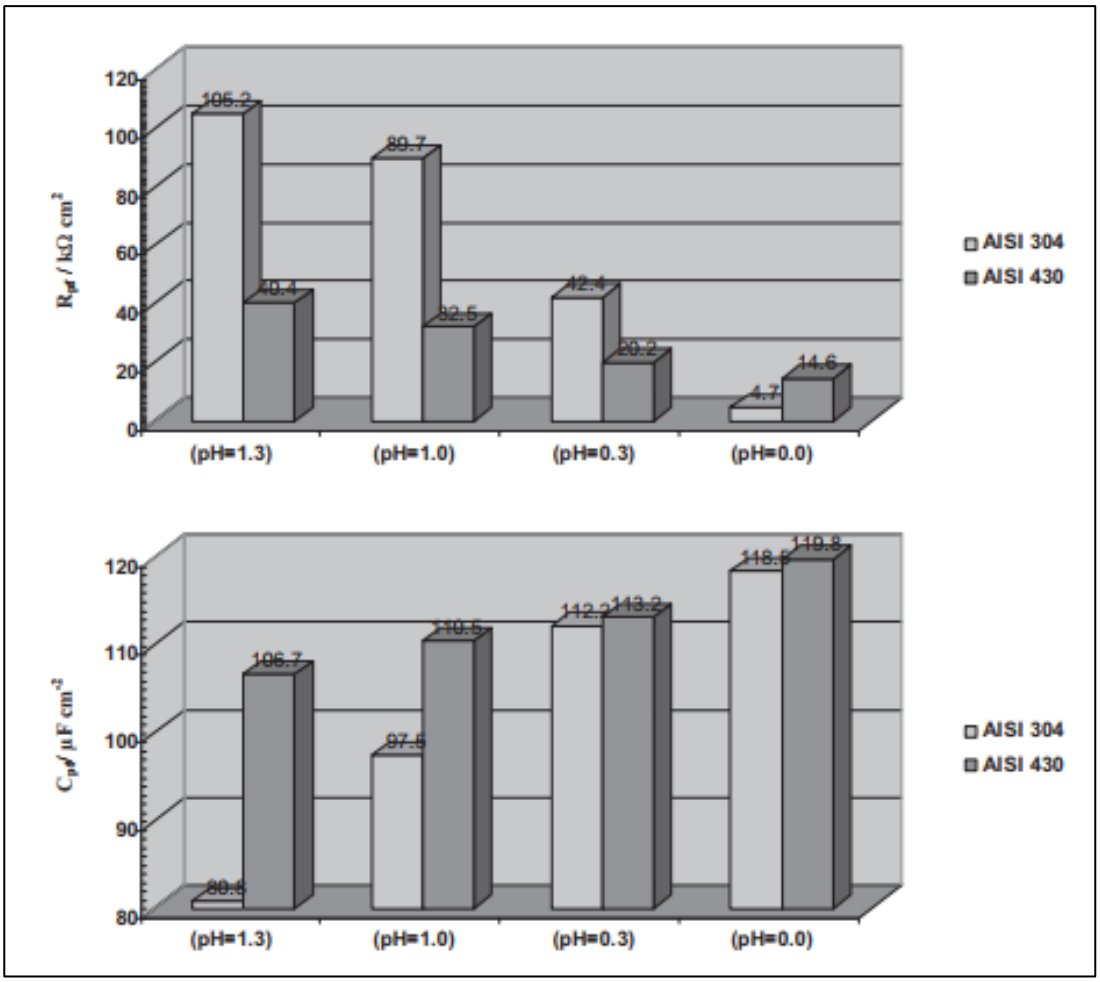

Figure 2-29: Effect of pH on (top) the passive film resistance and (bottom) passive film capacitance of AISI 304 and AISI 430 stainless steels in HNO_3 solutions 8 (Figure released under Creative Commons license from [101]).

In a report by Schmutz et al., simultaneous in-situ mass monitoring with quartz crystal microbalance (QCM) was used to study the mass loss of steel under acidic and alkaline pH conditions [103].

The data revealed selective mass loss of iron under acidic conditions, coupled with chromium enrichment of the passive layer. The opposite behaviour was observed at alkaline pH, where there was an increase in passive layer mass gain, with additional XPS data showing preferential migration of iron oxides at the surface layer.

This observation is in line with the predicted thermodynamically stable phases from the Pourbaix diagram of the Fe-H_2O system, seen in Figure 2-22. This is due to the lower dissolution rates afforded from thicker oxide film growth containing Fe(III) oxides which are more stable in alkaline conditions [104].

Under the current UK SNF management strategy, AGR SNF is wet stored in low chloride and alkaline pond waters dosed to pH 11.4 to reap the positive benefits of a decreased passivation potential.

Storage in alkaline conditions also increases the potential range over which the steel remains passive and by driving the potential at which transpassivity occurs, to more positive values [3, 105, 106].

In a study by Howett et al., LSV measurements were conducted on unsensitised 20/25/Nb stainless steel AGR cladding, in a pH 11.4 simulant pond water electrolyte, and in an undosed pH 7 equivalent, to investigate the effect of alkaline pH on the corrosion susceptibility of AGR cladding [3].

The polarisation curves of Figure 2-30 shows the differences in the current response between the undosed and pH 11.4 dosed solution. The pH 7 data shows the presence of metastable pitting corrosion from ~0.4 V, whereas the pH 11.4 data does not show any signs of pitting corrosion. The region of passivity is also larger in the pH 11.4 data, indicating greater corrosion protection to the AGR cladding.

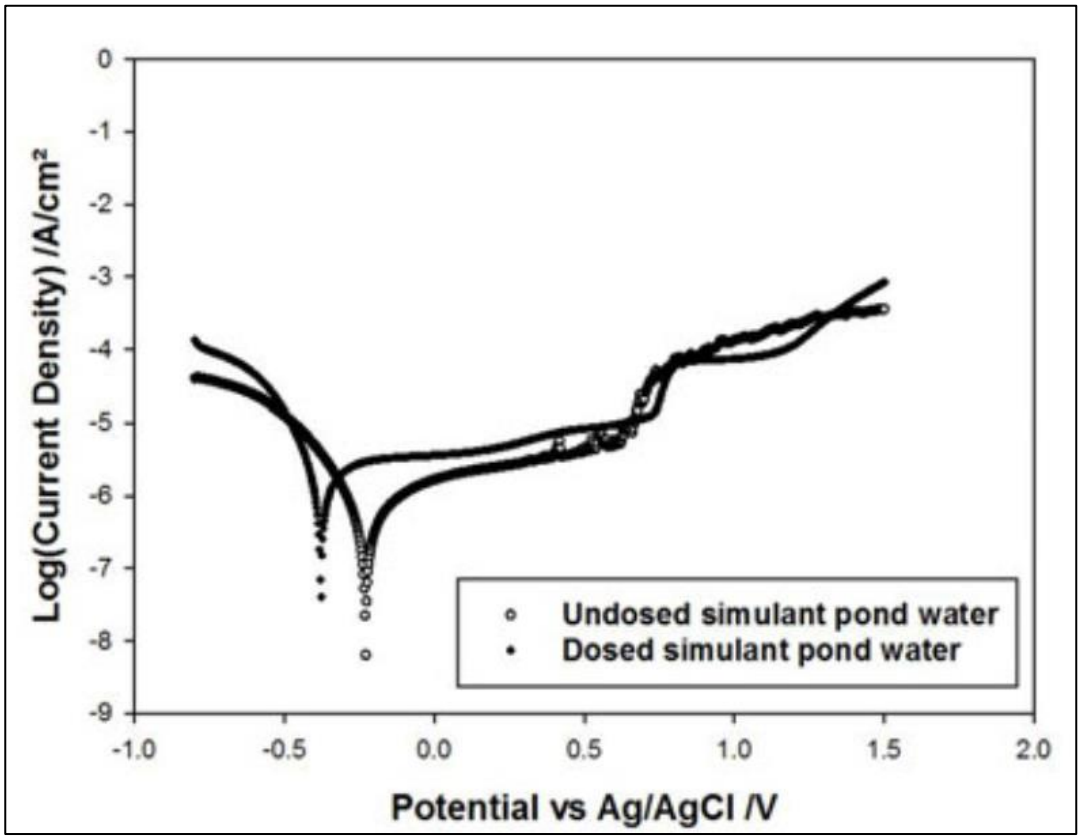

Figure 2-30: Polarisation curves of AGR cladding in undosed simulant pond water solution and in dosed simulant pond water solution at pH 11.4 (Figure taken with permission from [3]).

2.3.3.4 Radiation Induced Segregation

Radiation Induced Segregation (RIS) is a phenomenon that occurs in stainless steels when the material is subjected to neutron irradiation at temperatures ranging between 250 – 600 °C.

The mechanism is described as diffusive fluxes of point defects to sinks (low energy sites), such as near grain boundaries or grain surfaces and due to the varying diffusion rates of the alloying elements, this will cause a change in local elemental compositions [107]. Thus altering the mechanical and structural properties of the steel.

For Fe-Ni-Cr alloy austenitic steels, the typical mode of local composition change from RIS is depletion of Cr at the grain boundaries and replacement by Ni, as seen in Figure 2-31, which show the changes in percentage composition between the Fe, Ni and Cr contents at the surface of an irradiated stainless steel sample, as a function of the relative distance from the measured grain boundary. The data shows the depletion of Fe and Cr content towards the grain boundary and the increase in Ni content towards the grain boundary.

This is of particular relevance to the study presented in Chapter 6, where the corrosion behaviour of real legacy AGR SNF is discussed, and we are therefore concerned with the corrosion susceptibility of AGR cladding after reactor irradiation.

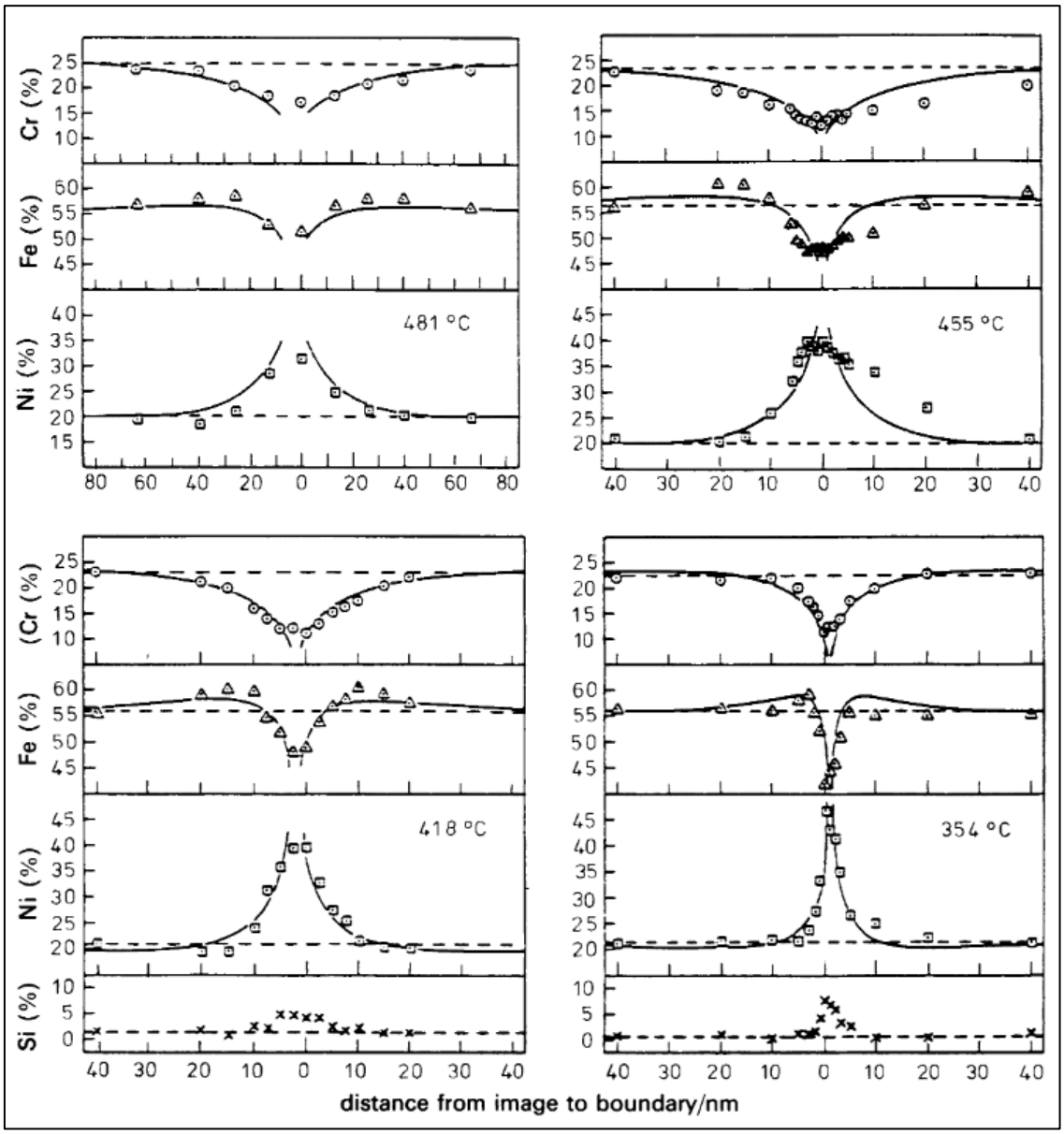

Figure 2-31: Experimental vs. calculated elemental profiles of Fe, Ni, Cr and Si of irradiated austenitic stainless steel (Figure taken with permission from [107]).

In a similar study by Ashworth et al., RIS studies of 20/25/Nb were carried out at temperatures between 200 and 500 °C [108]. It was found that depletion of Cr and enrichment of Ni at the grain boundaries was the most prominent up to 450 °C, with no segregation detected at 200 °C and a reduction in segregation at a higher temperature of 500 °C.

In an AGR reactor, different sections of the reactor core will be subjected to different regional temperatures, therefore, only certain parts of the fuel stringer may be affected by RIS, with the most severe effects occurring in the range of

400 – 420 °C. Fuel elements towards the lower stringer positions experience lower temperatures and are therefore most likely to experience RIS [11, 109, 110].

Thus, this strong dependence of the extent of radiation induced segregation on temperature means that not all AGR cladding will experience the most negative effects of Cr depletion at boundaries. In the worst cases, results of such RIS can include, but are not limited to, decreased corrosion resistance, susceptibility to intergranular corrosion attack (IGA) or intergranular stress corrosion cracking (IGSCC) [111, 112].

Similar levels of Cr depletion may also take place due to thermal sensitisation, electron radiation, proton irradiation, or heavy ion irradiation. To combat IGSCC, wet storage ponds for AGR SNF are kept to low chloride concentrations (< 0.1 ppm) and dosed with NaOH to pH 11.4; this has been shown to inhibit IGSCC for over 20 years of spent fuel storage [112].

2.4 Knowledge Gap

This section summarises the key knowledge gaps identified from the literature review presented in Section 2.2, on the corrosion studies of UO_2 and SIMFUELs and in Section 2.3, on the corrosion studies of 20/25/Nb stainless steel AGR cladding, and how these knowledge gaps are addressed by the further studies carried out in this thesis:

- Majority of published studies on uranium oxide fuels and associated spent fuel simulants are based on the research of materials related to Light Water Reactor fuels and CANDU Pressurised Heavy Water Reactor fuels.
- There is minimal research on the electrochemical corrosion behaviour of AGR SIMFUELS, including specific factors affecting corrosion, such as the influence of radiolysis products and dopants. The work presented in this thesis aims to address this knowledge gap by presenting studies to understand the baseline behaviour of AGR SIMFUELs, under conditions relevant to UK long term pond storage, using a combination electrochemical techniques and μ-Raman spectroscopy.

- There is minimal research on AGR fuel corrosion concerning the behaviour at the fuel pellet and cladding interface. The work presented in this thesis aims to address this knowledge gap by studying the electrochemical corrosion behaviour of coupled / composite electrode systems consisting of both AGR cladding and AGR SIMFUEL pellets.
- There is minimal research on the electrochemical corrosion behaviour of legacy AGR SNF. The work presented in this thesis aims to address this knowledge gap by conducting the first ever electrochemical studies on a sample of legacy AGR SNF.

2.5 Concluding Remarks

Having now discussed the background electrochemistry theories and concepts, in Section 2.1 and provided a summary of the literature studies that are relevant to the electrochemical corrosion studies of UO_2 / AGR SIMFUELs and 20/25/Nb stainless steel AGR cladding, in Section 2.2 and 2.3, respectively.

The next chapter describes the experimental techniques and materials used for the study of the aforementioned materials and the study of the legacy AGR SNF electrode.

3 Experimental Techniques and Materials

This chapter describes the fabrication and preparation of the materials used for the studies presented in this thesis, and presents the experimental methods and techniques used for the voltammetry and μ-Raman spectroscopy studies of such materials.

3.1 Materials

3.1.1 Simulant Pond Water Solutions

All electrolyte solutions were purged with nitrogen gas to remove oxygen, unless otherwise stated.

Simulant Pond Water (SPW) solutions were prepared in deionised water using the ion composition shown in Table 3-1. The solutions are dosed with NaOH depending on the desired pH (pH 8, 11.4 or 12.5). The ion composition in the SPW solution was obtained from sample data recorded from the Sellafield AGR storage pond [15].

Ion	**Concentration / μmol/dm^3**
Na^+	$5.4x10^3$
Ca^{2+}	2
K^+	5
Cl^-	30
SO_4^{2-}	2
OH^-	balance

Table 3-1: Simulant Pond Water solution ion composition.

Simplified Simulant Pond Water (SSPW) solutions were prepared with NaCl (30 μmol/dm^3) in deionised water. Dosed with NaOH depending on desired alkalinity (pH 8, 11.4 or 12.5). The addition of 30 μmol/dm^3 chloride ions is used to simplify the SPW solution by removal of the other supporting ions, allowing for easier solution preparation, especially during the experimental campaign involving real irradiated spent AGR fuel in hot-cells at the UK National Nuclear Laboratory Windscale facility (NNL, Sellafield, UK). The removal of the other ions will not affect the electrolyte solutions as they are not of interest to the studies conducted, only the chloride ions are relevant. The solution has been tested and compared with the SPW solution electrochemically to verify compatible suitability.

Background electrolyte solutions were prepared with Na_2SO_4 (0.5 mol/dm^3) in deionised water, at solution pH typically between pH 5.5 and 6.

3.1.2 Undoped-UO_2 and AGR SIMFUELs

As discussed in Chapter 1 Section 1.4.3, undoped-UO_2 and AGR SIMFUEL pellets were fabricated by the UK National Nuclear Laboratory (NNL, Springfields, UK). The SIMFUELs represent spent UO_2 fuel pellets that have been cooled for over 100 years post reactor irradiation and simulates two degrees of burn-up, one “low” and one “high”.

The low burn-up SIMFUEL, at 25 GWd/tU, represents ~4.6 years in-reactor irradiation time and the high burn-up SIMFUEL, 43 GWd/tU, represents ~7.8 years in-reactor irradiation time.

Pellets were prepared using the compositions shown in Table 3-3. The simulated spent fuel compositions were calculated using the fuel inventory code, FISPIN (Burstall, R.F., UKAEA Risley Nuclear Power Development Establishment, 1979 [113]). Hiezl et al., 2015 [46] provides a detailed report on the preparation and characterisation of the AGR SIMFUELs.

In general, the pellets were made by combining depleted uranium dioxide with non-radioactive elements in order to simulate the fission products found in real SNF. The specific steps involved in the fabrication of the SIMFUEL pellets are as follows [46]: A combination of 60 g blend of UO_2 and oxides (fission product

surrogates) were mixed, weighed and ball milled for 12 h using ZrO_2 milling media. Then sieved through a 1.14 nm sieve and pre-compacted at 75 MPa to produce granules. 0.2 wt.% of zinc stearate was added as a lubricant. The granules were then uniaxially pressed at 400 MPa to form pellets. These pellets were then sintered at a standard gas mix for AGR fuel manufacturing of 99.5 vol.% H_2 and 0.5 vol.% CO_2, at 5 °C/min to 300 °C then 15 °C/min to 1730 °C, for a total of 300 min. The resulting pellets were then cooled at a rate of 15 °C/min to room temperature.

Figure 3-1 and Figure 3-2 shows the shape and size of a typical pellet of undoped-UO_2 or SIMFUEL. The approximate surface area for the exposed UO_2/SIMFUEL pellet is ~0.7088 cm^2.

An additional set of SIMFUELS were prepared at a simulated burn-up of 43 GWd/tU but with additional high lanthanide doping and another with additional high lanthanide and chromium doping.

For the 43 GWd/tU high lanthanide-doped, and 43 GWd/tU high lanthanide and chromium-doped SIMFUEL pellets, simulations were conducted in FISPIN to give a composition representing a post-reactor irradiation cooling period of over 100,000 years.

The resultant fission product inventories can be seen in Table 3-3. For the work presented in this thesis, SIMFUEL pellets fabricated according to compositions of both 100 years and 100,000 years cooling periods will be treated as equivalents as the overall fission product inventory compositions do not vary significantly between the two cooling time period scenarios.

These modified 43 GWd/tU SIMFUELs contain a comparatively higher concentration of lanthanide/rare-earth oxides, such as: Nd_2O_3, La_2O_3 and Y_2O_3. The 43 GWd/tU SIMFUEL with an additional chromium doping contains 0.1 at.% of Cr_2O_3 added to its composition.

Table 3-2 shows the relative bulk uncompensated resistances for undoped UO_2, 25 GWd/tU and 43 GWd/tU SIMFUEL, including the high lanthanide and high lanthanide + chromium doped SIMFUELs. The uncompensated resistances, R_u, were determined using the Autolab NOVA current-interrupt method, via the

Metrohm Autolab potentiostats; the method is described in Section 3.2.3. The measured resistances enable qualitative comparison between the UO_2 and SIMFUELs. They show that the R_u decreases across the UO_2 samples with increasing doping level.

Table 3-4 shows the reported grain sizes and densities of the UO_2, 25 and 43 GWd/tU SIMFUEL pellets (100 year cooling time dataset), previously determined and reported by Hiezl et al., 2015 [46]; bulk densities were calculated using Archimedes' method, and grain sizes were determined using a grain boundary interception method.

Grain sizes for the SIMFUELs are reported to be at the lower range of real AGR SNF. Which, as described in Chapter 1 Section 1.4.3, the density of the pellets can be seen to decrease as doping or simulated burn-up is increased; this is attributed to secondary phase formations or increased porosity due to trapped gas during oxide reduction.

The U/O ratios of the as-received samples of undoped UO_2 and SIMFUEL pellets have previously been determined and reported by Wilbraham et al. using a combination of XRD, XPS, and Raman microscopy [38]. All samples were found to be close to stoichiometric if not slightly hyperstoichiometric, similar to previously reported O/U ratios in real and simulated LWR fuels.

	UO_2	25 GWd/tU	43 GWd/tU	43 GWd/tU High Ln	43 GWd/tU High Ln + Cr
R_u (Ω)	8994	89.80	49.97	31.31	21.52

Table 3-2: Relative bulk material resistances of undoped UO_2 and SIMFUELs, measured using IR interrupt method.

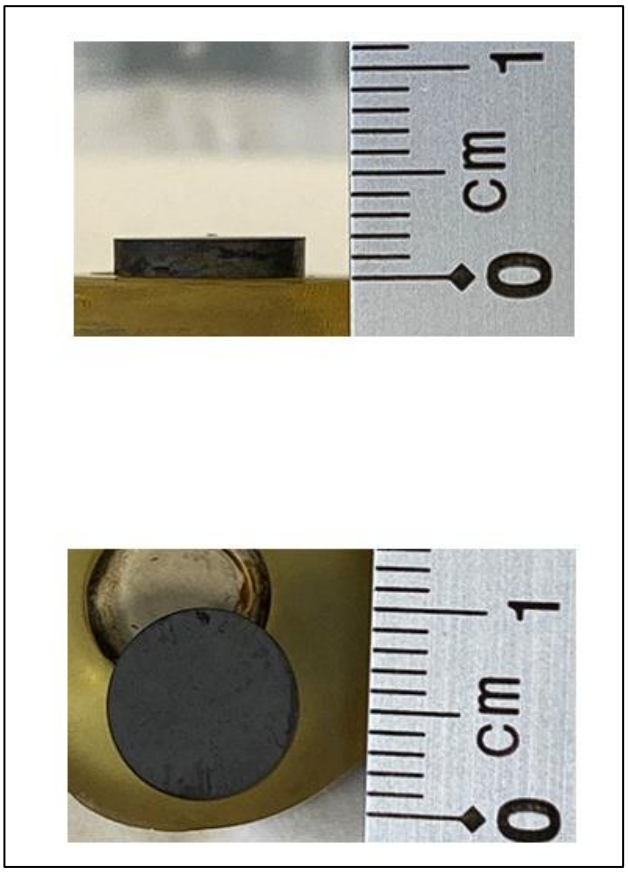

Figure 3-1: A typical shape and size of a SIMFUEL or UO_2 pellet.

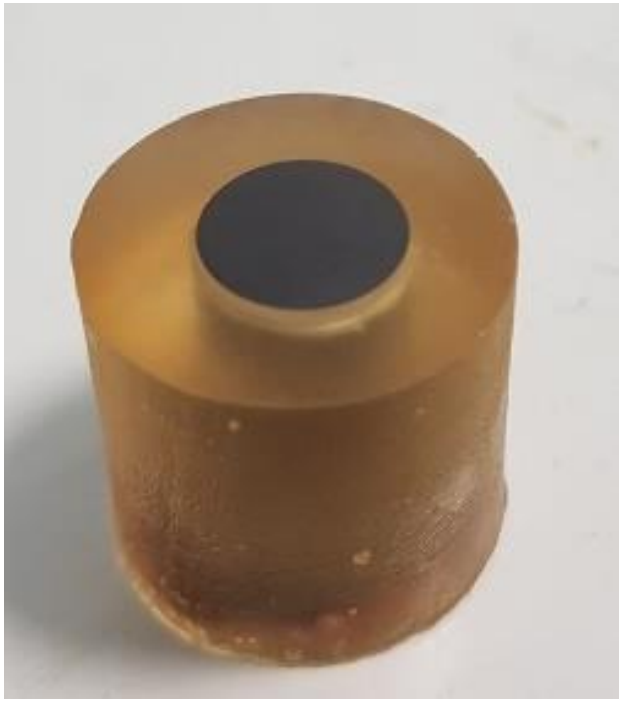

Figure 3-2: SIMFUEL pellet mount on brass and encased in resin.

Oxides	100 Years Cooling Time		100,000 Years Cooling Time	
	25 GWd/tU	43 GWd/tU	43 GWd/tU	
			High Lanthanide	High Lanthanide with Chromium
UO_2	95.705	92.748	90.515	90.415
Nd_2O_3	0.761	1.284	2.500	2.500
ZrO_2	0.793	1.276	1.289	1.289
MoO_3	0.614	1.027	1.034	1.034
RuO_2	0.512	0.892	0.898	0.898
$BaCO_3$	0.328	0.576	0.608	0.608
CeO_2	0.297	0.499	0.502	0.502
PdO	0.195	0.425	0.427	0.427
Rh_2O_3	0.080	0.115	0.115	0.115
La_2O_3	0.156	0.256	1.000	1.000
SrO	0.081	0.126	0.112	0.112
Y_2O_3	0.095	0.149	1.000	1.000
Cr_2O_3	0.000	0.000	0.000	0.100

Table 3-3: Atomic percentage composition of SIMFUEL pellets calculated using FISPIN [46].

	Undoped UO_2	25 GWd/tU	43GWd/tU
Grain size	9.7 ± 2.3 µm	4.21 ± 0.59 µm	2.95 ± 1.3 µm
Density	10.62 g cm^{-3}	9.76 g cm^{-3}	9.67 g cm^{-3}

Table 3-4: Average bulk grain size and density for SIMFUEL pellets [46].

3.1.3 Legacy AGR Spent Nuclear Fuel

A cross-sectional sample of legacy AGR spent nuclear fuel was obtained and prepared for electrochemical measurements by the UK National Nuclear Laboratory (Windscale, Sellafield, UK).

The sample thickness is approximately ~4 – 5 mm, obtained by cross-sectional cutting of an AGR fuel pin, exposing the ring of 20/25/Nb cladding and the annular fuel pellet, see Figure 3-3.

The fuel sample was mounted on a brass mount and encased in Araldite resin to form a “lollipop” electrode, suitable for electrochemical measurements. A further brass rod was screwed into the brass mount allowing for electrical conductivity from the surface of the UO_2 and cladding to reach the potentiostat connectors, see Figure 3-4 and Figure 3-5. Figure 3-6 shows a non-radioactive

laboratory equivalent “lollipop” electrode containing a sample of 20/25/Nb cladding, to highlight the similarities between the choice of electrode shape.

The irradiated AGR SNF fuel sample was originally obtained by NNL as part of Sellafield’s Post Storage Examination programme. The fuel was irradiated in a commercial AGR between 1983 – 1989, achieving a fuel element average burn-up of 12.2 GWd/tU and a stringer mean burn-up of 20.2 GWd/tU, located at element 1 position during in-reactor operation. The fuel arrived at Sellafield site in 1990 and was stored in dosed ponds until 2014, where it was taken to Windscale labs and cut for examination.

The fuel sample in question has previously been subjected to microscopy studies as part of NNL’s Strategic Research programme, looking at crack pattern variations throughout a fuel pin, published by Thomas R.N. et al., [40]. The spent AGR fuel pin cross-sectional segment was characterised via a method of sequential grinding and polishing to investigate the three-dimensional fracture network using an optical microscope.

The elemental composition of the fuel sample has been calculated and provided by NNL using a FISPIN inventory calculation, based on the real fuel burn-up of 12.2 GWd/tU and a cooling time of 30 years. Table 3-5 shows the elemental percentage mass of the majority contributing elements in the AGR fuel sample, giving an approximate UO_2 percentage by mass of 98%. The approximate surface area for the exposed annular UO_2 pellet is ~1.3346 cm^2 and the approximate surface area for the exposed steel cladding is ~0.1241 cm^2.

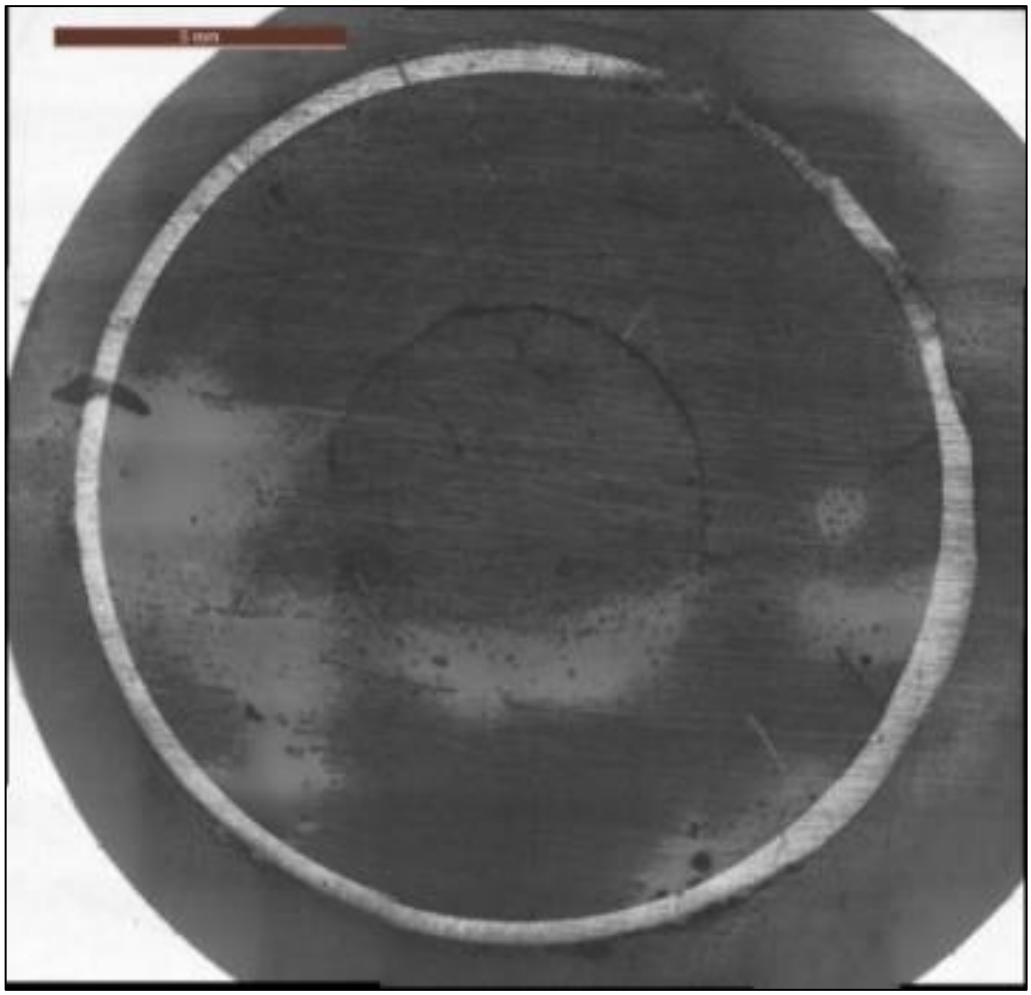

Figure 3-3: Top cross-sectional view of AGR fuel showing outer cladding and inner annular fuel pellet.

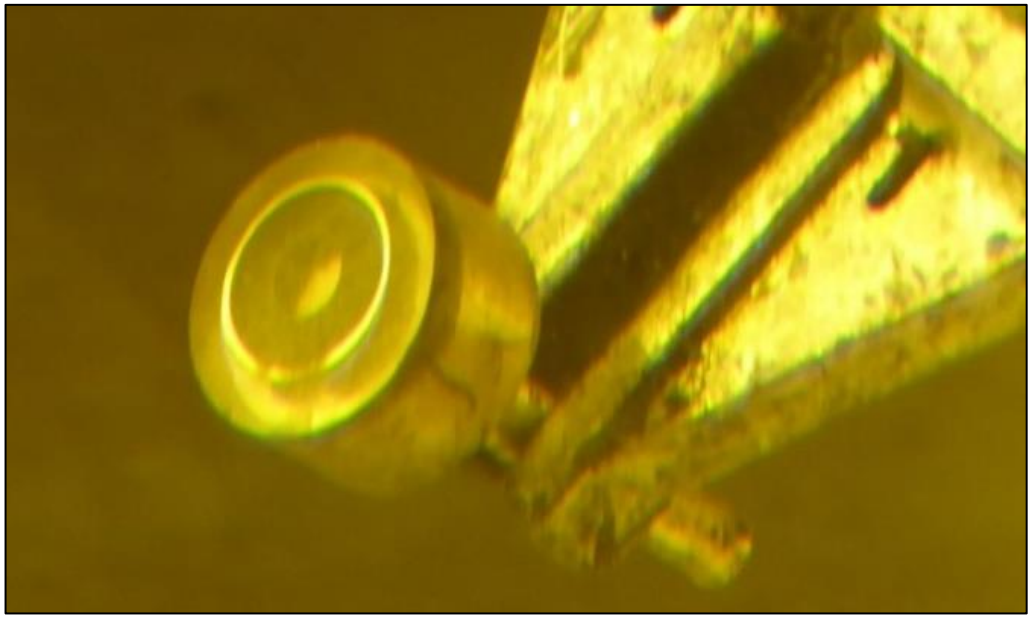

Figure 3-4: Cross-section of AGR fuel pin mounted on brass and encased in resin to form an electrode.

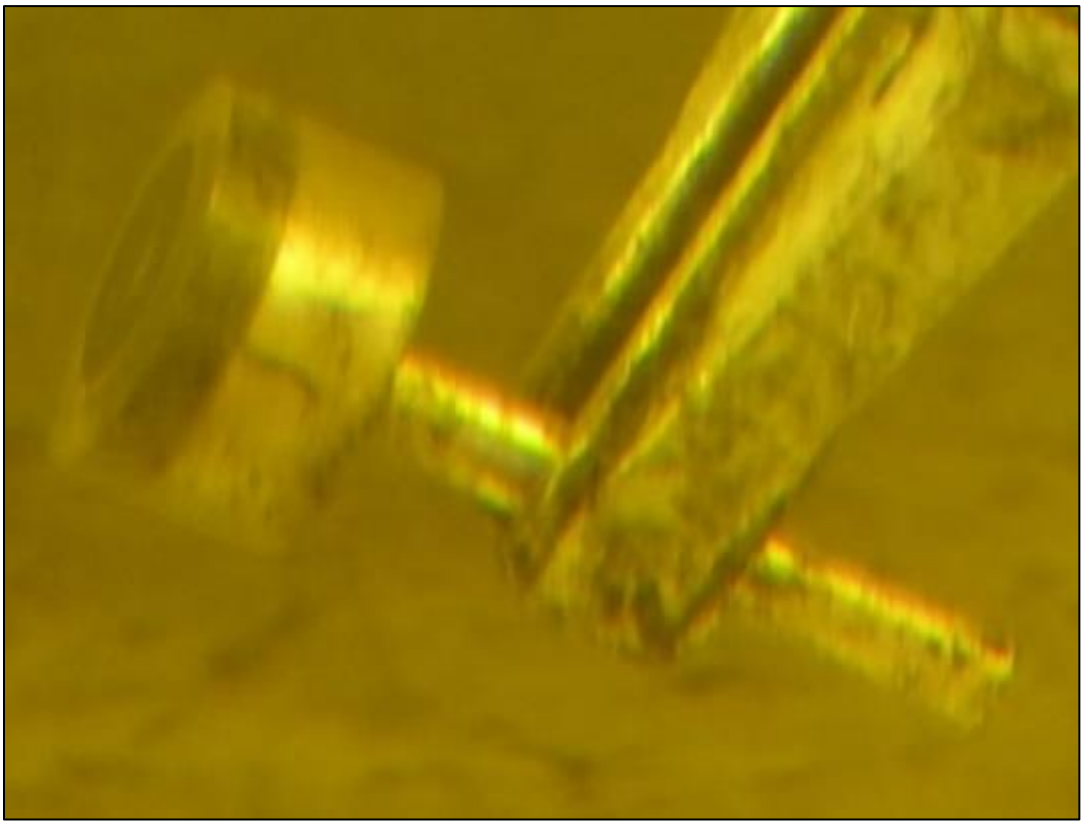

Figure 3-5: Cross-section of AGR fuel pin mounted on brass and encased in resin to form an electrode (side view).

Figure 3-6: Non-radioactive 20/25/Nb cladding encased in resin and a detached brass rod.

Element	Percentage Mass
U	86.71%
O	11.85%
Pu	0.29%
Xe	0.16%
Zr	0.14%
Nd	0.14%
Mo	0.11%
Cs	0.08%
Ce	0.08%
Ba	0.07%
Ru	0.06%
La	0.04%
PR	0.04%
Sm	0.03%
Tc	0.03%
Pd	0.02%
Sr	0.02%
Y	0.02%
Rh	0.02%
Am	0.02%
Te	0.01%
Rb	0.01%
Kr	0.01%
Np	0.01%
I	0.01%

Table 3-5: Elemental mass percentage composition of legacy AGR SNF sample.

3.1.4 20/25/Nb Austenitic Stainless Steel AGR Cladding

The material used for cladding measurements is a non-sensitised 20/25/Nb austenitic stainless steel AGR cladding. The cladding material has previously been generally discussed in Chapter 1 Section 1.4.4 and contains 20 wt.% Cr and 25 wt.% Ni.

Table 1-2 shows the wt.% composition of the steel. This non-radioactive material is the same manufactured cladding used in the production of AGR fuel pins. The cladding was provided by UK NNL and sourced from Westinghouse Springfields Fuels Ltd in Preston, UK.

The cladding tube was cut perpendicular to the length of the tube in order to make cross-sectional pieces for fabrication into electrodes, shown in Figure 3-7 and Figure 3-8, allowing for the surface of the cross-sectional metal ring to be exposed for electrochemical measurements. The approximate surface area for the exposed steel cladding is ~0.2662 cm^2.

Component	Cr	Ni	Nb	Mn	Si	C	N	Fe
% wt.	20.12	24.75	0.70	0.62	0.57	0.049	0.016	balance

Table 3-6: Chemical composition of 20/25/Nb stainless steel obtained from NNL via manufacturer.

Figure 3-7: Segment of 20/25/Nb stainless steel AGR cladding mounted onto a brass base.

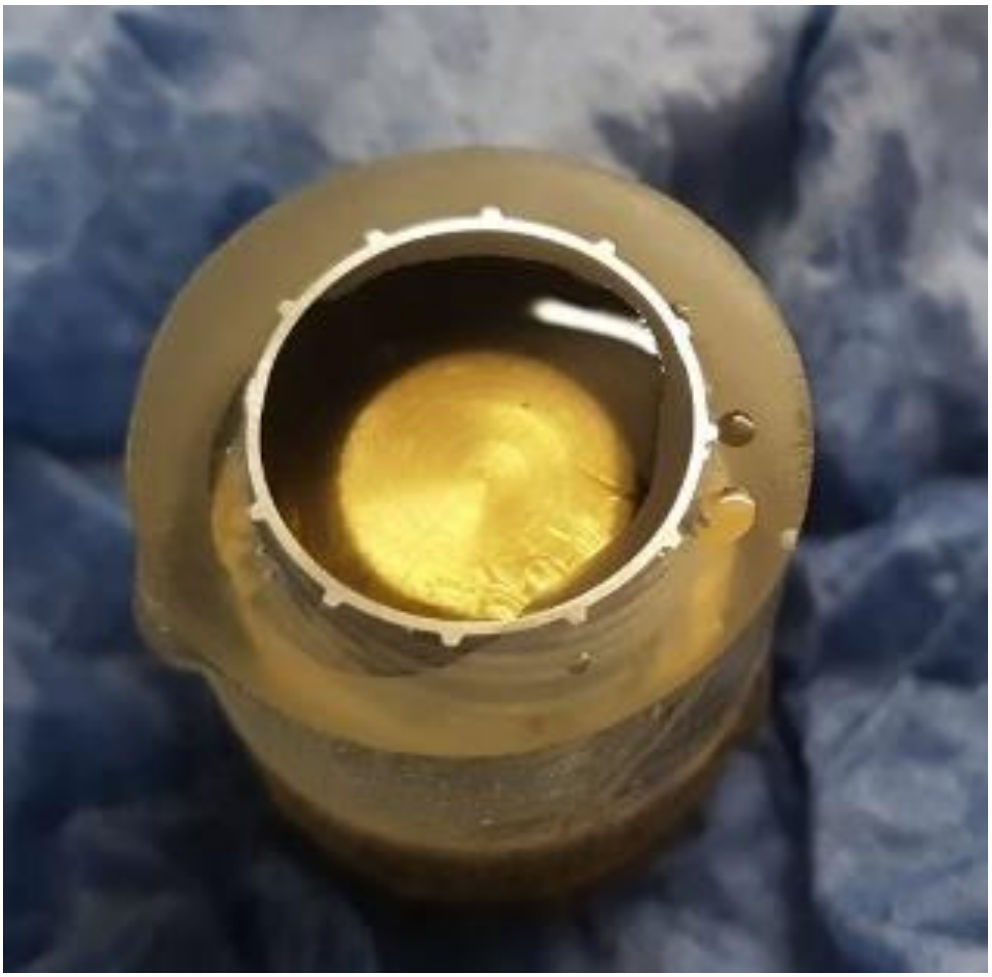

Figure 3-8: Segment of 20/25/Nb stainless steel AGR encased in resin to form an electrode.

3.2 Voltammetric Methods for Corrosion Study

3.2.1 Electrode/Sample Preparation

Working electrodes for the SIMFUEL pellets and 20/25/Nb cladding were fabricated using the same method. The pellet or cladding was mounted on a brass base, adhered using a conductive silver epoxy paste, before being placed into a PTFE mould and encased in a 2-part epoxy resin, Figure 3-9.

Once the resin cured, the electrodes were removed from the mould, and the excess resin was sanded away until the surface of the pellet or cladding was exposed, forming a disc-shaped electrode for the pellets and a ring-shaped electrode for the cladding.

The rear of the brass mount contains a threaded screw hole allowing a brass rod to be inserted, this serves as a physical connection point to the potentiostat

wires, allowing electrical conductivity from the selectively exposed surface of the electrode to the potentiostat.

As well as separate disc-shaped pellet electrodes and ring-shaped cladding electrodes, composite fuel pellet and cladding electrodes were fabricated where a sample of pellet and cladding, in contact with each other, were mounted together on the same brass contact. All three types of electrodes are shown in Figure 3-10.

The working surfaces of the electrodes were polished before all measurements. 20/25/Nb electrodes were polished using sandpaper from 600 to 1200 grit, followed by 6 μm, 3 μm and 1 μm diamond polishing paste. SIMFUEL electrodes were polished using sandpaper from 600 to 1200 grit, unless otherwise stated. Table 3-7 shows the calculated electrode surface areas for all the samples/electrodes used.

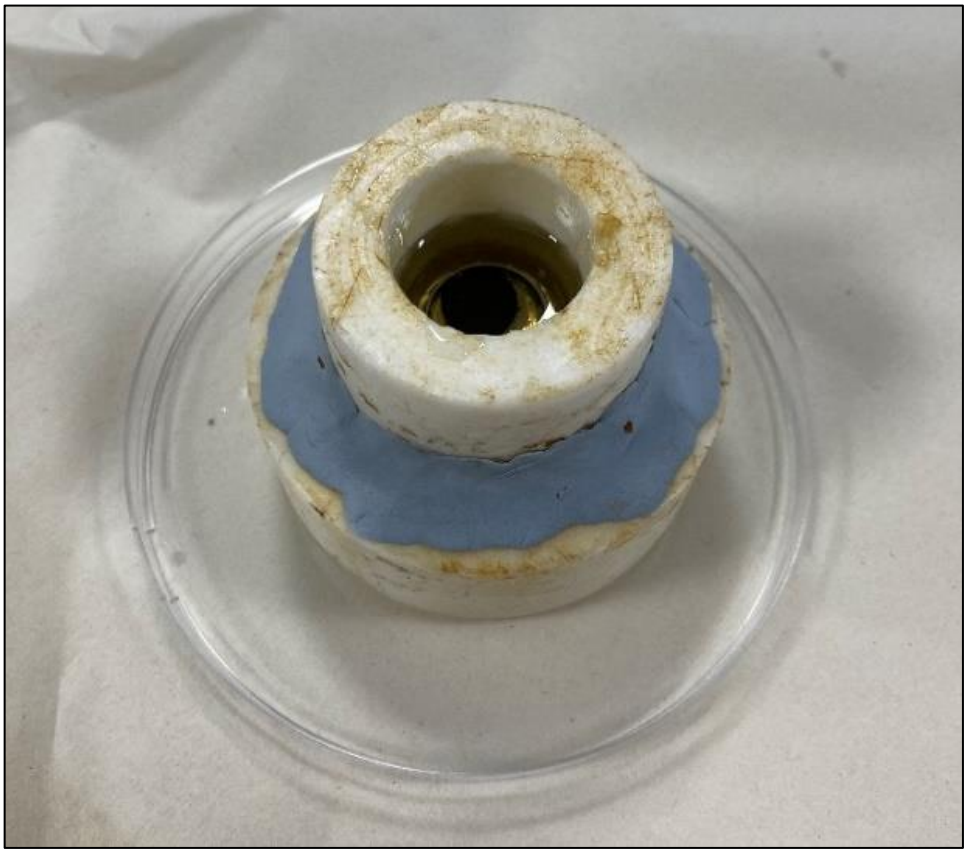

Figure 3-9: PTFE mould containing sample and resin.

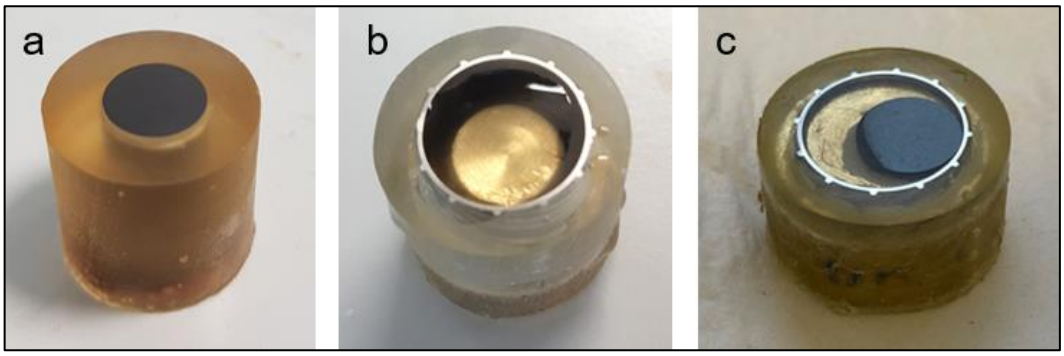

Figure 3-10: (a) SIMFUEL pellet electrode (b) 20/25/Nb AGR cladding electrode (c) composite electrode containing 25 GWd/tU SIMFUEL coupled with 20/25/Nb AGR cladding.

	UO_2/SIMFUEL	20/25/Nb AGR cladding	AGR fuel - UO_2	AGR fuel - cladding
electrode surface area (cm^2)	~ 0.7088	~ 0.2662	~ 1.3346	~ 0.1241

Table 3-7: Table of electrode surface areas.

3.2.2 Experimental Setup for Electrochemical Measurements

Voltammetry measurements were carried out using a 3-electrode cell setup, described in Chapter 2 Section 2.1.3, consisting of a pellet, cladding or composite pellet/cladding working electrode, a silver-silver chloride (Ag|AgCl) reference electrode and a pure platinum counter electrode.

Unless otherwise stated, measurements were carried out in a glass beaker containing the measurement electrolyte of interest, similar to the setup shown in Figure 3-11.

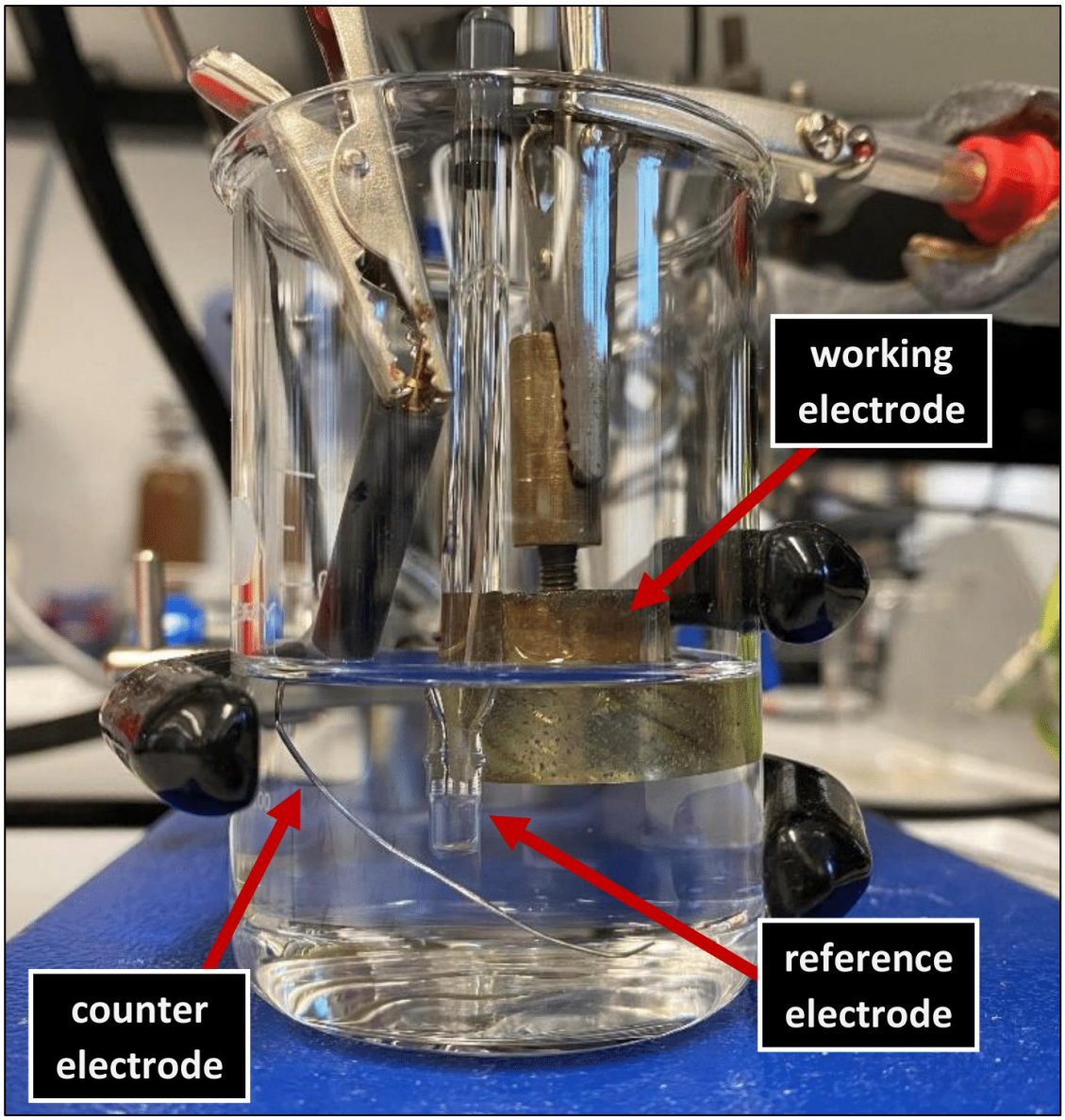

Figure 3-11: 3-electrode cell in a beaker with Pt wire counter, Ag|AgCl reference and 20/25/Nb cladding electrode.

Potentiostats: Voltammetry measurements were carried out using a range of different potentiostat instruments, depending on the measurement requirements and the physical constraints of specific laboratories and/or locations. Specific instruments will be identified in the results chapter where necessary. Below is a list of all potentiostats used and their corresponding software package:

- Metrohm Autolab PGSTAT128N with Metrohm Autolab NOVA software package for potentiostat control and data acquisition (Metrohm AG, Ionenstrasse 9100, Herisau, Switzerland)

- Metrohm Autolab PGSTAT10 with Metrohm Autolab NOVA software package for potentiostat control and data acquisition (Metrohm AG, Ionenstrasse 9100, Herisau, Switzerland)
- PalmSens EmStat3+ with PalmSens PTrace software package for potentiostat control and data acquisition (PalmSens B.V., Randhoeve 221, 3995 GA Houten)
- Solartron Analytical 1280B with ZPlot software for running AC voltammetry measurements (Solartron Metrology**,** Steyning Way, Bognor Regis, West Sussex PO22 9ST), with CorrWare software for running DC voltammetry and general potentiostat control. ZView and CView for data analysis (Scribner Associates Inc., 150 East Connecticut Avenue, Southern Pines, North Carolina, USA 28387)

Reference electrodes: Previously described in Chapter 2 Section 2.1.2. All electrochemical measurements were carried out using Ag|AgCl reference electrodes. Two models/brands of reference electrodes were used, depending on the physical space constraints of the measurement environment:

- EDT directION E8195 double junction reference electrode (Ag|AgCl) (EDT directION, Unit 5, Waldershare Park, Dover, CT15 5DQ)
- BASi MF-2052 reference electrode (Ag|AgCl) (Alvatek Ltd, Unit 11, Westwood Court, Brunel Road, Southampton, SO40 3WX)

Counter electrodes: All electrochemical measurements were carried out using platinum metal counter electrodes, in the form of a Pt wire, coil or mesh (Alvatek Ltd, Unit 11, Westwood Court, Brunel Road, Southampton, SO40 3WX). Different shapes/constructions were used depending on the measurement conditions and the surface area required.

3.2.3 Current-Interrupt Method

The current-interrupt method can be used to determine the internal uncompensated resistance of a three-electrode electrochemical cell set-up. The technique is based on the application of Ohm's law:

$$V = IR$$

Equation 3-1

This method can be performed using a potentiostat. During a current-interrupt measurement, the current flow is interrupted for a short interval (10 to 30,000 µs) and the resultant voltage is recorded. The voltage difference immediately before and after the current interrupt is then divided by the current to obtain the uncompensated resistance value.

Uncompensated resistance, R_u, measurements, were carried out using a 3-electrode cell setup and performed using Metrohm Autolab NOVA software's built in current-interrupt methodology.

3.2.4 Linear Sweep Voltammetry

Linear sweep voltammetry (LSV) is a potentiostatic polarisation based method, in which a potential is applied to the working electrode in an electrochemical cell. The potential is thus ramped at a fixed scan rate [mV/s] and the resulting current response is recorded. LSV measurements can typically be presented as polarisation curves of log(I) versus potential, as shown in Figure 3-12. These plots can give information about the cathodic and anodic processes taking place at the working electrode [114].

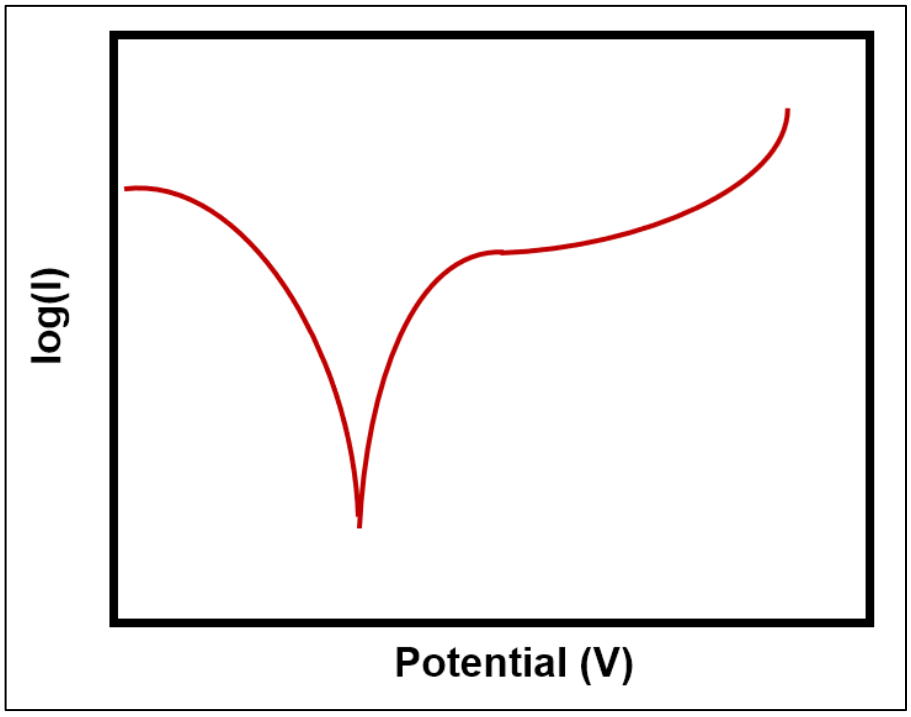

Figure 3-12: A generic polarisation plot following European conventions.

In general, LSV measurements were performed at a scan rate of 1 mV/s, between potential limits of ~-0.7 to ~1.5 V, unless otherwise stated. LSV measurements were typically without OCP stabilisation prior to the application of potential, unless otherwise stated. These parameters were adjusted in order to fit the measurement objective and desired data outputs. Each results chapter will specify the scan rate and potential range used for data acquisition, where necessary.

Current density values were obtained by calculating the current per surface area of the working electrode. Electrode surface areas can be found in Table 3-7.

By default, the majority of the polarisation curves in this thesis are presented as surface-area-normalised current densities. This is due to the type of working electrodes used during certain measurements. Where appropriate, polarisation curves that are presented with non-surface-area-normalised current values will be highlighted with reasoning provided in the text.

3.2.5 Cyclic Voltammetry

Cyclic voltammetry is also a type of potential sweep experiment but differs from the LSV method as the scanned potential is reversed at the end of the first scan until it reaches a potential, which is also the starting potential for first and subsequent scans. The plot of a CV produces a cyclic graph of the current response observed during the forward scan (oxidation) and reverse scan (reduction), as shown in Figure 3-13. This provides a full image of the cathodic and anodic processes taking place on the electrode surface [115].

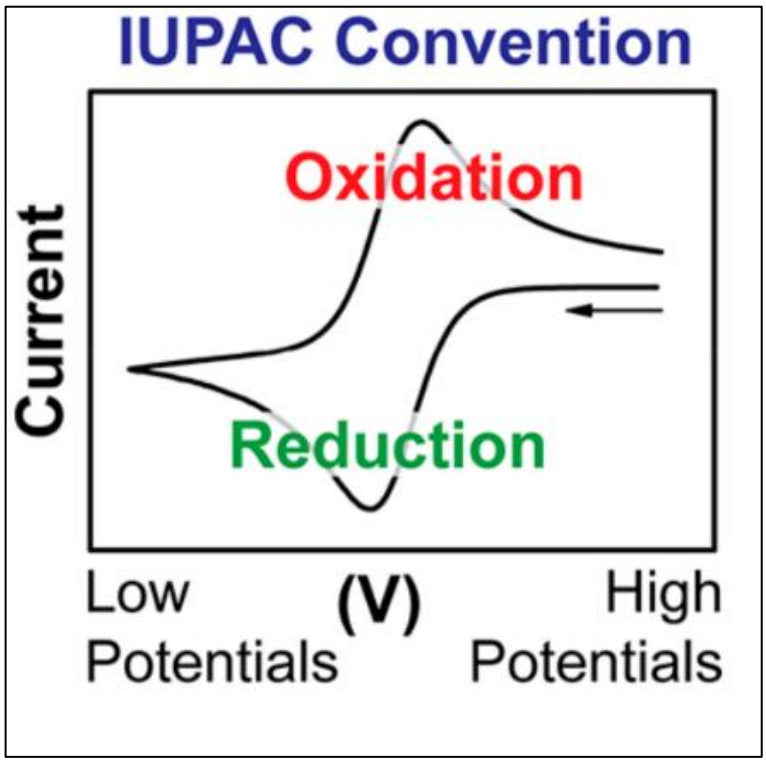

Figure 3-13: Example of a typical CV plot [115].

In general, CV measurements were performed at a scan rate in the range of 1 to 100 mV/s, with an upper and lower vertex potential of 0.4 V and -1.5 V, respectively. Typically, 3 scans were performed with the data taken from the second scan. These parameters were freely adjusted in order to fit the measurement objective and desired data outputs. Each results chapter will specify the scan rate and potential range used for data acquisition.

3.2.6 Open Circuit Potential

Open Circuit Potential (OCP) is a measure of the system's resting potential over time at steady state equilibrium. The OCP is used in conjunction with polarisation scan methods to understand what electrochemical processes are occurring at the working electrode at equilibrium, under the conditions of interest.

OCP measurement were also carried out before LSV measurements in order for the electrochemical system to stabilise, prior to the application of potential to the system, with respect to the OCP.

In general, OCP measurements were carried out using a 2-electrode cell setup, consisting of a working electrode and a reference electrode. The measurement procedure does not require any application of voltage from the potentiostat and is simply a record of the measured voltage as a function of time. Each results chapter will specify the length of time used for data acquisition.

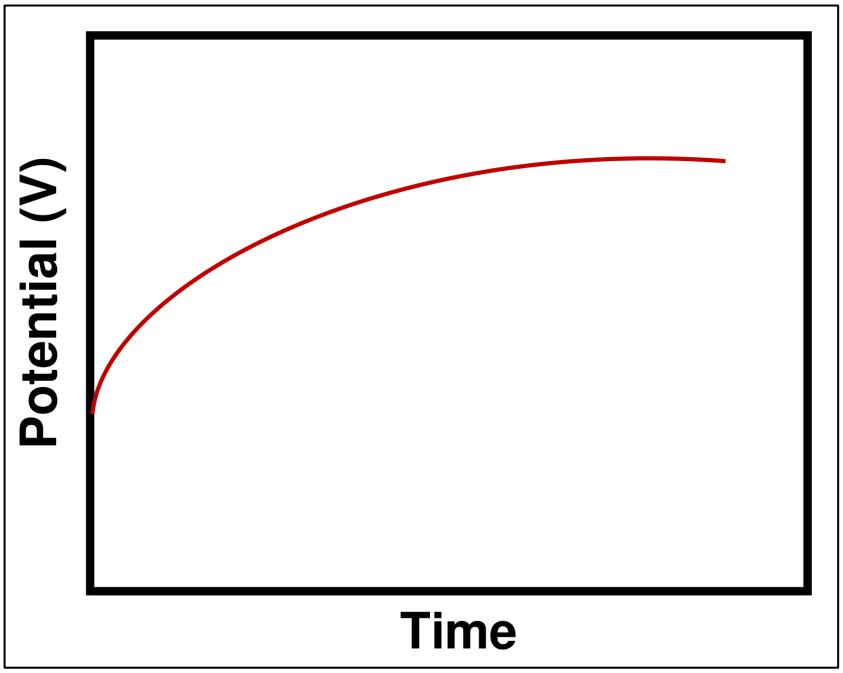

Figure 3-14: Example of a typical OCP plot [115].

3.2.7 Electrochemical Impedance Spectroscopy

According to Ohm's law, electrical resistance is the measure of resistivity of the electrical current flow through a circuit component, defined as the ratio between the voltage, E and current, I. Electrochemical Impedance Spectroscopy (EIS) can therefore be used to describe the impeding of current flow through the entire circuit with considerations for all circuit components.

Impedance is defined as a general form of electrical resistance and is a measure of a circuit's ability to resist the electrical current. Electrochemical processes can be regarded as being equivalent to electrical circuit elements.

For example, Faradaic processes, i.e., those which involve the transfer of charged particles across an electrode interface, without the progressive storage of charge in the electrode, can be generally modelled by a resistor, R, component. In contrast, non-Faradaic processes, i.e., those which involve the storage of charge at the electrode when a current flows, can generally be modelled by a capacitor, C, component.

Thus, in an electrical circuit containing components of R and C, these components would act to impede the flow of current through said circuit [116]. Impedance analysis of such electrical circuits can, therefore, provide information about the electrochemical processes.

Electrochemical impedance is typically measured by introducing a small sinusoidal potential over a constant applied potential and the response is a sinusoidal AC current, which can be used to determine the impedance. Figure 3-15 shows a sinusoidal current response, which is phase shifted with respect to the excitation signal but has the same frequency [117]. The response of the system to a frequency perturbation can reveal information relevant to the internal dynamics of the system under study.

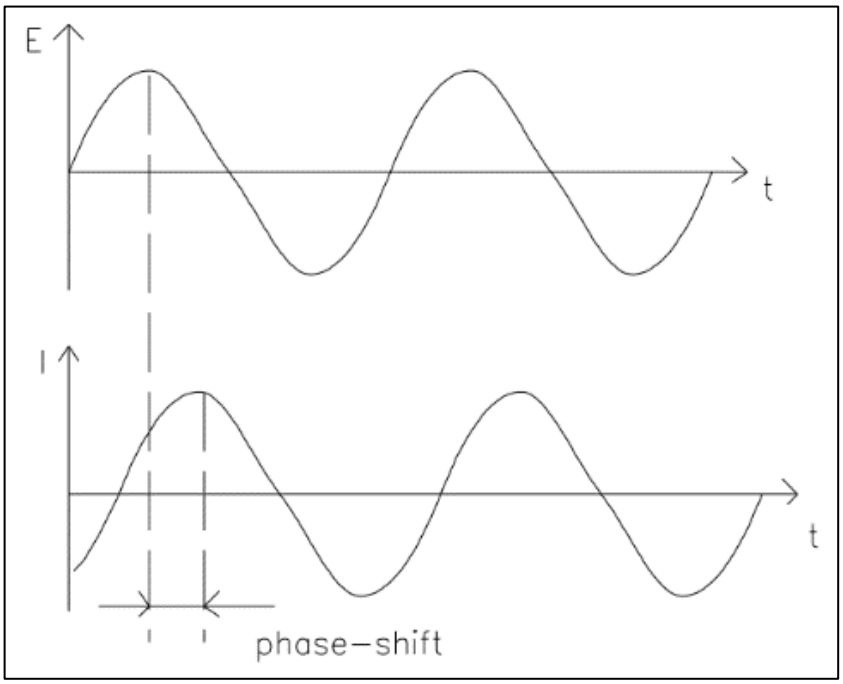

Figure 3-15: Sinusoidal potential excitation and current response [117].

Impedance, Z, is calculated using an expression analogous to Ohm's law, as seen in Equation 3-3, where the impedance is expressed as a magnitude, Z_0, and a phase shift, ϕ:

$$Z = \frac{E_t}{I_t} = \frac{E_0 \sin(\omega t)}{I_0 \sin(\omega t + \phi)} = Z_0 \frac{\sin(\omega t)}{\sin(\omega t + \phi)}$$

Equation 3-2

It can also be expressed as a complex function:

$$Z(\omega) = \frac{E}{I} = Z_0 \exp(\mathrm{j}\phi) = Z_0 (\cos\phi + \mathrm{j}\sin\phi) = Z' + \mathrm{j}Z''$$

Equation 3-3

Where Z' is the so-called real component and $\mathrm{j}Z''$ is the so-called imaginary component. Plotting the imaginary part versus the real part gives produces a "Nyquist Plot" (Figure 3-16), on these types of plots the impedance is represented as a vector of length $|Z|$ and the angle between that vector and the x-axis is the phase angle, ϕ ($\arg Z$).

However, Nyquist Plots do not give information about the frequency (ω) of each recorded data point only that with respect to the x-axis, high frequencies occur at the origin whilst low frequencies occur away from Z'= 0.

Depending on the electrical circuit that is being used as a model for the system under study, the Nyquist Plots can be used to deduce what electrochemical process may be occurring.

For instance, the Nyquist Plot in Figure 3-16 is generated from a simple equivalent circuit containing a resistor and capacitor in parallel, the single semi-circular shape being characteristic of a single “time constant”. Such a circuit could be taken to be representative of simple Faradaic and non-Faradaic processes occurring in parallel at the electrode-electrolyte interface – as described earlier – with the former represented by the resistor of Figure 3-17 and the latter represented by the capacitor of Figure 3-17.

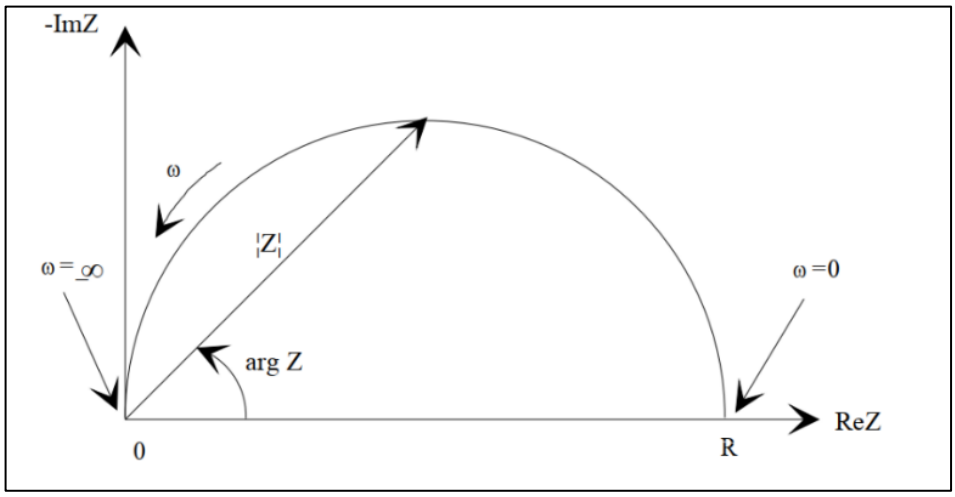

Figure 3-16: Components of a typical Nyquist Plot [117].

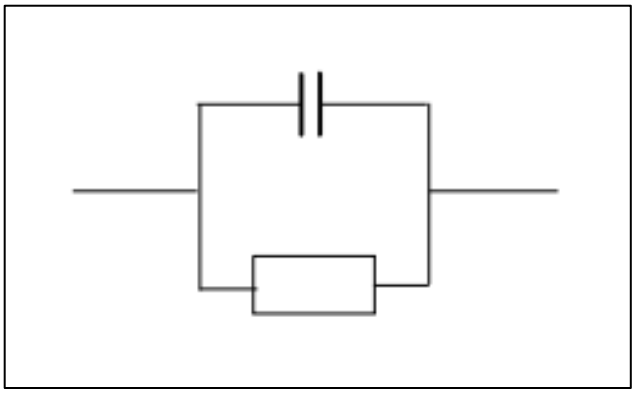

Figure 3-17: Equivalent circuit containing a resistor and capacitor in parallel to give a single time constant [117].

Bode plots are another representation of impedance measurements, these plots give the absolute value of the impedance, $|Z|$, and phase-shift, ϕ, as a function of the log frequency, $\log \omega$ as shown in Figure 3-18.

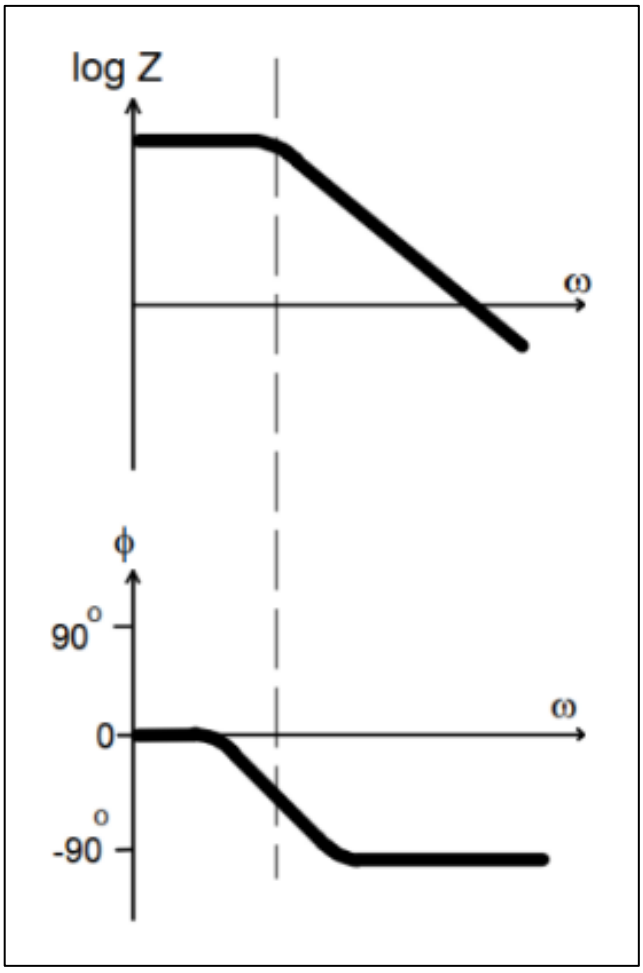

Figure 3-18: Components of a typical Bode Plot with one time constant [117].

EIS data is typically analysed by fitting to an equivalent electrical circuit, similar to the one in Figure 3-17. Modelling against an equivalent electrical circuit allows for reasonable comparison and relation between the electrical circuit components, e.g., resistors, capacitors, inductors, with the electrochemical processes within the system under study, e.g., electrolyte resistance, double layer capacitance, polarisation resistance, charge transfer resistance, diffusion.

The Simplified Randles Cell, Figure 3-19, is a common starting point for equivalent circuit modelling. This cell consists of components to model: (i) solution resistance, R_s, the resistance between the reference and working electrodes in electrolyte, (ii) electrical double layer capacitance, C_{dl}, at the interface between the electrodes and electrolyte and (iii) charge transfer or polarisation resistance, R_{ct} or R_p.

The process of extracting useful data from impedance measurements via this method requires iterative fitting, since fitting the data to a suitable model would be up to the interpretation of the data modeler.

Many suitable models may fit to a single data set and thus may also produce varying fitted values from the circuit components. The subtraction or addition of single cell components may change the fitting of the data. Therefore, the use of a fitting parameter, chi-squared χ^2, allows for reasonable judgement of the fitted values.

However, the fitting parameter should be used in conjunction with an appropriate Equivalent Electrochemical Circuit (EEC) model that represents the physical system under study and the circuit components should represent the electrochemical process occurring at the electrode-electrolyte interface.

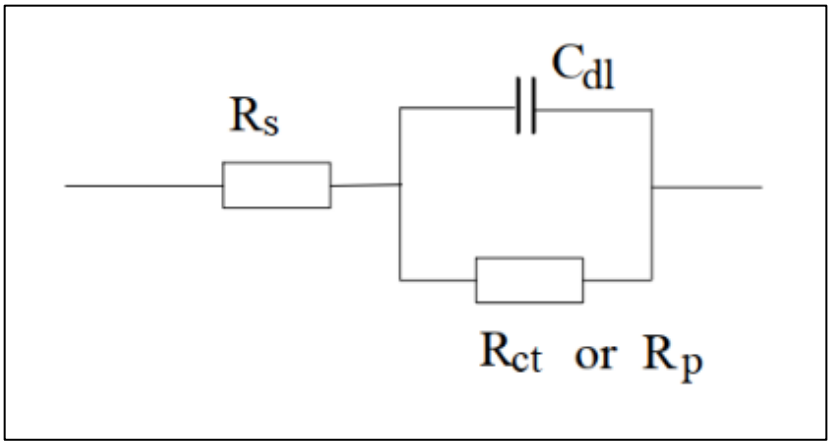

Figure 3-19: Simplified Randles Cell for equivalent circuit modelling [117].

In general, all EIS measurements were carried out using a 3-electrode cell setup. All measurements were carried out at a frequency range of 10,000 – 0.001 Hz, unless otherwise stated. Depending on the measurement type and/or objective, the applied potential during a measurement will either be at 0 V versus the open circuit potential or a specific applied potential versus the open circuit potential. Each results chapter will specify the EIS parameters used for data acquisition where necessary.

3.3 Raman Spectroscopy

Raman spectroscopy is a non-destructive surface analytical method used to gain surface structural information of a material. Raman spectroscopy utilizes the inelastic scattering of light from a high-intensity laser, commonly referred to as Raman Scattering [118]. This differs from Rayleigh scattering, which is the elastic scattering of electromagnetic radiation, where the wavelength of the scattered light is unchanged.

The scattering process induces a shift in wavelength of the scattered light due to inelastic scattering when the incident light hits molecules of interest. The shift in wavelength will differ depending on the vibrational state of the molecule and can be higher (Stokes) or lower (anti-Stokes) in energy than the incident radiation. Raman spectra display the intensity of the scattered light as a function of its energy expressed in units of wavenumber, cm^{-1} [119].

3.3.1 μ-Raman spectroscopy

Raman Microscopes: The majority of the Raman measurements presented in this thesis were carried out on the 785 nm laser Raman microscope, with some work carried out on the 532 nm Raman microscope. Each laser wavelength type will dictate the shape and intensity of certain Raman peaks/signals, some of which are caused by resonance effects; these effects are described in the relevant results chapters as necessary.

Below is a list of the instruments used:

- B&W Tek 785 nm Voyage confocal Raman microscope (B&W Tek, LLC, 313 Enterprise Drive, Plainsboro, NJ 08536)
- XploRA One 532 nm Raman microscope (HORIBA UK Limited – Northampton, Kyoto Close Moulton Park, NN3 6FL, Northampton, UK)

μ-Raman spectroscopy was used for surface analysis of UO_2 and SIMFUEL samples. In general, spectra were obtained using a 50x objective lens focused on the surface of the sample. As part of the standard operating procedure, laser power was reduced from full strength to prevent thermal oxidation of the UO_2 to U_3O_8.

For each measurement, typically 10 to 20 spectra were captured across random locations over the sample surface in order to achieve an average, with care taken to avoid grey phases and noble metal deposits. Detailed spectra acquisition parameters are reported in the corresponding results chapters, as specific settings will differ depending on the measurement objective, desired data outputs, sample of interest, and the Raman microscope instrument used.

For clarity within this thesis, the terms: ‘Raman spectroscopy’ and ‘μ-Raman spectroscopy’ are not used interchangeably as they refer to different intentions.

Where ‘Raman spectroscopy’ is used, this refers to the overall general technique and theory of Raman spectroscopy, which can include the technique of μ-Raman spectroscopy.

Where ‘μ-Raman spectroscopy’ is used, this refers to the specific technique of μ-Raman spectroscopy in which the Raman laser can focused via high

magnification microscope objectives onto a small sample spot size. This is the main technique used within the studies of this thesis.

3.3.2 Spectra Fitting

Spectra fitting and deconvolution of SIMFUEL spectra was performed using an open-source general purpose peak fitting software, Fityk, developed and published by Marcin Wojdyr (Institute of High Pressure Physics, Ulica Okolowska 29/37, 01-142 Warsaw, Poland) [120]. Peak fittings were carried out in order to determine peak heights and peak height ratios, to support the studies of Chapter 7.

All spectra plots were baseline subtracted using the median point on all plots, typically around the 800 cm^{-1} region, and smoothed using 10 point-Adjacent-Averaging method. The baselines spectra were recorded on clean SIMFUEL samples following a reductive potential of -1.2 V for 15 min, this is discussed further in Chapter 7.

Prior to peak fitting, the imported spectral data is also linear-baselined between the region of approximately 390 – 650 cm^{-1} and fitted using Levenberg–Marquardt algorithm via a SplitPearson7 function.

After peak fitting, the peak heights for each of the three defect band contributions are recorded. This process is repeated for all the spectra. The ratios were then calculated by dividing the defect band peak height by the fundamental U-O stretch peak height. Peak height ratios were then averaged and plotted with their standard deviations (Refer to Chapter 7).

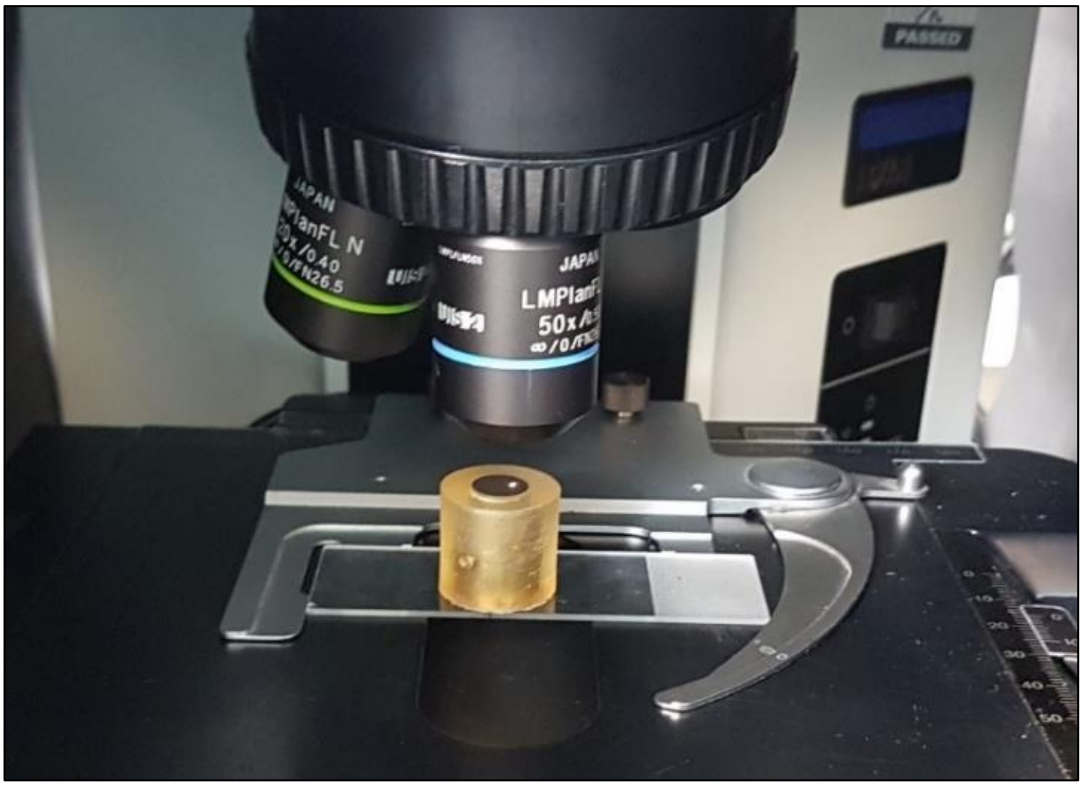

Figure 3-20: SIMFUEL electrode placed under 785 nm Raman microscope, ready for measurement.

4 Baseline Studies of AGR Spent Fuel Simulants

4.1 Introduction & Objectives

This chapter presents the baseline study of the main components/materials relevant to the studies of AGR SNF reported later in this thesis. The results presented in this chapter will focus on the following materials:

- undoped-UO_2
- lower simulated burn-up 25 GWd/tU AGR SIMFUEL (25-SIMF)
- higher simulated burn-up 43 GWd/tU AGR SIMFUEL (43-SIMF)
- 43 GWd/tU AGR SIMFUEL with higher lanthanide doping (43-hiLn)
- 43 GWd/tU AGR SIMFUEL with higher lanthanide and chromium-doped (43-hiLnCr)
- as-received non-sensitised 20/25/Nb stainless steel AGR cladding

These materials were studied using electrochemical methods in a standardised background electrolyte, to understand the baseline electrochemical behaviour and to allow comparisons between each of the materials.

Additionally, the 25 GWd/tU SIMFUEL and 20/25/Nb AGR cladding samples were also studied under simulated AGR pond storage conditions, to allow comparison of the baseline electrochemical behaviour with the coupled electrode studies of Chapter 5 and the legacy AGR SNF electrode studies of Chapter 6.

In addition to the voltammetry measurements, μ-Raman spectroscopy measurements were also conducted on the same materials, to obtain a baseline Raman study of these materials and also to support the μ-Raman spectroscopy and electrochemical oxidation studies of Chapter 7.

As mentioned above, the studies presented in this chapter will form the baseline dataset upon which subsequent electrochemical and Raman studies of these materials and the legacy AGR SNF, will be compared against. The electrochemical and Raman measurement conditions used in the following sections will vary depending on the scenario being investigated and will be described in their respective sections.

4.2 SIMFUEL SEM Characterisation

This section presents a review and summary of the SIMFUEL SEM characterisation results excerpted from Zoltan Hiezl's thesis, "Processing and Microstructural Characterisation of UO_2-based Simulated Spent Nuclear Fuel Ceramics for the UK`s Advanced Gas-cooled Reactors" [47]. The excerpted SEM images and grain sizes of the SIMFUELs were obtained from 25-SIMF, 43-SIMF, 43-hiLn, and 43-hiLnCr samples. The SIMFUEL pellets used by Zoltan Hiezl are from the same batch of SIMFUEL pellets manufactured by NNL (see Chapter 3) and same as those used in the studies presented in this thesis.

Figure 4-1, Figure 4-2, Figure 4-3, and Figure 4-4 shows the SEM images for the 25-SIMF, 43-SIMF, 43-hiLn, and 43-hiLnCr SIMFUEL samples, respectively. From the visual inspection, we can see that the grain sizes decrease as the doping increases. The smallest grain sizes are seen with the 43-hiLn and 43-hiLnCr SIMFUEL samples. This is confirmed by the average bulk grain size measurements, reported in Table 4-1 below.

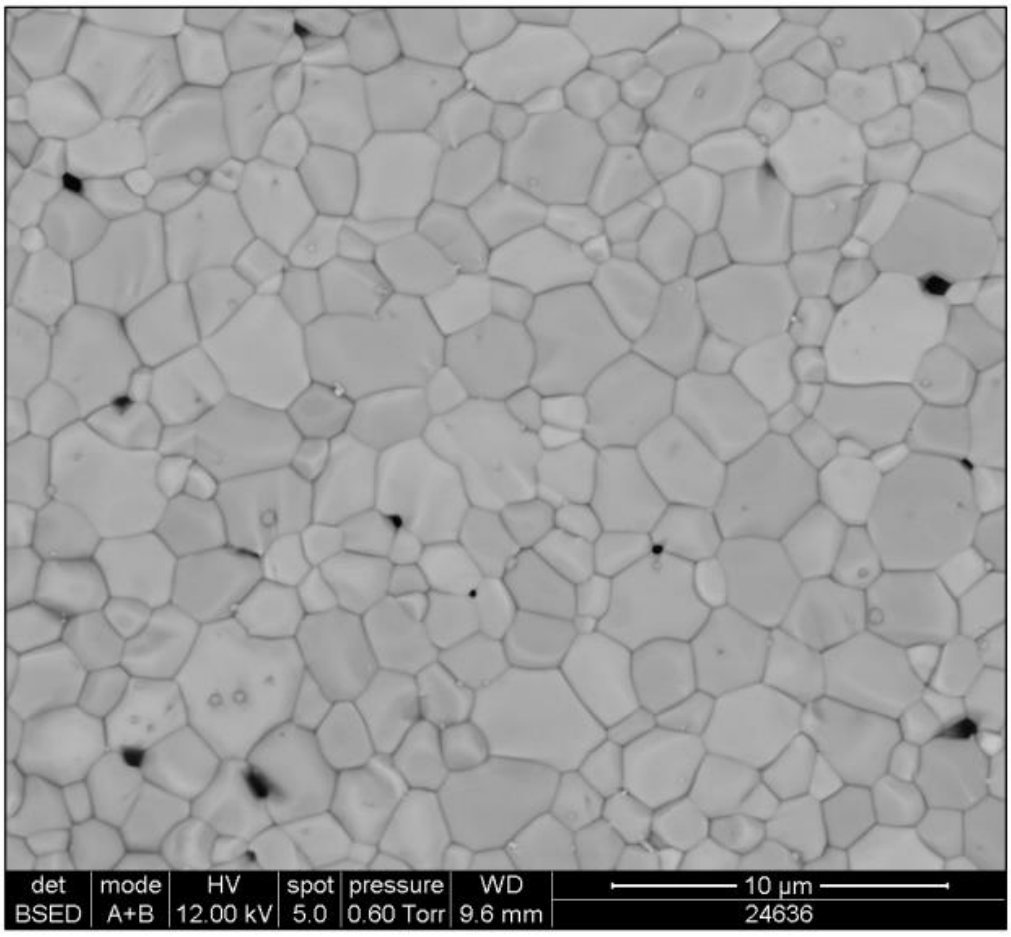

Figure 4-1: Typical microstructure of 25-SIMF. The grains shown here are larger than that of the 43-SIMF (Figure excerpted from Zoltan Hiezl's thesis under a Creative Commons Attribution Non-Commercial No Derivatives licence [47]).

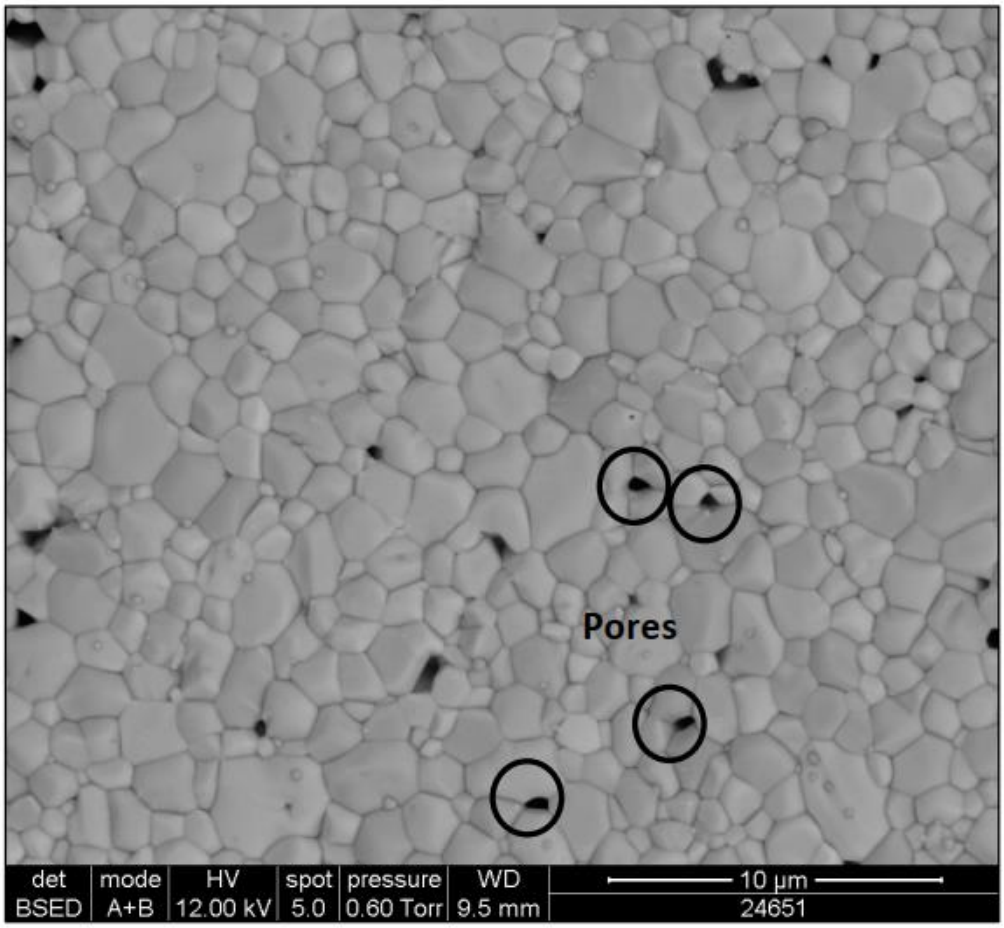

Figure 4-2: Typical microstructure of 43-SIMF. The grains shown here a smaller than that of the 25-SIMF. The black circles show the location of pore on the surface of the SIMFUEL (Figure excerpted from Zoltan Hiezl's thesis under a Creative Commons Attribution Non-Commercial No Derivatives licence [47]).

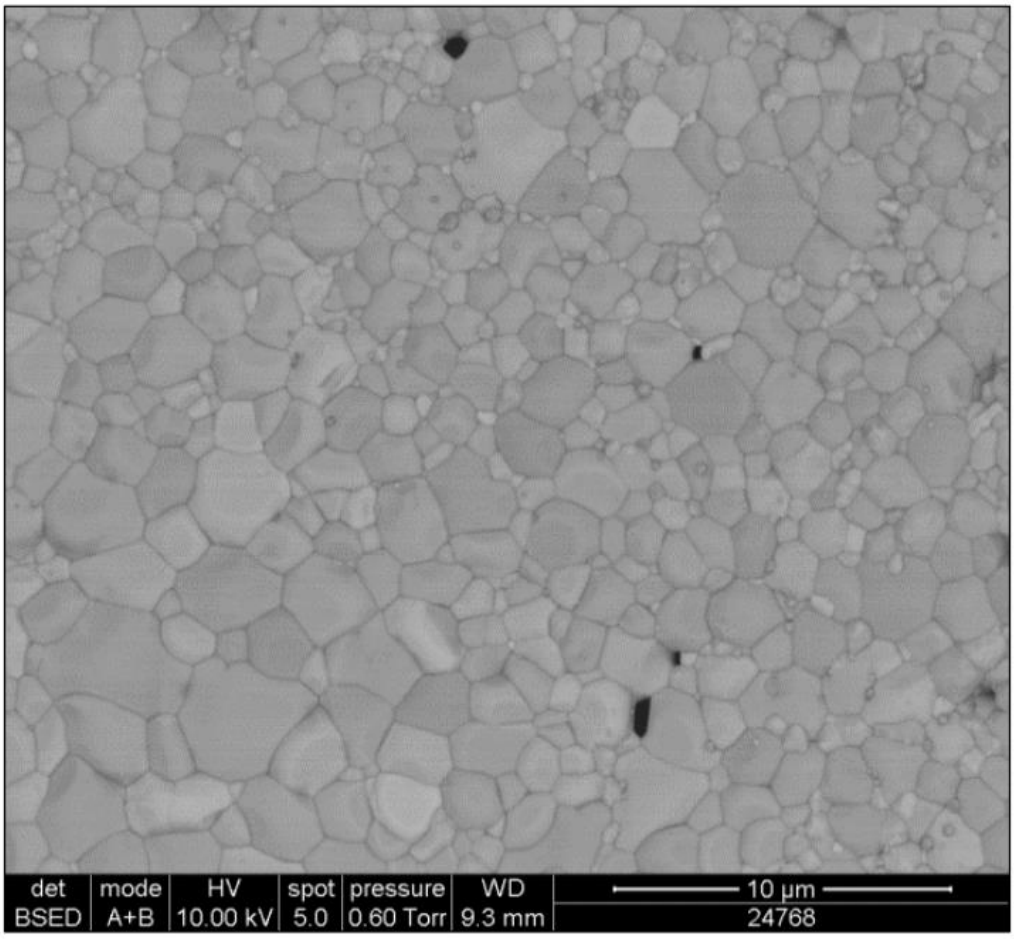

Figure 4-3: Typical microstructure of 43-hiLn. The grains shown here in the Ln-doped SIMFUELs are smaller than that of the non-Ln-doped 43-SIMF (Figure excerpted from Zoltan Hiezl's thesis under a Creative Commons Attribution Non-Commercial No Derivatives licence [47]).

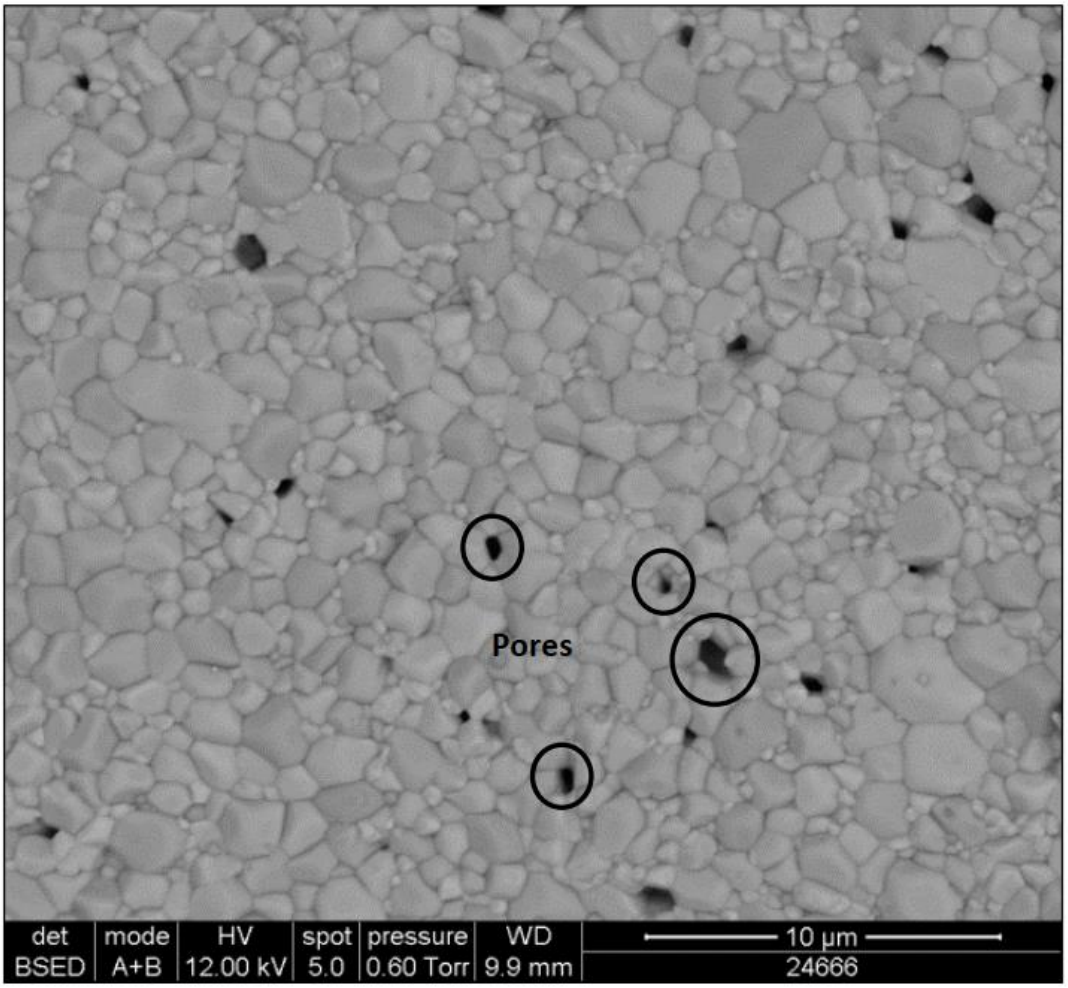

Figure 4-4: Typical microstructure of 43-hiLnCr. The grains shown here in the Ln-doped SIMFUELs are smaller than that of the non-Ln-doped 43-SIMF. The black circles show the location of pore on the surface of the SIMFUEL (Figure excerpted from Zoltan Hiezl's thesis under a Creative Commons Attribution Non-Commercial No Derivatives licence [47]).

Table 4-1 shows the average bulk grain sizes of the 25-SIMF, 43-SIMF, 43-hiLn, and 43-hiLnCr SIMFUEL samples. The average grain sizes were calculated using the grain boundary interception method.

The results show that the average bulk grain sizes decrease with increased doping. Significant grain size decrease is seen for the additional-Ln-doped and Cr-doped SIMFUELs. However, the 43-hiLnCr SIMFUEL with additional Cr_2O_3 doping exhibits a slight grain size increase, relative to the 43-hiLn. The grain growth phenomenon seen with Cr_2O_3-doped UO_2 is likely a result of enhanced grain boundary diffusion in the UO_2 matrix due to the presence of Cr^{3+} in the UO_2 [121, 122].

	25-SIMF	43-SIMF	43-hiLn	43-hiLnCr
Grain size	5.02 ± 0.82 mm	3.56 ± 0.845 mm	1.62 ± 0.360 mm	1.96 ± 0.555 mm

Table 4-1: Table of SIMFUEL average bulk grain sizes excerpted from Zoltan Hiezl's thesis [47].

4.3 Baseline Electrochemical Study

In this section, baseline OCP, CV, and LSV measurements have been conducted on electrodes of undoped-UO_2, SIMFUELs and 20/25/Nb AGR cladding, in 0.5 mol/dm^3 Na_2SO_4 at solution pH and purged with Nitrogen. The data acquired from measurements of the 43-hiLn and 43-hiLnCr SIMFUELs will be compared with the standard 43-SIMF to compare the effects of increasing the doping of lanthanide and/or chromium content.

4.3.1 Undoped-UO_2, 25 and 43 GWd/tU SIMFUELs

Electrochemical measurements were carried out on electrodes of undoped-UO_2, 25-SIMF and 43-SIMF in a 0.5 M Na_2SO_4 electrolyte. This is a commonly used background supporting electrolyte and is chosen for its sufficient ionic strength as a voltammetry electrolyte medium [123] and for its chemical inertness with UO_2 in that it does not chemically enhance UO_2 dissolution [39].

Measurements were carried out at the solution pH, typically pH ~ 6 to 6.5, and all solutions were sparged with N_2. The method and parameters for OCPs, CVs, and LSVs measurements follow the standard methods described in Chapter 3 Section 3.2.

For convenience, OCPs, CVs, and LSVs measurements are defined briefly as follows: (a) Open Circuit Potential (OCP) is a measure of the system's resting potential over time at steady state equilibrium, (b) Linear sweep voltammetry (LSV) is a potentiostatic polarisation based method, in which a potential is applied to the working electrode in an electrochemical cell, and (c) Cyclic voltammetry (CV) is also a type of potential sweep experiment but differs from the LSV method as the scanned potential is reversed at the end of the first scan until it reaches the starting potential again.

Figure 4-5 shows the cyclic voltammograms recorded for each of the materials under the measurement conditions described above. The form of the CVs and magnitudes of the currents are as expected for each of the three materials. The trends observed in the behaviour of current response and the shape of the CVs, across each sample, are consistent with existing literature on the analogous CV

studies of undoped-UO_2 and UO_2-based SIMFUELs [15, 31, 34, 41, 64, 76, 79, 124-126].

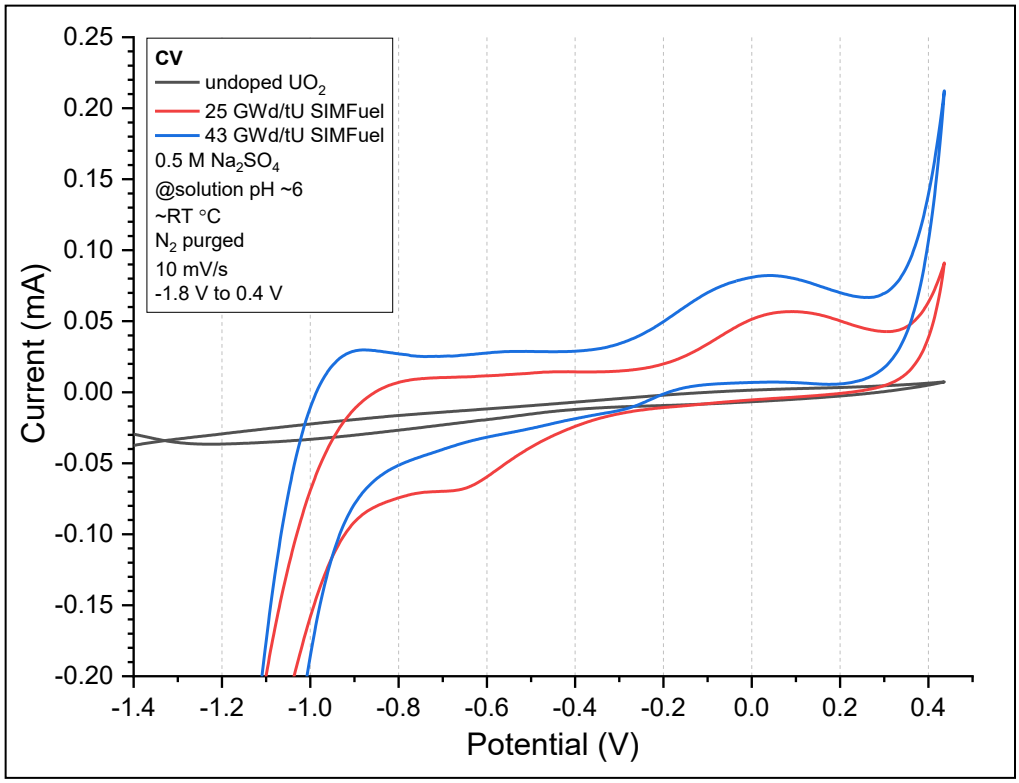

Figure 4-5: Cyclic voltammogram plots of current vs. time for (i) undoped-UO_2 (ii) 25 GWd/tU SIMFUEL and (iii) 43 GWd/tU SIMFUEL, measured in 0.5 mol/dm^3 Na_2SO_4 electrolyte.

In general, these observed current response trends are associated with the increased reactivity due to the increased dopant density going from pure UO_2 to SIMFUELs and improved conductivity due to decreased material resistivity, also due to increased dopant density.

These factors, which affect the corrosion behaviour of such materials, are further discussed in Chapter 2 Section 2.2.4.4. The features of the UO_2/SIMFUEL CVs can be assigned according to the following oxidation and reduction processes, in the following current regions [64]:

In the forward anodic potential scan direction:

- Between ~-0.8 to -0.2 V, the current is attributed to the oxidation of UO_{2+x} to $UO_{2.33}$ at the grain boundaries – bulk oxidation is not expected as UO_2 is considered thermodynamically stable, any oxidation will result in increased hyperstoichiometry.

- Between ~-0.2 to 0.2 V, the current is attributed to the oxidation of bulk UO_2 to UO_{2+x} in the grains via the incorporation of oxygen interstitials into the UO_2 matrix.
- Between ~0.2 to 0.4 V, the current is attributed to the onset of oxidation of UO_{2+x} to aqueous UO_2^{2+} via irreversible oxidation in the form of uranyl ion dissolution.

In the reverse cathodic potential scan direction:

- Between ~-0.3 to 0.1 V, the current is attributed to the reduction of precipitated/adsorbed U(VI) species formed during the anodic scan to UO_{2+x}.
- Between ~-0.9 to -0.7 V, the current is attributed to the reduction of $UO_{2.33}/UO_{2+x}$ oxide layer species, formed during anodic scan.

The regions of current activity described above are also present in the CVs of the undoped-UO_2, albeit with less magnitude, thus appearing relatively flat in comparison to the SIMFUEL CVs. Between the potentials of -0.9 V and -1.4 V, there is a large difference in the magnitude of current between the undoped-UO_2 and SIMFUELs; this increased current activity observed in the latter is associated with the hydrogen evolution process from the reduction of H_2O, taking place at the surface of the SIMFUELs.

That hydrogen evolution process is not seen over the same potential range in the undoped-UO_2 electrode, suggests that certain fission product simulants incorporated into the SIMFUEL compositions are electro-catalytically promoting the H^+ reduction process. This is most likely due to the noble metal particles incorporated into SIMFUELs to simulate the ε-particles that are precipitated in the UO_2 matrix of real AGR SNF. The associated literature review and discussion of this feature can be found in Chapter 2 Section 2.2.1 and 2.2.4.4.

Figure 4-6 shows the recorded OCPs of the undoped-UO_2 and SIMFUELs, recorded in 0.5 M Na_2SO_4 electrolyte over a period of 15 hours. The OCP acquisition time was sufficient for the electrochemical system to reach its equilibrium potential, evidenced by the OCP becoming near-invariant with measurement time.

By comparing the OCP values of each material with their respective CVs, we can qualitatively predict the electrochemical process that may be taking place when the material is at its equilibrium potential.

Undoped-UO_2 exhibits an equilibrium OCP of ~0.001 V, which sits in the potential region where in-grain oxidation of bulk UO_2 to UO_{2+x} is expected to take place. In comparison, both SIMFUELs exhibit an OCP of ~0.12 V, which also sits in the potential region associated with the onset of oxidation of UO_2 to UO_{2+x} in the grains, albeit at a more positive potential than that seen on undoped-UO_2. This suggests that this oxidation on SIMFUELs has a greater thermodynamic driving force and electrochemical rate parameter than on undoped-UO_2.

These observations suggest that the SIMFUELs are likely more susceptible to corrosion than pure UO_2, under these OCP measurement conditions. The observed increase in anodic activity when undoped-UO_2 is doped with simulant fission and activation products – such as lanthanides and rare earth elements in the 3+ oxidation state – is consistent with previous SIMFUEL studies [15, 41, 83, 126].

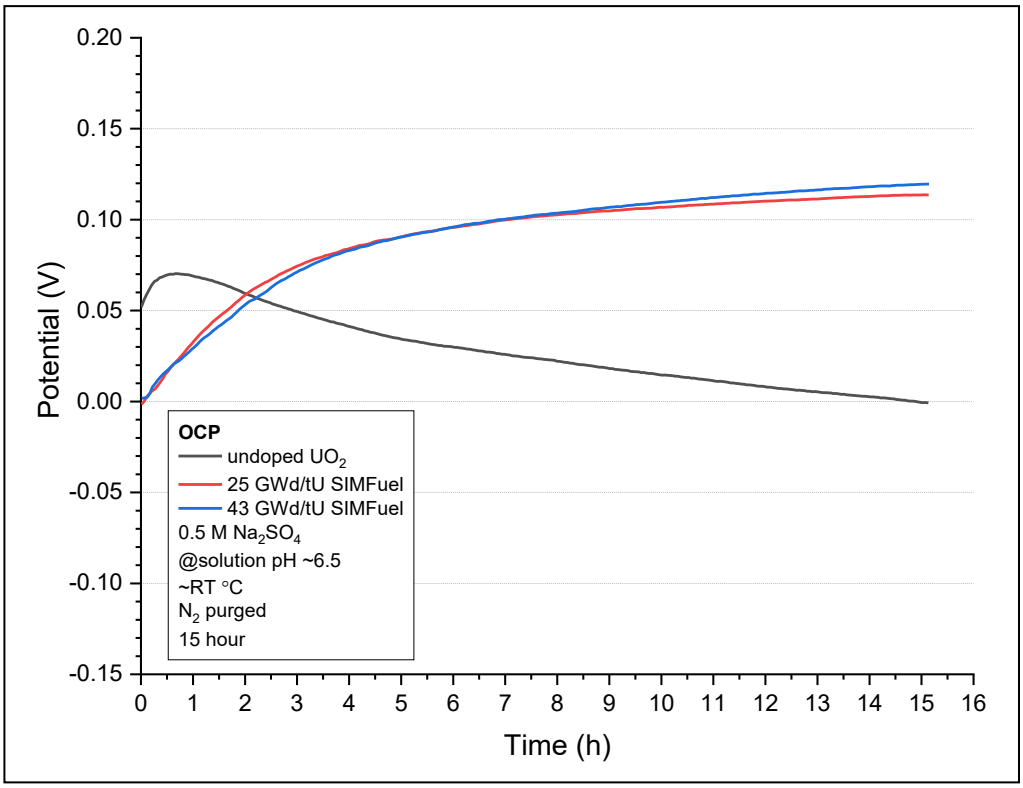

Figure 4-6: OCP plots of potential vs. time for (i) undoped-UO_2 (ii) 25 GWd/tU SIMFUEL and (iii) 43 GWd/tU SIMFUEL, measured over a period of 15 hours in 0.5 mol/dm^3 Na_2SO_4 electrolyte.

Figure 4-7 shows the polarisation curves for the undoped-UO_2 and SIMFUELs, recorded at a sweep rate of 1 mV/s in 0.5 M Na_2SO_4 electrolyte. The change in magnitude of the current response during polarisation of the electrode material provides information on the possible surface reactivities of the material during overpotential conditions.

Each plot displays the current response as a function of applied potential, analogous to the CVs of Figure 4-5. However, the finer details in the form of oxidation peaks, as seen in the latter, are not present in the polarisation curves due to the use of a logarithmic y-axis scaling.

Instead, these polarisation curves can be used to conveniently identify and attribute regions of electrochemical activity and/or passivity and facilitate a more direct comparison of the electrochemistry of the SIMFUELs with respect to that of undoped-UO_2, the latter appearing as a near featureless CV in the voltametric data of Figure 4-5. From Figure 4-7, it can be seen that UO_2 exhibits the same LSV behaviour and thus electrochemistry as the SIMFUELs, albeit with much lower currents.

In this instance, Figure 4-7 shows that each material passes a small but finite current in the potential region immediately positive of the Potential of Zero Current (PZC) and stretching from ~-0.3 to -0.1 V up to 0.2 V, associated with the oxidation of UO_2 to UO_{2+x} in the grains, as seen in the CVs.

We can also observe that the PZC values are not coincident with the OCP values of Figure 4-6, this is unexpected but can be attributed to the samples used in the LSV measurements of Figure 4-7 having been exposed to a period of reduction in the potential range negative of the PZC towards ~-0.7 V. In contrast, the samples in the OCP measurements of Figure 4-6 were not exposed to such reductive stress.

Once the applied potential increases past ~0.2 V, the current response increases drastically for the SIMFUELs, this correlates to the oxidation of UO_{2+x} to aqueous UO_2^{2+}. In contrast, the undoped-UO_2 polarisation curve remains at a steady gradient, indicating reduced oxidative activity across the entire potential sweep range.

At potentials positive of 0.6 V, the currents observed from the SIMFUELs plateau are most likely due to precipitation at the electrode surface of the electrogenerated UO_2^{2+} as a U(VI) oxyhydroxide phase. This precipitation will be driven by the high local concentration of UO_2^{2+} generated by the high oxidation currents as seen on the SIMFUELs.

Such large currents are not seen for the undoped-UO_2 sample, thus precluding the generation of a high local UO_2^{2+} concentration, preventing U(VI) oxide phase formations, hence the extended plateau as seen in the undoped-UO_2 LSV trace.

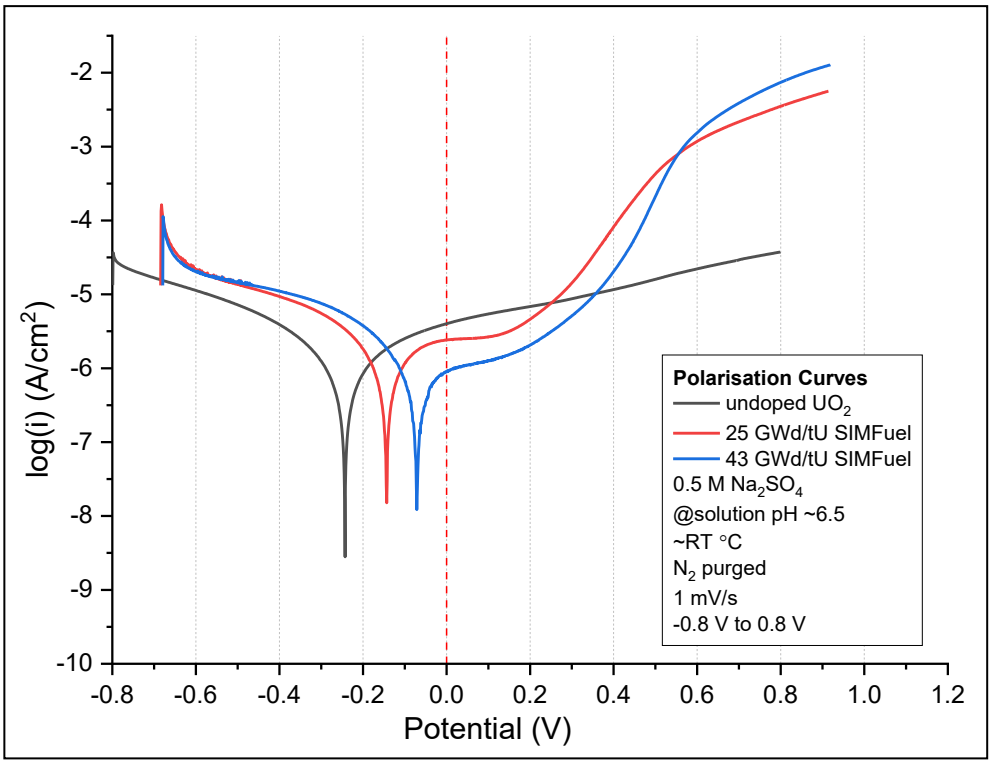

Figure 4-7: Polarisation curves showing non-surface-area-normalised current density vs. potential for (i) undoped-UO_2, (ii) 25 GWd/tU SIMFUEL and (iii) 43 GWd/tU SIMFUEL, measured in 0.5 mol/dm^3 Na_2SO_4 electrolyte.

4.3.2 High Lanthanide-doped and High Chromium-doped SIMFUELs

Electrochemical measurements were carried out on electrodes of a 43 GWd/tU simulated burn-up SIMFUEL with higher lanthanide doping (43-hiLn) and a 43 GWd/tU simulated burn-up SIMFUEL with higher lanthanide and chromium doping (43-hiLnCr).

The following measurements are compared with the previous measurements on a 43 GWd/tU simulated burn-up SIMFUEL (43-SIMF), presented in Section 4.3.1. Measurements were carried out in a 0.5 M Na_2SO_4 electrolyte at the solution pH typically ~ 6 to 6.5 and sparged with N_2. The method and parameters for OCPs, CVs, and LSVs measurements follow the standard methods described in Chapter 3 Section 3.2.

Figure 4-8 shows the cyclic voltammograms for each of the two SIMFUELs. The shape/form of the CVs can be described similarly to the CVs of the 25-SIMF and 43-SIMF SIMFUELs of Figure 4-5. Each region of anodic/cathodic current activity corresponds to the same electrochemical processes as described in

Section 4.3.1. However, the magnitude of currents for the 43-hiLn and 43-hiLnCr are higher in all potential ranges than that of the standard 43-SIMF.

This observation can be attributed to the effects of charge compensation processes taking place due to lanthanide-(III) ion incorporation into the UO_2 matrix. The addition of lower valence Ln(III) ions into the U(IV) matrix requires charge compensation to maintain charge balance.

The mechanism of charge compensation can be accomplished by: (i) generation of oxygen vacancy sites and/or (ii) ionisation of U(IV) ions to U(V)/U(VI) [126]. This U(V)/U(VI) generation occurs by the removal of electrons from the 5f sub-band in the electronic band structure of UO_2, thus generating holes in that band and giving rise to increased conductivity.

This phenomenon has also been reported in studies of LWR SIMFUELs [31]. Therefore, the increased currents observed in the CVs of Figure 4-8, relative to the CVs of the standard 43-SIMF, can be tentatively assigned to charge compensation mechanism (ii) and will lead to an expected increase in the corrosion susceptibility of the 43-hiLn and 43-hiLnCr, compared to the 43-SIMF.

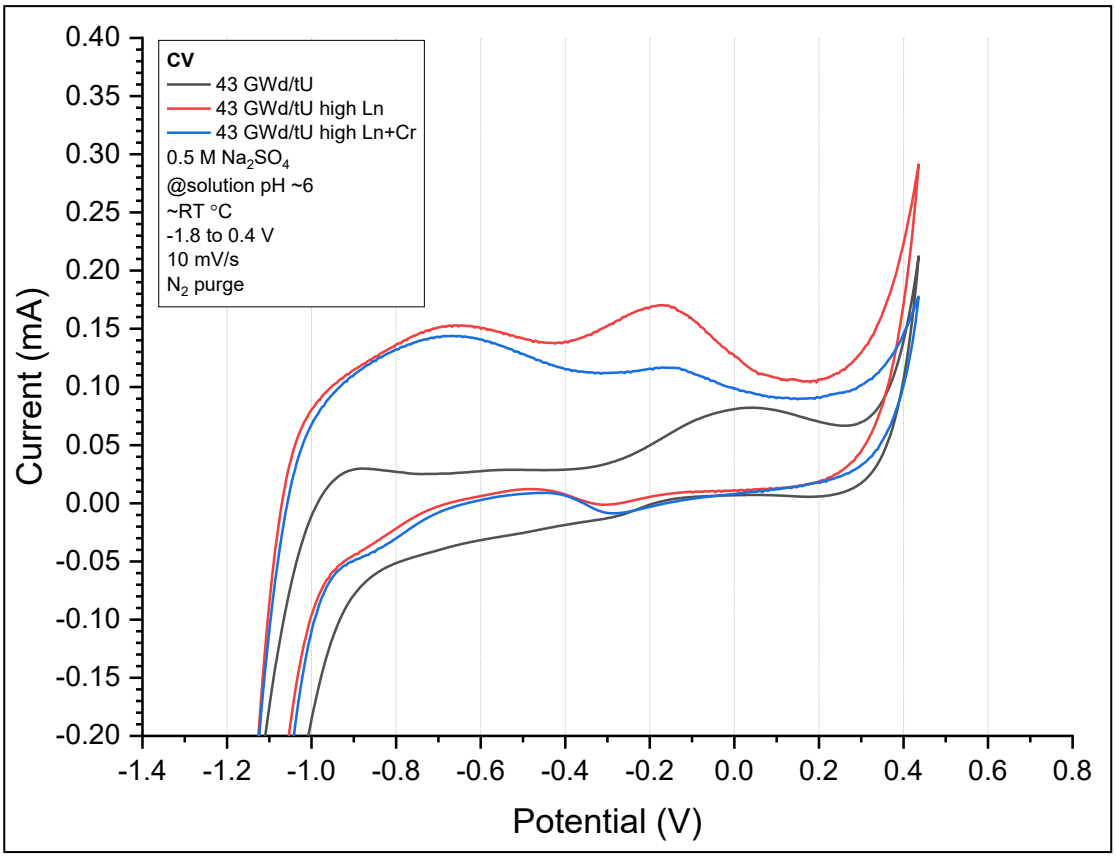

Figure 4-8: Cyclic voltammogram plots of current vs. time comparing 43-SIMF with 43-hiLn and with 43-hiLnCr, measured in 0.5 mol/dm^3 Na_2SO_4 electrolyte.

Comparing between the CVs of the 43-hiLn and 43-hiLnCr, the addition of Cr to the SIMFUEL matrix results in a CV with a reduced current response, relative to the Cr-free sample.

The addition of Cr into UO_2-based fuel compositions has been hypothesised to improve the performance of the fuel during irradiation, by increasing the fuel matrix average grain size, fuel density, and plasticity [127-129].

In theory, it would be expected that larger grain sizes would lead to reduced grain boundary densities and thus translate to reduced currents in the region of ~-0.8 to -0.4 V. However, the SEM images of Figure 4-4 in Section 4.2 shows that the introduction of Cr and Ln(III) content results in reduced grain sizes compared to the 43-SIMF prepared in the absence of additional Cr and Ln(III).

This reduced grain size is seen for both the 43-hiLN and 43-hiLnCr SIMFUEL samples, suggesting that it is the addition of the Ln(III) content that is

decreasing its grain size during sintering. This is further supported by the near identical grain sizes of the 43-hiLn and 43-hiLnCr, as shown above in Table 4-1.

Bearing this similarity, it is interesting to observe that the difference in current magnitude in the potential range ~-0.8 to -0.2 V, where the oxidation of UO_{2+x} at the grain boundaries occurs, is not very significant between the CVs of the Cr-doped and Cr-free samples. This suggests that the current enhancement seen for both samples compared to the 43-SIMF can be attributed to the smaller grain sizes/larger density of grain boundaries presented by 43-hiLn and 43-hiLnCr SIMFUEL samples.

In the potential region ~-0.4 to 0.2 V – where oxidation of UO_2 to UO_{2+x} on the grains is expected to occur – the Cr-doped sample exhibits more noticeably lower currents than the Cr-free sample, suggesting some type of property associated with the addition of Cr, which results in improved corrosion protection in the UO_2. This protection then extends into the potential range associated with UO_{2+x} to U(VI) oxidation as well.

Based on the observations obtained from these simple electrochemical measurements, it appears that the additional Ln(III) doping promotes the formation of smaller grains and thus the corrosion processes associated within the grain boundaries, whilst the addition of Cr content to the matrix protects against corrosion processes that occur on the grains itself. These effects warrant further study to understand them fully. However, such additional studies are beyond the scope of this thesis.

Figure 4-9 shows the recorded OCPs of the 43-hiLn and 43-hiLnCr compared with the standard 43-SIMF, recorded under similar conditions as above. The OCPs of all three samples are similar in value at ~0.12 V. When compared with their respective CVs, the OCPs sit in between the potential region associated with in-grain oxidation of UO_2 to UO_{2+x} and just before the potential region where the onset oxidation of UO_2^{2+} to U(VI) species is expected. From this observation, it can be inferred that the 43-hiLn and 43-hiLnCr SIMFUELs are not likely to experience significant spontaneous corrosion, under these OCP conditions.

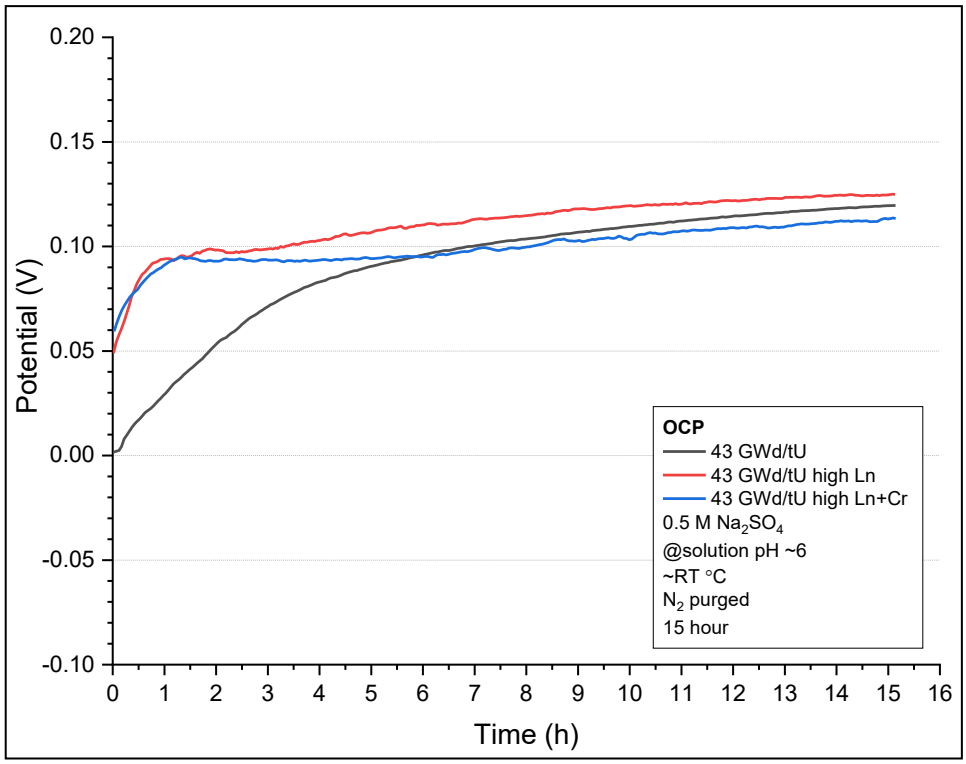

Figure 4-9: OCP plots of potential vs. time comparing 43-SIMF with 43-hiLn and with 43-hiLnCr, measured over a period of 15 hours in 0.5 mol/dm^3 Na_2SO_4 electrolyte.

Figure 4-10 shows the polarisation curves of the 43-hiLn and 43-hiLnCr compared with the standard 43-SIMF, recorded under similar conditions as above. The similarity in the current responses suggests that in terms of the general electrochemical processes occurring, the samples exhibit near identical behaviour when they are subjected to anodic polarisation.

The slightly lower current densities observed at potentials greater than 0.4 V for samples 43-hiLn and 43-hiLnCr again suggest a marginally reduced corrosion susceptibility for not only 43-hiLnCr as discussed above, but also the 43-hiLn sample. However, these observations should be treated with caution given the small changes evidenced.

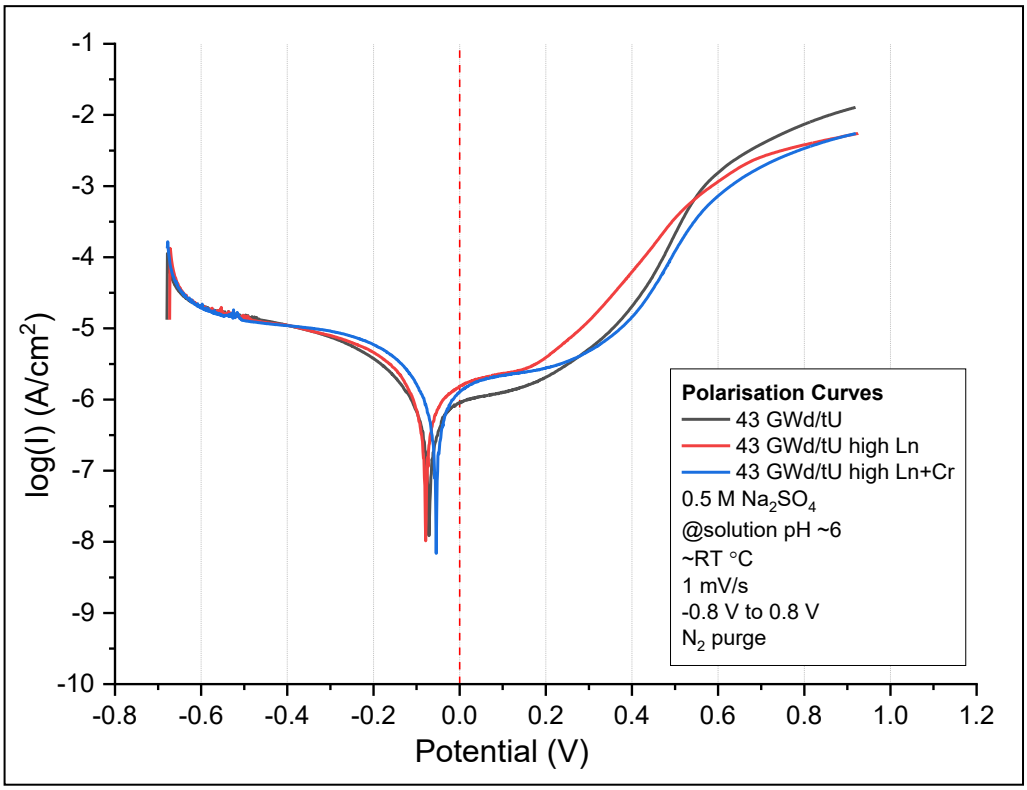

Figure 4-10: Polarisation curves showing surface-area-normalised current density vs. potential comparing 43-hiLn with 43-hiLnCr, measured in 0.5 mol/dm^3 Na_2SO_4 electrolyte.

4.3.3 20/25/Nb AGR Cladding

Electrochemical measurements were carried out on an electrode of unsensitised 20/25/Nb stainless steel AGR cladding. Measurements were carried out in a 0.5 M Na_2SO_4 electrolyte at the solution pH (typically pH ~ 6 to 6.5) and sparged with N_2. The method and parameters for OCPs, CVs, and LSVs measurements follow the standard methods described in Chapter 3 Section 3.2.

Figure 4-11 shows the polarisation curve of the cladding sample recorded under conditions as above. The shape and features of the plot bear good similarity to the polarisation curves of typical passivating stainless steels [130, 131]. The features of the polarisation curve can be assigned to the following electrochemical processes taking place at the surface of the cladding, in the following potential regions [132, 133]:

- Between ~ -1.0 to -0.7 V, the hydrogen evolution reaction is the dominant process taking place.

- Between ~ -0.7 to 0.2 V, passivation of the cladding occurs, where there is steady growth of a protective surface oxide film.
- Between ~ 0.2 to 1.2 V, pre-transpassive begins and selective dissolution of some of the Cr content of the passive film begins [134, 135].
- At potentials > 1.2 V, transpassivity occurs due to dissolution of the passive film and localised corrosion phenomena such as intergranular corrosion
- At potentials > 1.4V, secondary passivation occurs due to the electrogenerated metal ions in the solution phase locally exceeding their solubility and thus reprecipitating as oxides/oxyhydroxides at the electrode surface. Such secondary passivation layers are typically highly porous and iron-rich.

Figure 4-12 shows the recorded OCP of the AGR cladding sample recorded under similar conditions as above. When compared with the polarisation curve of Figure 4-11, the OCP value of ~0.04 V sits in the region where the surface of the steel is passivated. Thus, under these baseline conditions, the steel cladding is likely protected from corrosion by the formation of the protective passive surface oxide film.

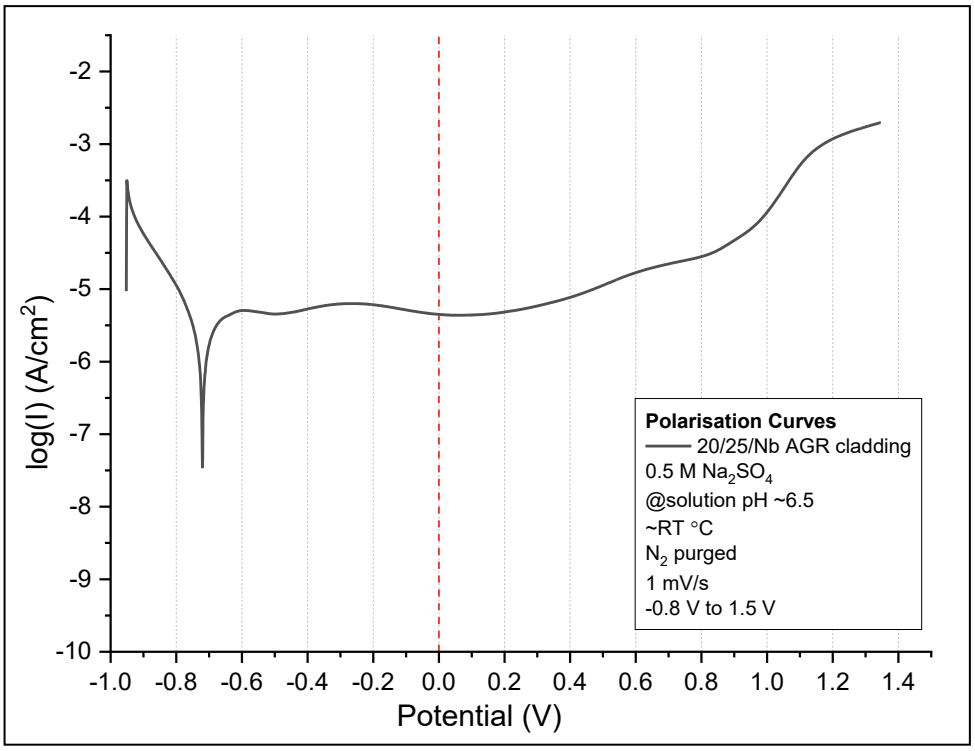

Figure 4-11: Polarisation curve showing surface-area-normalised current density vs. potential for 20/25/Nb stainless-steel AGR cladding, measured in 0.5 mol/dm^3 Na_2SO_4 electrolyte.

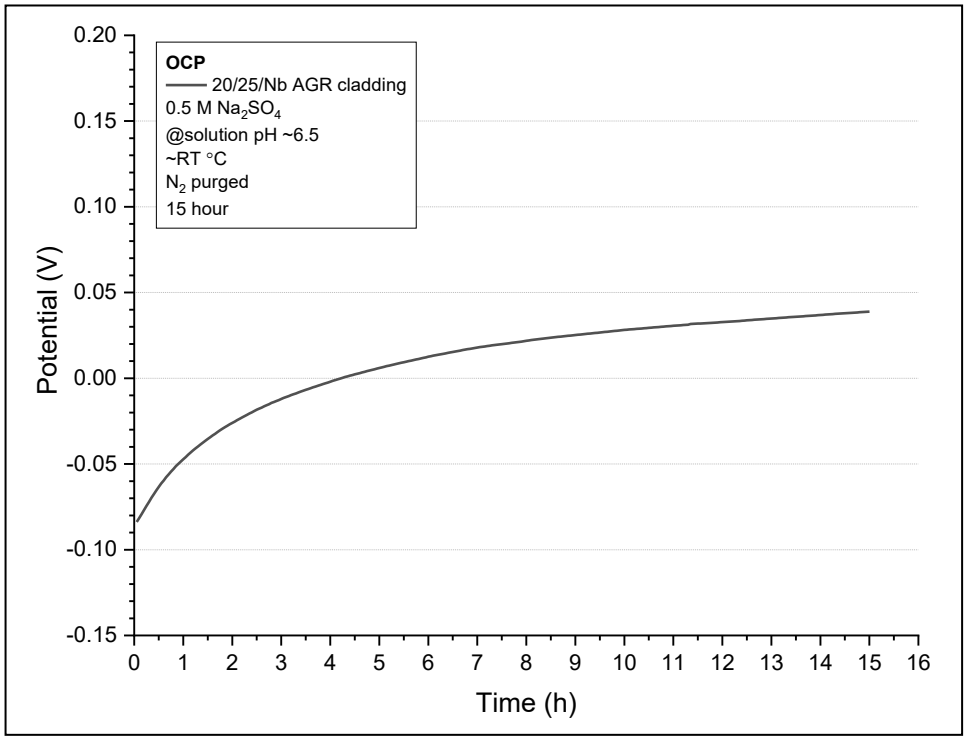

Figure 4-12: OCP plot of potential vs. time for 20/25/Nb stainless-steel AGR cladding, measured over 15 hours in 0.5 mol/dm^3 Na_2SO_4 electrolyte.

Having now discussed the electrochemical behaviour of undoped-UO_2, AGR SIMFUELs, and AGR cladding, using CV, LSV and OCP methods, under 0.5 mol/dm^3 Na_2SO_4 electrolyte conditions, the next section presents the baseline μ-Raman spectroscopy studies of the undoped-UO_2 samples and the AGR SIMFUELs.

4.4 Baseline μ-Raman Spectroscopy Study

This section presents the μ-Raman spectroscopy study of the undoped-UO_2 and SIMFUEL samples, providing a baseline Raman dataset to enable comparisons between the as-received samples and to inform the interpretation of μ-Raman spectroscopy measurements conducted during the electrochemical oxidation studies of Chapter 7.

Section 4.4.1 presents the measurements conducted using a 785 nm wavelength excitation laser-based μ-Raman spectrometer. These are then compared with the measurements conducted using a 532 nm wavelength excitation laser-based μ-Raman spectrometer, presented in Section 4.4.2. Discussions of the chosen Raman excitation wavelengths are presented in their respective results sections.

Section 4.4.3 presents the μ-Raman spectroscopy study for the 43-hiLn and 43-hiLnCr SIMFUELs, conducted using a 785 nm laser; this dataset will be compared with similar data obtained from the standard 43-SIMF sample.

4.4.1 785 nm Wavelength Excitation laser-based Raman Study of Undoped-UO_2, 25 and 43 GWd/tU SIMFUELs

The 785 nm excitation wavelength is commonly used for the Raman studies of UO_2 and SIMFUELs [136]. This particular excitation wavelength avoids any spectral interference in the acquired spectra, such as those that may be caused by resonance effects between the laser and active Raman modes. This is in contrast to the 532 nm excitation wavelength, used for the studies of Section 4.4.2, which does, in fact, cause Raman resonance effects.

Figure 4-13 shows the averaged Raman spectra for the samples of undoped-UO_2, 25-SIMF and 43-SIMF, acquired using the 785 nm laser-based Raman microscope according to the methodology described in Chapter 3 Section 3.3.

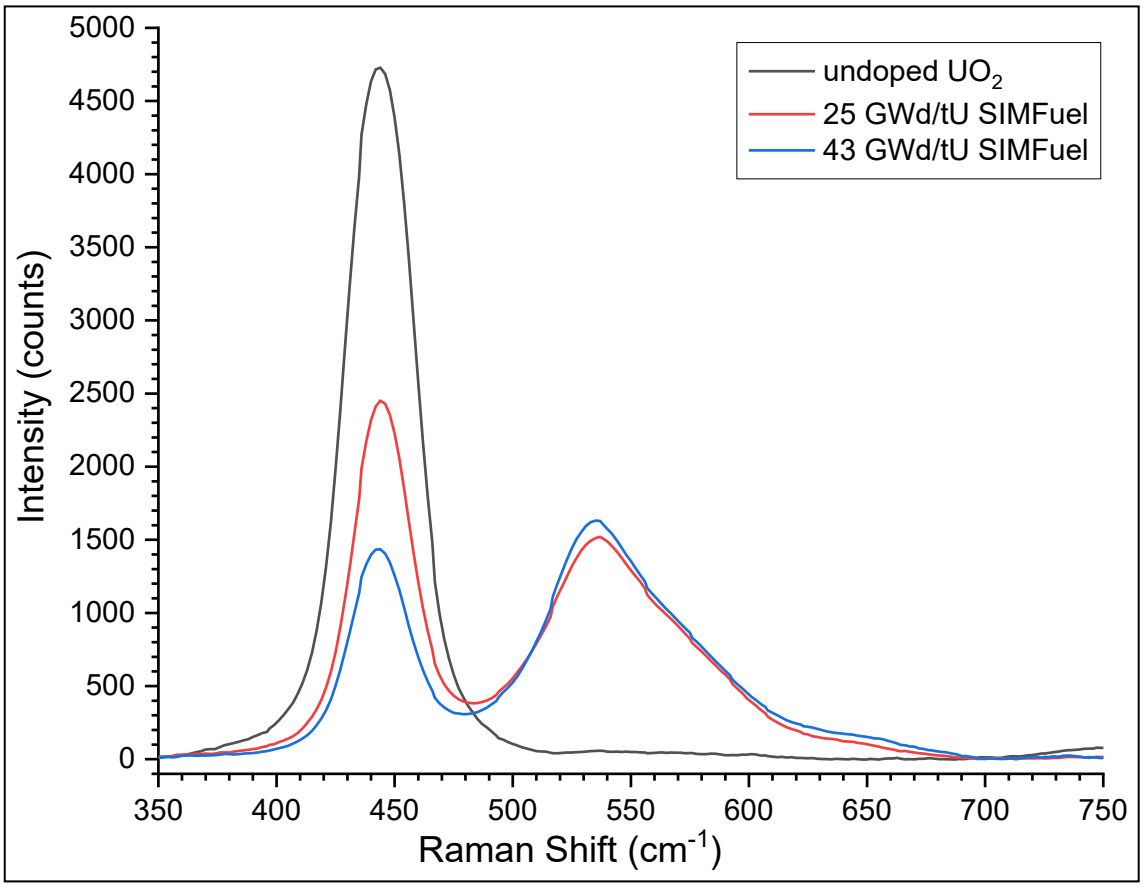

Figure 4-13: Averaged 785 nm μ-Raman spectra recorded from undoped-UO_2, 25 GWd/tU SIMFUEL and 43 GWd/tU SIMFUEL samples between the range of ~350 to ~750 cm^{-1}.

From this, it can be seen that the undoped-UO_2 spectra behaves as expected for a perfect cubic fluorite structure of pure UO_2, with an intense vibration at ~445 cm^{-1}, associated with the fundamental U-O stretch.

This is accompanied by a broad band at ~1150 cm^{-1}, shown in the expanded spectra in Figure 4-15, assigned as the 2LO (Longitudinal Optical) phonon, which itself is the first overtone of the LO phonon at ~574 cm^{-1} [38]. This fundamental LO phonon is not itself seen in the UO_2 spectra of Figure 4-13 and Figure 4-15 due to its observation being symmetry/selection rule forbidden from high crystallinity/defect-free materials such as the UO_2 sample under study here.

Further interpretation and discussions of the pure UO_2 Raman spectra can be found in Chapter 2 Section 2.2.1.

The Raman spectra of the SIMFUELs shown in Figure 4-13 are in line with other doped-UO_2 and SIMFUEL-related materials, as characterised by (i) the reduction in intensity of the peak associated with the U-O stretch at 445 cm^{-1} compared to that seen in the pure UO_2 spectrum, and (ii) the appearance of a broad band comprised of multiple overlapping peaks between ~500 to ~700 cm^{-1}.

This broad band is commonly associated with lattice damage, known as the so-called “defect band”. The deconvolution and interpretation of this band have previously been discussed in Chapter 2 Section 2.2.1, Section 2.2.4.4, and Section 2.2.5.

The intensity of the SIMFUEL U-O stretch decreases as dopant level increases and is directly related to the deviation from the perfect cubic fluorite lattice, indicating a defected UO_2 matrix. This can be seen in Figure 4-14, which shows a plot of the averaged ~445 cm^{-1} U-O stretch peak intensities as a function of effective burn-up for the undoped-UO_2 and SIMFUEL samples. These peak intensities were calculated by averaging the U-O peak heights across 10 – 20 Raman spectra for each of the UO_2 and SIMFUEL samples.

The largest relative decrease in peak intensity is observed between the undoped-UO_2 and the 25 GWd/tU SIMFUEL with error bars suggesting that the peak intensity difference between 25-SIMF and 43-SIMF is relatively small. The 2LO phonon at ~1150 cm^{-1} is also present in the SIMFUELs, this is shown in the expanded view spectra of the 25-SIMF in Figure 4-15.

However, the 2LO phonon band decreases in intensity in a manner analogous to U-O stretch band when moving from the pure UO_2 to 25 GWd/tU SIMFUEL sample. This is again due to deviation from the perfect cubic fluorite UO_2 [23], this time giving rise to defect sites within the SIMFUEL lattice that serves to act as phonon scattering centres, so impeding its propagation through the parent urania lattice.

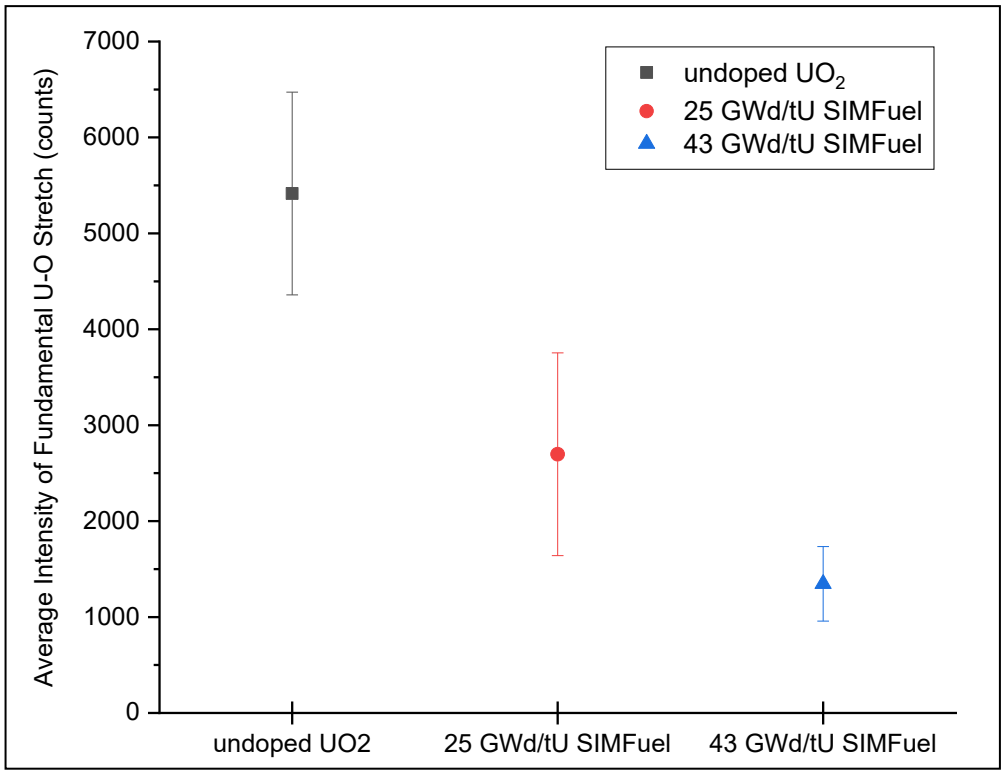

Figure 4-14: Average peak intensity of the fundamental U-O stretch at 444 cm^{-1}, with standard deviations for undoped-UO_2, 25 GWd/tU SIMFUEL and 43 GWd/tU SIMFUEL samples.

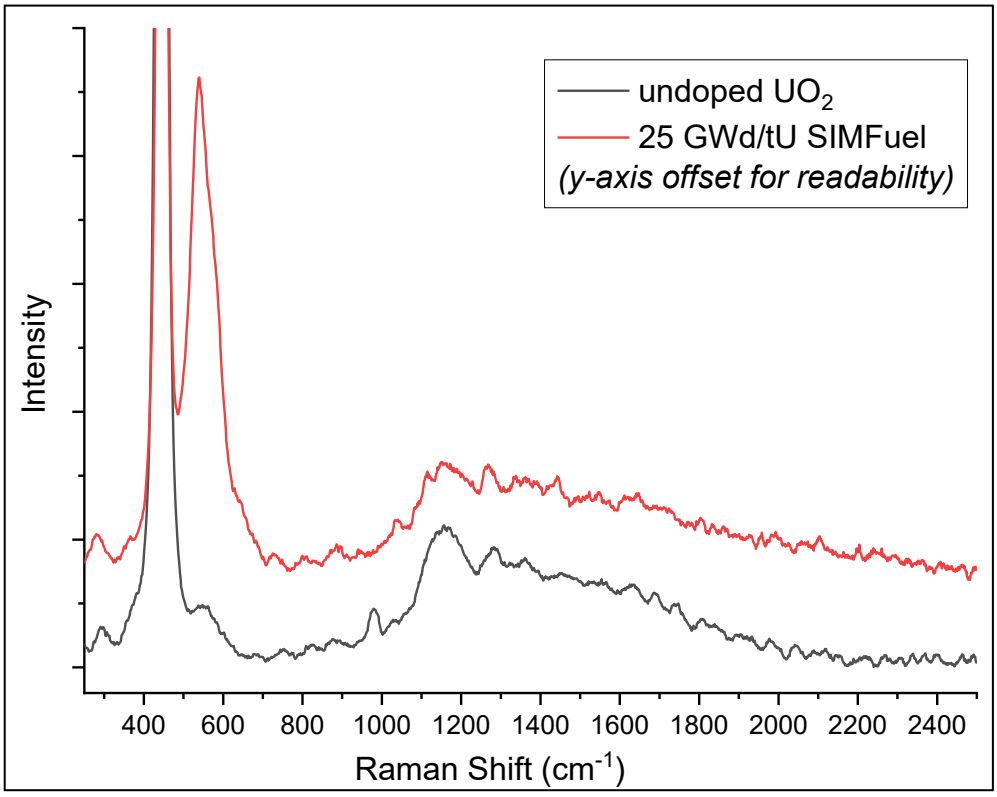

Figure 4-15: 785 nm μ-Raman spectra of undoped-UO_2 and 25 GWd/tU SIMFUEL showing the full recorded Raman range, highlighting the 2LO phonon peaks between ~800 and ~2200 cm^{-1}.

Figure 4-16 shows an expanded view of the fitted averaged Raman spectra of the 25-SIMF and 43-SIMF of Figure 4-13 with inclusion of the deconvoluted “defect band” between ~500 to ~700 cm^{-1}. Deconvolution was conducted as described in Chapter 2 and leads to the observation that the defect band is comprised of three separate peaks at ~535, ~575 and ~625 cm^{-1}.

A summary of the “defect band” peak assignments and interpretations can be found in Chapter 2 Section 2.2.1, Section 2.2.4.4, and Section 2.2.5.

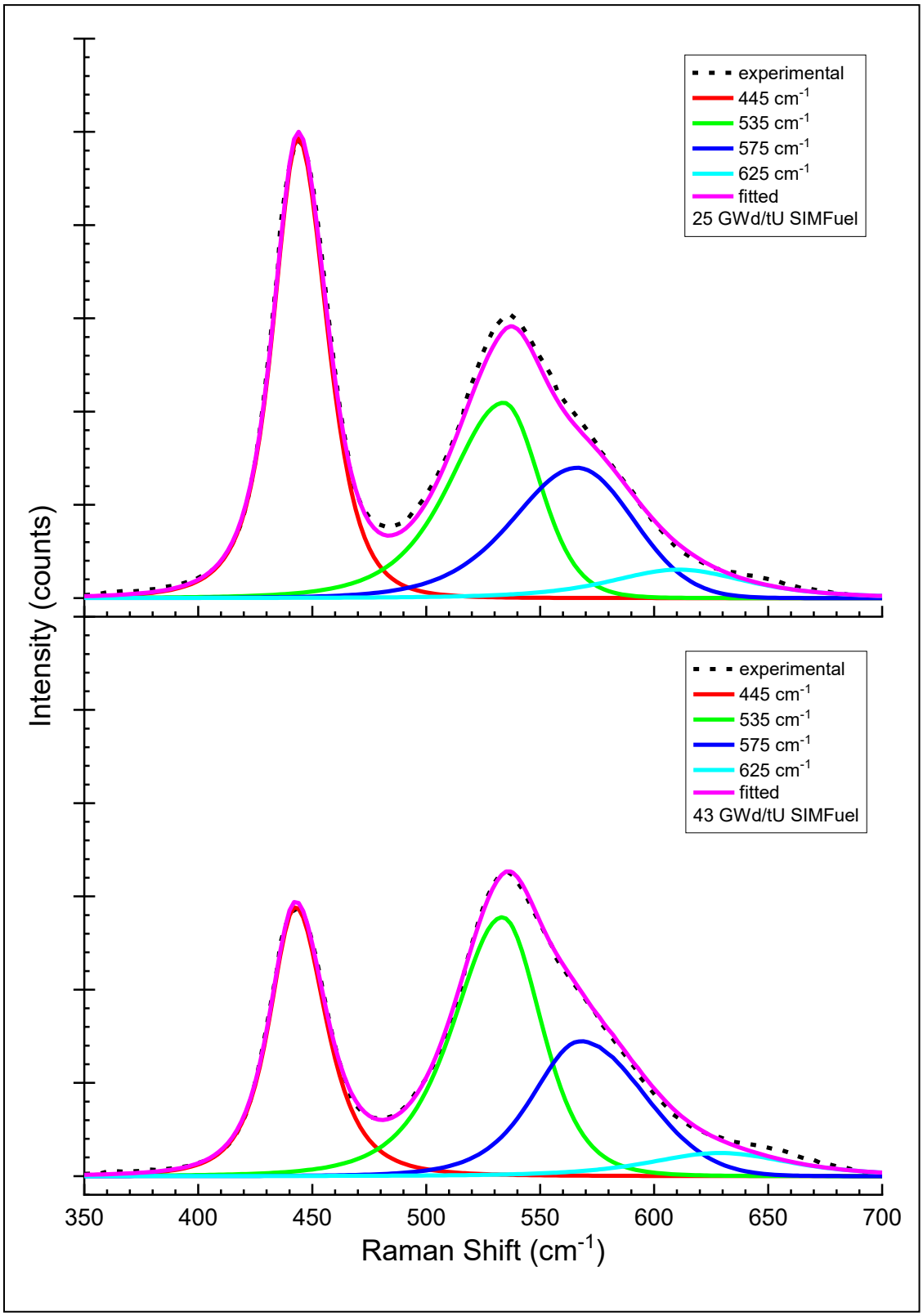

Figure 4-16: Peak fitting of the averaged 785 nm μ-Raman spectra of the 25 GWd/tU SIMFUEL (top) and 43 GWd/tU SIMFUEL (bottom), seen in Figure 4-13.

Figure 4-17 shows the calculated ratios of “defect band” peak intensities, with respect to the fundamental U-O stretch at ~445 cm^{-1}. This ratio approach allows for a relative comparison of the peak heights between the two SIMFUEL samples. By using this method to present peak heights as ratios versus their respective ~445 cm^{-1} peak, it compensates for the randomness in peak intensities across each spectrum when acquiring multiple Raman scans across the surface of a sample. This comparative view of the peak height ratios allows us to observe the large variation in Raman spectra recorded across random locations on the SIMFUEL sample surface.

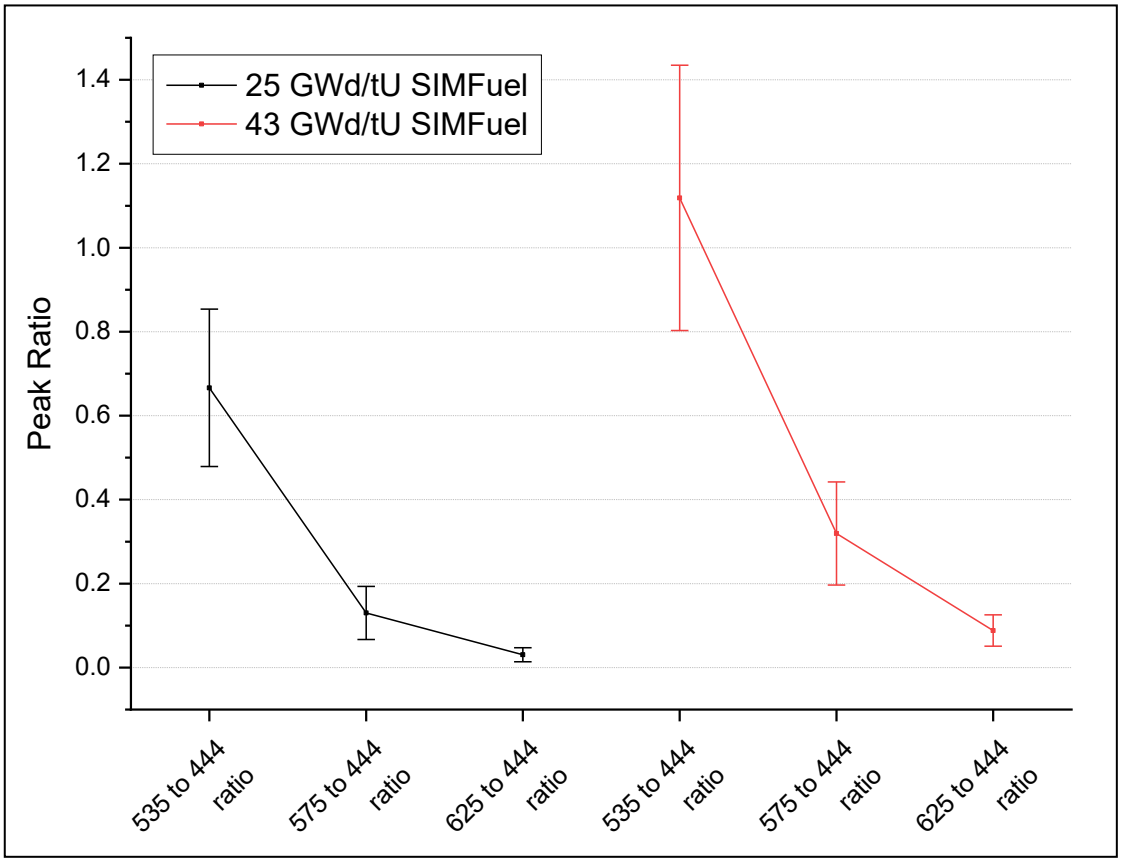

Figure 4-17: Average peak ratios with standard deviations of the three main deconvoluted peak components in the broadband between ~500 and ~700 cm^{-1}, recorded under baseline conditions using 785 nm Raman for 25 and 43 GWd/tU SIMFUEL.

The standard deviation error bars indicate the error in the peak fitting of the deconvoluted “defect band”. The proximity of the three overlapping contributing peaks, combined with the random variations in spectra peak intensities, makes the fitting of these peaks accurately a difficult task.

In general, the 43-SIMF “defect band” peak ratios are greater than those of the 25-SIMF, and in the case of the 43-SIMF, the intensity of the peak at ~535 cm^{-1}, is greater than that of the peak at ~445 cm^{-1}.

The more dopants that are incorporated into the UO_2 matrix, the more distorted and defected the lattice becomes, thus leading to decreased intensity of the fundamental U-O peak and increased intensity of “defect band” peaks. These general Raman observations and correlations of the SIMFUELs, have previously been discussed in Chapter 2 Section 2.2.4.4.

The most noticeable difference observed between the two SIMFUELs is associated with the peak at ~535 cm^{-1}. This peak is typically associated with oxygen-vacancy-induced lattice distortions, derived from the incorporation of lanthanide (III) dopants. From the peak ratio data of Figure 4-17, we can see that the ~535 cm^{-1} signal is typically greater in the 43-SIMF than in the 25-SIMF. This interpretation corresponds well with the above explanation, since the 43-SIMF contains a greater percentage of lanthanide (III) dopants.

The ~575 cm^{-1} peak is also attributed to the distortion of the cubic fluorite lattice either from (i) the addition of oxygen-interstitials due to oxidation / hyperstoichiometry or (ii) the oxygen-vacancy-induced lattice distortions from the incorporation of lanthanide(III) dopants, this phenomena is described in literature and previously discussed in Chapter 2 Section 2.2.4.4.

From Figure 4-17 we can see that the difference in ~575 cm^{-1} to 445 cm^{-1} peak intensity ratios between the two SIMFUELs is less pronounced than that of the ~535 cm^{-1} to 445 cm^{-1} peak intensity ratio. However, we can still observe an increase in both the 535 and 575 cm^{-1} peak intensity with increasing simulated burn-up.

The ~625 cm^{-1} peak is assigned to the clustering of oxygen interstitials within the U-O matrix to form cuboctahedrons, which in-turn, indicates the degree of UO_2 oxidation/hyperstoichiometry. Thus, this peak may also appear in the spectra of undoped-UO_2, and its intensity will increase with increased oxidation or hyperstoichiometry.

However, we know based on XPS and XRD data by Wilbraham et al., the 25-SIMF and 43-SIMF samples are near stoichiometric with respect to their O/U, both with compositions close to $UO_{2.03}$ – suggesting that the observed increase in the ~625 cm^{-1} peak between the 25-SIMF and 43-SIMF samples is more likely dominated by proximity to the much larger ~575 cm^{-1} peak, rather than an indication of increased UO_2 oxidation/hyperstoichiometry [38].

4.4.2 532 nm Raman Study of Undoped-UO_2, 25 and 43 GWd/tU SIMFUELs

Figure 4-18 shows the averaged Raman spectra for samples of undoped-UO_2, 25-SIMF and 43-SIMF, acquired using the 532 nm wavelength excitation laser-based Raman microscope according to the methodology described in Chapter 3 Section 3.3. The measurements conducted in this section are simply a repeat of the measurements conducted using the 785 nm wavelength excitation laser-based system in the previous Section 4.4.1.

The 532 nm excitation wavelength is known to induce Raman resonance effects, via multi-phonon scattering on defected and un-defected UO_2. As a result of this effect, the previously absent LO phonon band at ~575 cm^{-1} in undoped-UO_2 is now observable.

Additionally, due to the close proximity in energies of the UO_2 electronic band gap of 2.1 eV and the energy of the 532 nm laser, this also results in a favourable electron band gap resonance effect [136-138]. This phenomenon similarly affects the SIMFUEL to give a more intense peak at ~575 cm^{-1}; the accompanying 2LO phonon at ~1150 cm^{-1} is also substantially enhanced, as seen in the expanded view spectra of Figure 4-19.

Returning to Figure 4-18 we can see that, on average, all three samples appear to have almost equal peak intensities for the fundamental U-O stretch at ~445 cm^{-1} and that the undoped-UO_2 spectra is most easily distinguished from that of the SIMFUELs by its less intense broad defect band between ~500 and ~700 cm^{-1}.

However, closer inspection of the peak at ~445 cm^{-1} indicates that – as with the 785 nm Raman results above – the intensity of this peak does undergo a very

slight decrease in intensity as simulated burn-up is increased. As in Section 4.4.1, this is in accordance with the transition away from a perfect cubic fluorite lattice, towards a defected tetragonal lattice with cuboctahedral clusters, as more lanthanide (III) dopants are introduced to the UO_2 lattice.

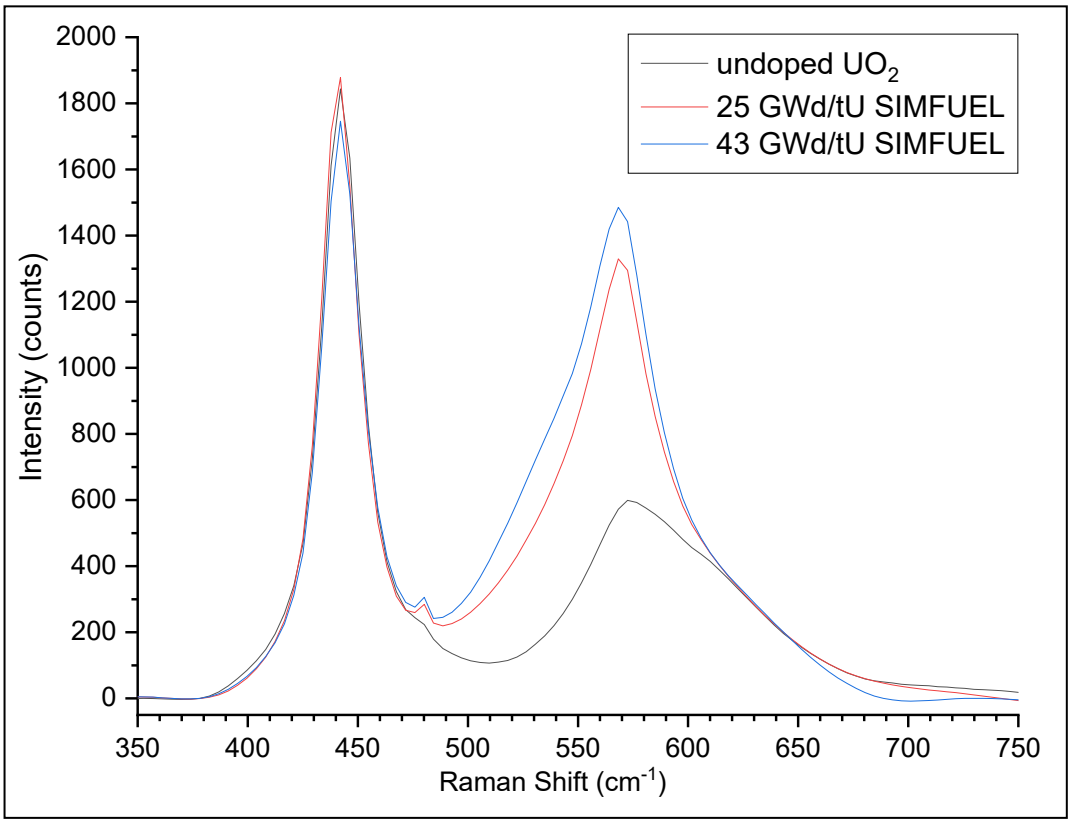

Figure 4-18: Averaged 532 nm μ-Raman spectra recorded from undoped-UO_2, 25 GWd/tU SIMFUEL and 43 GWd/tU SIMFUEL samples between the range of ~350 to ~750 cm^{-1}.

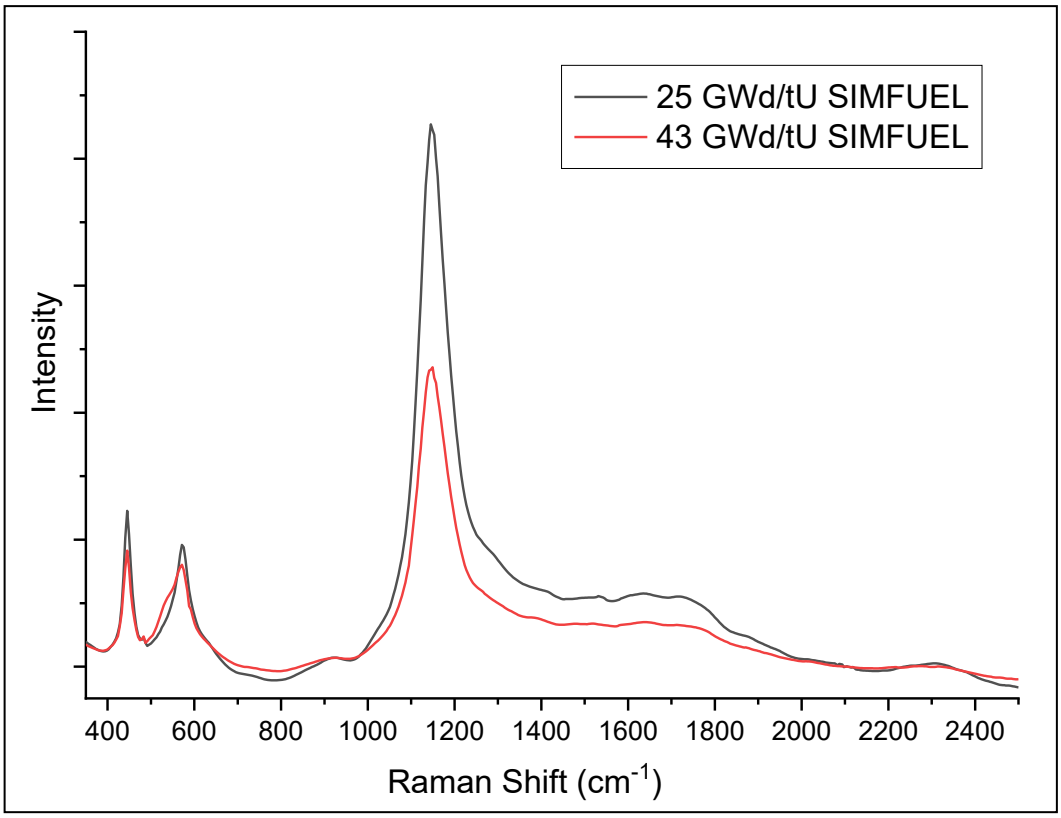

Figure 4-19: 532 nm Raman spectra of 25 and 43 GWd/tU SIMFUEL showing the full recorded Raman range, highlighting the 2LO phonon peaks between ~800 and ~2200 cm^{-1}.

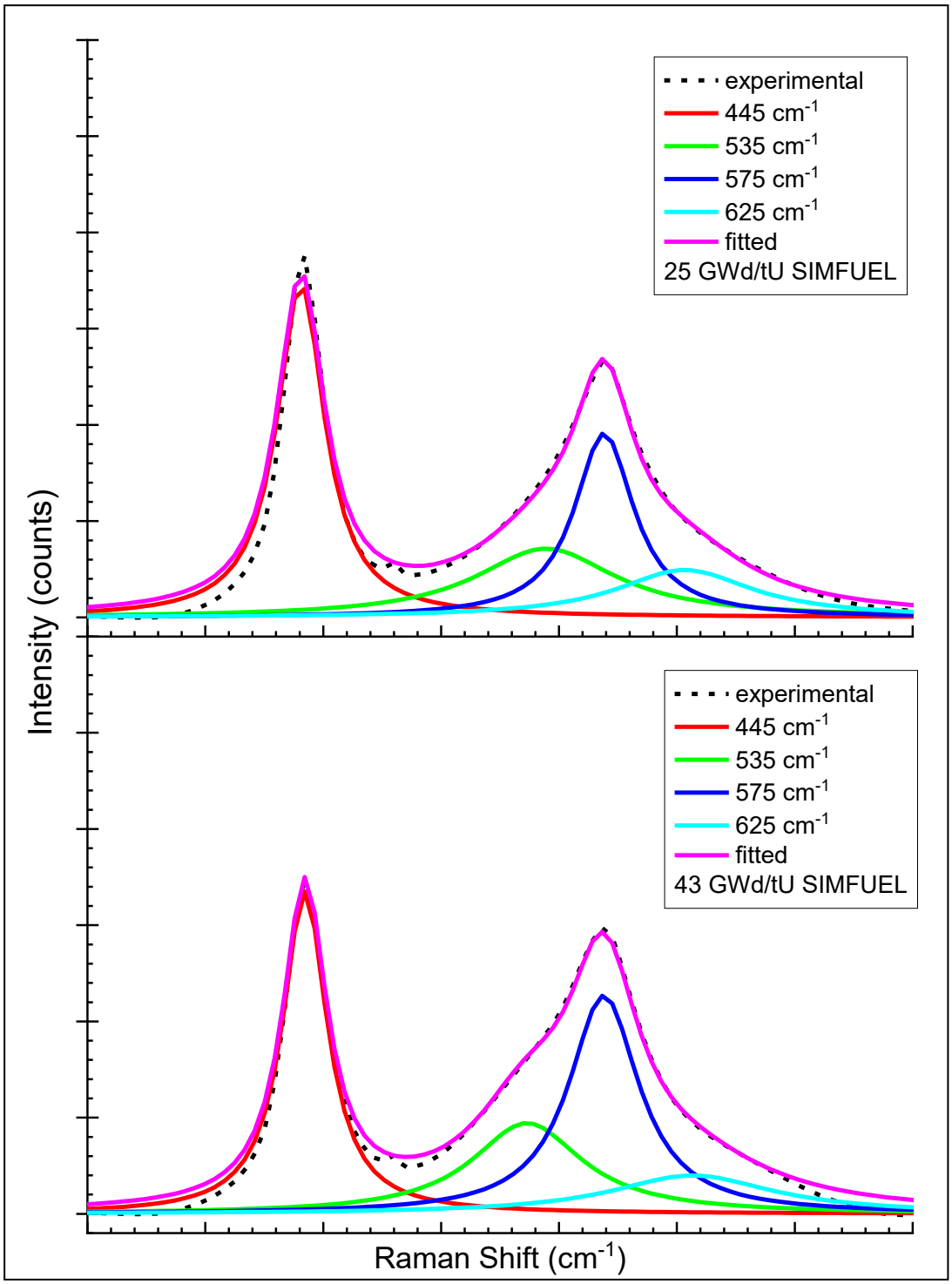

Figure 4-20: Peak fitting of the averaged 532 nm μ-Raman spectra of the 25 GWd/tU SIMFUEL (top) and 43 GWd/tU SIMFUEL (bottom), seen in Figure 4-18.

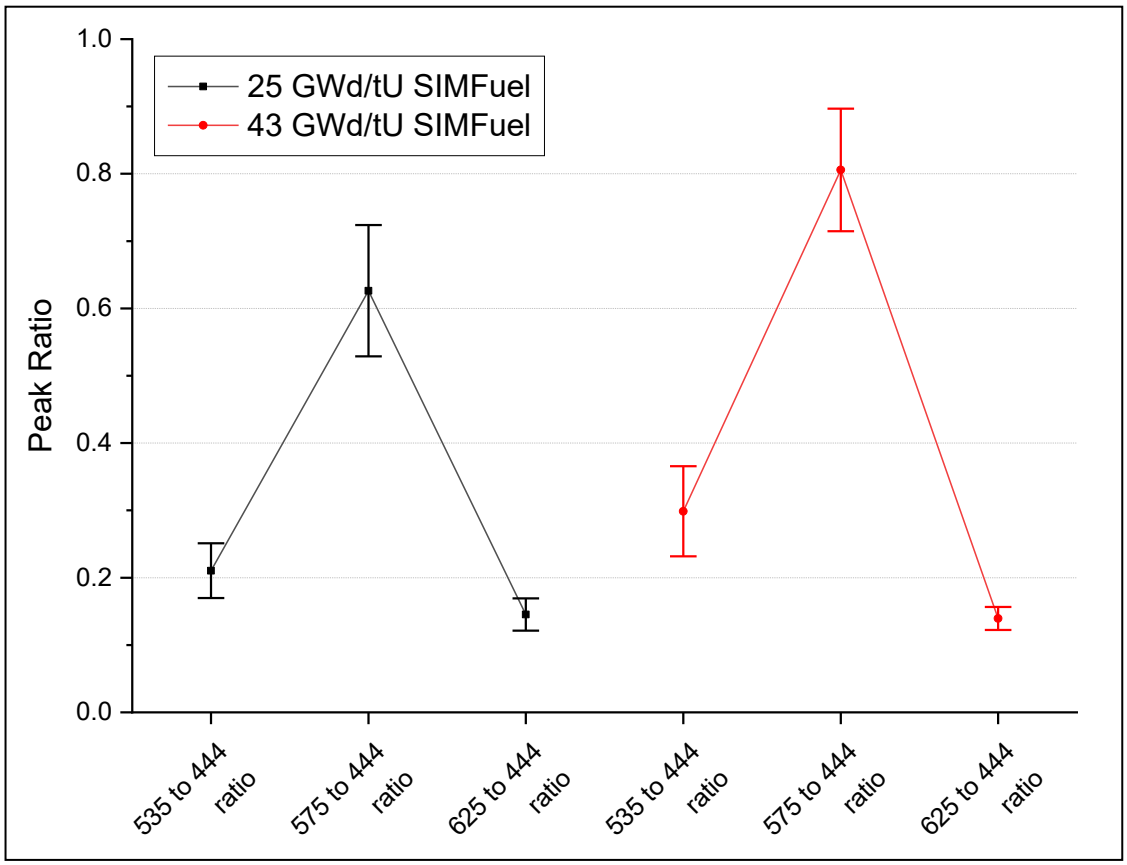

Figure 4-21: Average peak ratios with standard deviations of the three main deconvoluted peak components in the broadband between ~500 and ~700 cm^{-1}, recorded under baseline conditions using 532 nm Raman for 25 and 43 GWd/tU SIMFUEL.

Figure 4-20 shows the data for the 25-SIMF and 43-SIMF samples in Figure 4-18 overlaid with the deconvoluted “defect peaks” between ~500 to ~700 cm^{-1}. Figure 4-21 shows the calculated ratios of “defect band” peak intensities, with respect to the intensity of the peak associated with the fundamental U-O stretch at ~445 cm^{-1}.

From Figure 4-20, we can see that the ~625 cm^{-1} peak in both the SIMFUEL samples are more intense compared to the same peak, as seen in the 785 nm spectra of Figure 4-17. This increase is likely due to its adjacent proximity to the resonantly enhanced ~575 cm^{-1} peak. Also from Figure 4-20, it can be seen that the ~625 cm^{-1} peak intensities are similar in magnitude for both SIMFUEL samples, which could indicate that the stoichiometry across both SIMFUEL sample remains constant irrespective of dopant density – a finding in agreement

with that of Wilbraham et al., who report compositions of $UO_{2.03}$ for both samples (*vide supra*) [38].

Figure 4-20 also shows that the resonantly enhanced LO phonon at ~575 cm^{-1} is the dominant contribution to the broad “defect band”, rather than the ~535 cm^{-1} peak, as seen in the 785 nm spectra of Figure 4-17.

Finally, it is worth pointing out that the presence of the peak at ~630 cm^{-1} in the spectrum for the undoped-UO_2 is expected since its origins are derived from changes in the cubic fluorite lattice via the clustering of oxygen-interstitials, which itself is an indication of the degree of oxidation/hyperstoichiometry – which, as discussed above, Wilbraham et al., found to be low at ~$UO_{2.03}$.

4.4.3 High Lanthanide-doped and High Chromium-doped SIMFUELs

This section presents the μ-Raman spectroscopy study of the 43-hiLn and 43-hiLnCr SIMFUELs. Measurements were conducted using a 785 nm wavelength excitation laser-based μ-Raman spectrometer, according to the same measurement conditions as those used in Section 4.4.1. The results from this study are compared with the results of the standard 43-SIMF Raman study, presented in Section 4.4.1.

Figure 4-22 shows the averaged Raman spectra for samples of 43-hiLn and 43-hiLnCr versus 43-SIMF. Initial interpretations suggest that the introduction of the additional lanthanide dopants markedly increases the intensity of the “defect band” between ~500 to ~700 cm^{-1}, relative to the peak associated with the fundamental U-O stretch at ~445 cm^{-1}.

These observations further indicate the phenomenon of lattice distortion due to increased dopant incorporation, resulting in the transition away from a perfect cubic fluorite lattice towards a defected and distorted lattice.

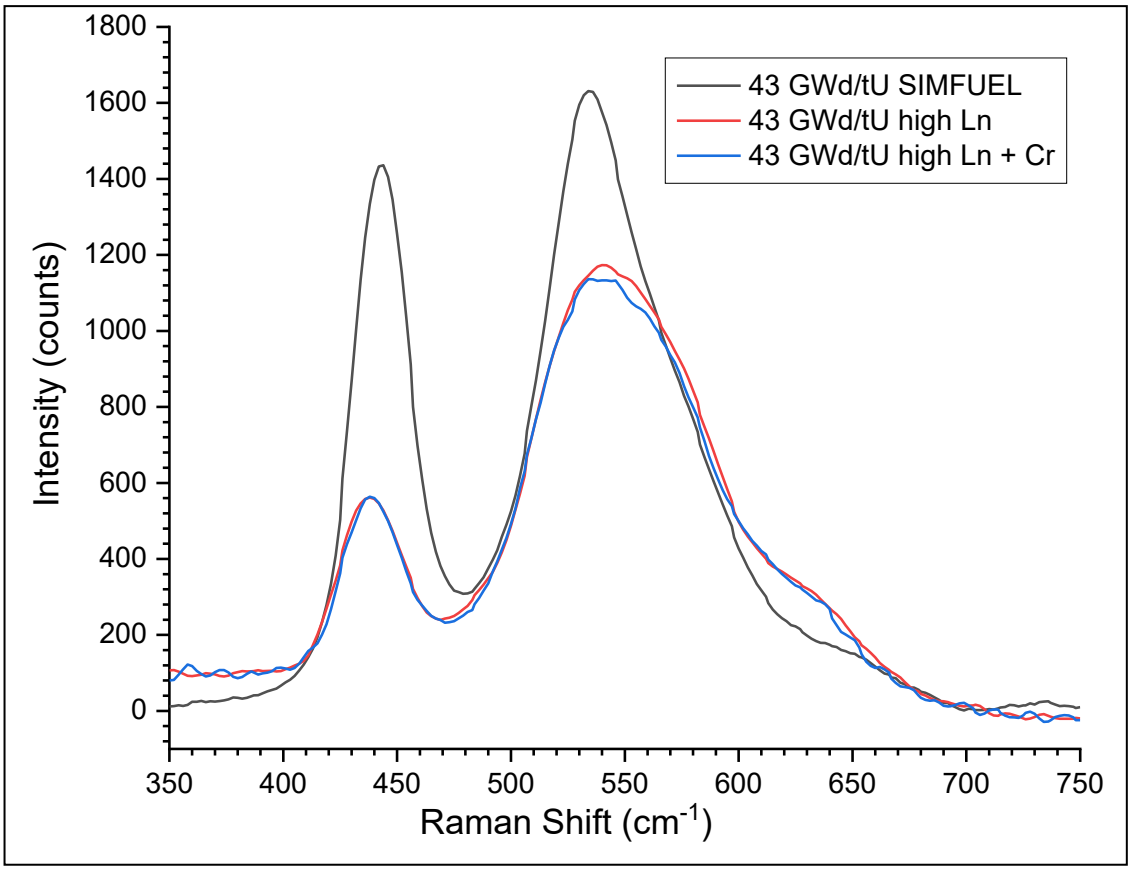

Figure 4-22: Averaged 785 nm μ-Raman spectra recorded from 43 GWd/tU, 43-hiLn and 43-hiLnCr SIMFUEL samples between the range of ~350 to ~750 cm^{-1}.

Figure 4-23 shows deconvolution as above of the "defect band" for the 43-hiLn and 43-hiLnCr samples and represents the deconvoluted spectrum of the 43-SIMF sample from Figure 4-16 for comparison. This reveals how the intensity of the three main contributing peaks varies as the dopant content is changed.

Similar to the standard 43-SIMF spectra represented from Figure 4-16, the ~535 cm^{-1} peak for the 43-hiLn and 43-hiLnCr samples exhibits the largest peak intensity, followed by the ~575 cm^{-1} and then ~625 cm^{-1}. As both the ~535 cm^{-1} and ~575 cm^{-1} peaks are associated with dopant incorporation, the growth in size, seen in both 43-hiLn and 43-hiLnCr, is expected.

The observed increase in relative intensity of the ~625 cm^{-1} peak in going from the 43-SIMF to 43-hiLn/43-hiLnCr is much more noticeable than the corresponding increase in the other two contributions at ~575 cm^{-1} and ~535 cm^{-1}. This observation most likely suggests that these high lanthanide/Cr-doped SIMFUELs are slightly more hyperstoichiometric than the standard 43 GWd/tU

SIMFUEL, the latter having a stoichiometry of ~$UO_{2.03}$ as reported by Wilbraham et al. [38].

The origin of this enhanced hyperstoichiometry is, however, unclear – although it may be related to the greater grain boundary density seen in the 43-hiLn and 43-hiLnCr samples compared to the 43-SIMF sample (see SEM images of Figure 4-3 and Figure 4-4 compared with Figure 4-2) – and should be the subject of future work.

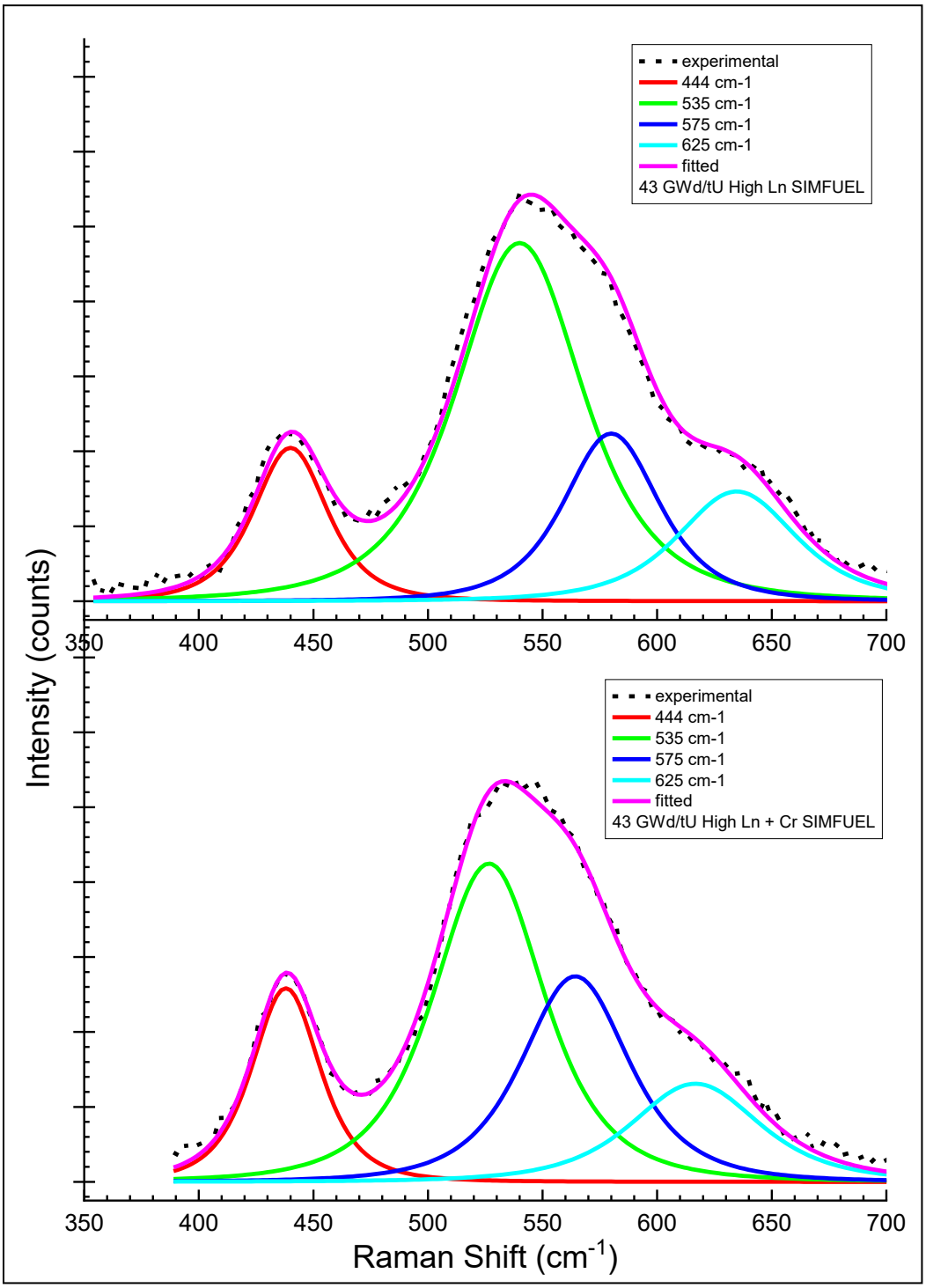

Figure 4-23: Peak fitting of the averaged 785 nm μ-Raman spectra of the 43 GWd/tU high Ln SIMFUEL (top) and 43 GWd/tU high Ln + Cr SIMFUEL (bottom).

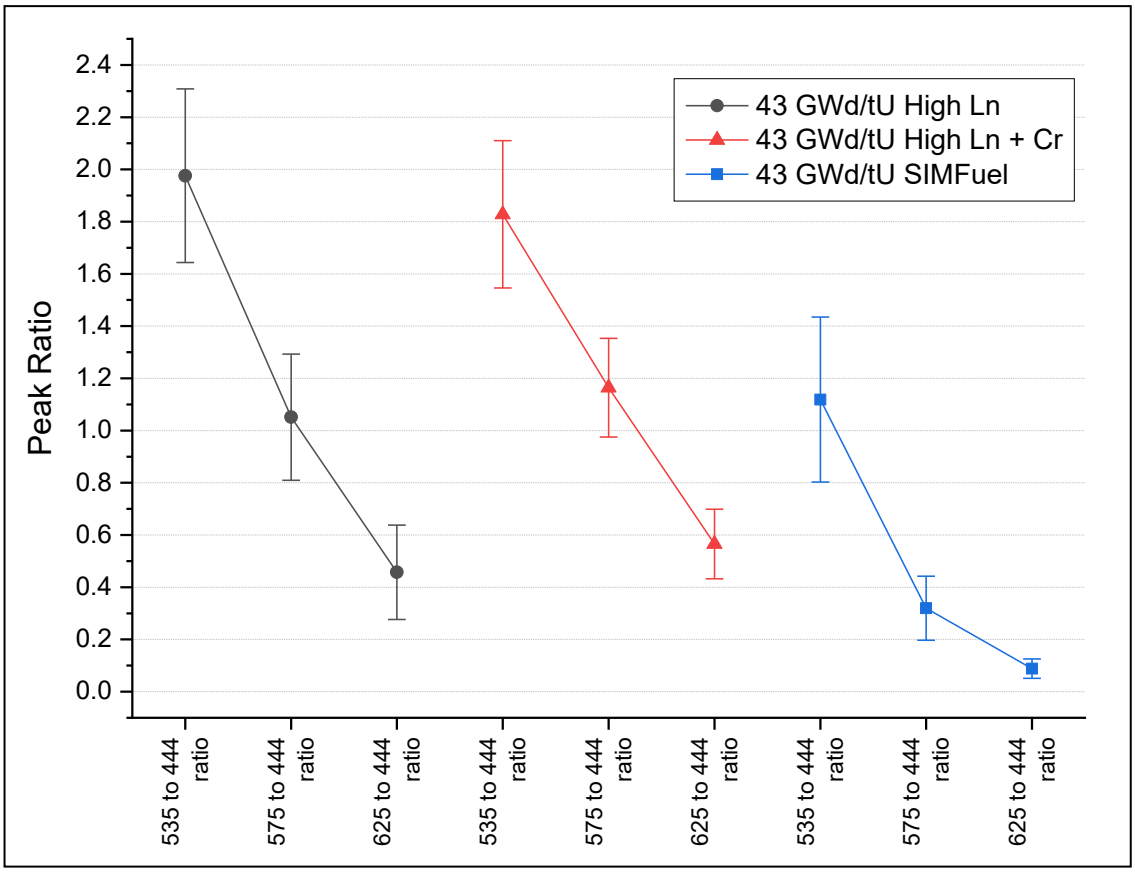

Figure 4-24: Average peak ratios with standard deviations of the three main deconvoluted peak components in the broadband between ~500 and ~700 cm^{-1}, recorded under baseline conditions using 785 nm Raman for 43 GWd/tU SIMFUEL, 43-hiLn and 43-hiLnCr.

The remainder of the thesis will not include further discussions or studies involving the 43-hiLn and 43-hiLnCr materials that were reviewed in this section. The subsequent chapters and studies will only present results and discussions of the materials that are relevant to the study of the real AGR SNF system and scenarios. Therefore, the 43-hiLn and 43-hiLnCr SIMFUEL voltammetry studies presented in Section 4.3.2 and the μ-Raman spectroscopy study presented here in this section will serve as additional supporting information.

Having now discussed the μ-Raman spectroscopy study of the undoped-UO_2 and AGR SIMFUELs, the next section presents the electrochemical study of the 25 GWd/tU SIMFUEL and 20/25/Nb stainless steel AGR cladding, conducted under electrolyte conditions relevant to the UK's AGR pond storage conditions.

4.5 Baseline Electrochemical Study in AGR Pond Storage Conditions

This section presents the electrochemical study of the 25 GWd/tU SIMFUEL and 20/25/Nb stainless steel AGR cladding, conducted under electrolyte conditions relevant to the UK's AGR pond storage conditions, specifically in Simplified Simulant Pond Water electrolyte solutions containing 30 μmol/dm^3 NaCl at pH 8, 11.4 and 12.5, as described in Chapter 3 Section 3.1.1.

In addition to these pond water simulant-based electrolytes, measurements were also conducted in NaCl solutions containing increasing concentrations of chloride from 0.1 to 100 mmol/dm^3, also at pH 8, 11.4 and 12.5. These measurements were only conducted on the lower simulated burn-up SIMFUEL sample, 25 GWd/tU SIMFUEL, due to its closer similarity in simulated burn-up to the real AGR SNF samples to be studied later in this thesis (Chapter 6 below). They are therefore expected to exhibit the greatest similarity to those conducted on the real AGR SNF samples (see Chapter 3 Section 3.1.3 above and Chapter 6 below).

Thus, OCP, LSV and EIS measurements were conducted to study the effects of chloride concentration on the corrosion behaviour of separate, i.e., not coupled, 25 GWd/tU SIMFUEL and 20/25/Nb AGR cladding samples. These results will serve as the reference baseline data for comparison with and thus, understanding the corrosion behaviour of both the coupled cladding-SIMFUEL electrode studies of Chapter 5 and the legacy AGR SNF studies of Chapter 6.

4.5.1 25 GWd/tU SIMFUEL

This section presents the electrochemical studies of the 25 GWd/tU SIMFUEL sample. The same methods and conditions for the measurements reported here are subsequently used for the electrochemical studies presented later in Chapter 5 and Chapter 6. This was so that the data reported in this chapter could be readily used as comparison reference baseline data in the interpretation of the data in Chapter 5 and Chapter 6.

Section 4.5.1.1 presents the electrochemical studies of the 25 GWd/tU SIMFUEL in SSPW solutions and Section 4.5.1.2 presents analogous studies in NaCl solutions.

As described above, the main electrochemical techniques employed here are those of OCP, LSV and EIS measurements. OCPs were recorded over a 15-hour period. LSV measurements were recorded between a potential range of -0.8 to 0.8 V at a potential scan rate of 1 mV/s. EIS measurements were conducted in accordance with the general method described in Chapter 3 Section 3.2.7 and conducted at 0.1 V intervals from -0.7 to 0.3 V.

Typically, cyclic voltammetric techniques are widely employed for the electrochemical studies of such UO_2-based materials. However, the data collected from the real AGR SNF studies of Chapter 6 was restricted to that obtainable from linear sweep voltammetry due to the experimental/practical difficulties encountered when recording such data from real AGR SNF samples. Thus, the SIMFUEL baseline/reference experiments reported in this chapter were similarly restricted to LSV-based analyses.

4.5.1.1 25 GWd/tU SIMFUEL in Simplified Simulant Pond Water

Here we present the electrochemical studies of 25-SIMF in SSPW solutions at pH 8, 11.4 and 12.5, using LSV, OCP and EIS measurements. Figure 4-25-(**Top**) shows the polarisation curves for the 25-SIMF, recorded in SSPW electrolyte, containing of 30 μmol/dm^3 NaCl at pH 8, 11.4 and 12.5. Figure 4 26-(**Bottom**) shows the polarisations curves excerpted from Figure 4-7 to allow for direct visualisation/comparison with Figure 4-25-(**Top**).

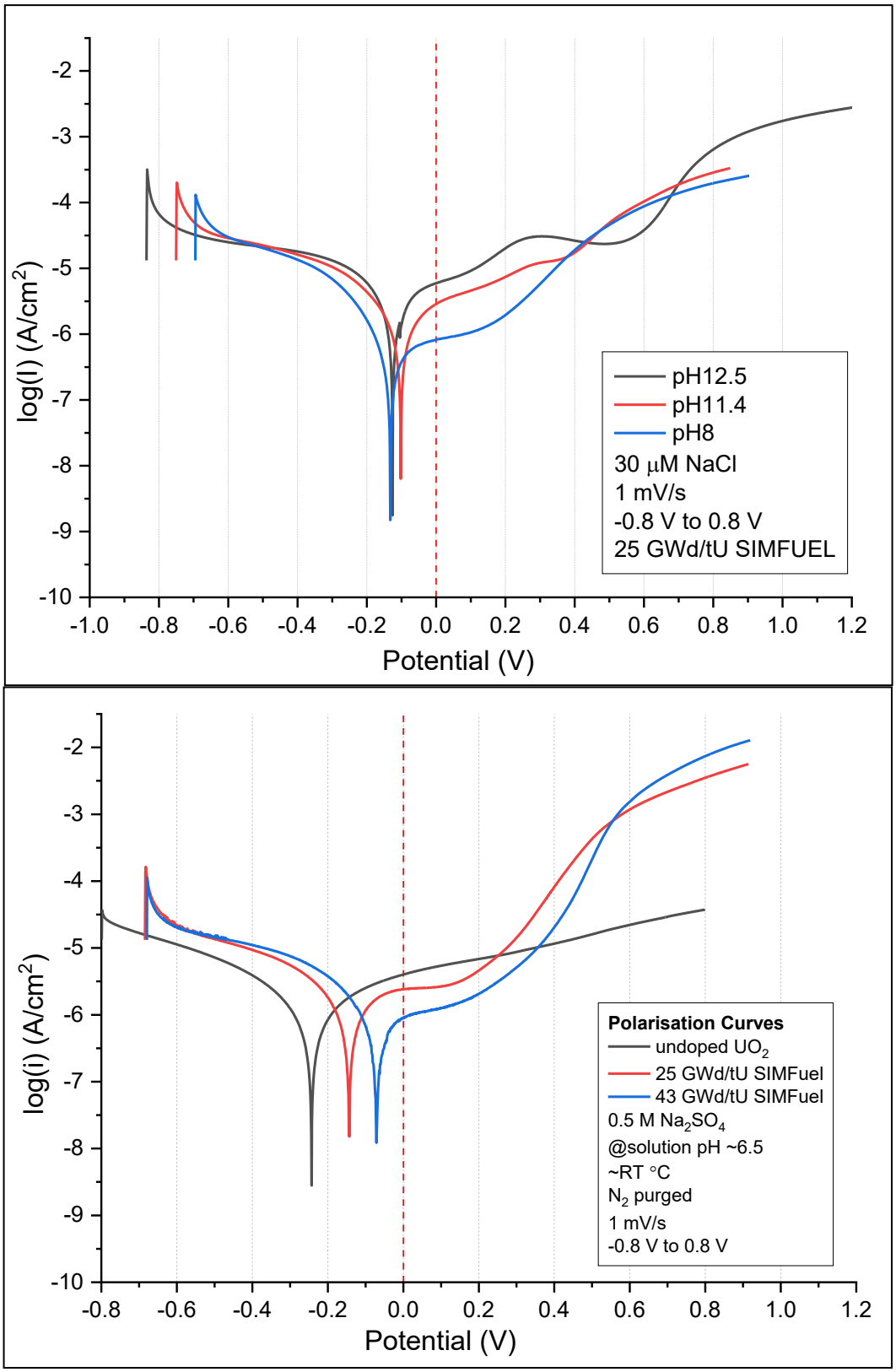

Figure 4-25: (**Top**) Polarisation curves obtained from LSV measurements of 25 GWd/tU SIMFUEL in SSPW at pH 8, 11.4 and 12.5. (**Bottom**) Taken from Figure 4-7, showing polarisation curves for (i) undoped-UO_2, (ii) 25 GWd/tU SIMFUEL and (iii) 43 GWd/tU SIMFUEL, measured in 0.5 mol/dm^3 Na_2SO_4 electrolyte at ~pH 6.5.

Similar to the polarisation curves of Figure 4-7 recorded in 0.5 mol/dm^3 Na_2SO_4 of Section 4.3.1, the general form of the polarisation curves can be described as follows:

- For the region of potentials negative of the PZC, the high current density cathodic slope is a result of the hydrogen evolution reaction from the reduction of water.
- For the region of potentials positive of the PZC, the observed anodic currents may be attributed to a series of different oxidation processes taking place on the surface of the 25-SIMF.

By analogy with the data of Figure 4-7, recorded at the lower pH of ~6.5 and allowing for the higher pHs used in Figure 4-25-(**Top**), the processes can be listed in order of increasing positive potential as follows [81]:

- Immediately positive of the PZC, the current may be attributed to the onset of oxidation of UO_{2+x} to $UO_{2.33}$ in the grain boundaries. The effective overall equation describing this process is as follows:

$$2(0.33 - x)\, OH^- + UO_{2+x} \rightarrow UO_{2.33} + (0.33 - x)\, H_2O + 2(0.33 - x)\, e^-$$

Equation 4-1

- Positive of the potential region associated with the process effectively described by Equation 4-1, the current can be attributed to the onset of oxidation of bulk UO_2 to UO_{2+x} in the grains via the incorporation of oxygen interstitials into the UO_2 matrix. The effective overall equation describing this process is as follows:

$$2x\, OH^- + UO_2 \rightarrow UO_{2+x} + x\, H_2O + 2x\, e^-$$

Equation 4-2

- Positive of the potential region associated with the process effectively described by Equation 4-2, the current is attributed to the onset of oxidation of UO_{2+x} to U(VI) species. In the case of the data of Figure 4-7, recorded at ~pH 6.5, this resulted in the formation of aqueous uranyl ions. The effective overall equation describing this process is as follows:

$$2x\, H^+ + UO_{2+x} \rightarrow UO_2^{2+} + x\, H_2O + 2(1 - x)\, e^-$$

Equation 4-3

- At the higher pHs used here, some U(VI) oxide/oxyhydroxide phase formation may be expected.

The exact potential ranges over which Equation 4-1 to Equation 4-3 obtain depend upon pH. Given the effective forms of Equation 4-1 to Equation 4-2, the potentials at which they obtain may be expected to move in a negative direction with increasing pH i.e., the oxidation becomes easier from a thermodynamic perspective.

In contrast, and given its overall form, the potentials at which Equation 4-3 obtains may be expected to move to more positive values with increasing pH i.e., the oxidation becomes more difficult from a thermodynamic perspective. The exact ranges at which each oxidation process occurs are given below:

- At pH 8, Equation 4-2 occurs at ~ 0.1 – 0.2 V and gradually moves towards the negative direction with increasing pH. Whereas Equation 4-3 occurs at ~ 0.3 V and gradually moves towards the positive direction with increasing pH.
- At pH 11.4, Equation 4-2 occurs at ~ 0 V – 0.1 V and Equation 4-3 occurs at ~ 0.5 V.
- At pH 12.5, Equation 4-2 occurs at ~ - 0.1 V – 0.1 V and Equation 4-3 occurs at ~ 0.6 V.

The main difference between these two plots is the suppressed current densities of the SSPW data compared to the Na_2SO_4 data, across the full potential sweep range. This is likely due to a combination of the lower pH and the complexation of dissolved U(VI) with SO_4^{2-} ions to form soluble UO_2SO_4 and $UO_2(SO_4)_2^{2-}$ complexes, the case of the latter experiments [139].

The OCP plots in Figure 4-26 are also affected by pH like that seen in the polarisation curves of Figure 4-25. As pH increases, the OCPs become more negative, a general trend also observed in literature studies on SIMFUELs under similar conditions [124].

Comparing the OCP values with their respective polarisation curves in Figure 4-25, shows that increasing the pH shifts the equilibrium corrosion potential

more negative, away from the onset of in-grain oxidation and towards grain-boundary oxidation, thus further driving the corrosion potential further away from UO_2 dissolution. Therefore, under OCP conditions in moderate to high alkalinity and low chloride electrolytes, the 25-SIMF is unlikely to experience significant corrosion or dissolution.

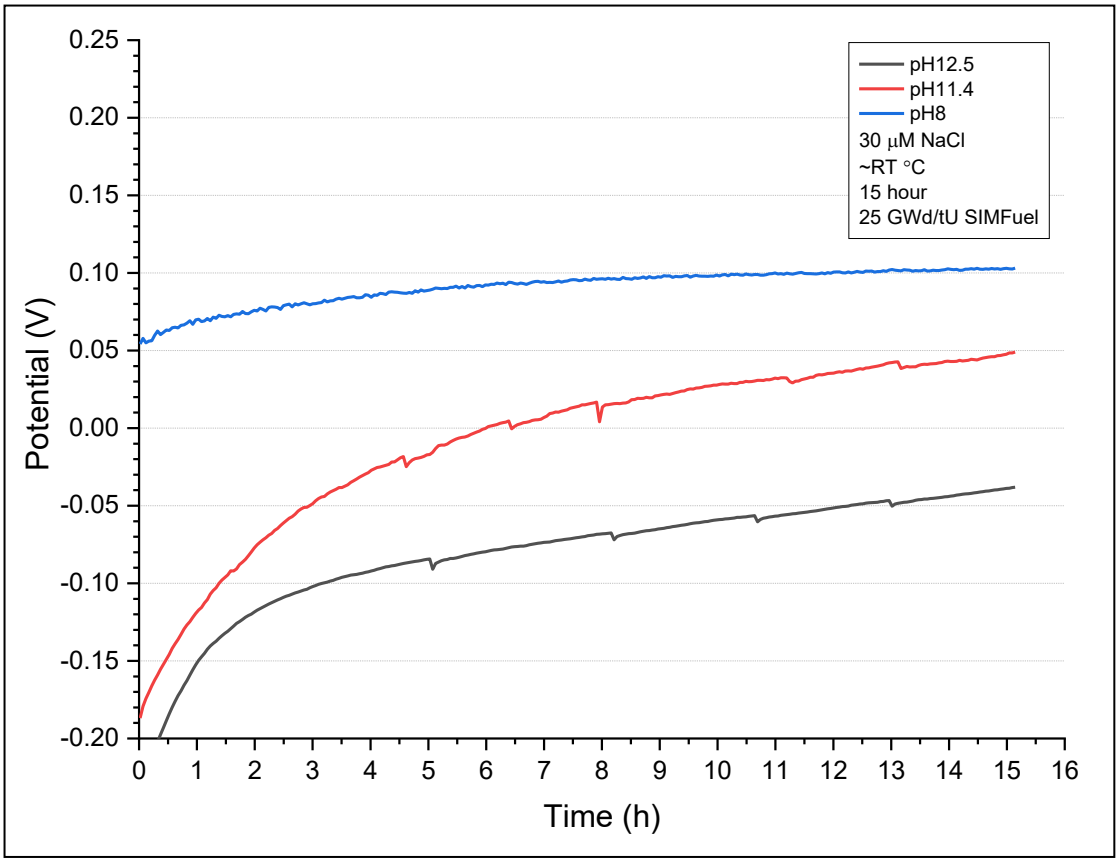

Figure 4-26: Plots of open circuit potentials vs. time of 25 GWd/tU SIMFUEL in SSPW at pH 8, 11.4 and 12.5.

Next, we present the results of electrochemical impedance spectroscopy (EIS) studies of 25-SIMF samples in SSPW solutions at pH 8, 11.4 and 12.5.

Figure 4-27, Figure 4-28, and Figure 4-29 show examples of Nyquist plots and Bode plots obtained from such studies at 100 mV intervals over a potential range of -0.7 to +0.3 V vs. Ag/AgCl. Each figure shows example plots recorded at approximately -0.5, -0.1 and +0.2 V for each pH studied. These figures are intended to convey the general shape and form of the Nyquist and Bode plots to allow qualitative comparison between plots at different potentials.

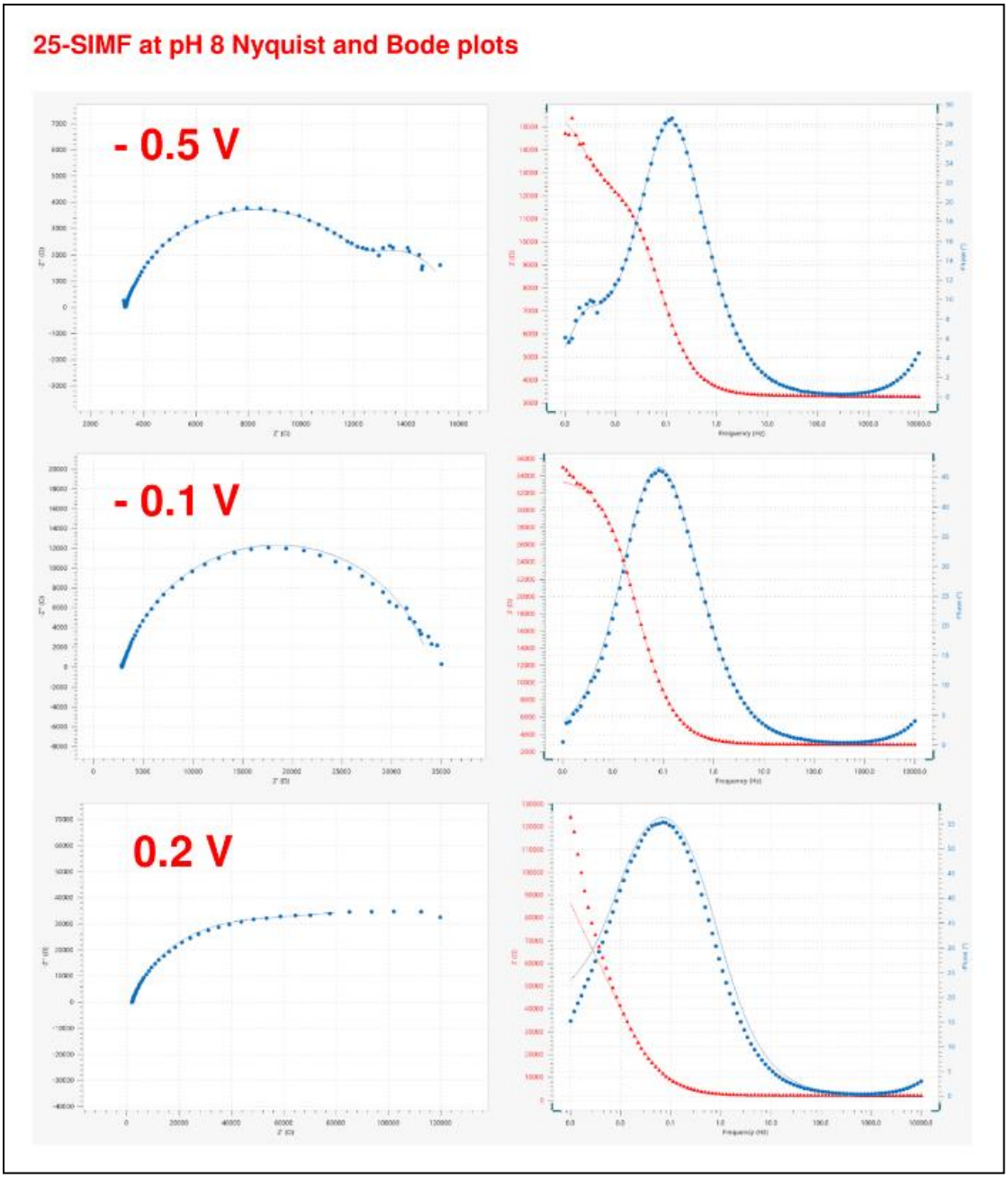

Figure 4-27: Examples of Nyquist and Bode plots generated from EIS circuit fitting of 25 GWd/tU SIMFUEL in 30 μM NaCl at pH 8 to show the general shape and form of the plots relatively to each other at different potentials.

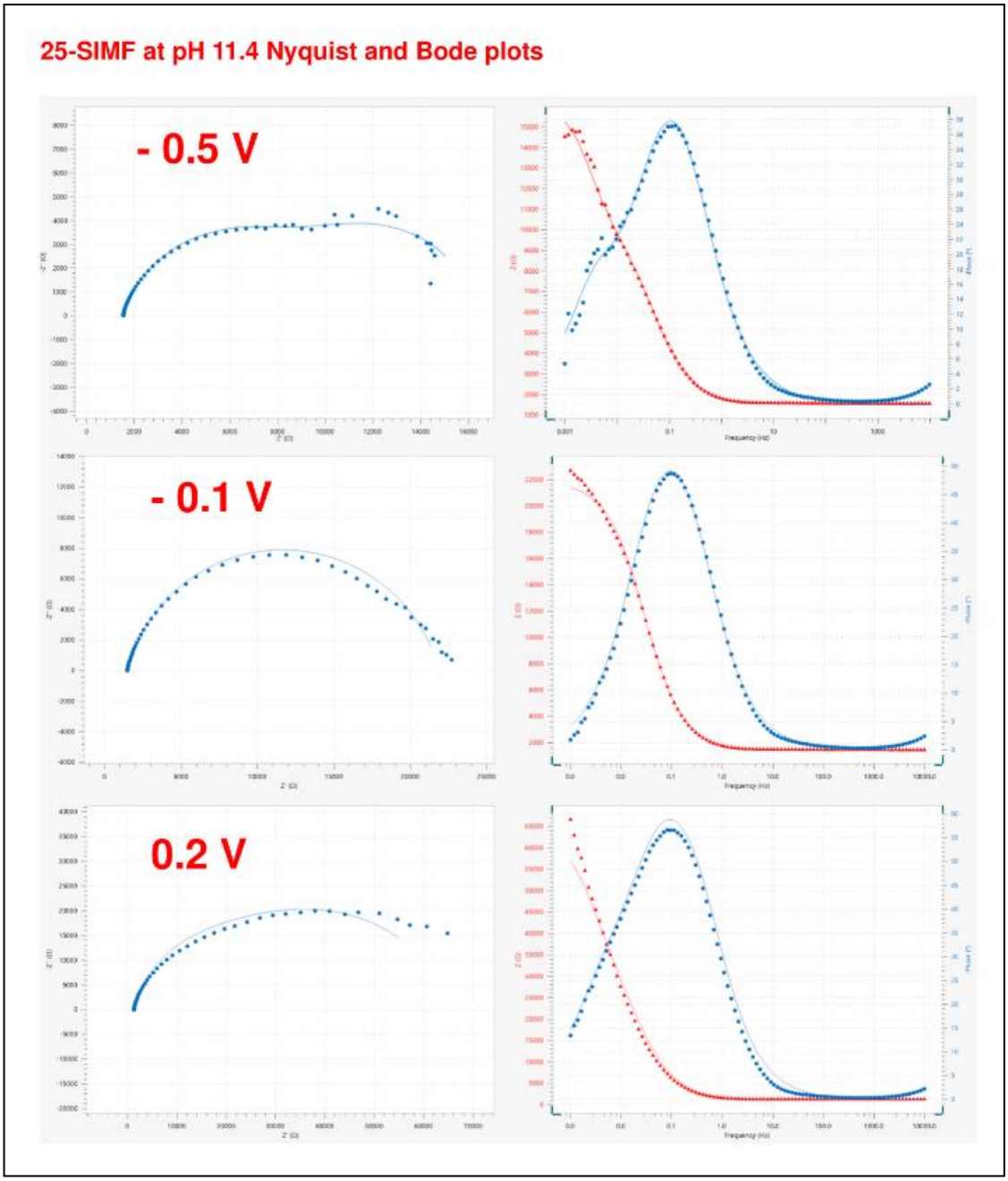

Figure 4-28: Examples of Nyquist and Bode plots generated from EIS circuit fitting of 25 GWd/tU SIMFUEL in 30 μM NaCl at pH 11.4 to show the general shape and form of the plots relatively to each other at different potentials.

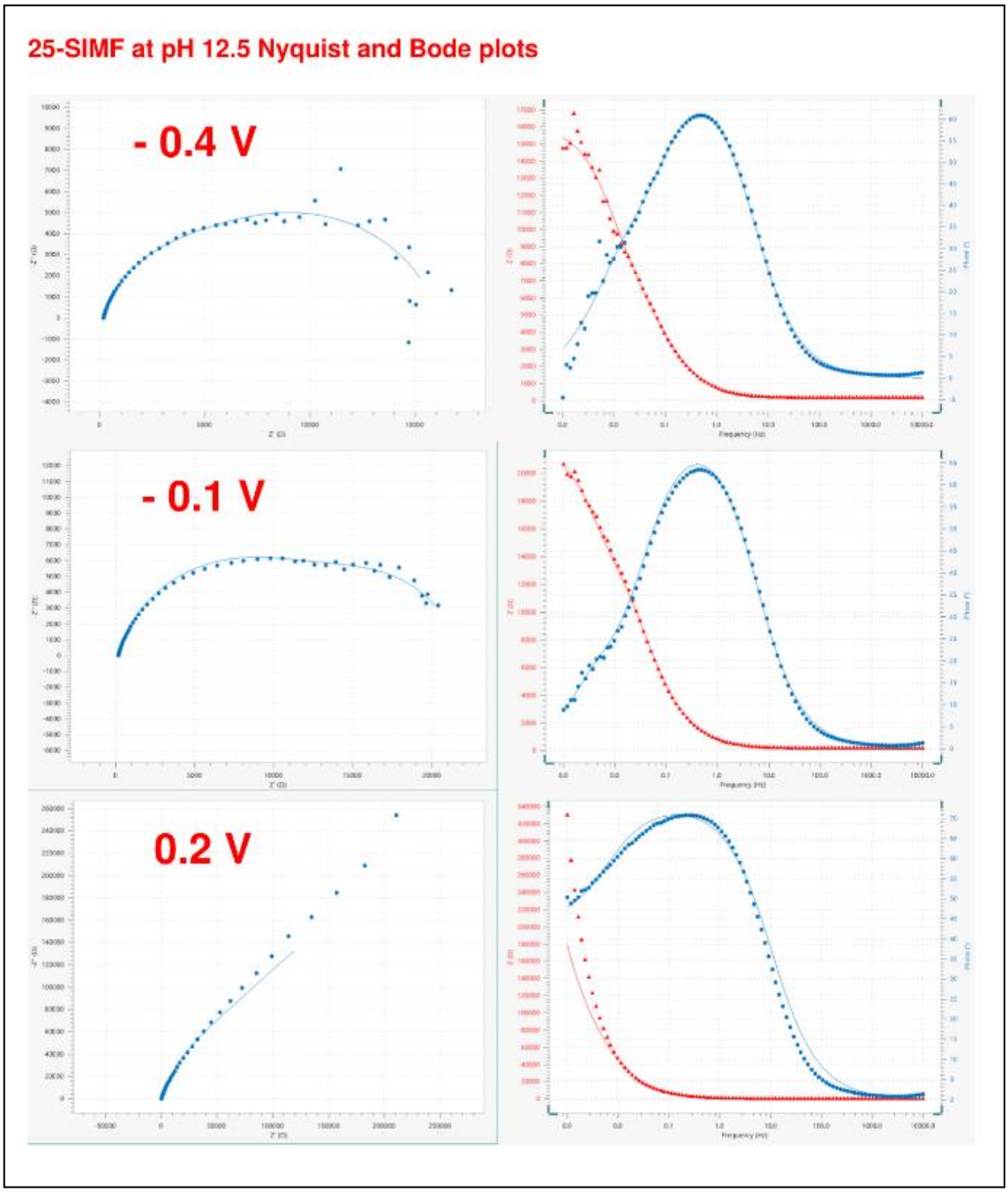

Figure 4-29: Examples of Nyquist and Bode plots generated from EIS circuit fitting of 25 GWd/tU SIMFUEL in 30 μM NaCl at pH 12.5 to show the general shape and form of the plots relatively to each other at different potentials.

As can be seen especially from the Nyquist and Bode plots obtained at an applied potential of -0.5 V, the responses are characterised by two time constants associated with high and low frequency responses – most especially evidenced by the presence of two semicircles in the Nyquist plots.

Thus, following the approach of Antozzi et al., we have, in the first instance, modelled these responses using two Randles circuits in series with a resistor

component [140]. The equivalent circuit is shown in Figure 4-30, with one Randles circuit modelling the low-frequency components of the EIS data, one modelling the high-frequency component whilst the series resistor includes contributions from, *inter alia*, the solution and contact resistances in the usual way.

The circuit components in each EEC are labelled accordingly in Figure 4-30, with respect to their equivalent assigned electrochemical process. The low frequency (LF) component can be modelled differently, either as LF-a or LF-b, depending on its electrochemical assignment as a function of applied potential. Justifications for the choice of EEC components used are presented later in this section.

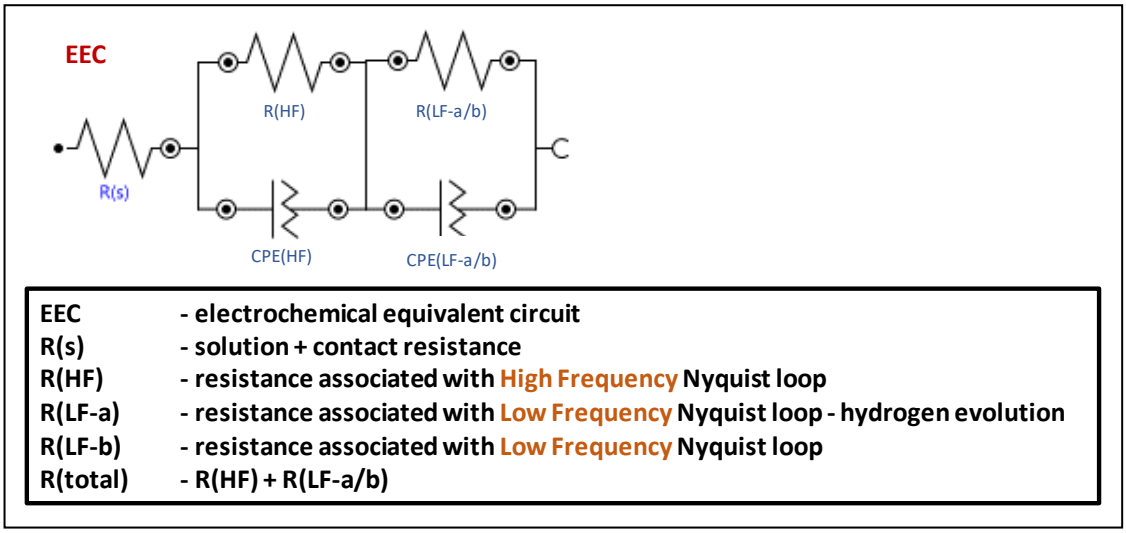

Figure 4-30: Electrochemical equivalent circuit used for EIS circuit fitting of 25 GWd/tU SIMFUEL in 30 μM NaCl at pH 8, 11.4 and 12.5.

Table 4-2 shows the fitted resistance values and Table 4-3 shows the fitted effective capacitance (C_{eff}) values, obtained from electrochemical equivalent circuit (EEC) fitting of the measured EIS data for 25-SIMF in the SSPW electrolyte at pH 8, 11.4 and 12.5.

Measurement parameters for EIS data acquisition follow the standard method detailed in Chapter 3 Section 3.2.7. The fitted values were generated using the EEC of Figure 4-30.

RESISTANCE - 25 GWd/tU SIMFUEL in 30 µmol/dm³ NaCl

Potential	EEC	R(s)	R(HF)	R(LF-b)	R(LF-a)	R(total)	EEC	R(s)	R(HF)	R(LF-b)	R(LF-a)	R(total)	EEC	R(s)	R(HF)	R(LF-b)	R(LF-a)	R(total)
V	a/b	kΩ	kΩ	kΩ	kΩ	kΩ	a/b	kΩ	kΩ	kΩ	kΩ	kΩ	a/b	kΩ	kΩ	kΩ	kΩ	kΩ
	pH8	pH8	pH8	pH8	pH8	pH8	pH11.4	pH11.4	pH11.4	pH11.4	pH11.4	pH11.4	pH12.5	pH12.5	pH12.5	pH12.5	pH12.5	pH12.5
-0.7	a	4.05	8.87	/	127.00	135.87	a	1.62	4.74	/	18.10	22.84	/	/	/	/	/	/
-0.6	a	3.58	7.67	/	9.37	17.04	a	1.61	2.78	/	15.90	18.68	/	/	/	/	/	/
-0.5	a	3.30	9.49	/	2.94	12.43	a	1.55	8.08	/	6.71	14.79	/	/	/	/	/	/
-0.4	a	3.06	14.80	/	1.09	15.89	a	1.49	11.80	/	3.82	15.62	a	0.172	4.17	/	11.80	15.97
-0.3	a	2.81	30.30	/	0.78	31.08	a	1.47	18.30	/	2.12	20.42	a	0.172	13.10	/	8.36	21.46
-0.2	a	2.29	120.00	/	0.31	120.31	a	1.41	48.00	/	3.32	51.32	a	0.170	23.50	/	9.50	33.00
-0.1	b	2.42	54.00	392.00	/	446.00	b	1.34	65.00	80.00	/	145.00	b	0.168	33.10	73.10	/	106.20
0	b	2.64	220.00	610.00	/	830.00	b	1.31	129.00	253.00	/	382.00	b	0.170	30.00	206.00	/	236.00
0.1	b	2.10	94.40	264.00	/	358.40	b	1.27	80.00	203.00	/	283.00	b	0.164	91.40	461.00	/	552.40
0.2	b	1.73	58.50	88.00	/	146.50	b	1.27	17.00	47.40	/	64.40	b	0.180	72.00	254.00	/	326.00
0.3							b	1.24	19.30	2.06	/	21.36						

EEC - electrochemical equivalent circuit
R(s) - solution + contact resistance
R(HF) - resistance associated with High Frequency Nyquist loop
R(LF-a) - resistance associated with Low Frequency Nyquist loop - hydrogen evolution
R(LF-b) - resistance associated with Low Frequency Nyquist loop
R(total) - R(HF) + R(LF-a/b)

Table 4-2: Table of fitted resistances from EIS circuit fitting of 25 GWd/tU SIMFUEL in 30 µM NaCl at pH 8, 11.4 and 12.5.

CAPACITANCE - 25 GWd/tU SIMFUEL in 30 µmol/dm³ NaCl

Potential	EEC	CPE(HF)	CPE(LF-b)	CPE(LF-a)	EEC	CPE(HF)	CPE(LF-b)	CPE(LF-a)	EEC	CPE(HF)	CPE(LF-b)	CPE(LF-a)
V	a/b	F	F	F	a/b	F	F	F	a/b	F	F	F
	pH8	pH8	pH8	pH8	pH11.4	pH11.4	pH11.4	pH11.4	pH12.5	pH12.5	pH12.5	pH12.5
-0.7	a	6.78E-04	/	3.99E-02	a	7.16E-04	/	2.86E-03	/	/	/	/
-0.6	a	4.01E-04	/	3.04E-02	a	6.35E-04	/	1.88E-03	/	/	/	/
-0.5	a	2.99E-04	/	2.62E-02	a	5.30E-04	/	8.76E-03	/	/	/	/
-0.4	a	2.62E-04	/	7.82E-02	a	4.46E-04	/	1.80E-02	a	5.57E-04	/	1.59E-03
-0.3	a	2.63E-04	/	2.02E-03	a	4.34E-04	/	6.65E-03	a	3.85E-04	/	6.18E-03
-0.2	a	2.98E-04	/	2.90E-08	a	4.98E-04	/	4.70E-03	a	3.60E-04	/	8.37E-03
-0.1	b	2.94E-03	4.38E-04	/	b	6.54E-04	2.10E-03	/	b	6.59E-04	1.18E-03	/
0	b	3.01E-04	6.50E-04	/	b	9.66E-04	1.86E-03	/	b	6.39E-04	8.60E-04	/
0.1	b	3.40E-04	9.62E-04	/	b	1.24E-03	1.58E-03	/	b	5.69E-04	1.45E-03	/
0.2	b	3.70E-04	4.50E-03	/	b	4.45E-04	1.18E-03	/	b	4.24E-04	1.32E-03	/
0.3	/				b	3.94E-04	1.01E-03	/	/			

EEC - electrochemical equivalent circuit
CPE(HF) - capacitance associated with High Frequency Nyquist loop
CPE(LF-a) - capacitance associated with Low Frequency Nyquist loop - hydrogen evolution
CPE(LF-b) - capacitance associated with Low Frequency Nyquist loop

Table 4-3: Table of fitted capacitance from EIS circuit fitting of 25 GWd/tU SIMFUEL in 30 µM NaCl at pH 8, 11.4 and 12.5.

The impedance of a CPE component, Z_{CPE}, can be expressed as Equation 4-4, where ω is the angular frequency, j is equal to $\sqrt{-1}$, Y_0 is the value of the fitted CPE component from the chosen equivalent circuit, with units of $S \cdot s^N$ (Siemens-seconds-to-the-power-N), and N is an exponent function associated with constant phase elements, with values of $0 < N < 1$.

Typically, when N = 0, it can be described an ideal resistor and when N = 1, the CPE can be described as an ideal capacitor with Y_0 being equivalent to the capacitance [141, 142].

$$Z_{CPE} = \frac{1}{Y_0(j\omega)^N}$$

Equation 4-4

Effective capacitance, C_{eff} values were calculated using Equation 4-5 [143-145], where R is the fitted resistance value of the parallel resistor component. Caution must be noted for the application of Equation 4-5 to account for its limits of applicability, bound by 0 < N < 1.

$$C_{eff} = \frac{(Y_0 \cdot R)^{\frac{1}{N}}}{R}$$

Equation 4-5

The values of N used for these fits were in the range of 0.7 ≤ N < 1, suggesting that detailed quantitative interpretation of some of the capacitance values determined from the CPE data here should be treated with caution.

However, since our focus below will be on the resistance data, with the capacitance/CPE data to be used only as an indicative guide in the interpretation of that data, we do not foresee that this will be a problem.

Other methods and equations for determining C_{eff} can be found in the literature of: Westing et al., [146], Hsu and Mansfield [147], and Byoung-Yong Chang [148].

Similar EECs have been used and reported in literature for the fitting of EIS measurements of UO_2-based materials. These typical two Randles EECs allow for the investigation of high and low frequency domains of the EIS data [149]. Justifications for the choice of EEC circuit component assignments are described in further detail as follows:

- R(HF) is a resistance associated with the high-frequency Nyquist loop and can be assigned to resistances associated with solid-state behaviours such as the electronic properties of the bulk electrode.

- R(LF) is a resistance associated with the low-frequency Nyquist loop. In this instance, R(LF) can be assigned to different processes depending on the potential applied to the electrochemical system:
    - R(LF-a) can be assigned to a charge transfer resistance from the hydrogen evolution process taking place at the electrode surface. This is consistent with the low-frequency semi-circle loop present in the Nyquist plots acquired at negative potentials where hydrogen evolution is most likely to occur. This assignment is also reported in previous literature, from EIS studies of materials undergoing similar hydrogen evolution reactions (HERs), typically involving reactions with adsorbed intermediate species, such as H_2 [140, 150-152].
    - R(LF-b) can be assigned to a charge transfer resistance from other electrochemical processes taking place at the electrode-electrolyte interface e.g. adsorption, oxidation or charge transfer.
- CPE(HF) is a capacitance associated with the high-frequency Nyquist loop and can be tentatively assigned to the capacitive contributions due to electronic properties of the bulk 25-SIMF, such as the bulk electrode capacitance. This capacitive contribution is present across the entire measured potential range.
- CPE(LF) is a capacitance associated with the low-frequency Nyquist loop and can be tentatively assigned to the electrochemical processes taking place at the 25-SIMF surface and is dependent on the applied potential, similar to R(LF).

The following EIS work aims to provide a simplified interpretation and understanding of the 25-SIMF material using the fitted resistance and fitted effective capacitance values. This will enable a suitable comparison between the EIS data of the AGR cladding and 25-SIMF, in support of the coupled-electrode studies of Chapter 5, and thus support the legacy AGR SNF studies of Chapter 6.

To further simplify the interpretation of the fitted resistance data shown in Table 4-2, we can use assumptions similar to that of Thevenin's theorem which states that:

"*Any linear circuit with voltage sources and resistances, can be replaced by an equivalent circuit containing only a single voltage in series with a single resistance connected across the load*" [153].

This enables us to further simplify the EECs and the fitted resistance values by summation of the in-series resistors to derive a 'total resistance' value, where R(total) = R(HF) + R(LF-a/b).

This approach reduces the complexity of the fitted EECs to a simple equivalent circuit containing the least amount of circuit components [154]. It also reduces the quantity of resistance values needed for interpretation and allows for a more practical comparison with the analogous EIS studies of AGR cladding, presented later in Section 4.5.2.1. The R(total) values can be found in Table 4-2.

Figure 4-31 shows a combination of overlaid plots comparing the change in R(total) as a function of applied potential, against their respective polarisation curves as a function of pH. From these plots, we can see that the total resistance of each system remains relatively unchanged during the HER region of applied potentials at < ~-0.3 V. From ~-0.3 V onwards, the resistances increase rapidly, reaching a maximum at ~0 to 0.2 V, before decreasing as applied potential increases.

The onset of R(total) increase at ~-0.3 V also coincides with the onset of the various UO_2 oxidation processes taking place at the 25-SIMF electrode surface, such as the oxidation of UO_2 to UO_{2+x} at the grain boundaries and on the grains, as discussed above in the interpretation of the 25-SIMF SSPW polarisation curves.

These surface oxidation processes are likely contributing to the formation and build-up of oxidised species at the SIMFUEL surface, hence the increase in resistance. At applied potentials greater than 0.2 V, the decrease in R(total) coincides with the onset of oxidation to U(VI) and dissolution. This effect has been observed in similar EIS and LSV studies of the 25-SIMF SIMFUEL as reported by Howett [39], with comparable results and trends observed for the 25-SIMF sample.

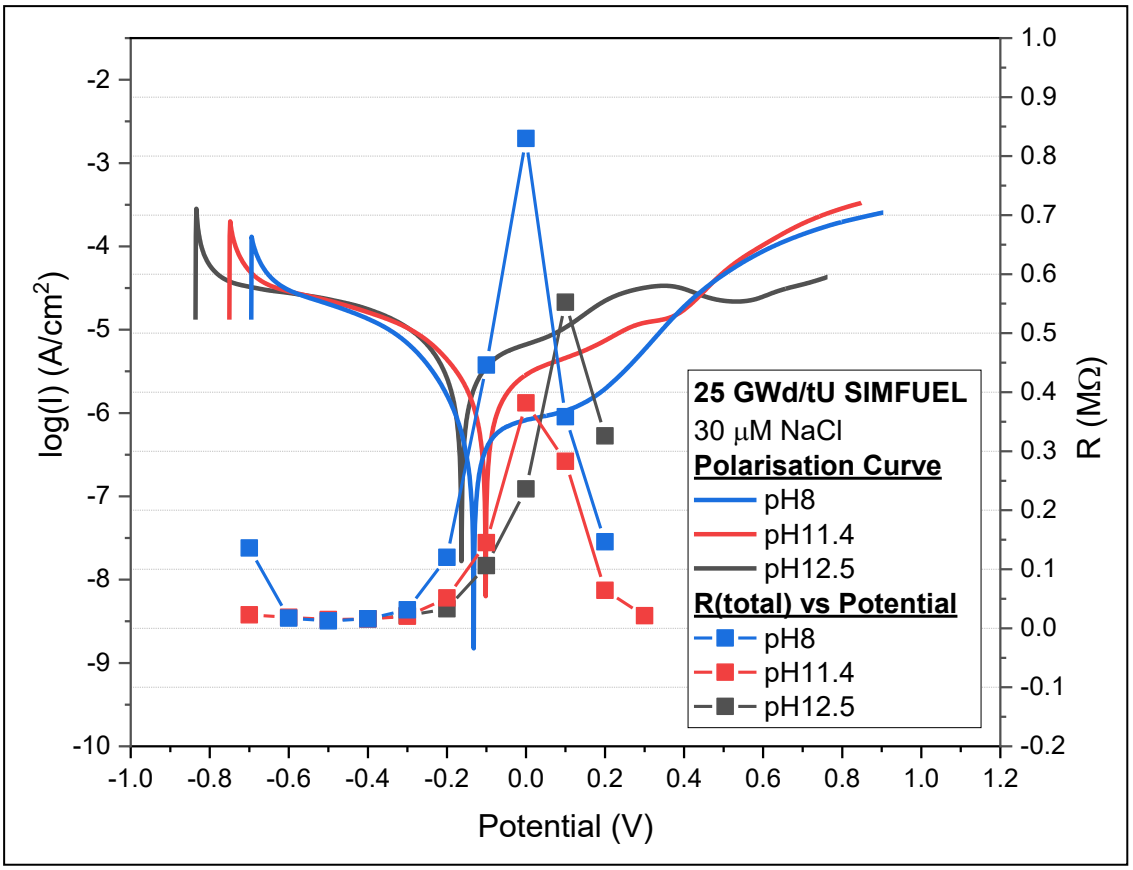

Figure 4-31: R(total) versus potential, overlaid with polarisation curves of 25 GWd/tU SIMFUEL taken from Figure 4-25.

Figure 4-32 shows plots of the fitted and calculated C_{eff} values as a function of applied potential, overlaid with their respective polarisation curves. Each graph shows the plots for each of the CPE components used in the EECs.

CPE(HF) and CPE(LF-b) plots are displayed using the same y-axis scaling across the three graphs, since the capacitance values are approximately between 0 – 5 mF. Whereas CPE(LF-a) plots are displayed with a different y-axis scaling across the three graphs to account for the larger variance in capacitances, since the range of capacitance values are between 0 – 50 mF.

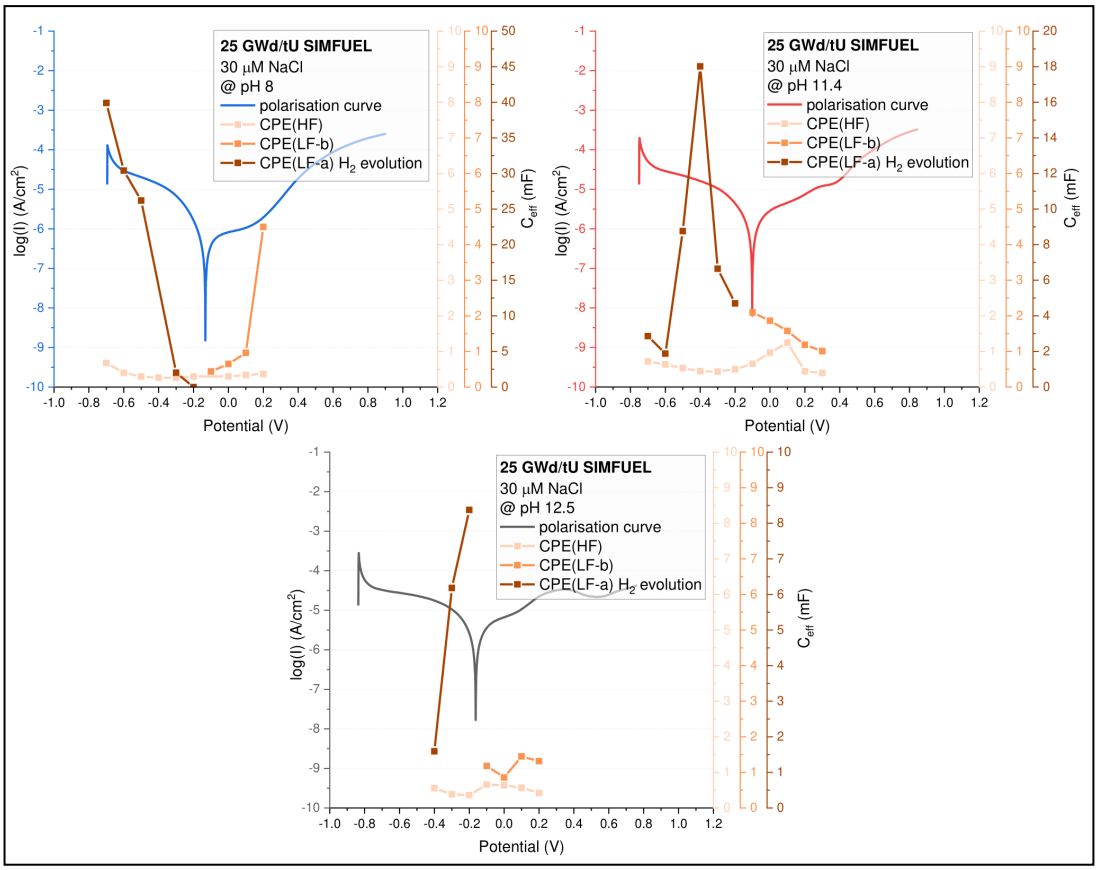

Figure 4-32: Fitted C_{eff} values of CPE(HF), CPE(LF-a) and CPE(LF-b) versus potential, at pH 8, 11.4 and 12.5, overlaid with polarisation curves of 25 GWd/tU SIMFUEL taken from Figure 4-25. (right-side CPE(LF-b) y-axis scales are different between each graph)

CPE(LF-a) values fluctuate the most compared to CPE(HF) and CPE(LF-b). This is likely due to experimental errors caused by the difficulties in obtaining good data in the low-frequency region at the negative applied potentials, which is typically associated with the HER process.

In this applied potential range, the data points are scattered due to gaseous bubble formation during the HER process. This leads to poor EIS fitting of the data points, resulting in inaccurate C_{eff} values. According to observations reported in the literature on the EIS studies of the HER process, the capacitance activity of CPE(LF-a) can be associated with the formation of intermediates arising from the multistep mechanism of the HER process on an active catalytic site [155, 156].

In the case of the SIMFUELs under study here, the catalytic sites are most likely to be associated with the noble metal/ε-particles – so catalysing the HER process.

As described above, CPE(LF-b) is fitted from the same low frequency Nyquist loop as CPE(LF-a), however, the assignment of the CPE is different once the applied potential increases above -0.2 V, where the HER process is no longer taking place. This is evident in the example Nyquist plots shown in Figure 4-27, Figure 4-28, and Figure 4-29.

The capacitance in this region can be assigned more generally and is likely derived from a combination of the electrochemical corrosion processes taking place. These electrochemical processes are only probed at the low-frequency domains, such as, the oxidation of UO_2 to UO_{2+x} at the grain boundaries and on the grains and the oxidative dissolution of UO_2 to UO_2^{2+} [157].

CPE(HF) is fitted from the high frequency Nyquist loop, observed across the whole applied potential range. The capacitance values are consistent across each pH and show little dependency on the applied potential and is therefore unlikely to be derived from the electrochemical corrosion processes.

The magnitude of the capacitances is also in good agreement with similar previous EIS studies on the 25-SIMF sample [39]. The assignment of EEC components at high-frequency domains are typically correlated to the capacitance derived from electronic effects such as the Double Layer capacitance and Space Charge capacitance, thus, the fitted values here can be tentatively represented by such processes.

Similar assignments of the high frequency CPE to the Space Charge Layer contribution have been reported in previous EIS studies of the 25-SIMF sample, which further provides support and evidence for this assignment [39].

4.5.1.2 25 GWd/tU SIMFUEL in Alkaline Chloride Water

Here we present the electrochemical studies of 25-SIMF in 0.1, 1.0, 10, and 100 mmol/dm^3 NaCl solutions at pH 8, 11.4 and 12.5, using LSV and OCP. Figure 4-33 shows the polarisation curves for 25-SIMF, recorded in NaCl electrolyte solutions containing 0.1, 1.0, 10 and 100 mmol/dm^3 chloride, at pH 8, 11.4 and

12.5. Figure 4-34 shows a zoomed-in view of the polarisation curves from Figure 4-33, between the potential region of -0.1 to 0.9 V, with the y-axis offset between each set of pH measurements, this is to enable clear visual comparison between the measurements at each pH.

The plots in Figure 4-33 exhibit the same trend as a function of pH as observed in the 25-SIMF SSPW polarisation curves recorded at low (30 μM) chloride and shown in Figure 4-25, Section 4.5.1.1. The general form of the 25-SIMF polarisation curves can be described similarly to the interpretations already provided throughout this chapter in the previous sections.

The presence of chloride and its increasing concentration does not appear to have a substantial effect on the electrochemical oxidation/corrosion processes taking place during the 25-SIMF polarisation measurements. This can be explained according to the same reasoning as with the 25-SIMF SSPW LSV studies presented in the above Section 4.5.1.1. The appearance of a trend indicating that the current density is exhibiting a dependence on [Cl^-], is likely due to the increase in ionic strength of the electrolytes as a function of chloride concentration.

Figure 4-35 shows the recorded OCP data. From these plots, it can be seen that the equilibrium OCP exhibits a similar dependence on pH as observed in the 25-SIMF SSPW OCP data recorded at low (30 μM) chloride and shown in Figure 4-26. Specifically, and as expected based on the low chloride data, the corrosion potential is shown to be driven more negative with increasing alkalinity.

Furthermore, the OCPs also show that there is no sign of chloride dependence. This is to be expected since chloride does not affect the oxidation of UO_2, and thus the OCPs are independent of NaCl concentration [158, 159]. With this in mind, the general trend of the OCPs can be described in accordance with the trends seen in the OCP plots of Figure 4-26.

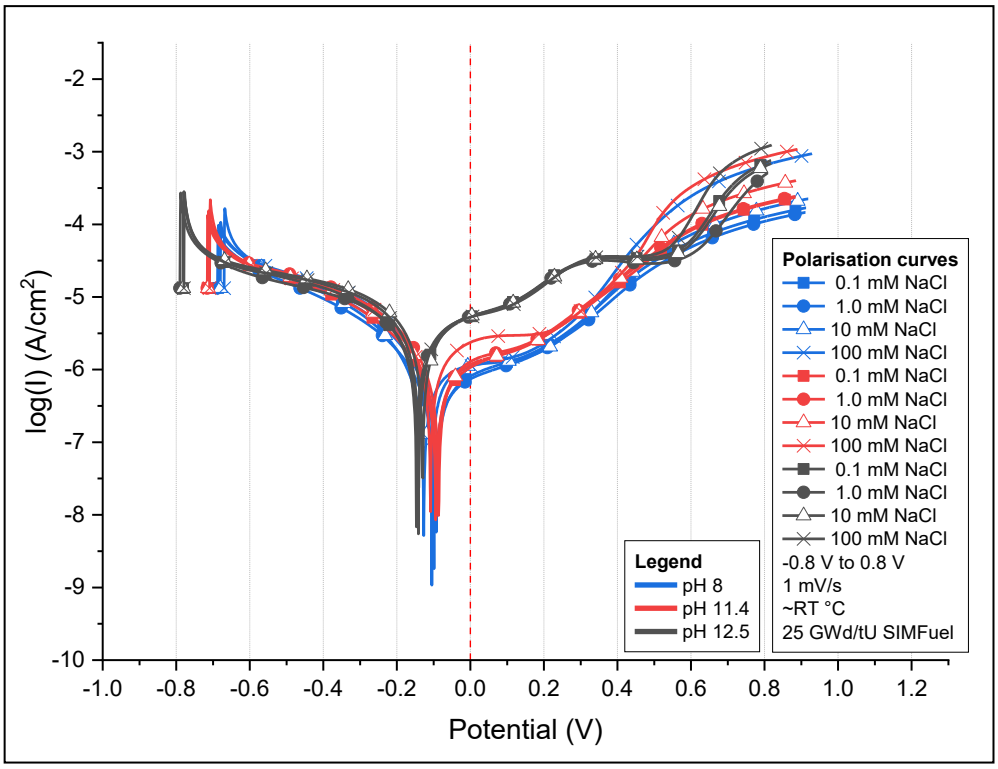

Figure 4-33: Polarisation curves obtained from LSV measurements of 25 GWd/tU SIMFUEL in 0.1, 1.0, 10, 100 mmol/dm^3 NaCl at pH 8, 11.4 and 12.5.

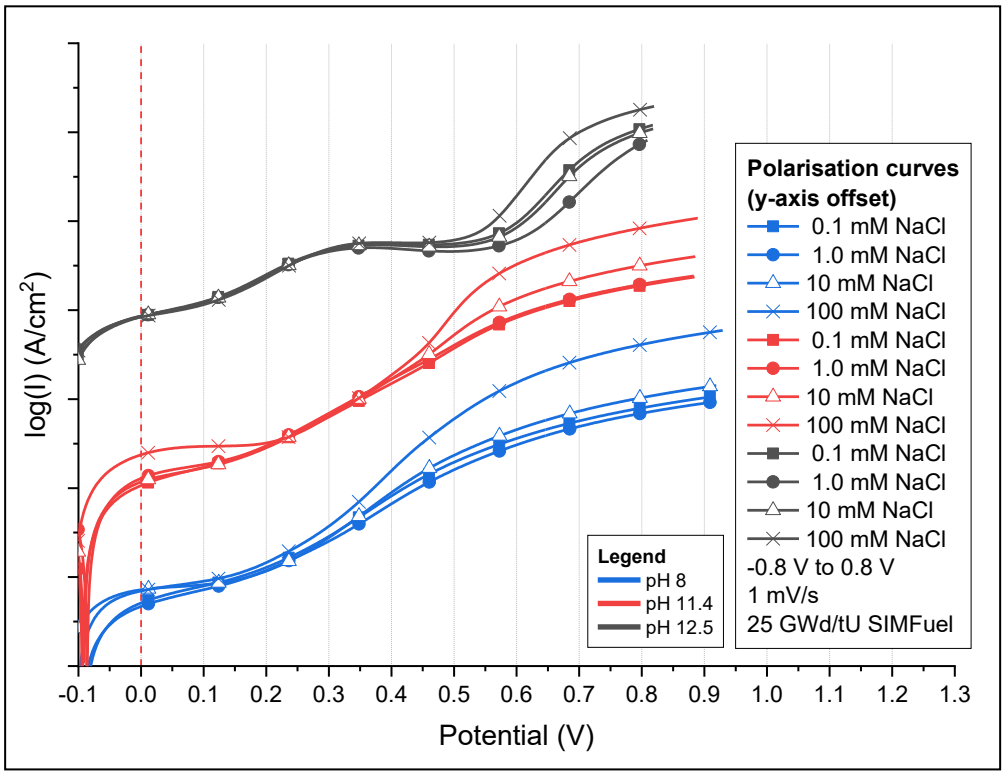

Figure 4-34: Polarisation curves showing a zoomed-in view with y-axis offset manipulated from Figure 4-33.

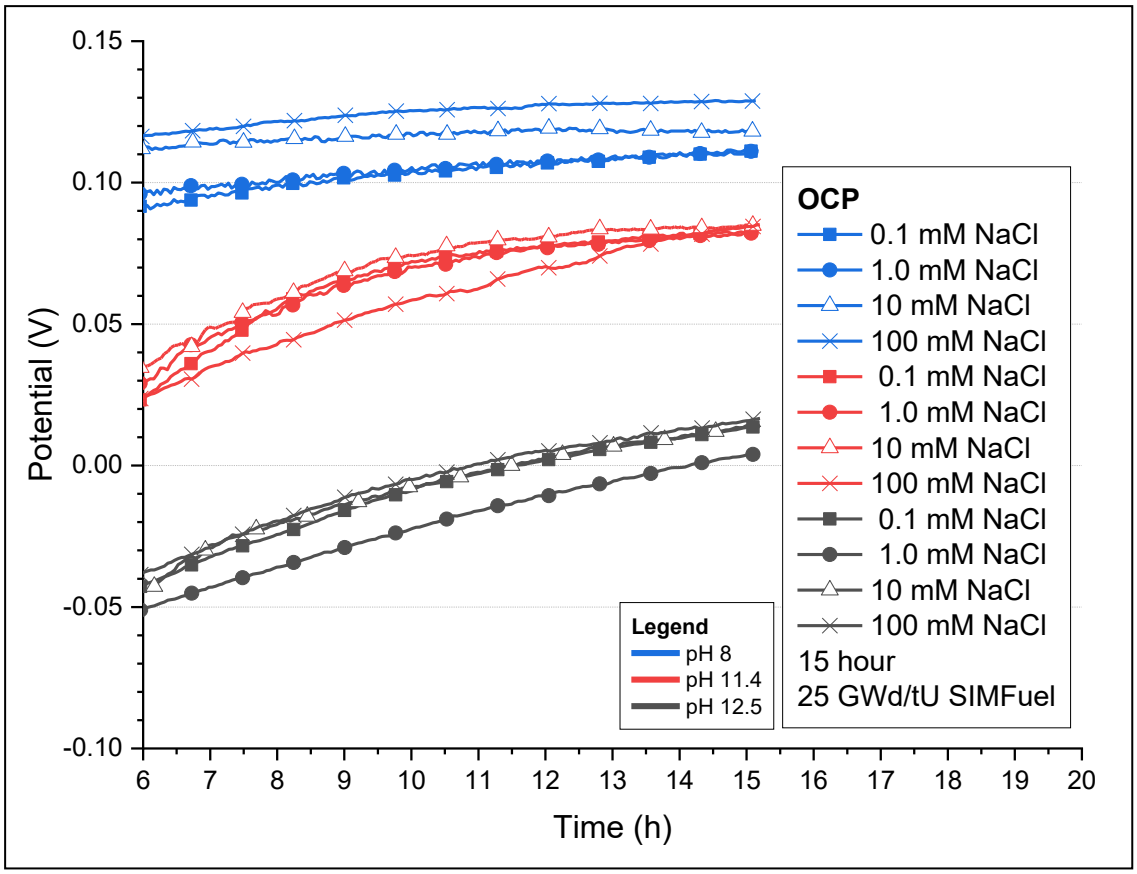

Figure 4-35: Plots of open circuit potentials vs. time of 25 GWd/tU SIMFUEL in 0.1, 1.0, 10, 100 mmol/dm^3 NaCl at pH 8, 11.4 and 12.5.

4.5.2 20/25/Nb AGR Cladding

This section presents the electrochemical studies of the 20/25/Nb stainless steel AGR cladding material. The measurements were conducted under the same methods and conditions as Section 4.5.1 and those used for the electrochemical studies presented later in Chapters 5 and Chapter 6.

Section 4.5.2.1 presents the electrochemical studies of 20/25/Nb AGR cladding in SSPW solutions and Section 4.5.2.2 presents the analogous studies in NaCl solutions. Similarly to Section 4.5.1, the main electrochemical techniques employed here are those of OCP, LSV and EIS measurements.

OCPs were recorded over 15 hours. LSV measurements were recorded between a potential range of -0.8 to 1.5 V at 1 mV/s. EIS measurements were conducted in accordance with the general method described in Chapter 3 Section 3.2.7 and conducted at 0.1 V intervals from -0.7 to 0.3 V.

4.5.2.1 AGR Cladding in Simplified Simulant Pond Water

Here we present the electrochemical studies of AGR cladding in SSPW solutions at pH 8, 11.4 and 12.5, using LSV, OCP and EIS measurements. Figure 4-36-(**Top**) shows the polarisation curves for the 20/25/Nb AGR cladding, recorded in SSPW electrolyte containing 30 μmol/dm^3 NaCl at pH 8, 11.4 and 12.5. Figure 4-36-(**Bottom**) shows the polarisations curve recorded in pH ~6.5 sulphate solution, excerpted from Figure 4-11 to allow for direct visualisation/comparison with Figure 4-36-(**Top**).

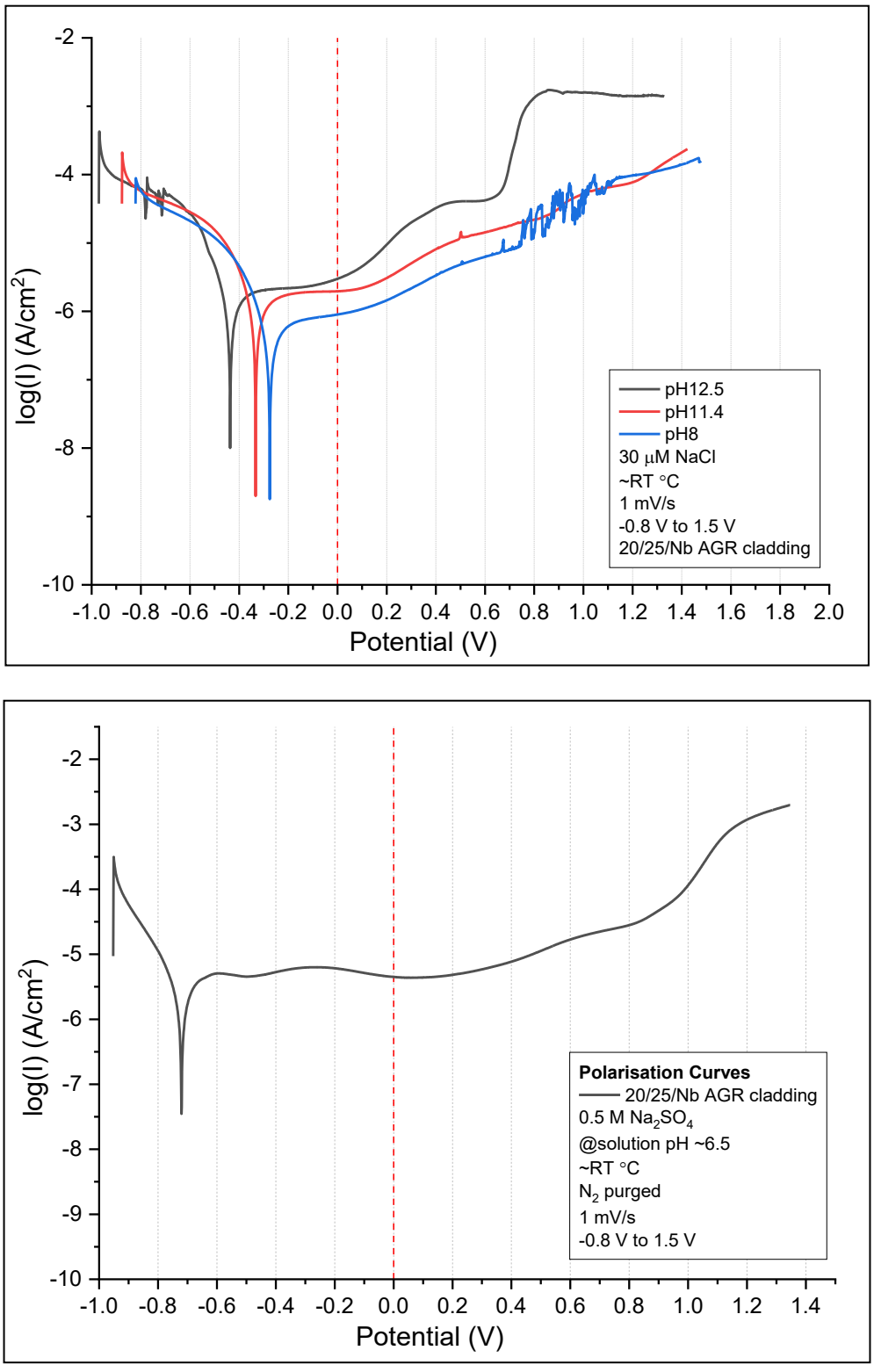

Figure 4-36: (**Top**) Polarisation curves obtained from LSV measurements of 20/25/Nb AGR cladding in SSPW at pH 8, 11.4 and 12.5. (**Bottom**) Taken from Figure 4-11, showing the polarisation curve for 20/25/Nb stainless-steel AGR cladding, measured in 0.5 mol/dm^3 Na_2SO_4 electrolyte at ~pH 6.5.

Figure 4-36 shows that he general form and features of the polarisation curves recorded in SSPW are similar to the analogous AGR cladding LSV measurements recorded in 0.5 M Na_2SO_4 of Figure 4-11 in Section 4.3.3. Thus, the interpretations of the polarisation curves in SSPW are similar to those described for the sulphate system in Section 4.3.3.

Specifically, ranges of interest within the potential window employed in LSVs of Figure 4-36 can be identified as follows: (i) the HER region, (ii) the passive region and (iii) the transpassive region.

However, and can be seen from Figure 4-36-(**Top**), the exact potential range over which each region extends varies with the pH of the electrolyte employed, due to a pH dependence effect on the corrosion behaviour of the AGR cladding. The influence of pH on the corrosion behaviour of stainless steels has been described previously in Chapter 2 Section 2.3.3.3.

In general, the increase in pH leads to improved corrosion protection on stainless steel materials by improving the passivating capability and minimising the corrosive effect of chloride [101, 102, 104, 106, 160]. Thus, the polarisation curves of Figure 4-36, as a function of pH, can be generally described as follows:

- As pH increases, the onset of passivation moves towards more negative potentials and the onset of the transpassive region moves towards more positive potentials, resulting in an overall increase in the total region at which the cladding is passive, thus improving the surface corrosion protection at higher pHs.
- At pH 8 there is evidence of localised corrosion attack at the steel surface as shown by the current spikes in the potential region between 0.6 V to 1.2 V. At low 30 $\mu mol/dm^3$ chloride concentrations employed here, this scenario can occur if the surface finish of the steel is imperfect, for example if pits/crevices are present on the cladding surface [131]. At this pH, there is also insufficient growth of passive film to afford enough protection via the passive film.
- At pH 11.4, the passive region is wider than at pH 8. There is no evidence of localised corrosion due to the chloride. The corrosion

protection afforded under such conditions is the reason for the current UK AGR SNF storage strategy.

- At pH 12.5 the onset of passivation occurs at even more negative potentials, between approximately -0.4 and 0 V. As the potential increases, the increase in current density in the potential region between 0 and 0.6 V, can be attributed to the pre-transpassive oxidation of Cr(III) to Cr(VI) in the passive layer and subsequent leaching into the solution [134, 135]. From ~ 0.6 to 0.8 V the large increase in current density is a combination of the strong pre-transpassive leaching of the chromium content and the oxidation of Ni(II) to Ni(III) [161]. Both oxidation processes are facilitated by high pH [161, 162].

Figure 4-37 shows the OCPs of the AGR cladding recorded under the same measurement conditions as above. The OCPs values are shown to decrease with increasing pH, this trend is consistent with the pH effect seen in the LSV data. As the pH becomes more alkaline the OCP of the AGR cladding is shifted further negative into the region of passivity relative to each respective polarisation curve of Figure 4-36.

This trend further reinforces the benefits of high pH on the corrosion protection of the passive film and steel surface. Therefore, under these OCP measurement conditions in SSPW at pH 8, 11.4 and 12.5, the AGR cladding is likely protected from corrosion by the surface oxide film.

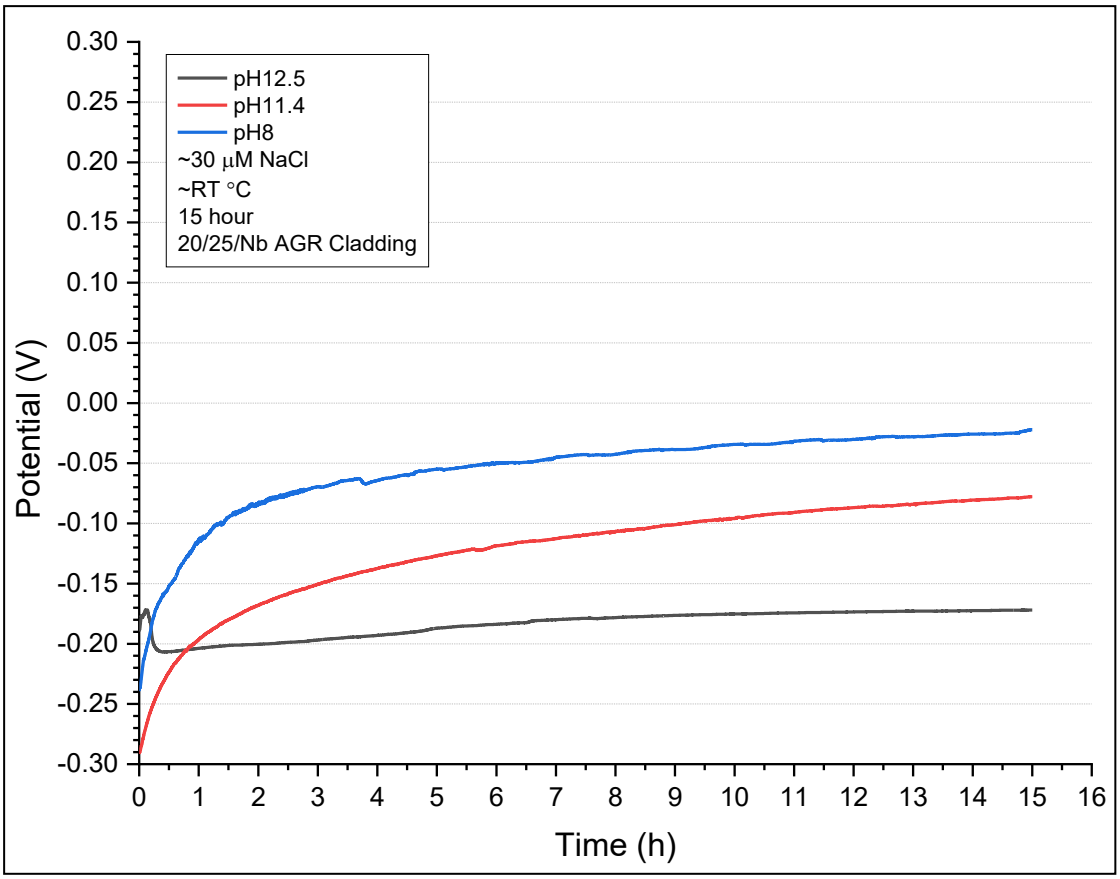

Figure 4-37: Plots of open circuit potentials vs. time of 20/25/Nb AGR cladding in SSPW at pH 8, 11.4 and 12.5.

Next, we present the electrochemical impedance spectroscopy (EIS) studies of AGR cladding in SSPW solutions at pH 8, 11.4 and 12.5.

Figure 4-38, Figure 4-39, and Figure 4-40 show examples of Nyquist plots and Bode plots obtained from such studies at 100 mV intervals over a potential range of -0.7 to +0.3 V vs. Ag/AgCl. Each figure shows example plots recorded at approximately -0.5, -0.1 and +0.2 V for each pH studied. These figures are intended to convey the general shape and form of the Nyquist and Bode plots to allow qualitative comparison between plots at different potentials.

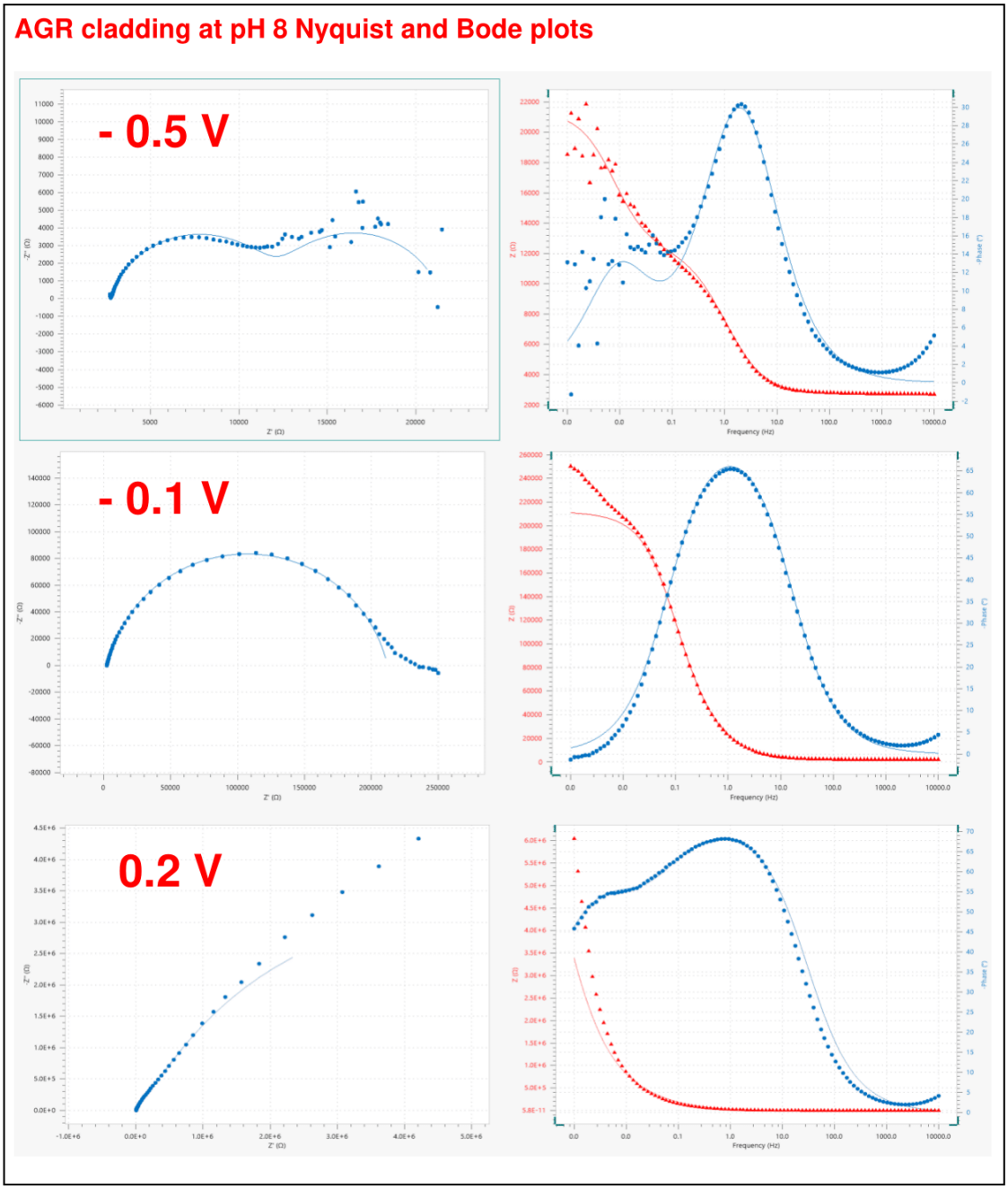

Figure 4-38: Examples of Nyquist and Bode plots generated from EIS circuit fitting of AGR cladding in 30 μM NaCl at pH 8 to show the general shape and form of the plots relatively to each other at different potentials.

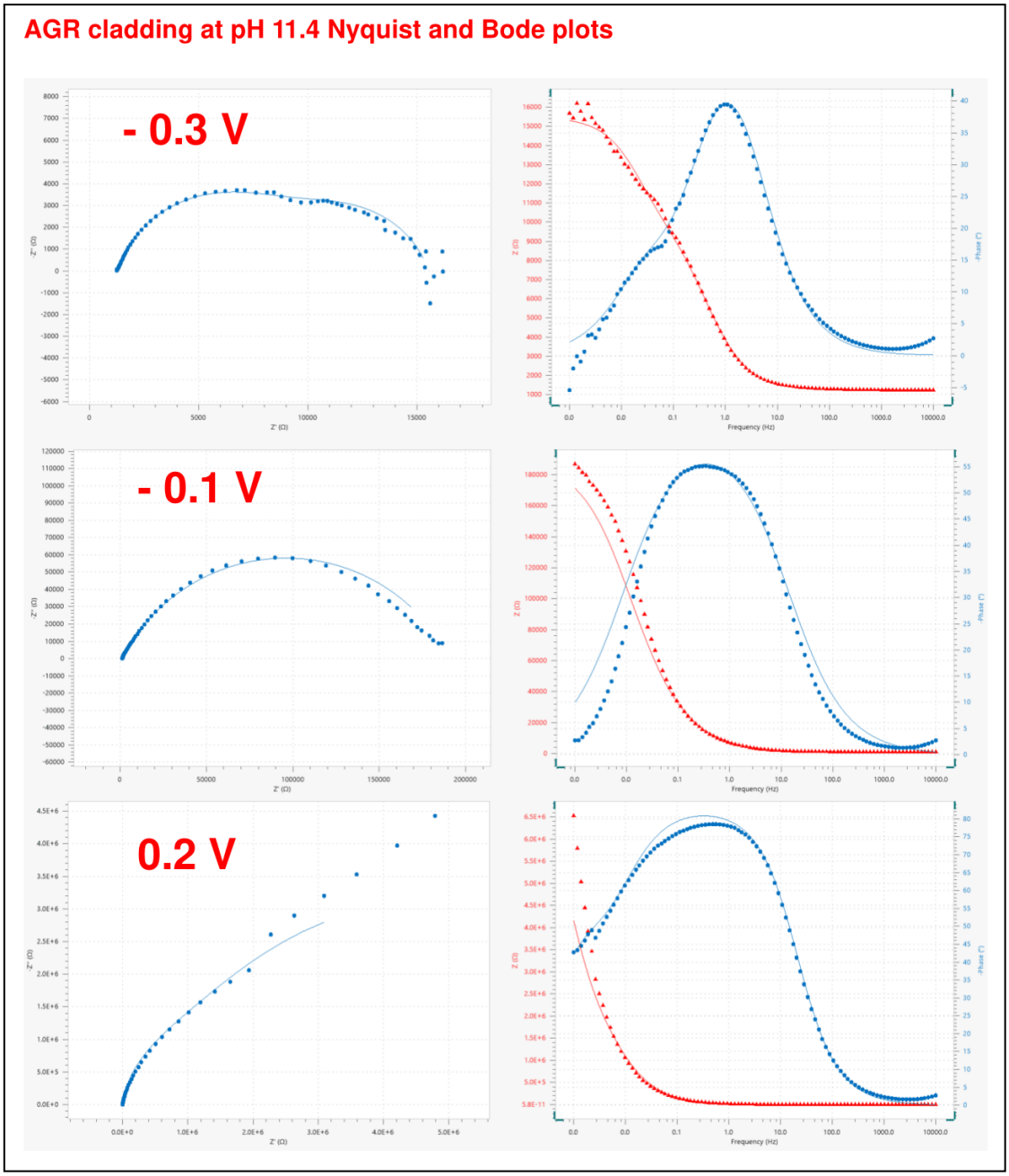

Figure 4-39: Examples of Nyquist and Bode plots generated from EIS circuit fitting of AGR cladding in 30 μM NaCl at pH 11.4 to show the general shape and form of the plots relatively to each other at different potentials.

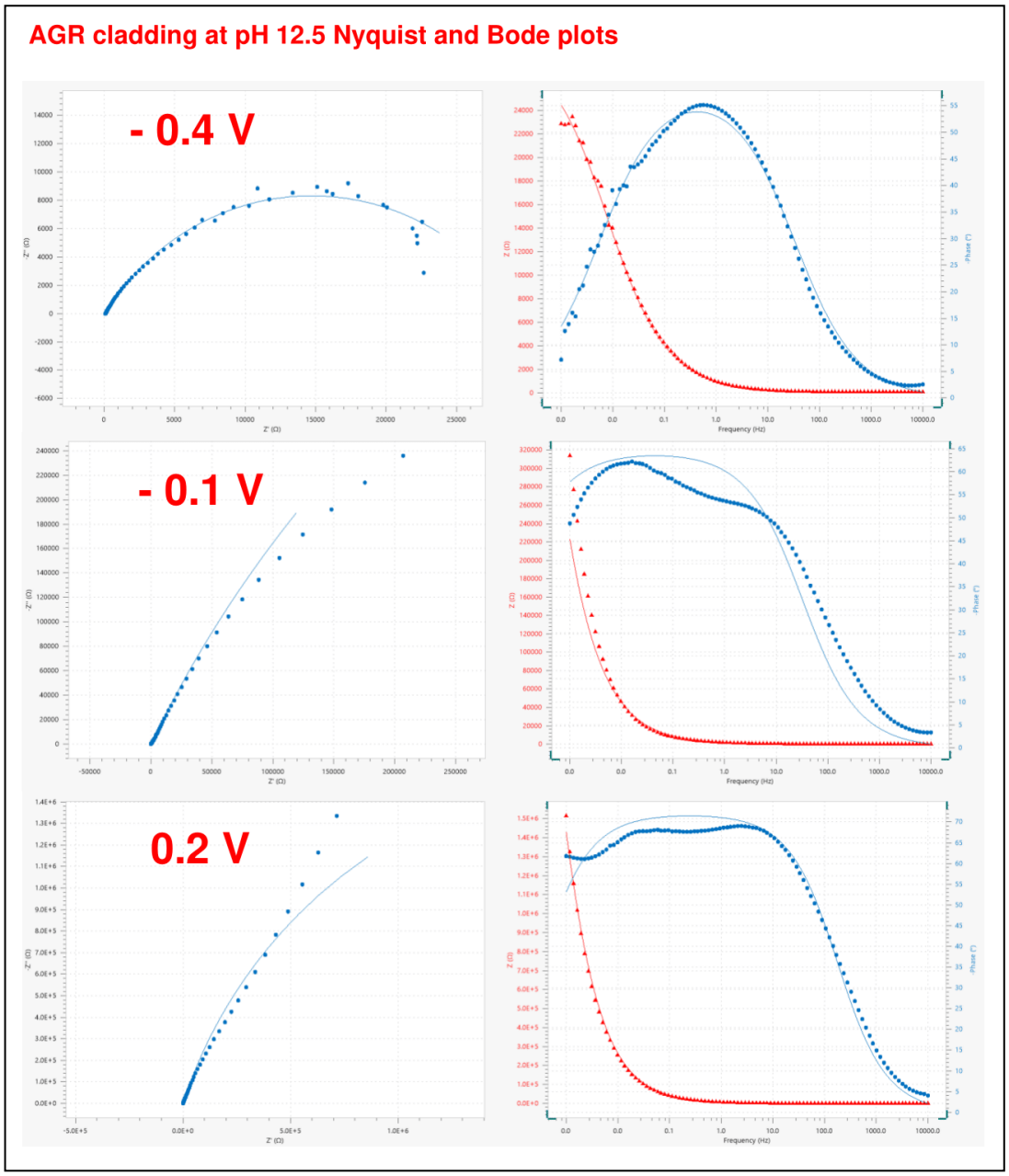

Figure 4-40: Examples of Nyquist and Bode plots generated from EIS circuit fitting of AGR cladding in 30 µM NaCl at pH 12.5 to show the general shape and form of the plots relatively to each other at different potentials.

Figure 4-41 shows the equivalent electrochemical circuits (EEC) used for fitting. All EECs were constructed from Randles circuits segments, similar to the 25-SIMF EIS data presented in Section 4.5.1.1.

The circuit components in each EEC are labelled accordingly in Figure 4-41 with respect to their equivalent assigned electrochemical process. There are three different EECs used, each assigned to different electrochemical processes as a function of applied potential. Justifications for the choice of EEC used are presented later in this section.

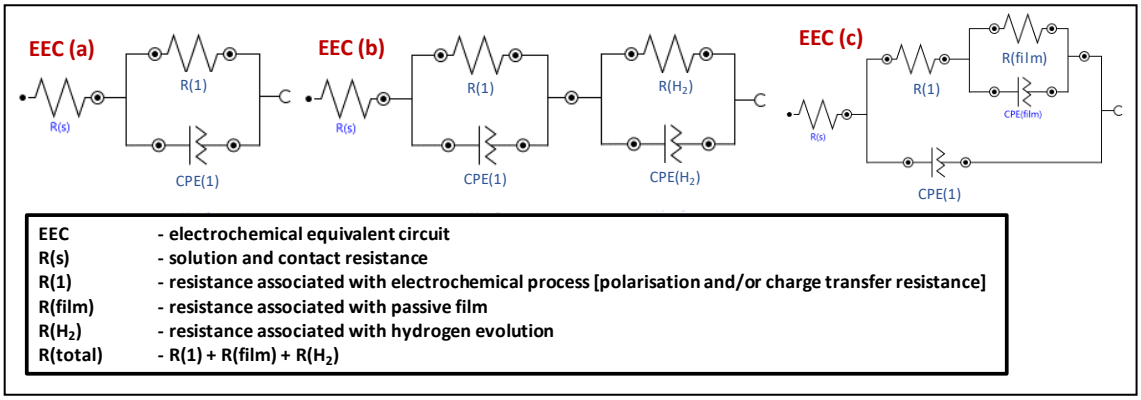

Figure 4-41: Electrochemical equivalent circuit used for EIS circuit fitting of 20/25/Nb AGR cladding in 30 µM NaCl at pH 8, 11.4 and 12.5.

Table 4-4 shows a table containing the fitted resistance values obtained from EEC fitting of the measured EIS data for 20/25/Nb AGR cladding in SSPW electrolyte at pH 8, 11.4 and 12.5. Measurement parameters for EIS data acquisition follow the standard method detailed in Chapter 3 Section 3.2.7. The fitted values were generated using the EECs of Figure 4-41.

20/25/Nb AGR cladding in 30 µmol/dm³ NaCl

Potential	EEC	R(s)	R(1)	R(film)	$R(H_2)$	R(total)	EEC	R(s)	R(1)	R(film)	$R(H_2)$	R(total)	EEC	R(s)	R(1)/R(total)
V	a/b/c	kΩ	kΩ	kΩ	kΩ	kΩ	a/b/c	kΩ	kΩ	kΩ	kΩ	kΩ	a/b/c	kΩ	kΩ
	pH8	pH8	pH8	pH8	pH8	pH8	pH11.4	pH11.4	pH11.4	pH11.4	pH11.4	pH11.4	pH12.5	pH12.5	pH12.5
-0.7	/	/	/	/	/	/	/	/	/	/	/	/	/	/	/
-0.6	/	/	/	/	/	/	/	/	/	/	/	/	/	/	/
-0.5	b	2.7	9.5	/	9.3	18.8	a	1.3	223.0	/	/	223.0	/	/	/
-0.4	b	2.6	10.2	/	4.4	14.6	b	1.3	9.0	/	18.0	27.0	a	0.09	29.2
-0.3	a	2.5	22.0	/	/	22.0	b	1.3	8.1	/	6.2	14.3	a	0.10	22.6
-0.2	a	2.3	55.0	/	/	55.0	a	1.2	32.3	/	/	32.3	a	0.10	78.4
-0.1	a	2.1	210.0	/	/	210.0	a	1.1	190.0	/	/	190.0	a	0.14	1760.0
0	a	1.9	1480.0	/	/	1480.0	c	1.2	370.0	990.0	/	1360.0	a	0.10	11000.0
0.1	c	2.0	850.0	8500.0	/	9350.0	c	1.2	1750.0	4330.0	/	6080.0	a	0.11	7370.0
0.2	c	1.8	1150.0	4440.0	/	5590.0	c	1.1	2500.0	6320.0	/	8820.0	a	0.11	4200.0
0.3	c	1.6	3320.0	7280.0	/	10600.0	c	1.1	2800.0	6320.0	/	9120.0	a	0.11	5020.0

EEC - electrochemical equivalent circuit
R(s) - solution and contact resistance
R(1) - resistance associated with electrochemical process [polarisation and/or charge transfer resistance]
R(film) - resistance associated with passive film
$R(H_2)$ - resistance associated with hydrogen evolution
R(total) - R(1) + R(film) + $R(H_2)$

Table 4-4: Table of fitted resistances from EIS circuit fitting of 20/25/Nb AGR cladding in 30 µM NaCl at pH 8, 11.4 and 12.5.

The type of EEC used to derive the values of Table 4-4 is dependent on the experimental pH and applied potential. The choice is justified and summarised as follows:

- EEC-(a) consists of a single Randles circuit and is the simplest form of the EEC commonly used for fitting stainless steel materials [163, 164]. In this study, the circuit is versatile and fits easily to the majority of the EIS data.
- EEC-(b) has further complexity introduced by the addition of a second Randles circuit which has been assigned to the HER process taking place at the electrode-electrolyte surface due to the reduction of H_2O. This EEC fits best at the more negative applied potentials where the HER is more likely to be taking place. The HER process can be identified in the Nyquist plots by the appearance of a second semi-circle loop appearing towards the low frequency domain [157]. However, the data points acquired in the region of potentials associated with the HER are typically scattered, likely caused by turbulent gaseous formations at the electrode surface during data acquisition.
- EEC-(c) has further complexity introduced by the addition of a second Randles circuit within the main Randles circuit; this setup is commonly used to account for surface oxide film growth at the electrode-electrolyte interface [165-167]. In this instance, the R(film) component has been assigned to the resistance of the oxide film.
- For the measurements conducted at pH 8 and 11.4, the EECs used are common to both. The example Nyquist plots of Figure 4-38 and Figure 4-39 show the progression EEC-(b) to EEC-(a) to EEC-(c) as the applied potential increases.
- For measurements conducted at pH 12.5, only EEC-(a) is used, independent of applied potential, as shown in the example Nyquist plots of Figure 4-40. At this pH, EEC-(b) and EEC-(c) are not used because the cladding is undergoing surface dissolution processes across the measured potential range.

The following EIS work aims to provide a simplified interpretation and understanding of the AGR cladding material using only the fitted resistance values.

For the purpose of this study, the assignment of CPE components and their associated C_{eff} values were not included, as they are not of interest or relevant to the interpretation. Rather, this study aims to enable comparison between analogous resistance elements within the AGR cladding and 25-SIMF EECs to support the interpretation of the studies of the coupled-electrode simulant system of Chapter 5 and, thence, the legacy AGR SNF studies of Chapter 6.

To simplify and facilitate this comparative EIS analysis, the complex EECs of Figure 4-41 can each be reduced to a simplified EEC containing the least number of circuit components.

Thus, EEC-(b) and EEC-(c) of Figure 4-41, can be expressed as a single Randles circuit, similar to EEC-(a). The associated resistances can be combined to give a total resistance, R(total), derived from the summation of R(1), R(film) or R(H_2). The R(total) values can be found in Table 4-4. This is a similar approach to that used in the 25-SIMF SSPW EIS studies of Section 4.5.1.1.

Figure 4-42 shows a combination of overlaid plots comparing the change in R(total) as a function of applied potential, against their respective polarisation curves, recorded at pH 8, 11.4, 12.5.

From these plots we can see that, in accordance with the behaviour observed in the polarisation curves, R(total) increases predictably near the potential region where the onset of passive layer growth is expected. The decrease in resistance observed at potentials positive of this point also correlates with the onset of transpassive dissolution and thinning of the passive layer; this effect is observed across each pH.

At pH 12.5, the onset of increase in R(total) occurs earlier, i.e. at more negative potentials, than at pH 8 and pH 11.4, mimicking the shift in the onset of passive layer formation seen in the polarisation curves. This effect has been observed in similar EIS and LSV studies of AGR cladding by Howett [39].

Similarly, in studies by Williamson [92], evidence of 316L stainless-steel passive layer growth was tracked by using EIS and similar observations were reported, correlating the increase in resistance with the formation of the passive layer.

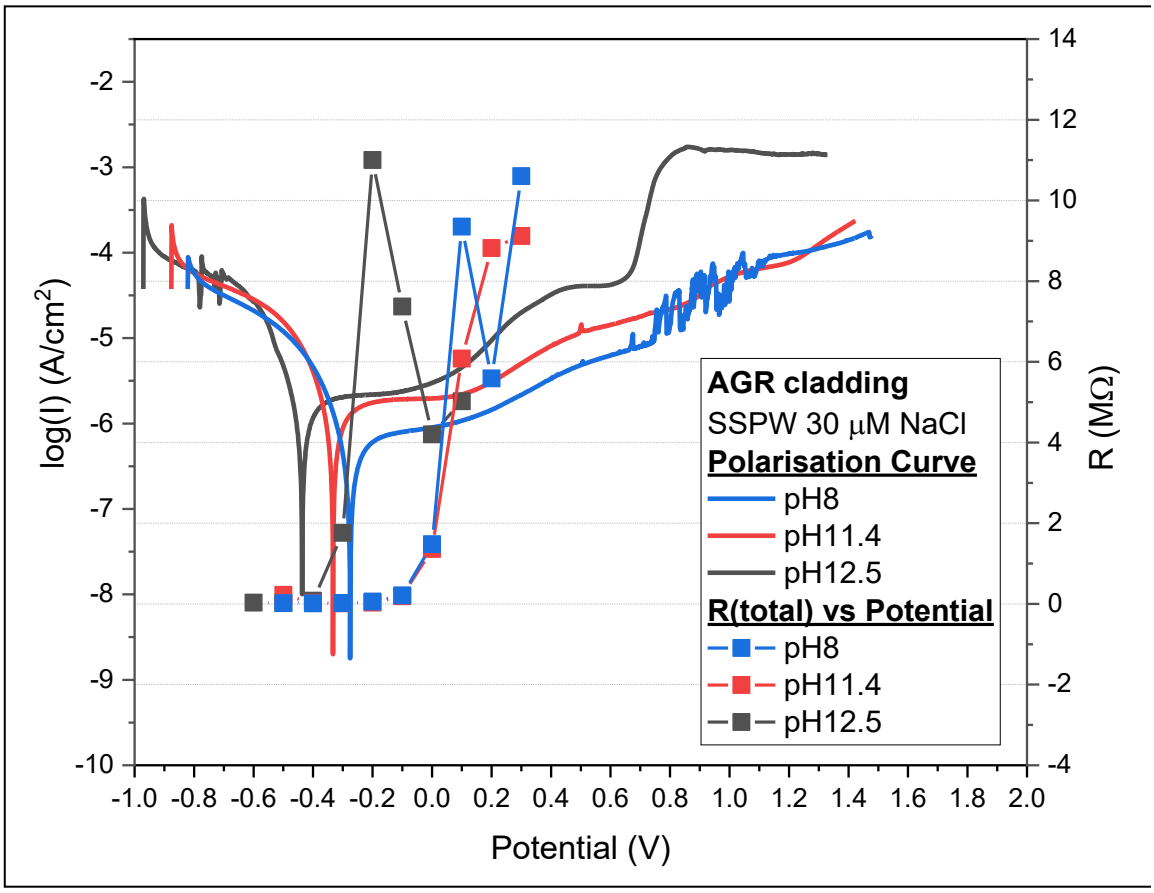

Figure 4-42: R(total) versus potential, overlaid with polarisation curves of AGR cladding taken from Figure 4-36.

4.5.2.2 AGR Cladding in Alkaline Chloride Water

Here we present the electrochemical studies of AGR cladding in 0.1, 1.0, 10, and 100 mmol/dm^3 NaCl solutions at pH 8, 11.4 and 12.5, using LSV and OCP.

Figure 4-43 shows the polarisation curves for AGR cladding, recorded in NaCl electrolyte solutions containing 0.1, 1.0, 10 and 100 mmol/dm^3 chloride, at pH 8, 11.4 and 12.5. At the lower concentration of 0.1 mmol/dm^3 NaCl, the recorded data at each pH is directly comparable with the AGR cladding SSPW data recorded at 30 mmol/dm^3 chloride presented in Figure 4-36 of Section 4.5.2.1.

The polarisation curves exhibit the same trend across each pH and the interpretation discussed in the AGR cladding SSPW LSV data can also be applied to the polarisation curves presented here. Overall, the pH dependence is the same as with the SSPW data and this dependence is also seen in the OCP data of Figure 4-45.

In general, the OCPs are driven more negative with increasing alkalinity, with no apparent trend associated with the increase in chloride concentration.

The effect of chloride on the electrochemical corrosion of AGR cladding is more apparent from the mode of presentation of polarisation curves shown in Figure 4-44. In this expanded view, each set of plots has been grouped by pH and offset vertically along the y-axis to better convey the differences. From these plots we can see that high chloride concentrations have a greater impact on the corrosion of the cladding at lower (but still alkaline) pH than at higher pH.

This suggests that with each pH increment, the protection afforded from the caustic dosing improves until it reaches pH 12.5, where no chloride dependence is seen, in chloride concentrations up to 100 mmol/dm^3, as the high pH 12.5 is able to afford a much greater corrosion protection than the lower pH 8 and 11.4.

However, under more realistic UK AGR pond storage scenarios, it is unlikely that the concentrations of chloride would ever reach such extreme values. Under more realistic/probable conditions, the current caustic dosing to pH 11.4 of AGR SNF storage pond conditions is expected to inhibit corrosion and maintain the structural integrity of the AGR cladding.

The main observations from the polarisation curves of Figure 4-43 and Figure 4-44 can be summarised as follows:

- At pH 8, 10 and 100 mmol/dm^3 NaCl, the polarisation curves show increased activity at potentials above 0.6 V, associated with the onset of transpassivity. The appearance of current response spikes also indicates the possibility of localised corrosion at the steel surface in the form of pitting or crevice corrosion.
- At pH 11.4, evidence of localised corrosion is only seen at 100 mmol/dm^3 NaCl which suggests that the increase in NaOH concentration going from

pH 8 to 11.4 is sufficient to suppress the corrosion seen at pH 8 in 10 mmol/dm^3 NaCl. Evidence of this can be observed in the passive region which has been extended beyond 0.6 V for the 0.1, 1.0 and 10 mmol/dm^3 NaCl curves.

- At pH 12.5, the influence of chloride on the electrochemical corrosion behaviour of the cladding appears to have diminished at all concentrations of NaCl. Each polarisation curve appears identical, and the region of passivation is larger than in pH 11.4 and 8. This suggests that pH 12.5 is more than enough to suppress chloride-induced corrosion attacks up to [NaCl] of 100 mmol/dm^3. The appearance of a transpassive region and a secondary passive region can also be described similarly to the AGR cladding SSPW polarisation curves presented in Section 4.5.2.1.

Figure 4-45 shows the OCPs plots of the AGR cladding recorded under the same electrolyte conditions. In general, there appears to be no correlation between the recorded OCPs and the concentration of chloride at each pH and the OCP values sit in the region of passivity. The OCP values are in line with the OCP values from the AGR cladding SSPW studies of Section 4.5.2.1 and Figure 4-37, suggesting that there is likely no deviation in the OCP when compared with 0.003 mM (30 μM) NaCl.

The pH 11.4 dataset contains an outlier at 0.1 mM NaCl; however, this does not impact the use of this information in the interpretations of the coupled-electrode and the legacy AGR SNF studies. Thus, the increase in chloride concentration, at the pHs explored here is unlikely to induce spontaneous corrosion of the AGR cladding under these measurement conditions.

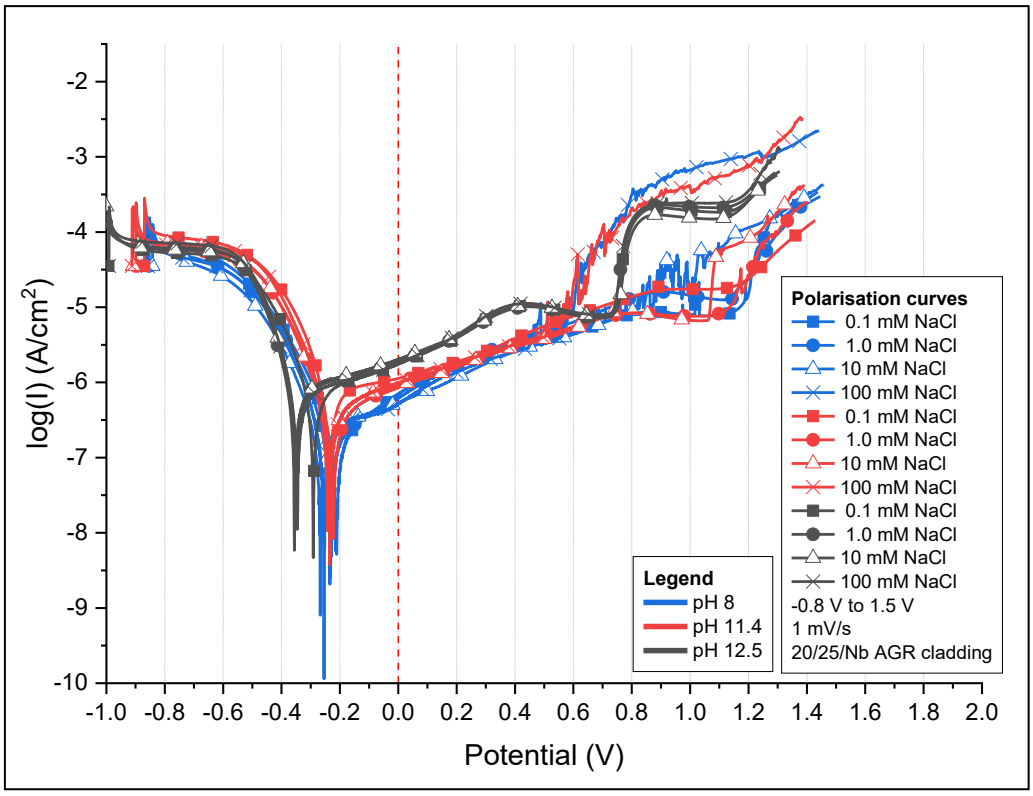

Figure 4-43: Polarisation curves obtained from LSV measurements of 20/25/Nb AGR cladding in 0.1, 1.0, 10, 100 mmol/dm^3 NaCl at pH 8, 11.4 and 12.5.

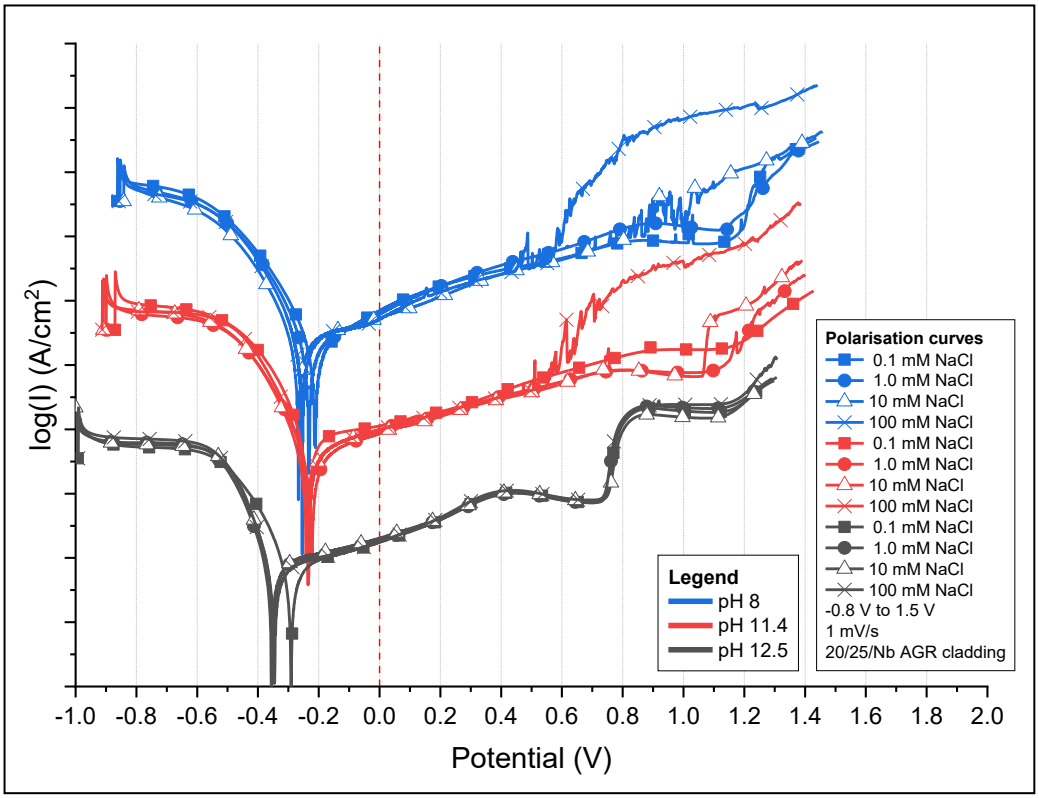

Figure 4-44: Polarisation curves with y-axis offset manipulated from Figure 4-43.

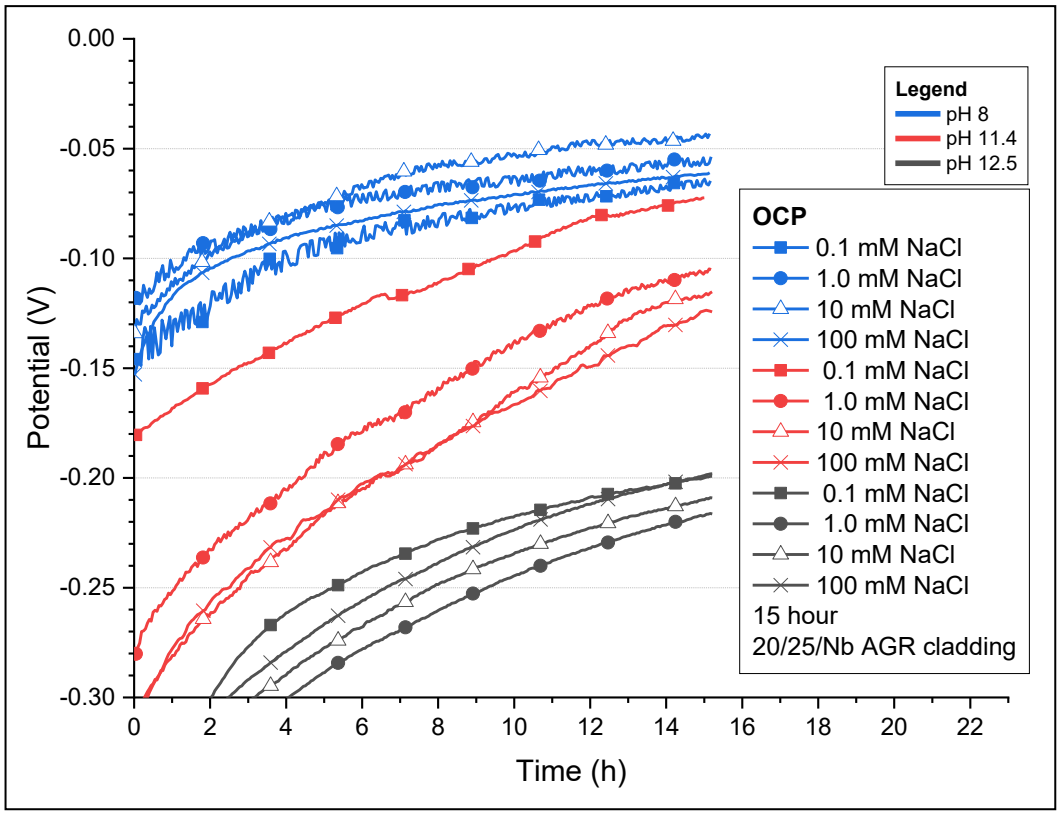

Figure 4-45: Plots of open circuit potentials vs. time of 20/25/Nb AGR cladding in 0.1, 1.0, 10, 100 mmol/dm^3 NaCl at pH 8, 11.4 and 12.5.

4.6 Summary

In this chapter we presented the baseline electrochemical, SEM, and μ-Raman spectroscopy studies on samples of: (a) undoped-UO_2 (b) lower simulated burn-up 25 GWd/tU AGR SIMFUEL (25-SIMF), (c) higher simulated burn-up 43 GWd/tU AGR SIMFUEL pellet (43-SIMF), (d) 43 GWd/tU AGR SIMFUEL with higher lanthanide doping (43-hiLn), (e) 43 GWd/tU AGR SIMFUEL with higher lanthanide and chromium-doped (43-hiLnCr), and (f) as-received non-sensitised 20/25/Nb stainless steel AGR cladding.

For each material, the baseline corrosion behaviour was studied using LSV and OCP in 0.5 mol/dm^3 Na_2SO_4 electrolyte, for μ-Raman spectroscopy studies, measurements were conducted using a 532 nm and a 785 nm laser excitation wavelength Raman microscope. The key points from the results are summarised as follows:

1. From previous SIMFUEL SEM studies published Zoltan Hiezl and excerpted from Zoltan Hiezl's thesis, "Processing and Microstructural

Characterisation of UO2-based Simulated Spent Nuclear Fuel Ceramics for the UK`s Advanced Gas-cooled Reactors" [47], SEM characterisation of the SIMFUELs shows that, broadly, the grain size decreases with Lanthanide (III) loading; the introduction of extra Cr to the highest Ln(III) loaded SIMFUEL results in only a marginal increase in grain size.

2. Voltammetry in Na_2SO_4 indicates that the electrochemical activity of the SIMFUELs increases with doping, a phenomenon attributed to the higher Ln(III) content and thus p-type conductivity of the SIMFUEL UO_2 matrix.
3. OCP measurements in Na_2SO_4 indicate that the Cr-free SIMFUELs exhibit OCP values which sit in the potential region more positive than that seen with undoped-UO_2 and associated with the onset of in-grain oxidation of UO_2 to UO_{2+x}. This suggests that SIMFUELs have a greater thermodynamic driving force towards oxidation and that the SIMFUELs are likely more susceptible to corrosion than undoped-UO_2, under these OCP measurement conditions.
4. Introduction of additional Ln(III) into the SIMFUEL matrix to give 43-hiLn, increases their electrochemical activity further compared to undoped-UO_2, again as a result of increased p-type conductivity, as above. However, from the CVs, there is a disproportionate increase in activity in the region where grain boundary oxidation is taking place, which we attribute to the presence of smaller grain sizes due to the additional Ln(III) loading.
5. Addition of Cr to the 43-hiLn SIMFUEL matrix to give 43-hiLnCr, suppresses its enhanced activity in the potential regions associated with in-grain oxidation processes – we attribute this to a Cr-derived corrosion inhibition effect within the grains, possibly analogous to that observed on stainless steels. However, this enhanced activity is unaffected in the region where grain boundary oxidation takes place - we attribute this to the Ln(III)-driven small grain boundary size.
6. In Na_2SO_4, 20/25/Nb AGR cladding is seen to exhibit behaviour similar to that seen previously i.e. a wide region of passivity positive of -0.6 V with the onset of pre-transpassivity occurring at 0.2 V and the onset of transpassivity occurring at voltages positive of 1.2 V. The OCP sits at ~0.05 V i.e. in the passive region.

7. Raman analysis of the SIMFUELs reveals that, as expected from earlier studies, the SIMFUELs become more defected with increased fission product loading, mainly due to the addition of oxygen vacancies to compensate for the incorporation of Ln(III) dopants into the UO_2 matrix.

The following sections provide a summary of the electrochemical studies of the 25-SIMF and AGR cladding conducted under simulated AGR pond storage conditions, presented in Section 4.5.

OCP, LSV and EIS measurements were conducted in Simulant Pond Water Solutions, containing 30 $\mu mol/dm^3$ NaCl, at pH 8, 11.4 and 12.5. Additionally, OCP and LSV measurements were also conducted in NaCl electrolytes containing 0.1, 1.0, 10 and 100 $mmol/dm^3$ NaCl, at pH 8, 11.4 and 12.5.

25 GWd/tU SIMFUEL

1. Polarisation curves from LSV measurements of 25-SIMF in SSPW have shown a general trend associated with the increase in alkalinity of the electrolyte solutions. As pH increases from 8 to 12.5, the current density also increases; this is associated with increases in electrochemical activity at the electrode-electrolyte interface. The features and trends of the polarisation curves acquired in SSPW electrolyte are similar to the polarisation curves obtained under baseline Na_2SO_4 electrolyte conditions.
2. OCP measurements of the 25-SIMF SIMFUEL in SSPW corroborates the pH effect seen in the polarisation curves. As pH increases, the open circuit potential becomes more negative. Comparison of the OCP values with their respective LSV data shows that increasing alkalinity shifts the equilibrium corrosion potential away from a region of potentials associated with active UO_2 dissolution.
3. EIS measurements of 25-SIMF in SSPW have shown that the fitted Electrochemical Equivalent Circuits can be simplified and reduced to more basic circuits and thus the resistance values can be interpreted as total resistances, R(total), of the electrochemical system. When the resistance values are visualised in combination with the polarisation curves, the resultant plots show a trend of increasing R(total) at the

region of potentials between ~-0.3 to 0.2 V. This observation corelates with the onset of various UO_2 surface oxidation processes taking place at the SIMFUEL surface, which includes the likely formation/build-up of surface oxide species.

4. Polarisation curves from LSV measurements of the 25-SIMF in alkaline chloride water have shown that the presence of chloride from 0.1 to 100 mM NaCl in solution, does not appear to affect the electrochemical/oxidation processes. The appearance of increasing current density with increasing chloride concentration is likely due to the accompanied increase in ionic strength of the electrolytes.
5. OCP measurements of the 25-SIMF in alkaline chloride water show no dependence on the increase in chloride concentration of the electrolytes, similar to the lack of chloride dependence as seen in the LSV measurements.

20/25/Nb AGR cladding

1. Polarisation curves from LSV measurements of AGR cladding in SSPW have shown a general trend as a function of increasing pH. As pH increases from 8 to 12.5, the AGR cladding becomes less susceptible to corrosion by chloride due to improved passivation of the steel surface.
2. OCP measurements of the AGR cladding in SSPW show a trend of decreasing OCP with increasing pH; the trend means a shift in the equilibrium corrosion potential of the cladding further towards negative potentials and into a region of passivity.
3. EIS measurements of the AGR cladding in SSPW have shown that the fitted resistance values can be interpreted and expressed in combination with the polarisation curves to visualise the trend of increasing total resistance, R(total), of the electrochemical system, as a function of applied potential. The results show that there is a correlation between the region of potentials associated with passive layer formation and the increase in R(total).
4. Polarisation curves from LSV measurements of the AGR cladding in alkaline chloride electrolytes have shown that there is a strong chloride effect at higher chloride concentrations and particularly at the lower pH 8

and 11.4 conditions. However, at pH 12.5, the effect of chloride is suppressed up to concentrations of 100 mM NaCl.

5. OCP measurements of the AGR cladding in alkaline chloride water show no correlation between the OCP values and chloride concentration. The recorded values are similar to those recorded under SSPW conditions.

5 Electrochemistry of Coupled 20/25/Nb AGR cladding and 25 GWd/tU AGR SIMFUEL

5.1 Introduction & Objectives

In the previous chapter, Section 4.5 presented the results and discussion of the single component electrochemical studies of the standalone 20/25/Nb stainless steel AGR cladding and 25 GWd/tU AGR SIMFUEL electrodes, under simulated AGR pond storage conditions. Thus, the experiments in this chapter are a continuation of those studies but with the coupled-electrodes comprised of both 20/25/Nb stainless steel AGR cladding and 25 GWd/tU AGR SIMFUEL and has been adapted from the publication of the preliminary results from this study, in Huang et al., [168].

This chapter presents a non-active electrochemical study on the coupling interaction between unirradiated 20/25/Nb stainless steel AGR cladding (as a surrogate for irradiated 20/25/Nb AGR cladding) and 25 GWd/tU AGR SIMFUEL (as a surrogate for irradiated AGR SNF), to support the analogous composite electrode studies of the real legacy AGR SNF, presented in Chapter 6.

This study also aims to address the knowledge gap in existing literature on the analogous electrochemical studies of the pellet-cladding interactions between AGR cladding and AGR SNF or SIMFUELs, and particularly in the study of coupled or composite electrodes [169, 170].

The primary objective of the study presented in this chapter was to explore routes to replicate the legacy AGR SNF composite electrode setup, seen in Figure 5-1(a).

Pursuant to this, two methods of electrode coupling were investigated to study the coupling between a sample of 25 GWd/tU SIMFUEL with a sample of 20/25/Nb AGR cladding. The two electrode coupling methods used are as follows:

a. Method-1 (M1) – consists of two separate resin cast “lollipop” electrodes of (i) a 25 GWd/tU SIMFUEL pellet, seen in Figure 5-1(c) and (ii) a cross-

sectional piece of 20/25/Nb AGR cladding, seen in Figure 5-1(e). These are coupled together via a conducting copper cable to form a single working electrode. Figure 5-1(d) shows the schematic for a typical electrochemical cell experimental circuit set-up used for Method-1 coupling, highlighting the single connection that electrically joins the SIMFUEL and cladding electrodes to the working electrode connector.

b. Method-2 (M2) – consists of a single “lollipop” electrode containing both a 25 GWd/tU SIMFUEL pellet and a cross-sectional piece of 20/25/Nb AGR cladding, cast together in resin to form a single composite electrode wherein both components are physically as well as electrically coupled, as seen in Figure 5-1(f).

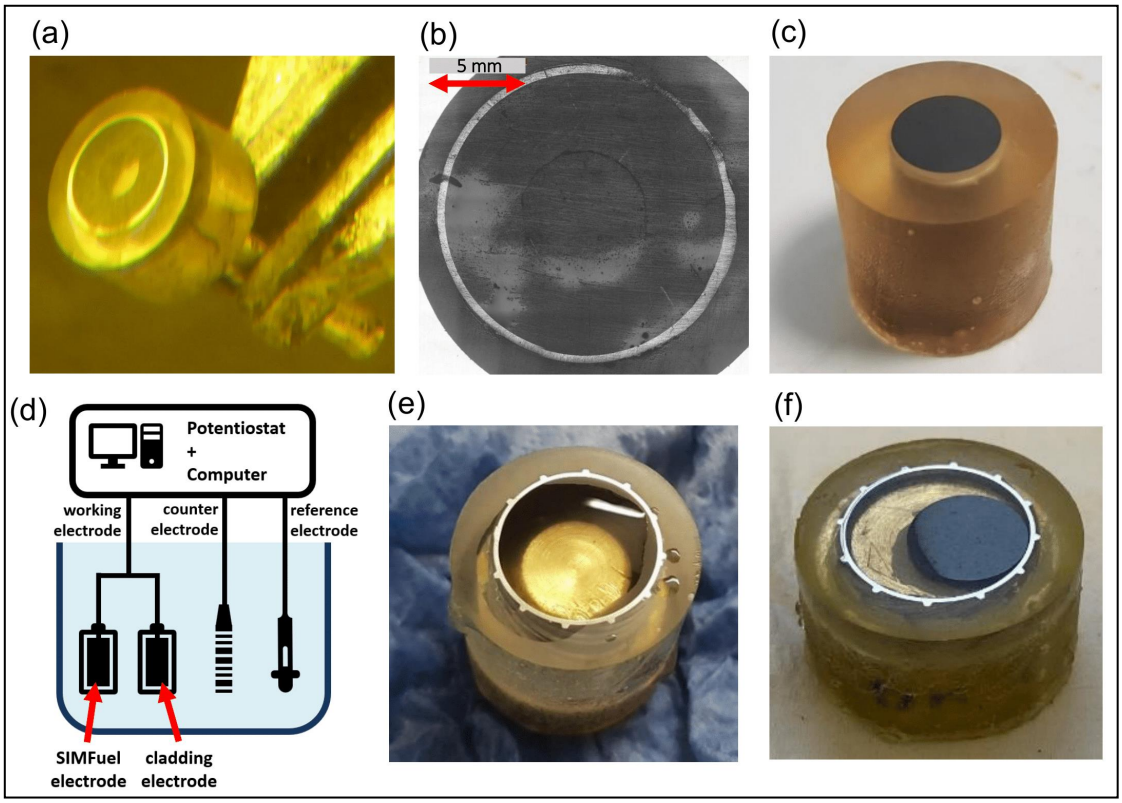

Figure 5-1: **(a)** side-on perspective view of AGR fuel cast in Araldite resin to form a “lollipop” electrode, **(b)** top-down photograph of AGR fuel electrode surface, **(c)** side-on view of 25 GWd/tU SIMFUEL pellet cast in resin to form an electrode, **(d)** schematic showing the circuit set-up used for coupling of the SIMFUEL electrode and cladding electrode in Method-1 (see text), **(e)** 20/25/Nb stainless-steel cladding cast in resin to form an electrode, **(f)** composite electrode comprised of a 25 GWd/tU SIMFUEL pellet and 20/25/Nb stainless-steel cladding cast into a single electrode for use in Method-2 studies (see text) Figure taken from Huang Y. et al., 2022 *[168]*.

These two coupling methods used will thus enable us to determine which mode(s) of SIMFUEL + cladding coupling will best replicate the real-fuel composite electrode system from the perspective of its corrosion behaviour.

Thus the single component electrochemical studies of the standalone AGR cladding and SIMFUEL electrodes, presented in Chapter 4 Section 4.5, and conducted under the same experimental conditions employed in the work of this chapter, will be used to inform the analysis of the results presented in this chapter.

For each coupling method, measurements were conducted across two different studies, to replicate the measurements carried out during the legacy AGR SNF experimental campaign, presented later in Chapter 6.

The first study was to investigate the electrochemical behaviour of the coupled electrode systems under conditions relevant to interim pond storage, using a Simplified Simulant Pond Water solution, SSPW, described in Chapter 3.

These experiments were intended to study the electrochemical behaviour of both coupled electrode systems under wet pond storage conditions and specifically at pHs of 8, 11.4 and 12.5, respectively representative of, undosed pondwaters, pondwaters subject to the current caustic dosing strategy, and pondwaters subject to a potential future dosing strategy.

The second study was to investigate the effect of chloride ion concentration on the electrochemical behaviour of both the coupled electrode systems in electrolyte solutions containing chloride concentrations at 0.1, 1.0, 10 and 100 mmol/dm^3 NaCl, dosed with NaOH to pH of 8, 11.4 and 12.5, again representative of, respectively, undosed pondwaters, pondwaters subject to the current caustic dosing strategy and pondwaters subject to a potential future dosing strategy. The concentration of chloride used in these measurements represents the increasingly severe maloperation scenarios where pond storage water experiences a drastic increase in chloride levels from an external source, e.g., sea water incursion.

Measurements were primarily carried out using OCP and LSV electrochemical techniques, under the same experimental methods and conditions as those

used in the analogous single component electrode studies presented in Chapter 4 Section 4.5.

The following results and discussions will enable assessment of the corrosion behaviour of these coupled/composite electrode systems and will enable comparison with the analogous single component electrode studies of Chapter 4 Section 4.5. These will, in turn, enable subsequent interpretation and comparison with the legacy AGR SNF studies presented later in Chapter 6.

5.2 Measurements in Simplified Simulant Pond Water

This section presents the comparative electrochemical study of the two-electrode coupling systems, Method-1 and Method-2, conducted using OCP and LSV studies in SSPW electrolyte solutions containing 30 μmol/dm^3 NaCl and dosed to pH 8, 11.4 and 12.5.

OCP measurements were recorded over a 15-hour period. LSV measurements were recorded between a range of -0.8 to 1.5 V at 1 mV/s. Electrolyte solutions were not purged to remove oxygen, to best simulate the conditions used in legacy AGR SNF studies, presented in Chapter 6.

The results and discussions presented in this section contain text and figures adapted from the publication of the preliminary results from this study, in Huang et al., [168].

As mentioned above, comparisons were made with the results from the single component studies of the standalone AGR cladding and SIMFUEL electrodes, presented in Chapter 4, Section 4.5, carried out under the same methods and conditions as the work presented in this chapter.

Experimental repeats for the OCP and LSV measurements were recorded to assess the repeatability of the measurements under each electrode coupling method. Discussions of the outcomes from the repeat datasets are provided in the following results and discussions sections.

5.2.1 Results & Discussion (OCP & LSV)

Figure 5-2(a) shows the measured OCP as a function of time for a series of experiments, recorded in accordance with M1 in SSPW at pH 8, 11.4 and 12.5.

These pH conditions are representative of, respectively, undosed pondwaters, pondwaters subject to the current caustic dosing strategy and pondwaters subject to a potential future dosing strategy.

For comparison, Figure 5-2(b) shows analogous OCP measurements conducted on standalone AGR cladding and 25-SIMF electrodes. Figure 5-2(c) shows polarisation curves, again measured in accordance with M1, recorded in SSPW at pH 8, 11.4 and 12.5. For comparison, Figure 5-2(d) shows analogous polarisation curves of standalone AGR cladding and 25-SIMF electrodes.

As seen in Figure 5-2(c) and in all subsequent polarisation curves shown in this chapter, the LSV data in the form of polarisation curves have been constructed using non-surface-area-normalised current values on the y-axis, unless otherwise stated.

This is due to the use of mixed-component coupled electrode systems of M1 and M2, which are comprised of two different electrode materials, each with different electrode surface areas that contribute to the total electrode surface area.

Thus, it would be inaccurate to calculate the surface-area-normalised current densities, given the uncertainty in the behaviour of the mixed-component coupled electrode systems. This adjustment will allow a qualitative comparison between the shape and form of the polarisation curves across the different studies presented in Chapters 4, 5, and 6.

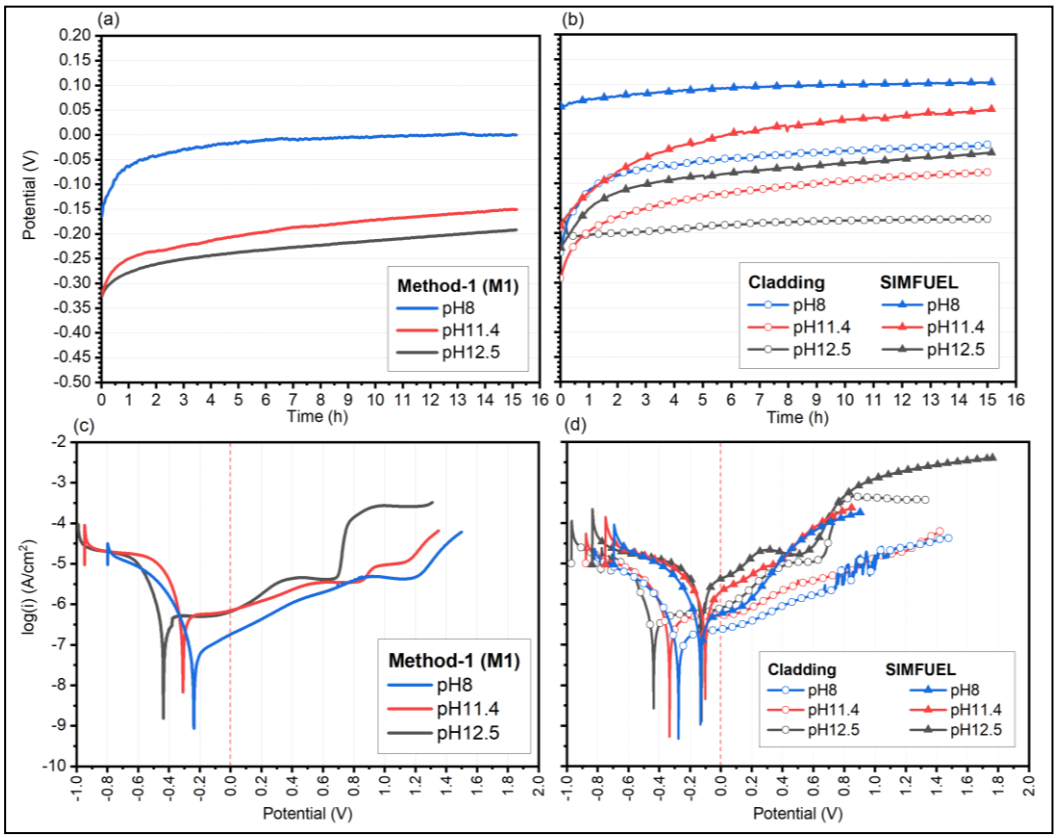

Figure 5-2: **(a)** OCP measurements as a function of time obtained during Method-1 studies of coupled 25-SIMF and cladding samples, compared with, **(b)** similarly recorded OCPs of separated cladding and 25-SIMF electrodes (OCP measurements recorded over 15 hours in 30 μmol/dm^3 NaCl), **(c)** Method-1 polarisation curves of coupled 25-SIMF and cladding samples compared with, **(d)** polarisation curves of separated cladding and 25-SIMF electrodes (LSV measurements recorded in 30 μmol/dm^3 NaCl, 1 mV/s scan rate)

Initial comparison of the M1 OCPs of Figure 5-2(a) with Figure 5-2(b), appears to show M1 OCP behaviour being more similar to that of the cladding OCP of Figure 5-2(b), suggesting that the anodic process that controls the mixed potential of the OCP is that which occurs on the cladding. Similarly, initial comparison of the M1 polarisation curves of Figure 5-2(c) with Figure 5-2(d), appears to show an LSV current response that, again, is similar to that of the cladding polarisation curve of Figure 5-2(d).

However, subsequent M1 experiment repeats, as shown in Figure 5-3, showed a range of results wherein the OCP and LSV data exhibited a mixture of SIMFUEL-dominated and cladding-dominated behaviour. Despite this, the general trend of decreasing OCP with increasing pH remains true regardless of the dominating electrode component.

For the cladding material, the increase in pH and associated decrease in OCP provides the steel with more protection against transpassive corrosion, by both driving the potential at which the onset of passive layer formation occurs, more negative and that at which the onset of transpassivity occurs, more positive.

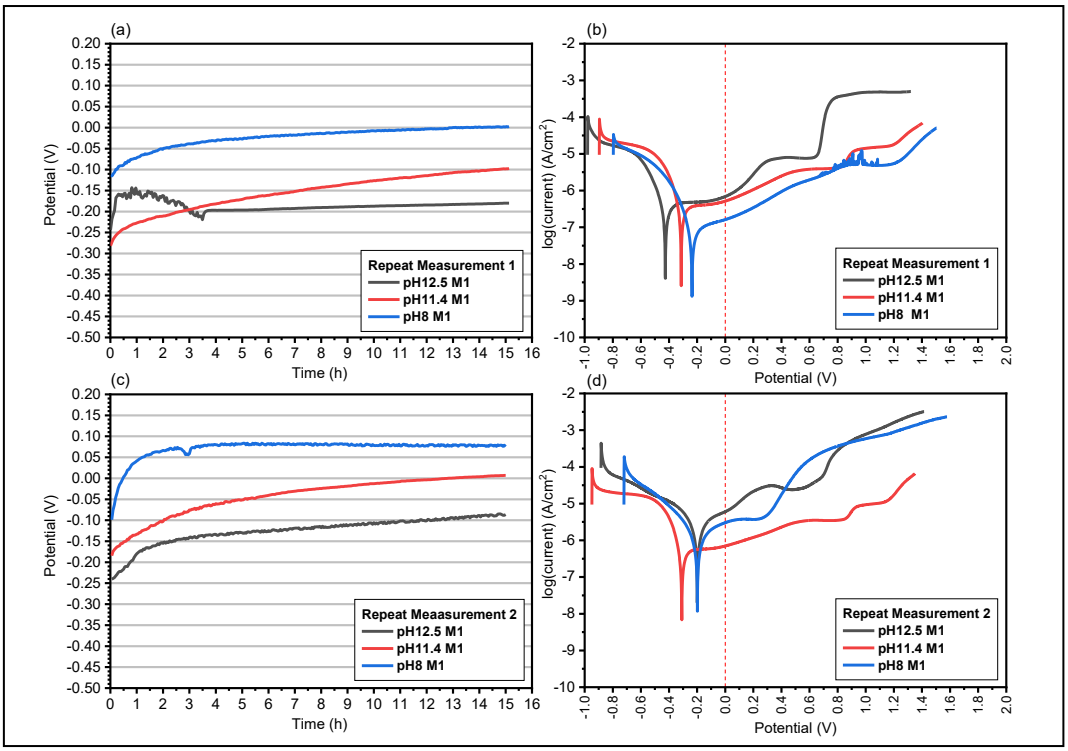

Figure 5-3: **(a)** experimental repeat no.1 of the OCP measurements shown in Figure 5-2(a), **(b)** experimental repeat no.1 of the LSV measurements shown in Figure 5-2(c), **(c)** experimental repeat no.2 of the OCP measurements shown in Figure 5-2(a), **(d)** experimental repeat no.2 of the LSV measurements shown in Figure 5-2(c). Experimental repeats were conducted according to the same methodologies and conditions as those used for Figure 5-2.

In any DC electrical system presenting more than one possible current path, the majority of the current will flow through the path with the least total resistance. Thus, the voltammetric behaviour of the coupled system will be predominantly controlled by the route that provides the least overall electrical resistance.

In the case of the experiments reported here, the overall resistance of the electrochemical system will be derived from a combination of the in-series contact, electrode material, bulk electrolyte and polarisation resistances, the last of these representing the electrochemical processes that occur at the surface of either the 25-SIMF or the cladding electrode.

On this basis, two current paths are possible in an M1 experiment, through the SIMFUEL or through the cladding, as observed in the LSV data. However, based on the data shown in Figure 5-2 and the repeat datasets of Figure 5-3, the preferred current path is not clear.

Figure 5-4(a) shows the measured OCP data, recorded in accordance with M2 in SSPW at pH 8, 11.4 and 12.5. For comparison, Figure 5-4(b) shows analogous OCP measurements of standalone AGR cladding and 25-SIMF electrodes under the same measurement conditions.

Comparison of the M2 OCPs in Figure 5-4(a) with the OCPs of Figure 5-4(b) suggests that OCP behaviour is dominated by the SIMFUEL component. This observation is consistent across experimental repeats, unlike the irreproducibility seen with the M1 OCP and LSV measurements.

Consistent with the M1 OCP data of Figure 5-2, the M2 OCPs are also driven more negative with increasing pH, which moves the equilibrium potential further negative of regions in the LSV (see Figure 5-4(c) and below) where oxidation of UO_{2+x} to UO_2^{2+} with subsequent dissolution occurs, i.e., oxidative dissolution becomes more unlikely as pH is increased [15].

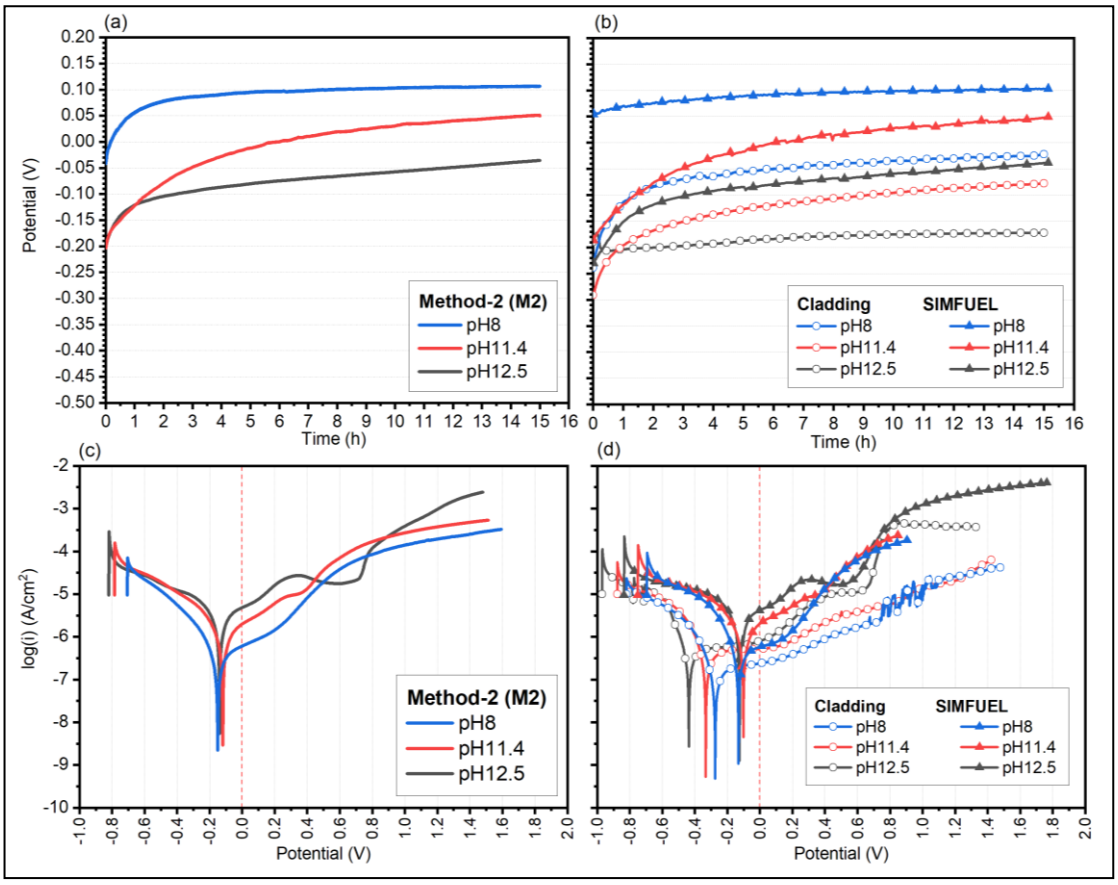

Figure 5-4: **(a)** OCP measurements as a function of time obtained during Method-2 studies of coupled 25-SIMF and cladding samples, compared with, **(b)** similarly recorded OCPs of separated cladding and 25-SIMF electrodes (OCP measurements recorded over 15 hours in 30 μmol/dm^3 NaCl), **(c)** polarisation curves of Method-2 coupled 25-SIMF and cladding samples compared with, **(d)** polarisation curves of separated cladding and 25-SIMF electrodes (LSV measurements recorded in 30 μmol/dm^3 NaCl, 1 mV/s scan rate)

Figure 5-4(c) shows polarisation curves, measured in accordance with M2 in SSPW at pH 8, 11.4 and 12.5, compared with Figure 5-4(d) which shows the analogous polarisation curves of the standalone cladding and SIMFUEL electrode.

Comparison of the M2 polarisation curves of Figure 5-4(c) with those of Figure 5-4(d), reveals an M2 current response that is similar to the SIMFUEL component.

Unlike the M1 measurements and its repeats, this observation is consistent across the M2 experimental repeats, suggesting that the combined M2 surface electrochemistry is reproducibly controlled by processes taking place at the 25-SIMF surface, such as the oxidation of UO_2 to UO_{2+x}, and that these must be

kinetically or thermodynamically more favourable than those happening at the cladding surface, where passivation of the steel surface is expected.

Since the voltammetric behaviour observed in the LSV data of the M2 experiment of Figure 5-4(c) can be seen to be dominated by that of the SIMFUEL component, the interpretation of the polarisation curves from the SSPW LSV studies of the 25-SIMF, presented in Chapter 4 Section 4.5.1.1, can also be applied to the M2 polarisation curves. Thus, the forms of the M2 polarisation curves shown in Figure 5-4(c) can be summarised as follows [32, 64]:

- At pH 8 and applied potentials < 0.2 V, the current reflects the oxidation of UO_2 to UO_{2+x} at the 25-SIMF surface. As applied potential increases above 0.2 V, the onset of anodic dissolution at the surface to produce UO_2^{2+} species takes place, which can further react with OH^- and H_2O to form a hydrated layer that may part-passivate the surface [66, 171].
- At pH 12.5 and applied potentials < 0.2 V, similar surface oxidation processes are taking place as those described at pH 8. At applied potentials > 0.2 V, the electrogenerated U(VI) reacts to form a hydrated layer that part-passivates the surface. At greater positive overpotentials, the breakdown of the hydrated layer occurs in the form of the soluble hydroxy-anion, $UO_2(OH)^-$, resulting in higher currents being passed [59, 172].
- At pH 11.4, the behaviour presents an intermediate between the two pH extremes described above, albeit with a closer resemblance to the behaviour at pH 8.

It is evident from the comparisons between the M1 and M2 data sets that the voltammetry behavior between the electrodes of M1 and M2 are different, despite both coupled-electrode systems and respective electrolytes being compositionally and electrically identical.

In Method-2, the 25-SIMF component dominates the electrochemical behaviour both under open circuit conditions and when under an applied potential. This behaviour is consistent across experiment repeats and provides confidence for the reproducibility of further M2 experiments.

We hypothesise that, initially, the current would be expected to travel from the external circuit to the electrode-electrolyte interface through the cladding component, since its bulk material resistance is less than that of the 25-SIMF component.

However, it appears that, under the low chloride, alkaline pH conditions explored here, the interfacial/polarisation resistance at the cladding-electrolyte interface is greater than that at the SIMFUEL-electrolyte interface – with the current then passing into solution through the latter, less resistive path.

Again, under the low chloride, alkaline pH conditions explored here, we would expect the cladding surface to be protected at OCP and potentials positive of OCP by a passivating oxide layer [106], and it may be this protective layer that is potentially inhibiting current flow at the surface of the cladding.

The SIMFUEL component, under the same conditions, would be at overpotentials suitable to initiate oxidation and dissolution, especially at pH 11.4 and 12.5, therefore allowing the passage of current across the SIMFUEL-electrolyte interface.

In Method-1, the experimental repeats of OCP and LSV measurements indicate that the preferred current path is inconsistent and unclear. The same reasoning used for explaining the behaviour of Method-2 should also apply to Method-1, since they are compositionally and electrically identical, differing only by the method of electrode coupling. This phenomenon where the M1 system exhibits a mixture of behaviors across experimental repeats, suggests the possibility of other factors.

Therefore, we hypothesise that under the experimental conditions employed in this study, due to the aforementioned passivating oxide layer – which might be expected to form over the potential range of approximately -1.0 to 0.7 V – the combined total resistances derived from the electrochemical processes associated with the AGR cladding must sometimes be greater than that of the combined total resistances of the same processes associated with the 25-SIMF, such that the preferred current path is through the SIMFUEL component.

As described above, under the applied potential conditions employed here, the dominant electrochemical process at the 25-SIMF surface is the oxidation of UO_2 to UO_{2+x} and subsequent oxidative dissolution via UO_2^{2+}, whilst on the steel surface, growth of the passive oxide layer is preferred – see Figure 4-36 and its interpretation.

The processes at the 25-SIMF surface are facile and may readily generate appreciable current through the electrode. In contrast, the processes at the AGR cladding surface may passivate the electrode surface, impeding current flow.

However, the passivation afforded at the cladding surface by the oxide layer may be compromised by adventitious corrosion processes such as pitting and crevice corrosion, therefore allowing current to pass through, as shown in the Method-1 experiments.

The inconsistency of current passage through the cladding under OCP and LSV measurement conditions, may also reflect the highly surface preparation dependent nature of such corrosion processes.

Additionally, from the studies presented in Chapter 4 Section 4.5.1.1and Section 4.5.2.1, electrochemical impedance spectroscopy measurements have been conducted on standalone electrodes of 25-SIMF and AGR cladding, respectively, under the same measurement conditions as those employed in this chapter.

The fitted resistance values were used to understand the inconsistency observed in the electrode current paths of the M1 electrode. From the plots of total resistance, R(total), versus applied potential (see Figure 4-42 and its interpretation), it was found that the resistance associated with the AGR cladding electrochemical system was approximately 5 – 10 times larger than the resistance associated with the 25-SIMF material, under the same applied potential measurement conditions.

This information may now be used to develop an understanding of the current path in the M1 and M2 combined electrode configurations, as follows.

Figure 5-5 shows a plot of the solution + contact resistance, R(s), as a function of applied potential for both the AGR cladding and the 25-SIMF – taken from Table 4-2 and Table 4-4. The data, methodology, and justifications used for EIS fitting are presented in Chapter 4 Section 4.5.2.1 and Section 4.5.1.1, respectively.

It can be seen from Figure 5-5 that, at all three pHs studied, the R(s) vs. applied potential plots for the AGR cladding and the 25-SIMF electrodes are very similar, suggesting that they arise from a common source.

Since the electrolyte is the only electrochemically resistive component common to both systems at any one pH, then this observed similarity supports the assignment of the R(s) in-series resistor component, as seen in the respective AGR cladding and 25-SIMF EECs (Electrochemical Equivalent Circuits) of Chapter 4 Section 4.5.2.1 Figure 4-41 and Section 4.5.1.1 Figure 4-30, as being due to the solution/contact resistance combination.

This observation provides further support towards the assignment of the remaining EEC resistor components as the combined total resistances, R(total), of either the AGR cladding or the 25-SIMF electrochemical systems.

This support for the assignment of R(total) then allows for comparisons to be made between the R(total) values of the AGR cladding and 25-SIMF electrodes and the differences between those values to be used in understanding the current path in the M1 and M2 experiments.

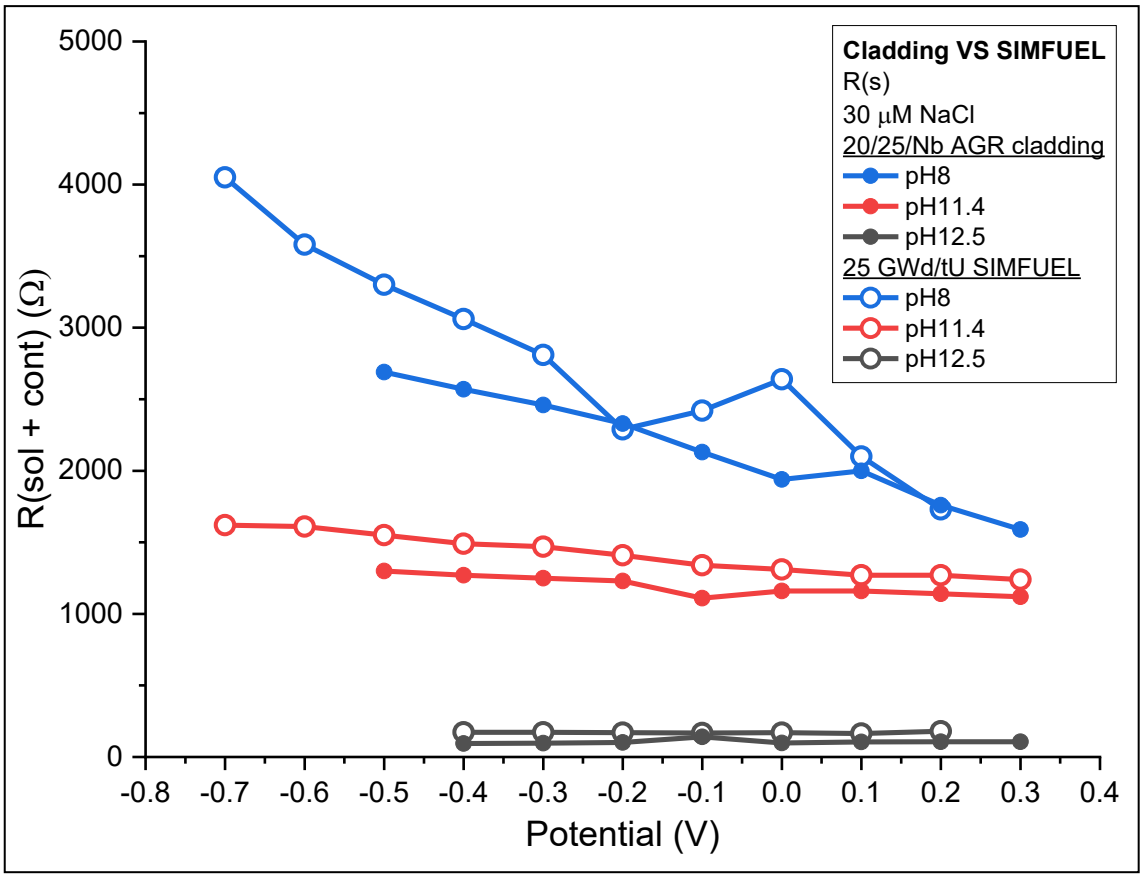

Figure 5-5: Plot of R(s) as a function of potential obtained from equivalent circuit fitting of EIS data comparing AGR cladding and 25-SIMF, measured in 30 μmol/dm^3 at pH 8, 11.4 and 12.5. Adapted from data presented in Chapter 4 Section 4.5.1.1 and Section 4.5.2.1.

Accordingly, Figure 5-6 (a combination of Figure 4-31 and Figure 4-42) shows a plot of total resistance values, R(total), as a function of applied potential for both separate AGR cladding and 25-SIMF electrodes when immersed in electrolytes at pH 8, 11.4, and 12.5 as before, and shown in this comparative form for the first time in this thesis.

These resistances are derived from electrochemical equivalent circuit fitting of EIS data, shown earlier in Table 4-2 and Table 4-4, with each value of R(total) representing the total of the bulk electrode, polarisation, charge transfer and space charge layer resistances that obtain at the applied potential in question for each electrode system.

The data, methodology, and justifications used for EIS fitting are presented in Chapter 4 Section 4.5.1.1 and Section 4.5.2.1. The resistance values remain relatively similar and constant during the initial application of potential below ~-0.2 V, but at applied potential increases above ~-0.2 V, the resistances for each

material increases, with AGR cladding becoming significantly more resistive than the 25-SIMF.

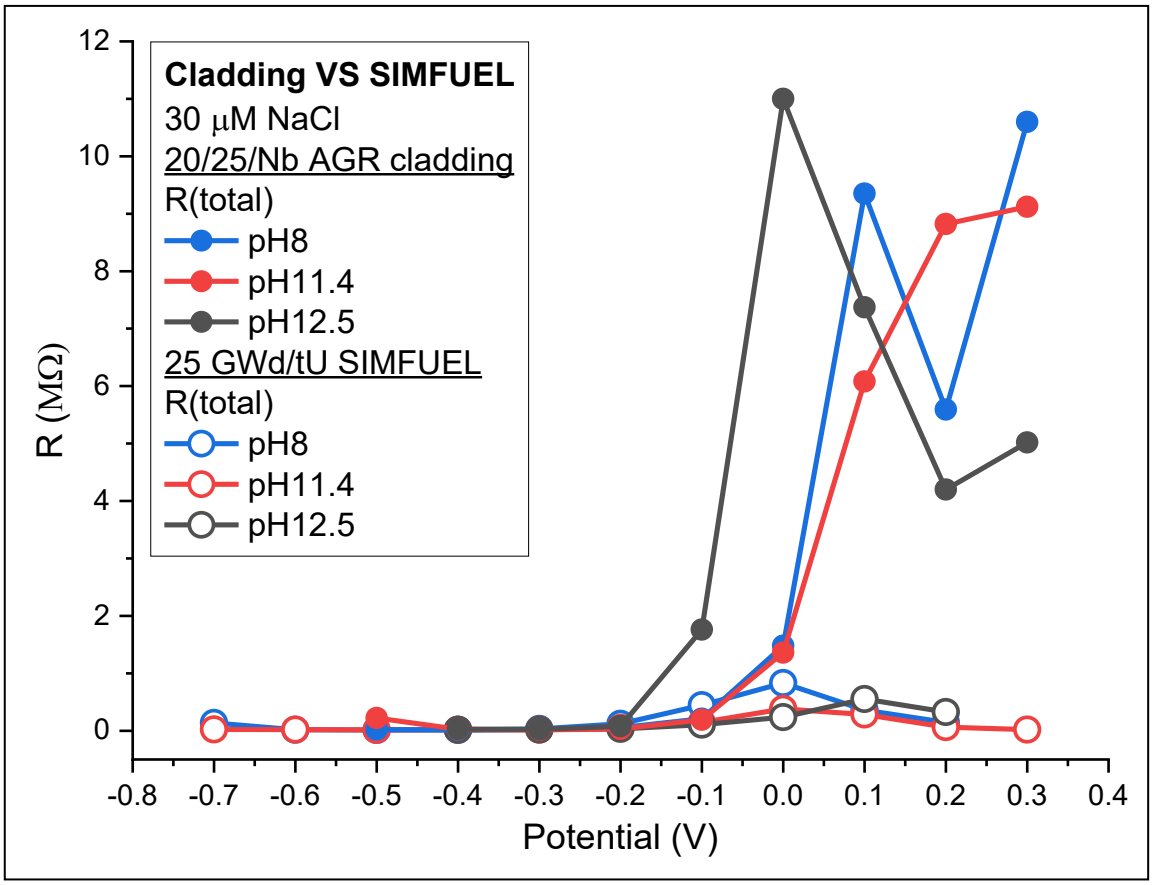

Figure 5-6: Plot of R(total) as a function of potential obtained from equivalent circuit fitting of EIS data comparing AGR cladding and 25-SIMF, measured in 30 μmol/dm^3 at pH 8, 11.4 and 12.5. Adapted from data presented in Chapter 4 Section 4.5.1.1 and Section 4.5.2.1.

These observations provide strong support to the hypothesis proposed above, in which the measured current is seen to be preferentially passing through the SIMFUEL component in M2 experiments, during the application of potential.

The increased resistance of the cladding material, at the overpotential range that is responsible for passive layer growth, is significantly larger than that of the 25-SIMF at the same overpotentials.

Thus, in an M2 experiment, the current is expected to preferentially pass through the SIMFUEL component. However, based on the LSV data of the M1 electrode, this effect is not seen during the M1 experiments despite the electrode system being electrically and compositionally identical, suggesting that other factors may be involved, as alluded to above.

These could include factors related to, for example, the method of electrode coupling and/or electrode surface finish effects:

Influence of surface finish

- A rough or uneven electrode surface finish can result in an increased surface area when compared to an equivalent polished or smooth electrode surface finish.
- This can result in changes to the current density due to the increased effective surface area available for electrochemical reactions to take place. In the case of stainless steel electrode surfaces, the presence of surface roughness, such as pits or cracks/crevices, can also act as preferential locations for localised corrosion due to the trapping of impurities that are favourable to steel corrosion i.e., trapped chloride ions. These preferential sites of localised corrosion can divert the flow of current during a voltammetry measurement.
- Differences in polishing between M1 and M2. The M1 individual components are polished separately and can achieve much better polishing due to better care taken when polishing individual standalone electrodes.
- Whereas the M2 composite electrode contains both the harder steel cladding material and the softer 25-SIMF pellet together in in electrode, resulting in an uneven polishing with a bias towards the harder steel cladding material, thus preventing the 25-SIMF from achieving a good polish.

Influence of electrode coupling method:

- The different methods in which the M1 and M2 electrodes are coupled may also influence the current path during electrochemical measurements.
- Figure 5-1(d) and (f) illustrates respectively, the M1 and M2 coupling methods, although both methods of coupling are electrically identical, we speculate that this could be introducing differences in the preferred current paths between M1 and M2, particularly in the case of the M2 electrode where both the SIMFUEL and cladding components are in

direct contact with each other, which may decrease the available current path options.

- For instance, in the case of M1, the current may only flow either through the cladding OR the SIMFUEL. Based on the R(total) data of Figure 5-6, it would be expected that the current would prefer to always flow through the SIMFUEL due to the resistive nature of the steel, this resistive nature presumably being derived predominantly from the passive layer on the steel given the metallic and thus highly conductive nature of the steel body.
- However, if that passive layer is disrupted due to surface finish effects described above, the primary source of resistance in the cladding current path may be removed and thus current switches from passing through the SIMFUEL to the cladding.
- In the case of M2, the current will most likely always pass to the electrode surface through the cladding, so obviating the expected greater resistance associated with the SIMFUEL bulk. However, once at the electrode surface, the current may then participate in interfacial charge transfer through either the steel with its associated passive layer, or the SIMFUEL.
- Given the non-passivated nature of the SIMFUEL surface over all potentials and solution conditions studied here, it is then likely that the SIMFUEL route will always be preferred electrically, irrespective of the surface condition of the passive layer on the steel.

Figure 5-7 shows a diagram summarising the preferred current paths of each coupled electrode system, M1 and M2; the arrows display the hypothesised current paths at each pH. The dashed line arrows indicate uncertainty in the current path behaviour of the M1 electrode, in which OCP and LSV results have shown a mixture of cladding-dominated and SIMFUEL-dominated behaviours. The solid line arrows indicate certainty in the current path of the M2 electrode, in which OCP and LSV measurements have shown a consistent SIMFUEL-dominated behaviour.

For best experimental consistency, Method-2 would be the preferred method of electrode coupling to employ for future electrochemical studies which involve

simulating the physical composition of a real spent fuel sample and simulating the close contact between the cladding component and UO_2 fuel pellet component.

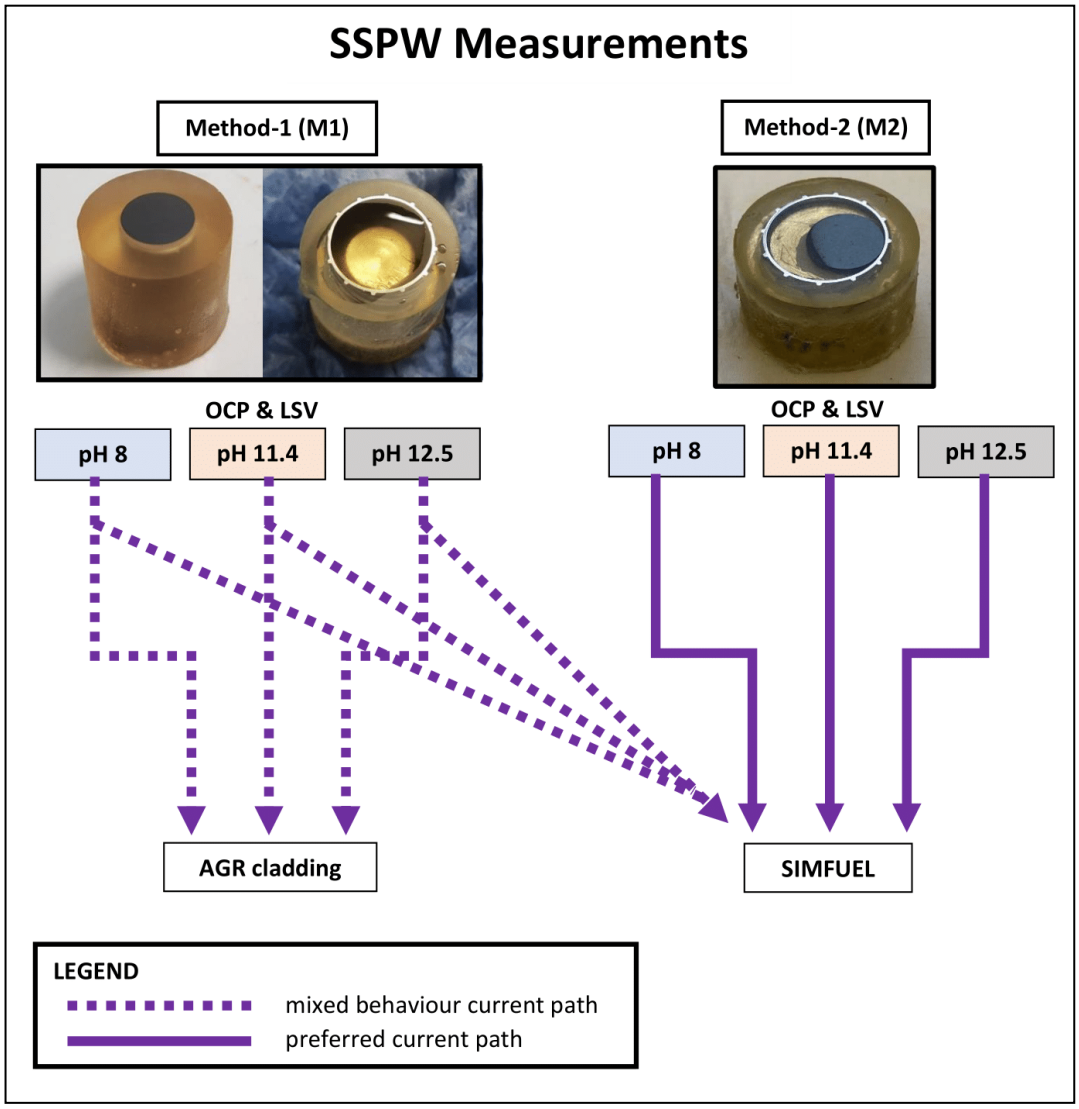

Figure 5-7: Diagram summarising the preferred current paths based on OCP and LSV data of Method-1 and Method-2 in SSPW conditions at pH 8, 11.4 and 12.5.

5.3 Measurements in Alkaline Chloride Water

This section presents the comparative study of the two-electrode coupling mechanisms, Method-1 and Method-2, conducted using alkaline chloride-containing electrolytes – specifically solutions containing concentrations of 0.1, 1.0, 10 and 100 mmol/dm^3 NaCl dosed to pH 8, 11.4 and 12.5. As before, OCP measurements were recorded over a 15-hour period.

LSV measurements were recorded between a range of -0.8 to 1.5 V at 1 mV/s. Electrolyte solutions were not purged to remove oxygen, to best simulate the conditions used in legacy AGR SNF studies, presented in Chapter 6.

As in the SSPW studies of Section 5.2, comparisons were made with the results from the single component studies of the standalone AGR cladding and SIMFUEL electrodes, described in Chapter 4 Section 4.5, and carried out using the same methods and under the same conditions as the work presented in this chapter.

Experimental repeats for the OCP and LSV measurements were recorded to assess the repeatability of the measurements under each electrode coupling method. Discussions of the outcomes from the repeat datasets are provided in the following results and discussions sections.

5.3.1 Results & Discussion (OCP & LSV)

Similarly to Section 5.2, the polarisation curves in this section will also be displayed using non-surface-area-normalised current values on the y-axis, unless otherwise stated and according to the same justifications.

Figure 5-8(a) shows the OCPs, measured as a function of time for experiments recorded in accordance with M1 in 0.1, 1.0, 10 and 100 mmol/dm^3 NaCl at pH 8, 11.4 and 12.5. For comparison, Figure 5-8(b) and (c) show the analogous OCP measurements conducted on standalone 25-SIMF and AGR cladding electrodes, respectively.

Initial comparison between the OCPs show a similarity between the M1 and AGR cladding data at pH 8 and 11.4 and a similarity between the M1 and 25-SIMF data at pH 12.5. However, subsequent M1 experimental repeats showed

a mixed behaviour in the OCP results – as seen in Figure 5-8(d). Wherein some data exhibited a SIMFUEL-dominated OCP behaviour and others a cladding-dominated OCP behaviour, independent of chloride concentration or pH.

The preferred current path is inconsistent and unclear; this uncertainty in the current path of the M1 electrode system under OCP conditions is the same as that observed in the Method-1 SSPW experiments, discussed in Section 5.2.

Figure 5-9(a) shows the measured OCPs for a series of experiments recorded in accordance with M2 in 0.1, 1.0, 10 and 100 mmol/dm^3 NaCl at pH 8, 11.4 and 12.5. For comparison, Figure 5-9(b) and (c) show the analogous OCP measurements conducted on standalone 25-SIMF and AGR cladding electrodes, respectively.

Comparison between the OCPs shows a similarity between the M2 and 25-SIMF data across all pHs. Here, the OCP behaviour is dominated by the SIMFUEL component, and this observation is consistent across experimental repeats and consistent with the Method-2 SSPW data of Section 5.2.

The OCP vs. time plots and their values as a function of pH, in Figure 5-8(a) and Figure 5-9(a), are consistent with observations from the analogous single component studies presented in Chapter 4 Sections 4.5.1.2 and 4.5.2.2. In general, the OCPs are driven more negative with increasing pH with the presence of chloride, up to 100 mM, having no effect on the OCPs of the standalone AGR cladding or 25-SIMF electrodes, and thus having no effect on the M1 or M2 electrodes.

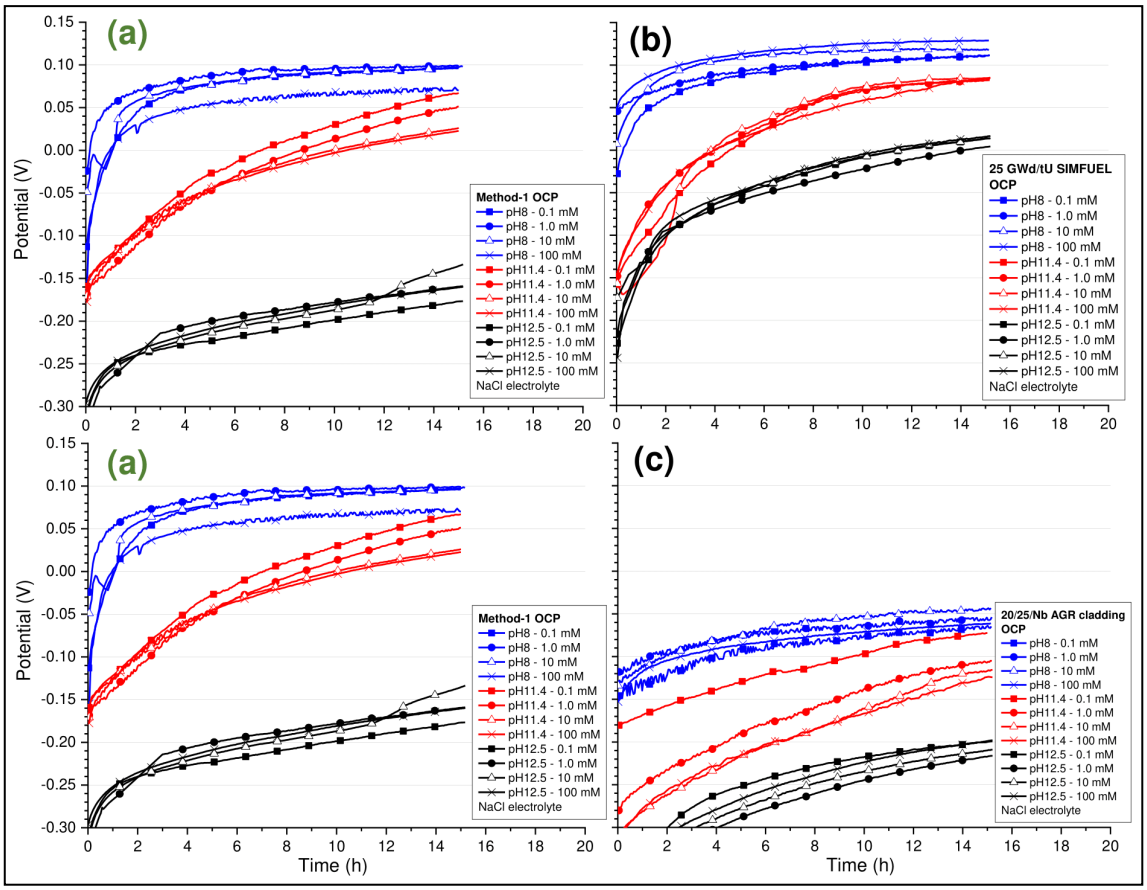

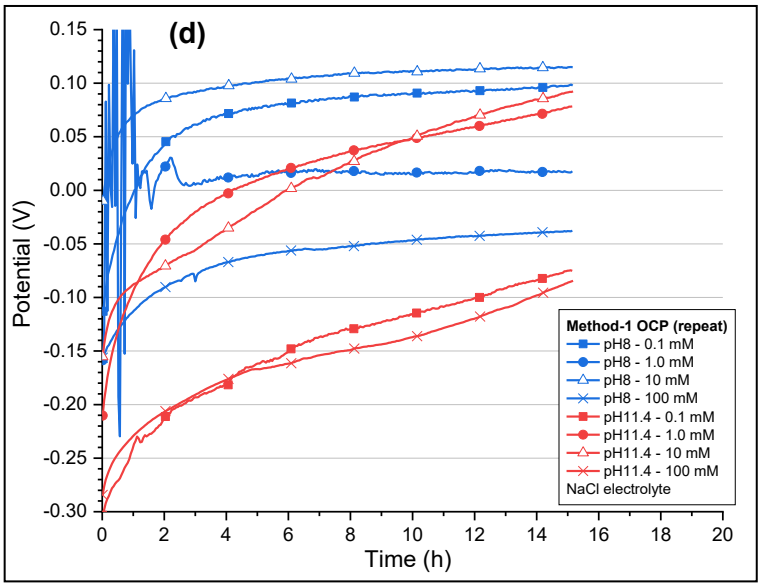

Figure 5-8: **(a)** Method-1 OCP measurements, compared with, **(b)** similarly recorded OCPs of 25-SIMF and with, **(c)** similarly recorded OCPs of AGR cladding (OCPs recorded over 15 hours in 0.1, 1.0, 10 and 100 mmol/dm^3 NaCl at pH 8, 11.4 and 12.5), **(d)** Method-1 OCP experiment repeat conducted at pH 8 and 11.4 to show the mixed behaviour occurring independent of [NaCl] and pH.

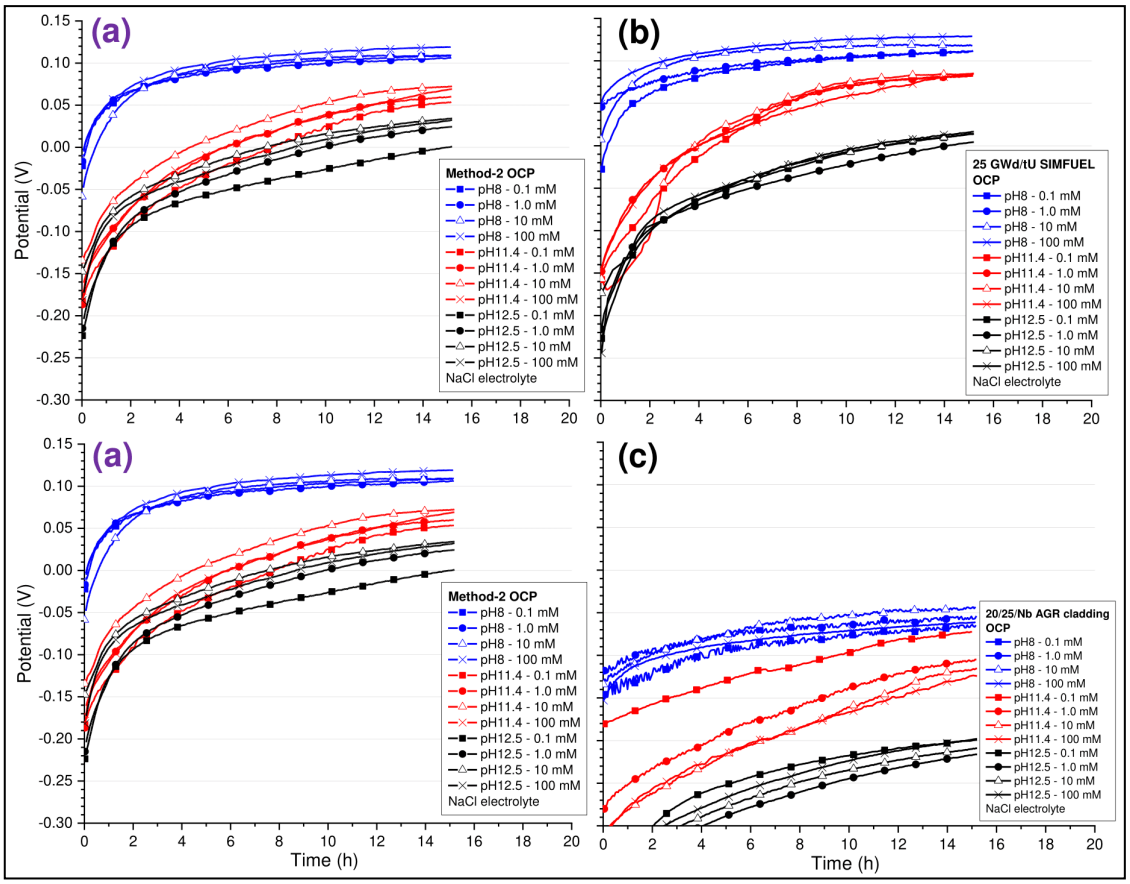

Figure 5-9: **(a)** Method-2 OCP measurements, compared with, **(b)** similarly recorded OCPs of 25-SIMF and with, **(c)** similarly recorded OCPs of AGR cladding (OCPs recorded over 15 hours in 0.1, 1.0, 10 and 100 mmol/dm^3 NaCl at pH 8, 11.4 and 12.5).

Figure 5-10(a) shows the polarisation curves measured in accordance with M1 in 0.1, 1.0, 10 and 100 mmol/dm^3 NaCl at pH 8, 11.4 and 12.5. For comparison, Figure 5-10(b) and (c) show the analogous polarisation curves from measurements conducted on standalone 25-SIMF and AGR cladding electrodes, respectively.

Similar to the OCP data discussed above, the M1 polarisation curves initially present a similarity with the AGR cladding data at pH 8 and 11.4 and a similarity with 25-SIMF data at pH 12.5. However, subsequent M1 experimental repeats showed a mixed behaviour in the LSV results – as seen in Figure 5-10(d), the uncertainty seen here is independent of the chloride concentration or pH.

The preferred current path of the M1 system under LSV measurement conditions is inconsistent and unclear, as with the M1 OCP measurements shown in Figure 5-8(a) and (d).

Figure 5-11(a) shows the polarisation curves measured in accordance with M2 in 0.1, 1.0, 10 and 100 mmol/dm^3 NaCl at pH 8, 11.4 and 12.5. For comparison, Figure 5-11 (b) and (c) show the analogous polarisation curves from measurements conducted on standalone 25-SIMF and AGR cladding electrodes, respectively.

Similar to the OCP data discussed above, the M2 polarisation curves exhibit electrochemical behaviour similar to the 25-SIMF data, suggesting that the applied potential behaviour is dominated by the SIMFUEL component. This observation is also consistent across experimental repeats.

The form of the polarisation curves and their values, in Figure 5-10(a) and Figure 5-11(a), are consistent with those observed in the analogous single component studies presented in Chapter 4 Section 4.5.1.2 and Section 4.5.2.2.

As with the observations from the SSPW studies, the electrochemical behaviour of the M1 and M2 coupled-electrodes, under LSV measurement conditions, is dominated by a single component – AGR cladding or 25-SIMF. This suggests that the coupling of the AGR cladding and 25-SIMF electrodes to form composite electrodes, does not alter the individual corrosion susceptibilities of the coupled systems in chloride concentrations up to 100 mM, at pH 8, 11.4, and 12.5, i.e., there are no synergistic/cooperative effects as a result of electrode coupling.

Corrosion behaviour and susceptibility of the coupled-electrode system is therefore best represented by the constituent components of the standalone AGR cladding or SIMFUEL electrodes.

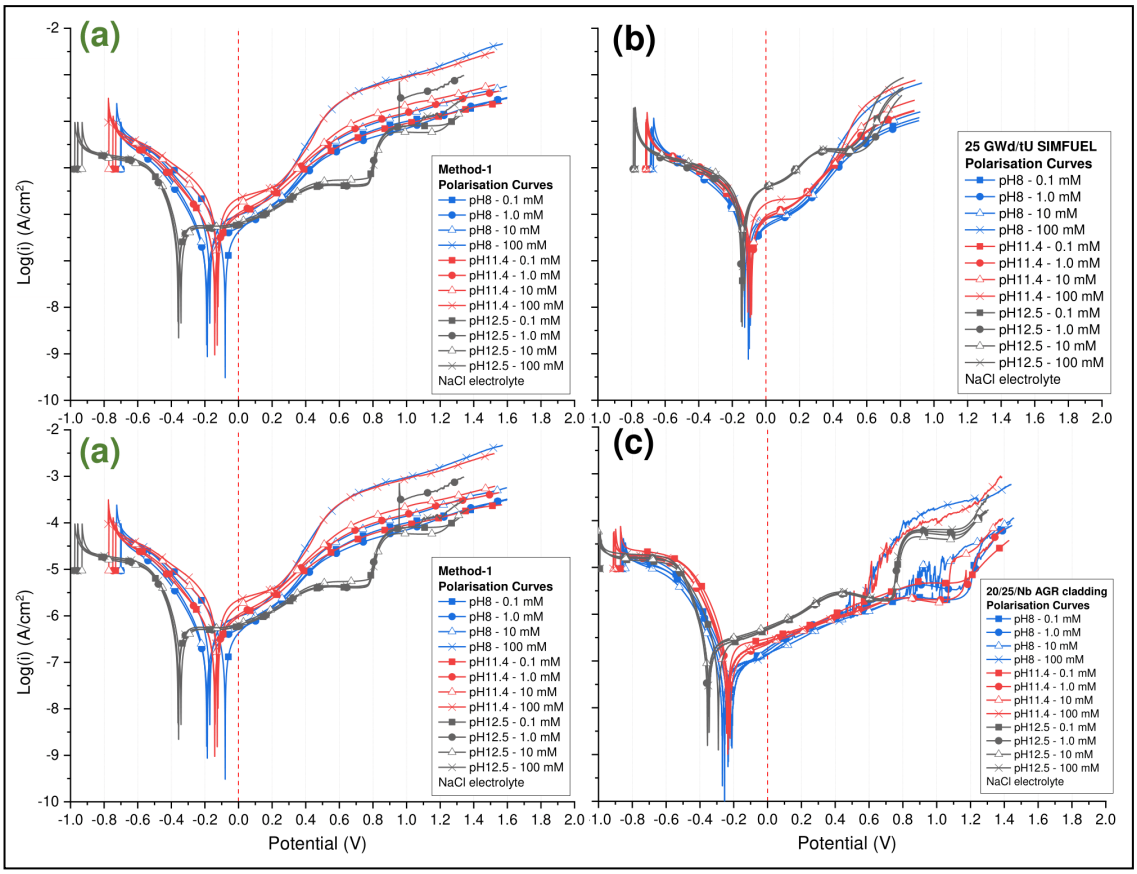

Figure 5-10: **(a)** Method-1 polarisation curves, compared with, **(b)** similarly recorded polarisation curves of 25-SIMF and with, **(c)** similarly recorded polarisation curves of AGR cladding (LSV measurements recorded in 0.1, 1.0, 10, 100 mmol/dm^3 NaCl at pH 8, 11.4 and 12.5, at 1 mV/s scan rate), **(d)** Method-1 LSV experiment repeat conducted at pH 8 and 11.4 to show the mixed behaviour occurring independent of [NaCl] and pH.

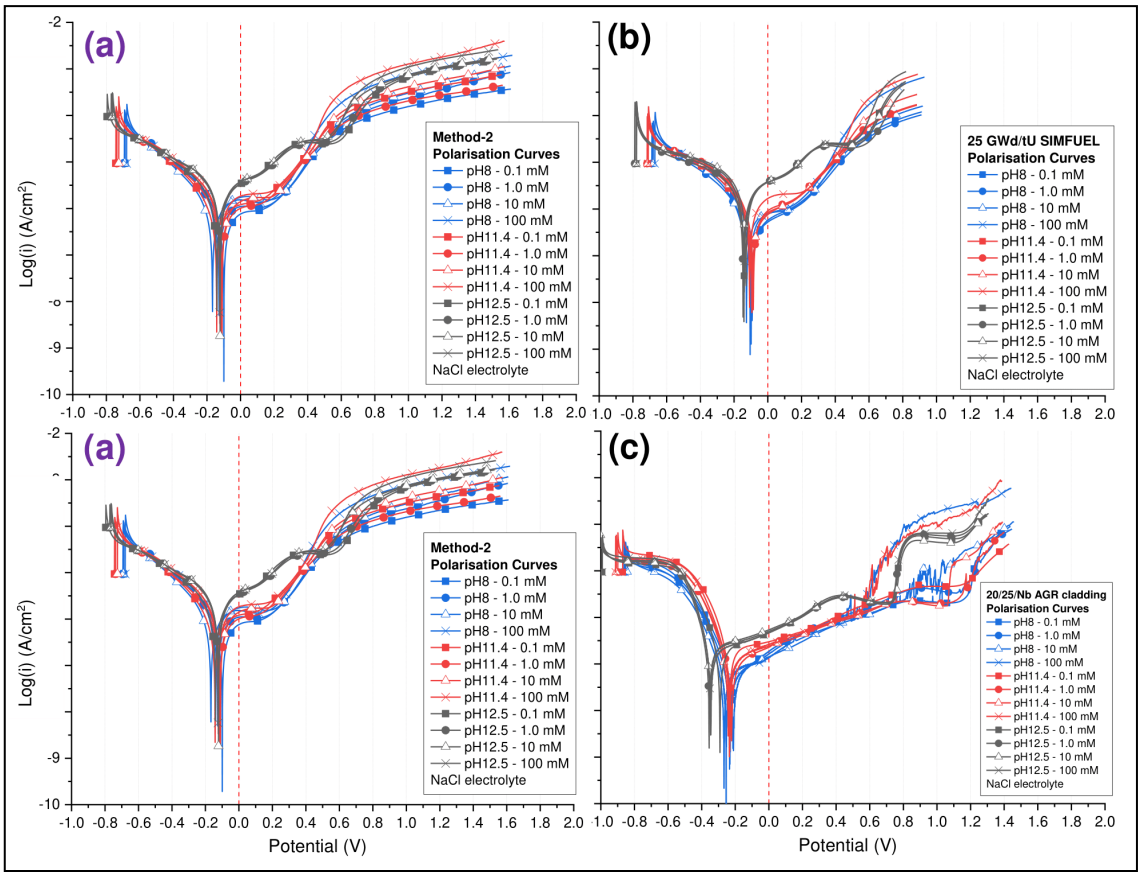

Figure 5-11: **(a)** Method-2 polarisation curves, compared with **(b)** similarly recorded polarisation curves of 25-SIMF and with **(c)** similarly recorded polarisation curves of AGR cladding (LSV measurements recorded in 0.1, 1.0, 10, 100 mmol/dm^3 NaCl at pH 8, 11.4 and 12.5, at 1 mV/s scan rate).

Figure 5-12 shows a diagram summarising the preferred current paths of each coupled electrode system M1 and M2. The same inconsistencies and trends are observed as with Figure 5-7; the M1 electrode produces data showing a mixture of cladding-dominated and SIMFUEL-dominated behaviour.

In contrast, the M2 electrode consistently produces data with SIMFUEL-dominated behaviour. The increase in chloride concentration is known to cause the breakdown of steel surface passive layers, making it more susceptible to corrosion [102].

The chloride dependence work discussed here has shown that increased chloride concentrations, of up to 100 mM NaCl, has no effect on the preferred current path of the M1 and M2 electrodes; the observations remain consistent with experiments conducted in SSPW 30 μmol/dm^3 NaCl, discussed in Section 5.2.

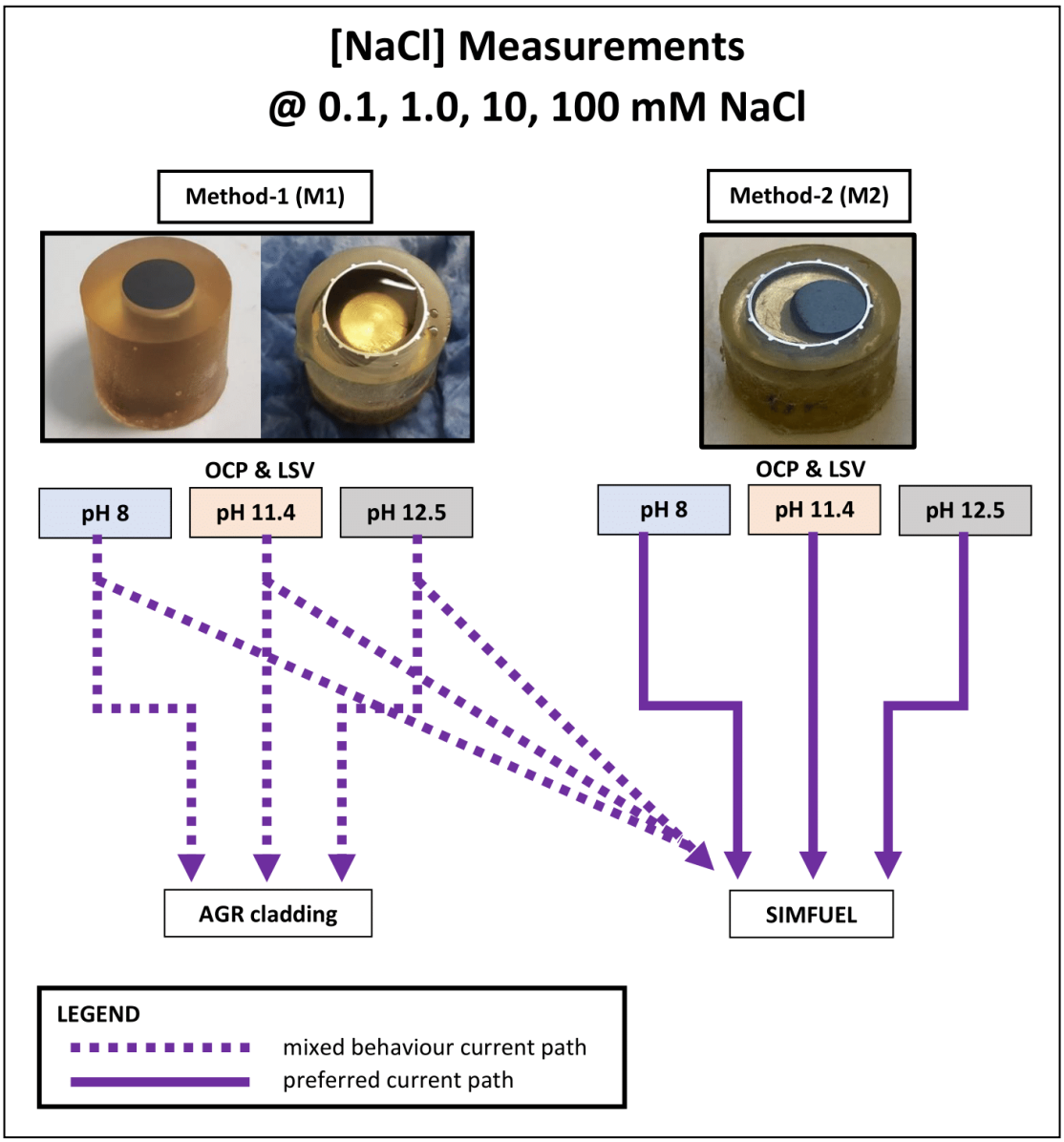

Figure 5-12: Diagram summarising the preferred current paths based on OCP and LSV data of Method-1 and Method-2 in various [NaCl] at pH 8, 11.4 and 12.5.

5.4 Summary & Further Work

In this chapter, we have demonstrated the use of simulant-based methods to replicate the electrochemical behaviour of a real AGR SNF electrode. Two mechanisms of electrode coupling were investigated, differing only by the mode of physical contact between the cladding and SIMFUEL. The two coupling methods show differing electrochemical behaviours in the simulant systems.

Measurements were conducted in the following simulant systems: Section 5.2 in SSPW 30 μmol/dm^3 NaCl at pH 8, 11.4 and 12.5 electrolyte solutions, and Section 5.3 in 0.1, 1.0, 10 and 100 mmol/dm^3 NaCl at pH 8, 11.4 and 12.5 electrolyte solutions.

This section provides a summary of the key findings.

1. Data from Method-2 experiments has shown that the SIMFUEL component dominates the electrochemical behaviour over all experiment types conducted. Thus, during M2 experiments, we hypothesise that the current path either: (i) passes wholly through the SIMFUEL material due to its lower total measured resistance, or (ii) passes through the cladding to the electrode-electrolyte interface, at which point it crosses into the SIMFUEL from which it drives the necessary Faradaic processes for interfacial electron transfer.
   In either case, the current passes into solution through the SIMFUEL-electrolyte interface and not the cladding due to the presence of a passivating layer at the cladding surface.
   However, the passage of the current to the SIMFUEL-electrolyte interface may be through either the cladding body or the SIMFUEL bulk – whichever has the lowest resistance.
   The data presented here does not allow for actual current route to the electrode-electrolyte interface to be unambiguously identified – although on a qualitative basis, it is not unreasonable to suggest that the resistance to the current passage through the metallic cladding body will be less than that through the ceramic SIMFUEL bulk and therefore the former will be preferred.
2. Data from Method-1 experiments has shown a deviation in experiment-to-experiment variation. Neither component dominates the observed electrochemical behaviour with no preference towards the SIMFUEL or cladding-dominated behaviour during either OCP or LSV measurements. However, it is hypothesised to be attributed to the influence of electrode surface finish and/or the method of electrode coupling.
3. Interpretation of EIS data from Chapter 4 Section 4.5.2.1 and Section 4.5.1.1, comparing the total resistances, R(total), of standalone

electrodes of AGR cladding and 25-SIMF, has shown that the cladding has an R(total) that is greater than that of the 25-SIMF, particularly at the overpotential range that is responsible for passive layer growth.
Hence, in the case of M2 the current could preferentially pass wholly through the SIMFUEL at these applied potentials. Although, as discussed in Conclusion 1 above, this possibility cannot be eliminated of the current passing to the electrode surface through the cladding before driving interfacial electron transfer processes on the SIMFUEL.

4. The observations relating to the behaviour of the preferred current paths during M1 and M2 OCP and LSV measurements, were not found to be correlated to the experimental parameters such as pH (at pH 8, 11.4 and 12.5) or chloride concentration (at 0.03, 0.1, 1.0, 10 and 100 mmol/dm^3).
5. Overall, the Method-2 electrode system gives the most consistent and reproducible results. The fabrication method also produces a “lollipop” electrode that better resembles the physical composition of a real AGR fuel pin cross-section, as the SIMFUEL pellet is in direct contact with the AGR cladding.
   For consistency, Method-2 would be the preferred method of electrode coupling to employ for future electrochemical studies that involve simulating the physical composition of a real spent fuel sample and simulating the close contact between the cladding and UO_2 fuel pellet.
6. Method-1 electrode system will require further work to determine the cause of the inconsistencies observed during the voltammetry measurements in both the presence and absence of chloride – although it is hypothesised that surface finish and mode of coupling may play a key role here.
7. Voltammetry data from both Method-1 and Method-2 can be deconvoluted and simplified to being dominated by one or the other of its individual dominant components. The recorded data is comprised of either the cladding or SIMFUEL component, with no evidence of a mixed/synergistic OCP or LSV behaviour arising from a combination of the two components.
   Therefore, it is more appropriate to use the single component voltammetry data of Chapter 4 Section 4.5 in conjunction with the M2

studies of this chapter, to support the real AGR SNF studies of Chapter 6. This eliminates the complexities and uncertainties associated with using M1 coupling method for the interpretation of the real AGR SNF composite electrode open circuit potentiometry or voltammetry.

5.4.1 Further Work

A recommendation for further work would be to conduct a repeat of the Method-2 measurements from the studies presented in this chapter, using undoped-UO_2 and unirradiated AGR cladding to form the working composite electrode. This would allow a comparison to be made between the electrochemical behaviour of the Method-2 composite electrode system against a baseline behaviour using the undoped-UO_2.

6 Electrochemical Studies of Legacy AGR Spent Nuclear Fuel

6.1 Introduction & Objectives

This chapter presents the first look at novel data gathered from the electrochemical study of a sample of legacy UK AGR SNF (irradiated in a commercial AGR between 1983 – 1989, fuel element average burnup of 12.2 GWd/tU and a stringer mean burn-up of 20.2 GWd/tU, located at element 1 position during in-reactor operation) (Figure 6-1), along with a discussion, due to the study's unique unconventional nature, of the experimental work methodology and measurement conditions.

For this study, a sample of irradiated AGR spent fuel was fabricated into an electrode suitable for electrochemical measurements, as described in Chapter 3 Section 3.1.3. The study was conducted in two parts.

The first involved an investigation of the spent fuel electrode's electrochemistry in a Simplified Simulant Pond Water (SSPW) composition, as described in Chapter 3. These measurements are intended to study the electrochemical behaviour of the AGR SNF at different solution pHs at 8, 11.4 and 12.5, representative of, respectively, undosed pondwaters, pondwaters subject to the current caustic dosing strategy, and pondwaters subject to a potential future dosing strategy.

The second part of the study looked at the effect of chloride ion concentration on the electrochemical behaviour of the AGR SNF at solution pHs at 8, 11.4 and 12.5, again representative of, respectively, undosed pondwaters, pondwaters subject to the current caustic dosing strategy, and pondwaters subject to a potential future dosing strategy. The electrolyte solutions also contained deliberately added chloride concentrations at 0.1, 1.0, 10, and 100 mmol/dm^3 NaCl and were dosed with caustic to the desired alkaline pH. The concentration of chloride used in these measurements represents the extreme scenarios where pond storage water has experienced a drastic increase in chloride levels.

These were the measurement conditions employed in the work described in the previous chapters – thus facilitating the use of the findings of those earlier studies in the interpretation of the data reported in this chapter.

Thus, the primary objective of this chapter is to report, analyse and interpret this novel dataset in order to derive information regarding the electrochemical behaviour of real AGR spent nuclear fuel under conditions relevant to UK pond storage.

However, a key secondary objective of this chapter is to explore and demonstrate the validity of using AGR-specific SIMFUELs as simulants for real AGR SNF. As alluded to above, both analyses will be supported by the baseline UO_2 and SIMFUEL studies from Chapter 4 and the cladding-SIMFUEL coupled electrode studies from Chapter 5.

6.1.1 Hot-cell Electrochemistry

Pursuant to the objectives described above, electrochemical open circuit potential (OCP) and linear sweep voltammetry (LSV) measurements were conducted using an electrode fabricated from a sample of real AGR spent nuclear fuel, see Figure 6-1, at the NNL Windscale Laboratory with the support of NNL technicians and researchers.

Due to the extremely radioactive nature of the spent AGR fuel sample, the experiments were conducted in a so-called hot-cell, also known as a cave, via the use of Master-Slave Manipulators (MSM).

This section will discuss the specific methodology and challenges associated with running such electrochemical measurements in a hot-cell and working with highly radioactive materials.

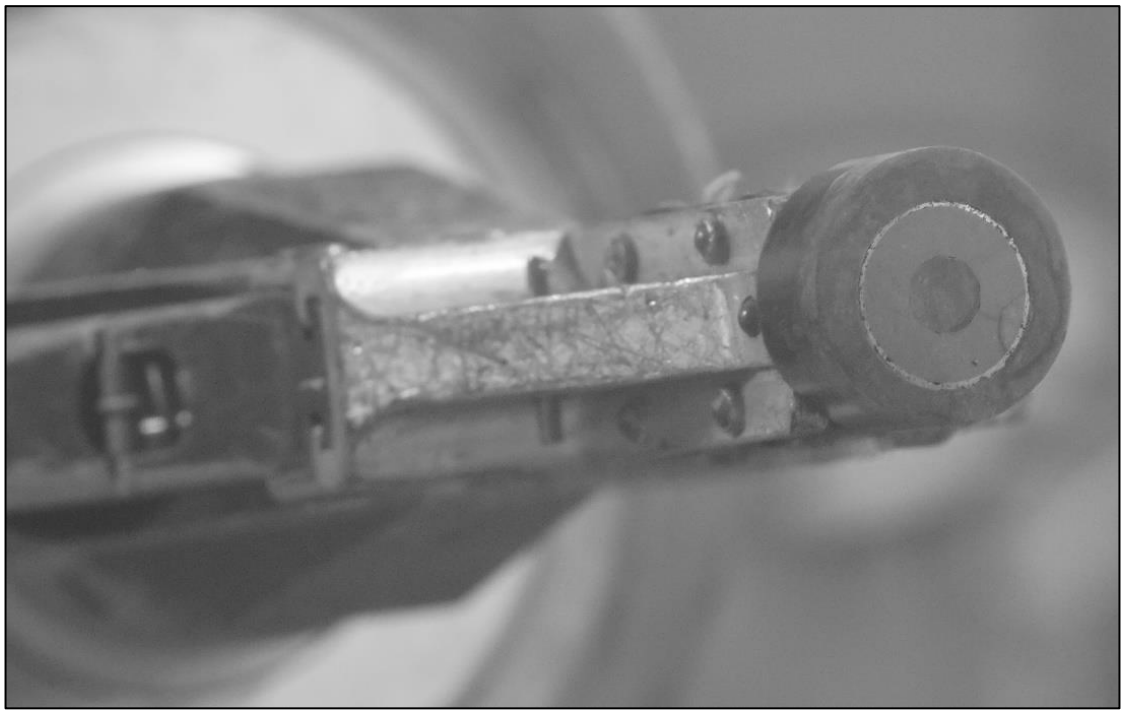

Figure 6-1: Photo of legacy AGR SNF electrode sample being held by MSM grips. The close-up shows the resin material encasing the SNF cross-section consisting of the lighter grey annular UO_2 fuel pellet and the shinier silver metal 20/25/Nb cladding ring around the fuel pellet.

Information on general electrochemical methods for OCP and measurements, including details of potentiostat and software used for the hot-cell experiments can be found in Chapter 3 Section 3.2.2.

The Solartron potentiostat and computer used for driving the electrochemical measurements were situated at the cave-face located outside of the hot-cell, a schematic of which is shown in Figure 6-2.

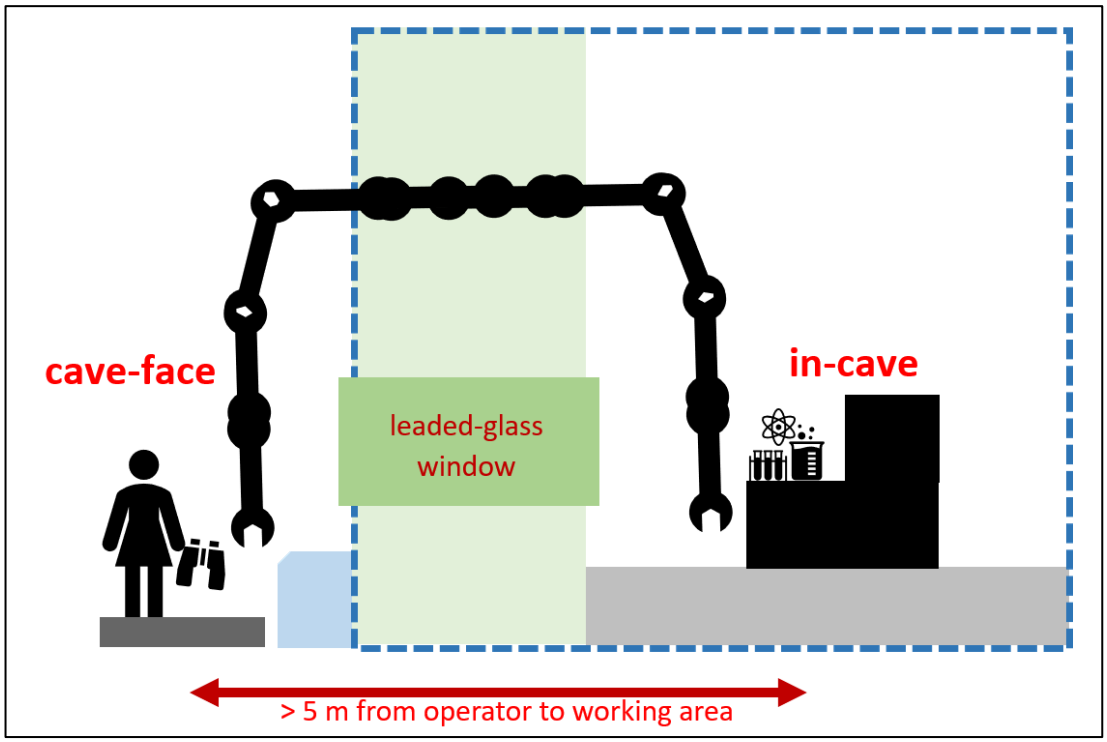

Figure 6-2: Schematic showing the approximate cross-sectional layout of the hot-cell.

The electrochemical cell used was a standard 3-electrode cell situated in-cave inside the hot-cell, separated by a ~2 m wall with a ~1 m leaded glass viewing window.

This gives an approximate distance of 5 m between operators/measurement instruments at the cave-face and the working area in-cave, again as shown in Figure 6-2.

The potentiostat interfaces with the electrochemical cell via a copper cable threaded through a special wire gland in the hot-cell wall. This enables electrical connectivity between the potentiostat and electrodes and is shown in Figure 6-3.

Figure 6-3: Photo of potentiostat wire gland and wire junction box (circled in red) enabling cable to be passed through cave wall and interface with electrodes in-cave. Junction box enables connection with the potentiostat.

The electrochemical cell setup in-cave is the same as the standard 3-electrode cell detailed in Chapter 3 Section 3.2.2, containing an Ag|AgCl reference electrode, Pt coil counter electrode and the AGR fuel working electrode, as shown in Figure 6-4.

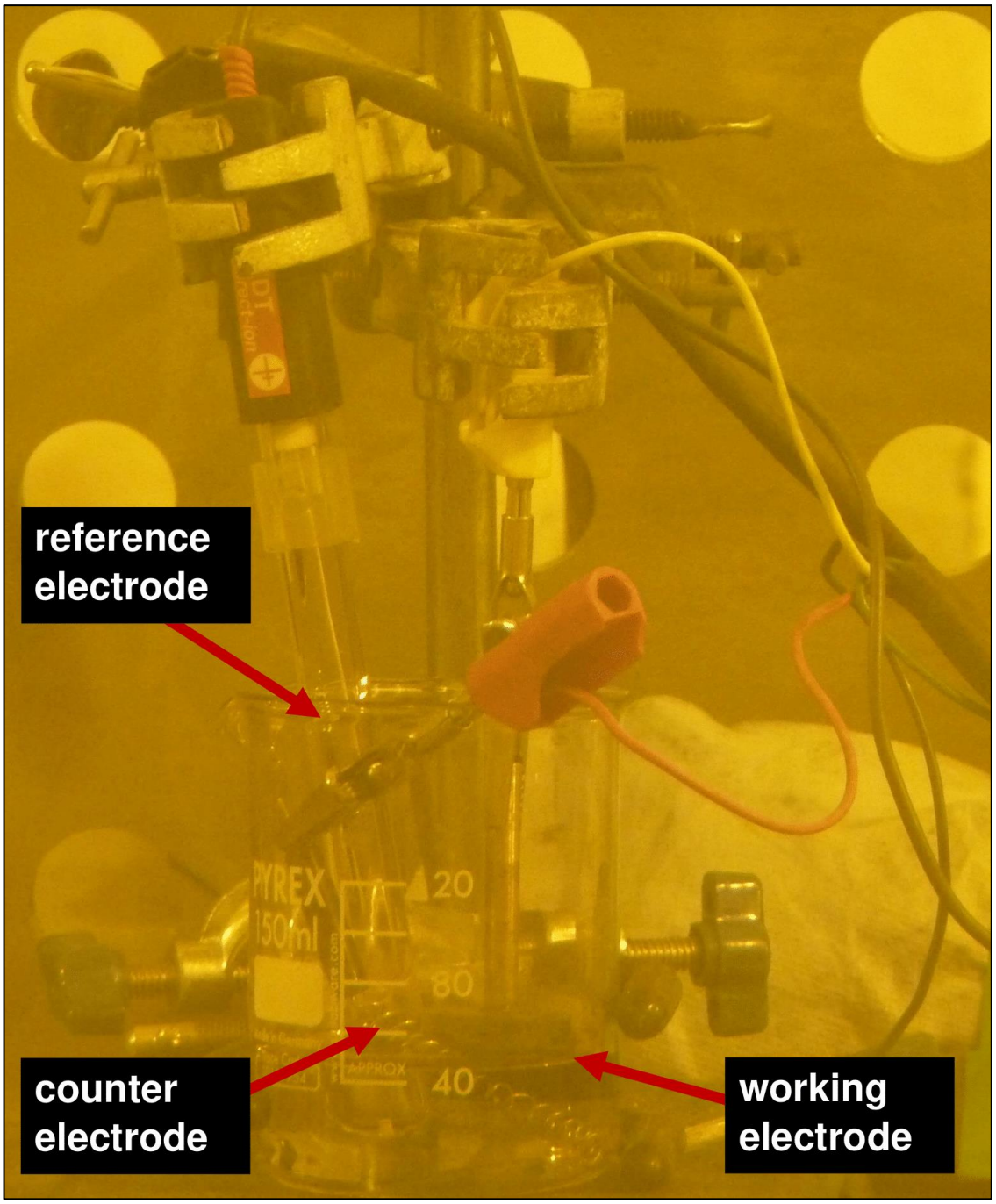

Figure 6-4: Photo of 3-electrode electrochemical cell set-up used during voltammetry measurements in the hot-cell.

Due to the space limitation of the working area and extreme conditions within the hot-cell, MSMs are required to manoeuvre the experimental apparatus and interact with the objects in-cave. This creates a major challenge for ensuring repeatability in the positioning of electrodes within the measurement beaker and electrolyte solution, as shown in Figure 6-5.

The difficulty of set-up during each measurement is further compounded by the non-MSM-friendly nature of some components used as part of the electrochemical cell. For example, retort stands, retort bossheads, and retort stand clamps – whilst standard commercial laboratory products – are not designed or easily modified to suit MSM handling.

The long distance between the cave-face and in-cave working area, combined with the reduced visibility of the leaded glass viewing window also introduces further difficulty during set up. These challenges notwithstanding, all possible care was taken to reproduce the arrangement of electrodes for each measurement.

The measurement conditions in the hot-cell differ from those in a standard research laboratory and cannot be monitored or adjusted as easily as in a traditional lab. The ambient temperature in-cave is reported to be between ~30 - 35 °C and can fluctuate daily and hourly. Compounding this difficulty, there is no temperature monitoring capability within the hot-cell; thus, no accurate reading can be determined.

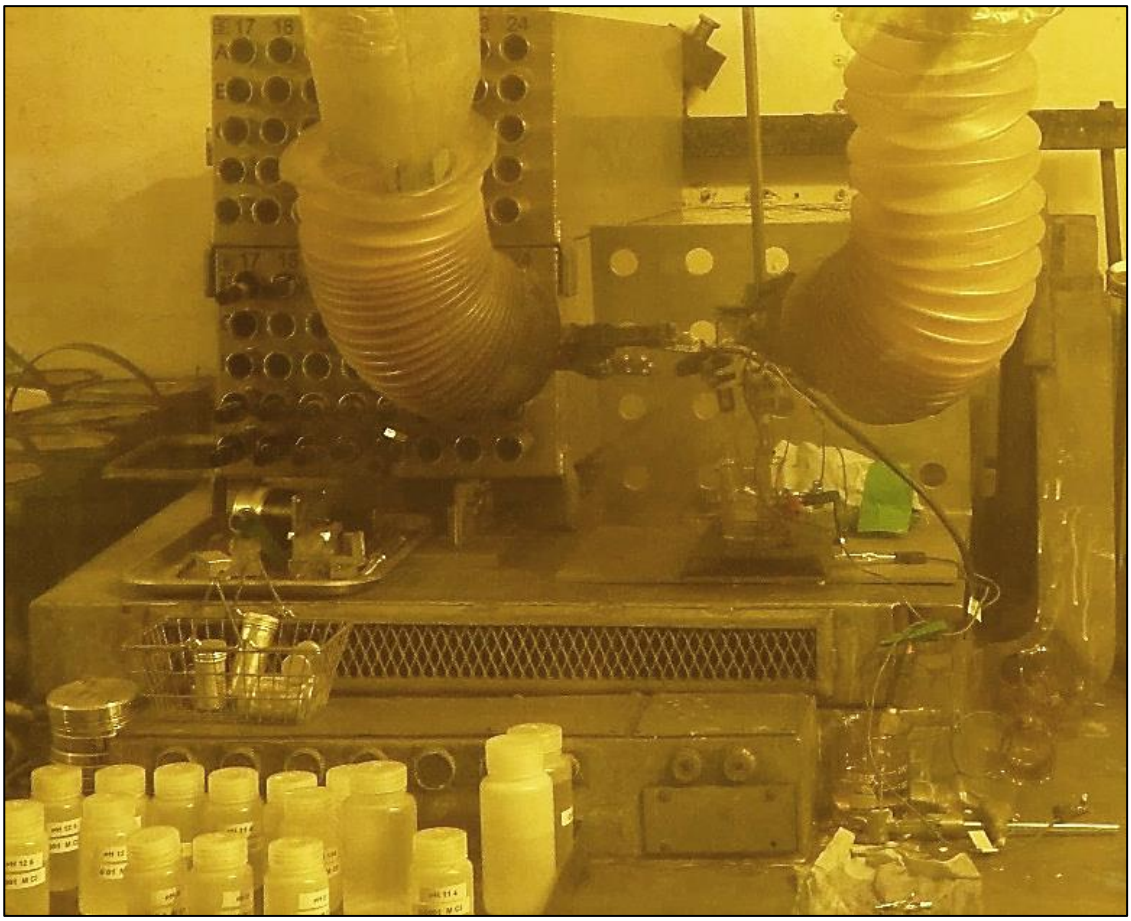

Figure 6-5: Photo of working area showing the location of the electrochemical cell apparatus (mid right), location of the electrolyte solution bottle (bottom left) and the relative position and size of the MSM arms.

At the working area there is also a region of increased airflow caused by ventilation draughts. These two effects in combination cause an increased rate of evaporation of the electrolyte solutions. This can be problematic for measurements due to the length of a typical measurement, ~17 hours (due to the length of time of experimental set-up plus length of LSV or OCP runtime), as the electrolyte solutions will evaporate steadily, leading to an increased concentration and a change in pH over time.

Increasing temperature also has a direct effect on solution pH by driving the water dissociation equilibrium towards the forward reaction, which translates to a decrease in pH. Table 6-1 shows the calculated pH values for each dosed electrolyte solution pH at 25 °C compared with an estimated hot-cell temperature of 30 and 35 °C. The comparison shows that the solution pHs are affected by a similar amount; however, the differences in pH are minor and not considered a major controlling factor in any corrosion behaviour observed.

30 μmol/dm^3 NaCl	25°C	30°C	35°C
pH	8	7.8	7.7
pH	11.4	11.2	11.1
pH	12.5	12.3	12.2

Table 6-1: Table of calculated electrolyte solution pHs at 25, 30 and 35°C.

Reference electrodes are also affected by temperature changes. An increase in temperature will cause a negative shift in the reference potential of a non-saturated Ag|AgCl reference electrode due to the increase in saturation of salt in the electrode solution and this effect is much stronger in electrodes with a saturated chloride filling solution. For a saturated Ag|AgCl reference electrode the temperature coefficient is estimated to be -0.13 mV/ºC [173].

However, again, under the estimated temperature conditions in the hot-cell, this potential shift is not considered significant enough to cause large data errors, relative to the standard operating error of the reference electrode used and the standard variations between measured data.

A more challenging issue encountered with reference electrode upkeep was the lifetime limitations and condition of the electrode caused by temperature effects. Figure 6-6 shows the storage conditions of the “working reference” electrode used in the experiments described below and the “golden reference” that was used only for the calibration of the “working reference”.

Calibration of the “working reference” electrode was carried out with respect to the “golden reference” every two to three measurements, in order to monitor for any abnormal potential shifts. However, both were stored in an open beaker containing a solution of 3 M NaCl which was prone to evaporation. Storage in a closed container was considered but deemed impractical due to poor accessibility with MSMs.

In order to maintain the accuracy and functionality of the reference electrodes, the following actions were taken:

- The storage solution was monitored regularly to prevent the electrodes from drying out.

- The “working reference” electrode and “golden reference” electrode were replaced regularly (approx. once every 3 weeks) to eliminate errors that may have been carried forward from the electrode calibrations.

Figure 6-6: Photo of temporary refence electrode storage beaker containing 3 mol/dm^3 NaCl with working reference electrode (left) and “golden reference” for calibration purposes (right).

The increased ambient temperature within the hot-cell can be at least in part attributed to radioactive materials surrounding the working area and directly adjacent to the electrochemical cell. The presence of nuclear materials near the working area can also increase the local radiation dose, which can have implications for the level of water radiolysis induced in the electrolyte solutions.

Due to a combination of the alpha field and near-field alpha field derived from the surrounding nuclear materials as well as the alpha field from the AGR fuel

sample itself, the electrolyte solutions in-cave are expected to generate water radiolysis products. The mechanisms and possible effects of this are discussed in Chapter 2 Section 2.2.4.2. In light of this, it would not be unreasonable to assume that a saturation level of hydrogen peroxide is reached in the electrolyte solutions, over time.

High radiation dose can also be a nuisance when working with non-radiation resistant ancillary electrochemical cell materials. Radiation induced degradation of the plastics in the banana electrode connectors and the electrodes themselves can occur over a short time relative to the typical length of an experimental work campaign. This causes plastic debris to fall into the electrolyte during set-up and measurements, potentially contaminating the system under study.

Other forms of contamination may arise during in-cave measurements. The majority are related to routine tasks due to the difficulty of washing and rinsing the glassware and electrodes between measurements as the use of MSMs limits the handling dexterity required when performing what would otherwise be simple tasks when conducted on a non-active laboratory bench, see Figure 6-7.

Beakers and electrodes can only receive a light rinse of water in between measurements and so may still be carrying traces of the electrolyte solution used in the previous experiment. To a certain degree, this is solved by planning measurements to start with electrolytes containing the lowest chloride concentrations and the lowest pH and moving towards high chloride concentration and high pH with each subsequent measurement.

The rinsing and polishing of the AGR fuel working electrode may also introduce errors and contamination to the measurements, again due to lack of dexterity and practicality imposed by the use of MSMs, as shown in Figure 6-8. Improper and infrequent polishing of the electrode surface between measurements can lead to build-up of corrosion products and salts deposited as a result of electrolyte evaporation at the surface of the electrode.

If the electrode is not polished sufficiently to refresh the surface post measurement, this can negatively impact the corrosion behaviour of the UO_2 spent fuel or cladding material as a result of the build-up of chloride salts in pits

and crevices, which can then further corrode the materials or enhance corrosion when under measurement conditions.

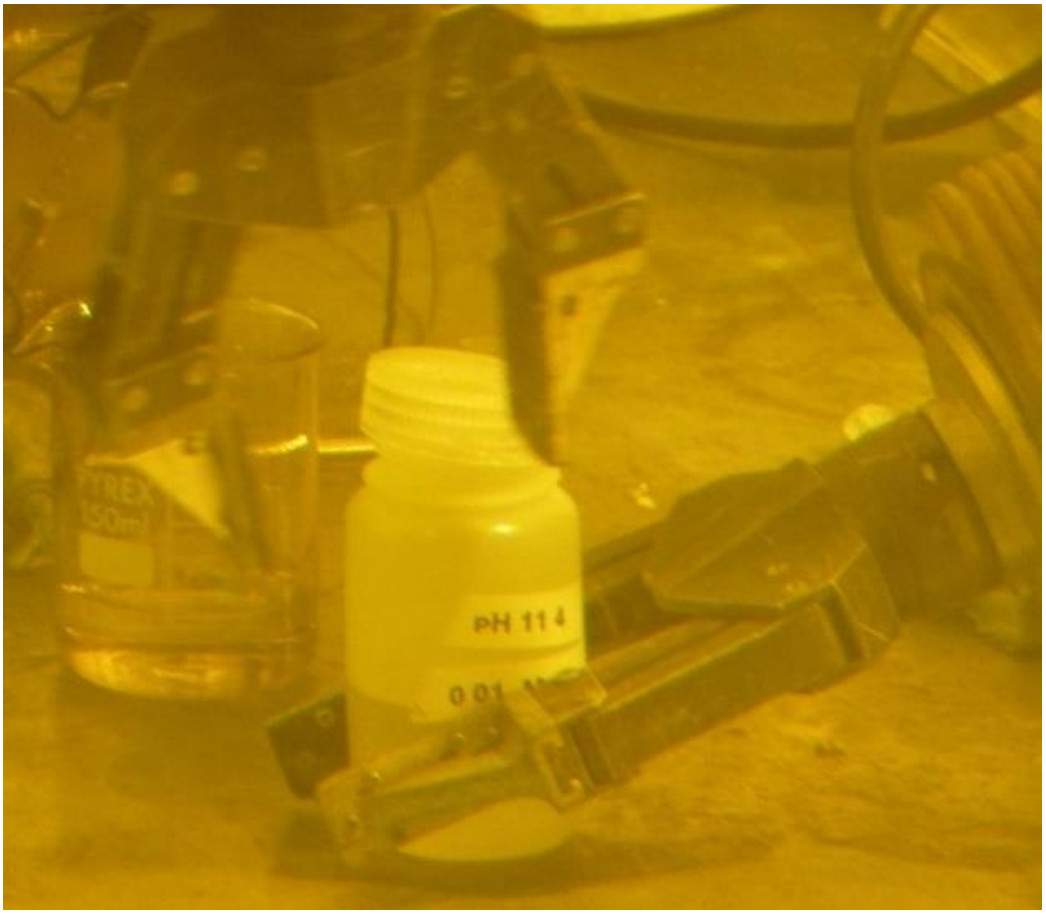

Figure 6-7: Photo of MSM being used to open lid of solution container to be poured into beaker.

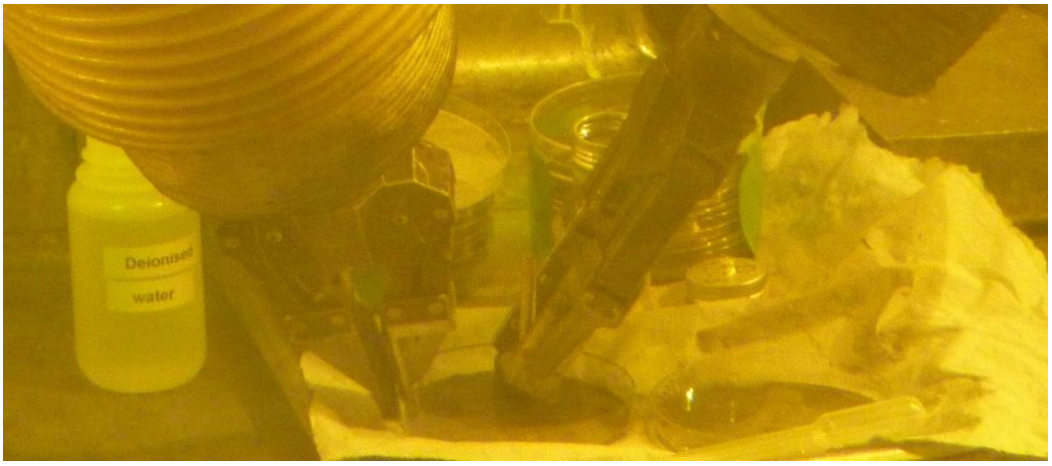

Figure 6-8: Photo of AGR fuel sample electrode being polished using MSMs on a piece of 1200/600 grit sandpaper in a petri dish.

As seen in Figure 6-9 , the combination AGR fuel electrode employed in the studies reported here consists of both the cladding and the AGR fuel pellet. The difference in material hardness causes variations in the relative heights of the two components of the electrode surface during in-cave polishing with the MSM. The harder steel material requires more robust and extensive polishing to refresh the surface. This is in contrast to the softer UO_2 material, which requires comparatively less polishing to refresh the surface. However, in the case of the AGR fuel electrode, the quality and quantity of *any* polishing was impeded due to the limited dexterity and practicality of polishing via MSMs.

Unfortunately, this especially inhibited the polishing of the cladding surface, which allowed the build-up of pits and crevices over the eventual three-month period of the entire experimental campaign. This scenario was unavoidable due to the lack of a dedicated polisher in the hot-cell.

Evidence of pitting on the cladding surface of the AGR fuel electrode can be seen in Figure 6-9. These images were recorded after several experiment runs with evidence of pitting being seen on both the ‘before’ and ‘after’ images, albeit with less pitting on the former.

It is noteworthy that a similar state of surface corrosion is also apparent in the Method-2 studies of Chapter 5, shown in Figure 6-10, the figure shows the composite SIMFUEL-cladding M2 electrode towards the end of the experimental campaign, where the AGR cladding component of the M2 electrode also exhibited evidence of pitting and crevice corrosion, particularly on the inner wall of the cladding, where crevice corrosion is more likely to occur due to the formation of a gap as the resin shrinks after the electrode fabrication process.

However, combined with the appearance of pits scattered randomly across the cladding cross-section, it is more likely that these corrosion mechanisms are caused by long-term build-up of corrosion micro-cells due to imperfect polishing or refresh of the Method-2 electrode surface in between measurements, similar to the phenomenon occurring with the real AGR fuel electrode.

This assumption is further supported when the real AGR fuel electrode is compared with electrodes containing only the simulant AGR cladding material,

where, as a result of the greater ease with which these electrodes can be effectively polished, no evidence of pitting or crevice corrosion is seen.

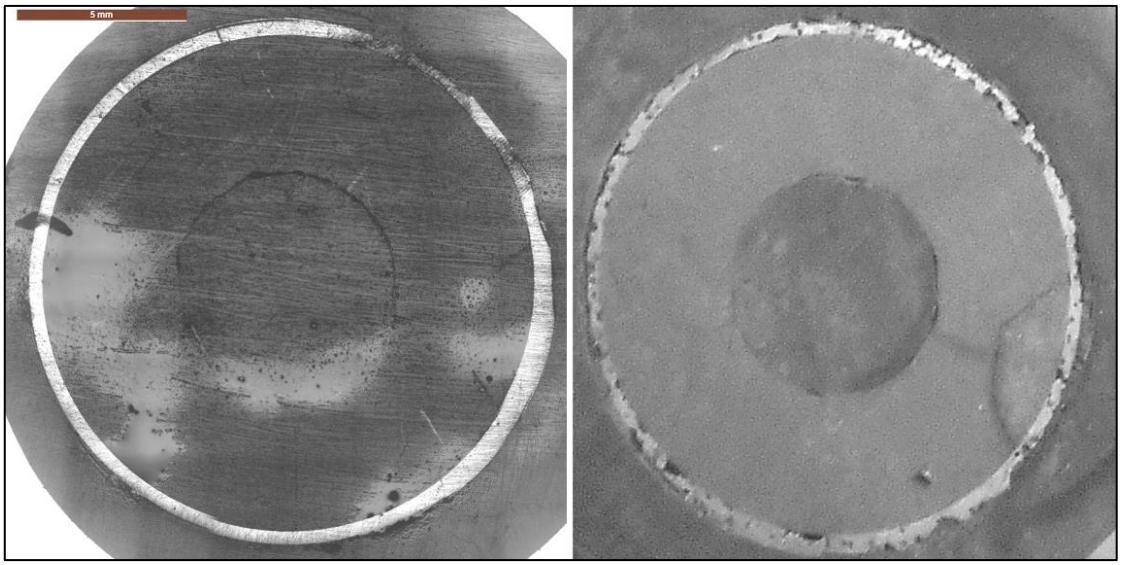

Figure 6-9: Photo of AGR fuel working electrode surface, before (left) and after (after) the experimental campaign. Pitting and crevice corrosion is present on the cladding surface.

Figure 6-10: Photo of M2 electrode showing pitting formation near the inside wall of the cladding component (The dark brown marks on the surface of the 25-SIMF are corrosion spots where dissolution of the UO_2 has taken place during the electrochemical measurement. These spots are removed and the surface refreshed during the polishing stage).

6.2 Measurements in Simplified Simulant Pond Water

This section presents an electrochemical study of legacy spent AGR nuclear fuel using a simplified simulant pond water (SSPW) electrolyte solution of 30 μmol/dm^3 NaCl dosed to pH 8, 11.4 and 12.5. All open circuit potentials (OCPs) were recorded over a 15-hour period, this length of time being chosen to satisfy both hot-cell access scheduling constraints and to allow enough time to achieve a suitable resting potential. LSV measurements were recorded over a potential of -0.8 to 1.5 V at a scan rate of 1 mV/s, immediately following the 15 hour OCP stabilisation. Electrolyte solutions were not purged with inert gas to remove oxygen as this capability was not available at the hot-cell facility.

An EIS study was planned and conducted as part of the work campaign, analogous to the EIS studies presented in Chapter 4 on the standalone single-component electrodes of AGR cladding and 25-SIMF. However, the data obtained in-cave was extremely noisy and deemed unsuitable for analysis. This is in part due to the complications arising from carrying electrochemical measurements in a hot-cell, as discussed in Section 6.1.1.

Further EIS work on AGR fuels in hot-cell conditions would require more accurate and repeatable experimental setups – including greater reproducibility in working electrode positioning relative to the reference electrode - and ideally include, for ease of data interpretation, measurements performed on electrodes of single component cladding and single component UO_2 fuel pellet samples.

6.2.1 Results & Discussion (OCP & LSV)

Based on the conclusions of Chapter 5, it was recommended to use the standalone single component electrode studies of Chapter 4 Section 4.5 in conjunction with the M2 surrogate composite electrode studies of Chapter 5 to support the interpretation of the electrochemical data obtained from the real AGR composite electrode.

This avoids the ambiguities around the current path arising from the inconsistent voltammetric behaviour exhibited by the Method-1 coupled electrode system. By comparing directly with the single component studies of AGR cladding and 25-SIMF, as well as the M2 surrogate composite electrode

studies, we can provide a feasible explanation of the voltammetry behaviours and predict current paths observed in the real AGR fuel system.

Thus Figure 6-11 shows: (i) the OCP vs. time data recorded during experiments conducted using the real AGR fuel composite electrode in SSPW electrolyte dosed to pHs 8, 11.4 and 12.5 in turn; and (ii) for ease of comparison, the analogous OCP plots recorded from single component cladding and 25-SIMF electrode studies, originally presented in Chapter 4, and the Method-2 coupled electrode studies of Chapter 5.

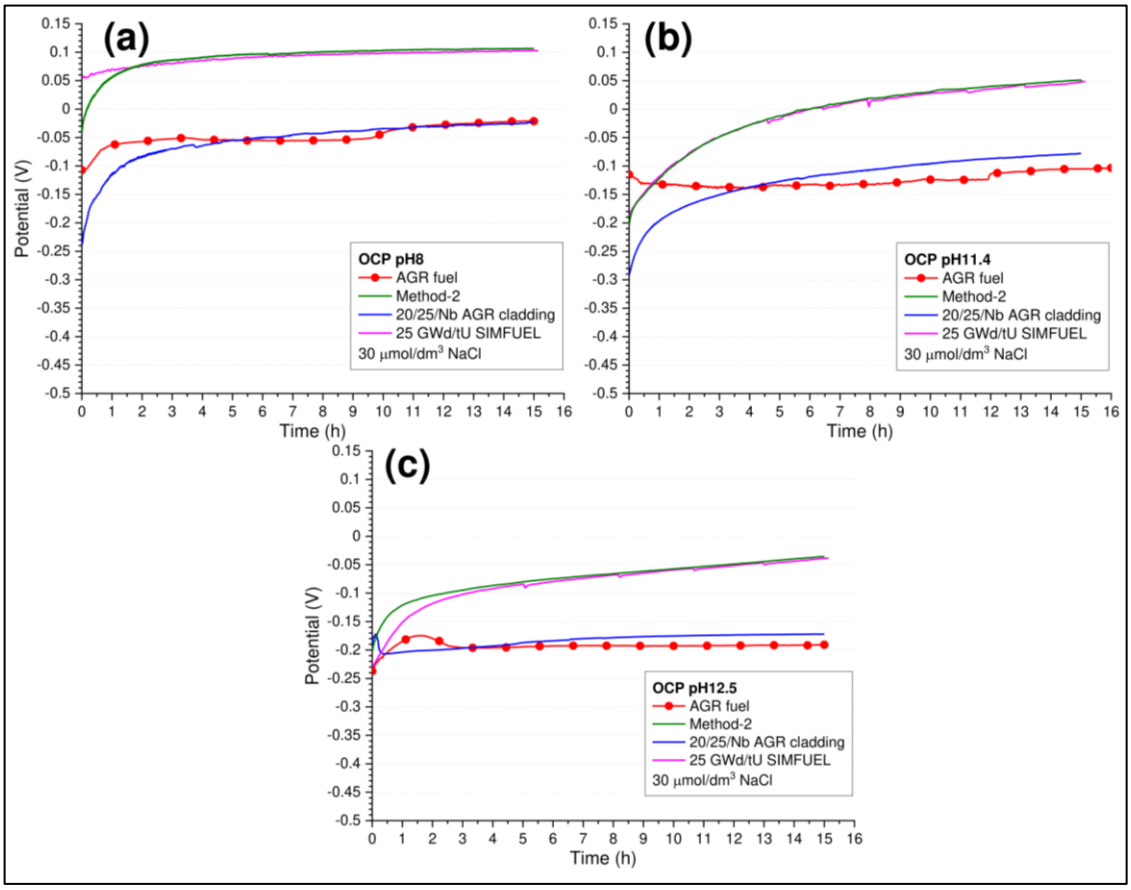

Figure 6-11: OCP measurements as a function of time comparing 25-SIMF, Method-2, Method-1, AGR fuel and AGR cladding, recorded over 15 hours in 30 μmol/dm^3 NaCl at (a) pH 8, (b) pH 11.4 and (c) pH 12.5.

The previously observed decrease in open circuit potential with increasing alkalinity is seen for each electrode type, including the real AGR fuel composite electrode. Detailed inspection of the data presented in Figure 6-11 reveals a consistent similarity between the OCP traces recorded from the real AGR fuel composite electrode and the single component AGR cladding electrode at each pH studied – suggesting that the real AGR fuel composite electrode's exchange

current path is dominated by the cladding component when under open circuit conditions.

This is in contrast to conclusions drawn from the M2 composite electrode work of Chapter 5 – particularly the exchange current path observed in the M2 experiments where the physical coupling of the cladding and SIMFUEL electrode most closely resembles that of the composite AGR fuel electrode under study here.

Specifically, the M2 experiments found that the mixed potential of the OCP measurements conducted were controlled by the interfacial electron transfer processes occurring at the **SIMFUEL component** of the simulant composite under all experimental conditions interrogated.

We attributed this observation to the presence of a coherent passivating layer on the steel surface that then inhibited interfacial electron transfer across the steel-electrolyte interface and thus the passage of any exchange current associated with the mixed potential at that steel surface.

No such passivating layer exists on the SIMFUEL component of the simulant M2 composite electrode, so allowing for higher exchange currents across the SIMFUEL-electrolyte interface, said higher exchange currents then dominating the mixed potential established.

In contrast, and as can be seen from Figure 6-11, the OCP values recorded from the real AGR composite electrode are controlled by the **cladding component** of the real AGR composite electrode, suggesting that in the case of the real AGR electrode system, interfacial electron transfer is more facile at the cladding surface than the UO_2 surface i.e. there is relatively less resistance to interfacial electron transfer at the surface of the irradiated cladding of the real AGR composite than at the surface of the unirradiated cladding of the simulant M2 composite surrogate. Possible explanations for this are as follows:

One explanation is based on the different surface finishes that may be obtained on the real and surrogate composite systems. The surface of the simulant composite electrode was easily polished by metallographic techniques that typically result in a mirror finish on metals – facilitating the consequent formation

under OCP experimental conditions of a **coherent**, **non-porous**, passivating oxide at the cladding surface of the simulant composite electrode, with the consequence that the mixed potential is then controlled by the SIMFUEL component.

In contrast, the surface of the real AGR electrode was extremely difficult to polish effectively (*vide supra*) with the possibility that, at the start of an OCP measurement, any oxide layer formed will be defected as opposed to coherent. These defects may then more readily allow for the passage of an exchange current across the steel-electrolyte interface than across the UO_2-electrolyte interface, resulting in the mixed potential of the OCP measurement on the real AGR fuel electrode then being controlled by the former.

An alternative, and perhaps more likely, explanation is based on the Radiation Induced Segregation (RIS) of the alloy components that occurs in the irradiated cladding of the real AGR sample, said RIS being absent in the unirradiated cladding of the M2 surrogate composite.

RIS is described in Chapter 2 Section 2.3.3.4 and can be summarised as the process of in-reactor neutron irradiation induced matrix damage, leading to changes in the local elemental composition. The RIS of AGR cladding can alter the composition of the Fe-Ni-Cr alloy at temperatures between 200 – 500 °C, leading to depletion of Cr and enrichment of Ni at the grain boundaries, which can cause increased localised corrosion susceptibility / suppressed passive film growth.

As described in Chapter 3, it is known that the AGR fuel sample used in this study has come from element-1 position in the reactor core and is therefore subjected to operating conditions that are known to induce RIS [40]. The resultant decreased corrosion resistance / passive film growth on the irradiated cladding in the real AGR composite sample could then contribute to the observed preferred path of the exchange current to be through the irradiated cladding-electrolyte interface. This may make the surface of the irradiated cladding more susceptible to corrosion when compared to the unirradiated (and thus fully passivated) cladding, and especially when under the non-polarising

conditions typical of open circuit potential measurements conditions, where passive film growth may only occur at a low formation rate [3].

The net result of the RIS of the irradiated cladding may then be that the interfacial electron transfers associated with the exchange current occur more easily at the less corrosion resistant cladding than at the UO_2 surface of the real AGR fuel sample.

As discussed in Chapter 5 and above, the reverse will then be true at the surface of the M2 SIMFUEL-unirradiated cladding surrogate, where the interfacial electron transfers associated with the exchange current occur more easily at the SIMFUEL surface than at the more easily/effectively passivated unirradiated cladding surface.

Let us now move on to discuss the LSV data recorded from the real AGR fuel composite electrode – and especially the effect that the applied oxidative potential-driven growth of the passive layer at the irradiated cladding surface may have on the above-described RIS-derived corrosion vulnerability of that material.

Figure 6-12 shows the LSV data recorded during experiments conducted using the real AGR fuel composite electrode in SSPW electrolyte dosed to pHs 8, 11.4 and 12.5. For ease of comparison, Figure 6-12 also presents the analogous LSV plots recorded from single component cladding and 25-SIMF electrode studies, originally presented in Chapter 4.

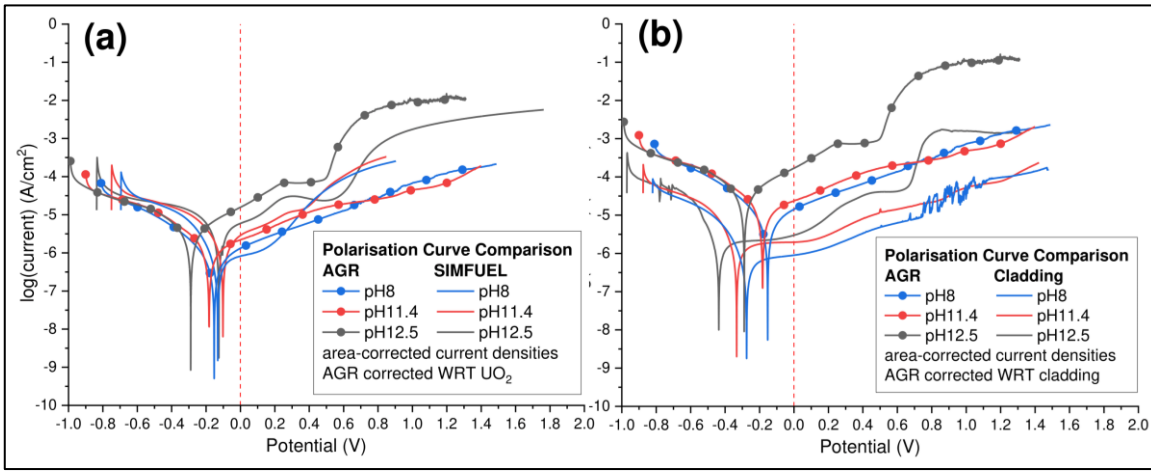

Figure 6-12: Polarisation curves obtained from LSV measurements recorded in 30 μmol/dm^3 NaCl, at pH 8, 11.4 and 12.5 of (a) AGR fuel compared with 25-SIMF and (b) AGR fuel compared with AGR cladding.

The polarisation curves of Figure 6-12 are displayed with surface-area-normalised current densities on the y-axis. In each graph, the current data obtained from the real AGR fuel electrode has been surface-area-normalised with respect to the component of the composite electrode that is being compared with its non-active surrogate. This is indicated in the legend box of each graph.

Thus in Figure 6-12(a), where the polarisation curves recorded from the real AGR fuel electrode are being compared with the polarisation curves recorded from the 25-SIMF electrode, the current in the former has been normalised with respect to the cross-sectional area of UO_2 fuel pellet presented to solution, whilst the current in the latter has been simply normalised with respect to the 25-SIMF electrode area.

In contrast, in Figure 6-12(b), where the polarisation curves recorded from the real AGR fuel electrode are being compared with the polarisation curves recorded from the cladding electrode, made from a cross section of unirradiated 20/25/Nb cladding tube, the current in the former has been normalised with respect to the cross-sectional area of the cladding component of the composite electrode presented to solution, whilst the current in the latter has been simply normalised with respect to the unirradiated cladding electrode area.

Taking each figure in turn, it can be seen from Figure 6-12(a) that the polarisation curves obtained from the real AGR fuel exhibit a number of similarities to those recorded from the 25-SIMF, especially with respect to measured current densities at any one potential and pH, and polarisation curve shape and form. This is especially true at pH 12.5.

In contrast, it can be seen from Figure 6-12(b) that, at any one potential and pH, there is a clear difference between the current densities recorded from the real AGR fuel electrode and those recorded from the unirradiated cladding electrode. The shape and form of the polarisation curves also reveal subtle differences, in particular, the presence of a noticeably large passive region between ~-0.4 V and ~0.2 V in the cladding data, which is absent in the AGR fuel data.

Additionally, at pH 8, the presence of pitting spikes in the cladding electrode polarisation curves at high potentials is also absent in the AGR fuel data. Figure 6-12(a) and (b) therefore suggest that the real AGR fuel electrode's log(current density) vs potential response is most similar to that of the SIMFUEL and thus most likely dominated by the UO_2 fuel component rather than the cladding component of the composite electrode.

Figure 6-13 shows the data of Figure 6-12 recast as polarisation curves where the current data has not been normalised to electrode area. This mode of presentation also allows for the incorporation of the polarisation curves recorded using the Method-2 surrogate composite electrodes (where uncertainty as to the current path previously prevents the observed current being normalised to the area of a specific surrogate composite electrode component with any confidence).

Whilst the quantitative current density-based comparisons of Figure 6-12 are now not possible, it is still possible to make qualitative comparisons between the shape and form of the plots and, given the close match of the areas of the cladding and UO_2 fuel components of the real fuel electrode with their respective surrogates, a degree of semi-quantitative comparison of the observed currents.

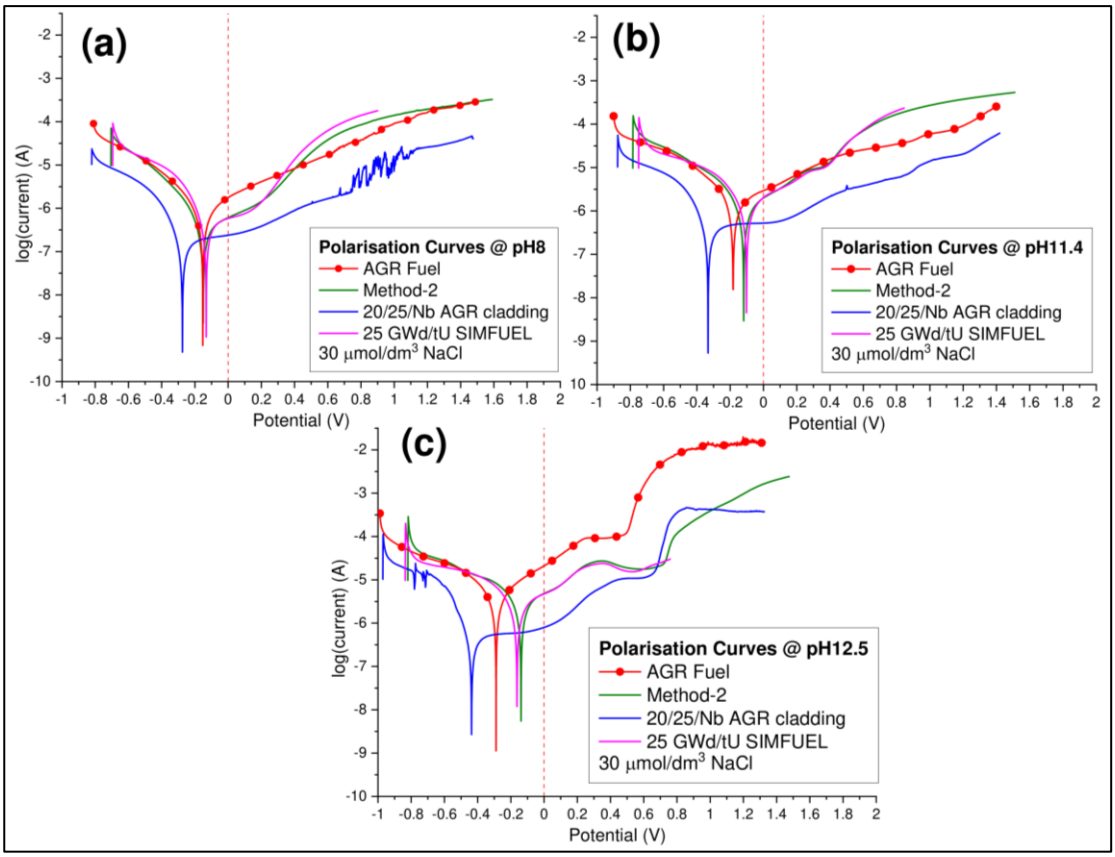

Figure 6-13: Polarisation curves comparing Method-2, 25-SIMF, AGR fuel, and AGR cladding, obtained from LSV measurements recorded in 30 μmol/dm^3 NaCl at (a) pH 8, (b) pH 11.4 and (c) pH 12.5.

Thus, Figure 6-13(a), (b) and (c) show polarisation curves measured at pH 8, 11.4 and 12.5, respectively. Each figure shows and allows comparison of the polarisation curve data recorded from the real AGR fuel electrode, unirradiated 20/25/Nb cladding electrodes, the 25-SIMF electrode, and unirradiated cladding/25-SIMF surrogate composite electrode coupled via Method-2.

It is evident from these plots that even without surface-area-normalised current densities, the real AGR fuel electrode polarisation behaviour bears a closer resemblance to that of the 25-SIMF electrode than that of the unirradiated cladding electrode.

With these considerations, we can infer the following for the sample of AGR fuel electrode used for this experiment campaign:

- When under OCP measurement conditions in Simplified Simulant Pond Waters of 30 μmol/dm^3 NaCl at pH 8, 11.4 and 12.5, the AGR fuel

electrode is exhibiting a behaviour apparently dominated by the 20/25/Nb cladding component.

As discussed above, this suggests that under OCP conditions, the combinations of resistances experienced by the mixed electrode must be lower in the cladding component compared to the UO_2 component, and consequently, the preferred current path is through the cladding.

The explanation underlying this conclusion is similar to that given in Chapter 5 Section 5.2.1 – that is, in a DC electrical system, the current flow will pass through the path of least total resistance. Given that there are two possible current paths in the composite AGR fuel electrode, either through the metallic cladding or the ceramic UO_2, the path via the stainless-steel cladding material is more likely, considering its properties as a metallic conductor with a lower bulk material resistance.

The opposite observation in the M2 coupled surrogate system can be attributed to either more effective polishing of the cladding, and/or absence of RIS of the cladding in the surrogate system. These allow for the formation of a more effective/coherent passivation layer on the cladding surface, making the cladding/electrolyte interface more resistive than the 25-SIMF / electrolyte interface and resulting in the current passing through the SIMFUEL surface to solution in the M2 surrogate system.

- However, when an external voltage is applied to the real AGR fuel electrode, as in the LSV experiments of Figure 6-12 and Figure 6-13, interfacial current flow appears to pass through the irradiated fuel component of the composite electrode rather than the cladding i.e. opposite behaviour to that observed for the real fuel electrode under net-zero current OCP conditions.

  The behaviour exhibited by the real AGR fuel sample under applied potential conditions is then the same as that observed for the Method 2 simulant composite electrode system, allowing us to infer that the cladding/electrolyte interface is here more resistive than the real AGR fuel/electrolyte interface.

  The most immediately obvious reason for this reversal in the behaviour of the real AGR fuel composite system is that the applied potentials of

the LSV experiments results in the formation of a passivating oxide layer on the cladding, even in the face of the surface finish / RIS effects that inhibit oxide layer formation under OCP conditions i.e. the applied potentials are strong enough to overcome these oxide growth retarding factors, so resulting in a passive oxide at the cladding surface and thus the routing of the oxidative current through the un-passivated UO_2 component of the AGR fuel composite electrode.

In previous chapters, the comparison of OCP values with their polarisation curves allowed a prediction of the material's corrosion behaviour when under open circuit conditions in the measurement electrolyte. However, since the OCP values of Figure 6-11 for the AGR fuel, represents the cladding component behaviour, they cannot be compared with the polarisation curves of Figure 6-13, as those represent the behaviour of the UO_2 component.

Thus, the best approximation would be to interpret the apparent cladding-dominated OCP measurements on the real AGR fuel sample by assuming that they behave the same as the standalone AGR cladding. Such interpretations have been discussed previously in Chapter 4 Section 4.5.2.1, in which it was demonstrated that the cladding OCP values sit comfortably in the passive region of their respective polarisation curves.

Since we hypothesise that the real AGR fuel's cladding component is the dominant current carrier under OCP conditions, this would similarly suggest that under SSPW conditions, the cladding component would remain protected from corrosion by the surface oxide film – specifically as can be seen from Figure 6-11, at pH 11.4 the OCP of the real fuel composite electrode is -0.15 V and this sits squarely in the cladding's passive range of -0.4 to 0.2 V as seen in Figure 6-13(b).

This OCP also sits 150 mV negative of the onset potential for the oxidation of UO_2 to UO_{2+x} as described by Equation 4-2 in Section 4.5.1.1, suggesting that the UO_2 component would consequently be protected via a pseudo-cathodic protection mechanism, with the cladding component acting as the "sacrificial anode".

With regard to the LSV data and polarisation curves of Figure 6-12 and Figure 6-13, as described above we can conclude that the sample of AGR fuel electrode used for this experimental campaign, when under LSV applied potential conditions in Simplified Simulant Pond Waters of 30 μmol/dm^3 NaCl at pH 8, 11.4 and 12.5, is exhibiting a behaviour likely dominated by the UO_2 fuel pellet component. Thus, by comparing data of the AGR fuel electrode with that of the 25-SIMF electrode, as shown in Figure 6-12(a), the polarisation curves, in accordance with Section 4.5.1.1, can be summarised as follows:

- At pH 8, the onset of oxidation of bulk UO_2 to UO_{2+x} in the grains via the incorporation of oxygen interstitials into the UO_2 matrix occurs at ~ 0.1 – 0.2 V. The onset of oxidation of UO_{2+x} to U(VI) species occurs at ~ 0.3 V.
- At pH 11.4, the onset of oxidation of bulk UO_2 to UO_{2+x} in the grains occurs at ~ 0 – 0.1 V and the onset of oxidation of UO_{2+x} to U(VI) species occurs at ~ 0.5 V.
- At pH 12.5, the onset of oxidation of bulk UO_2 to UO_{2+x} in the grains occurs at ~ - 0.1 – 0.1 V and the onset of oxidation of UO_{2+x} to U(VI) species occurs at ~ 0.6 V.

The experimental campaign on real AGR spent fuel has shown that planning and conducting electrochemical corrosion experiments in hot-cell / cave environments and conditions is very challenging. However, with this in mind, the LSV data obtained are consistent with the following high-level summary as follows:

The similarities between the real AGR fuel and 25-SIMF shown in the LSV measurements suggest that the AGR fuel surface electrochemistry is driven by the more favourable processes taking place at the UO_2 surface, rather than at the cladding surface.

This is due to the electrochemistry being governed by the electrode component that experiences the least total resistance, which in this case appears to be the UO_2 component as the applied voltages associated with the LSV scan, drives the formation of a resistive passive oxide on the cladding surface.

The latter difference in resistances between the cladding and UO_2 component, and the effect it has on the current path has previously been demonstrated

using resistance data obtained from EIS studies of standalone AGR cladding and 25-SIMF, presented in Chapter 5 Section 5.2.1 – which showed good evidence that the cladding component becomes significantly more resistive than the 25-SIMF component, over the potential range at which the passive layer growth is occurring.

This supports the explanation of the LSV behaviour of the Method-2 electrode, which shows a SIMFUEL-dominated behaviour and can also be applied to explain the UO_2-dominated behaviour of the AGR fuel under LSV conditions.

Furthermore, these studies of the legacy AGR SNF in SSPW 30 μmol/dm^3 NaCl at pH 8, 11.4 and 12.5 have also shown that these conditions provide the expected benefits for sufficient corrosion protection under the current UK AGR SNF pond storage strategy.

The OCP and LSV data suggest that under such storage conditions, both components of the mixed-electrode system are expected to be in a potential region where surface oxide formation is taking place at the cladding and no active dissolution is occurring at the UO_2.

Additionally, these studies have shown for the first time, that the use of analogous materials such as non-active 20/25/Nb AGR cladding and lower-activity 25 GWd/tU AGR SIMFUELs are good surrogates for simulating and representing the corrosion and voltammetric behaviour of the real legacy AGR SNF.

6.3 Measurements in Alkaline Chloride Water

This section presents the electrochemical study of legacy spent AGR nuclear fuel using a series of alkaline chloride water electrolyte solutions containing concentrations of 0.1, 1, 10 and 100 mmol/dm^3 NaCl dosed to pH 8, 11.4 and 12.5. All OCPs were recorded over a 15-hour period, this length of time was chosen to satisfy both hot-cell access scheduling constraints and to allow enough time to achieve a suitable resting potential. LSV measurements were recorded over a potential of -0.8 to 1.5 V at a scan rate of 1 mV/s. Electrolyte solutions were not purged with inert gas to remove oxygen as this capability was not available at the hot-cell facility.

6.3.1 Results & Discussion (OCP & LSV)

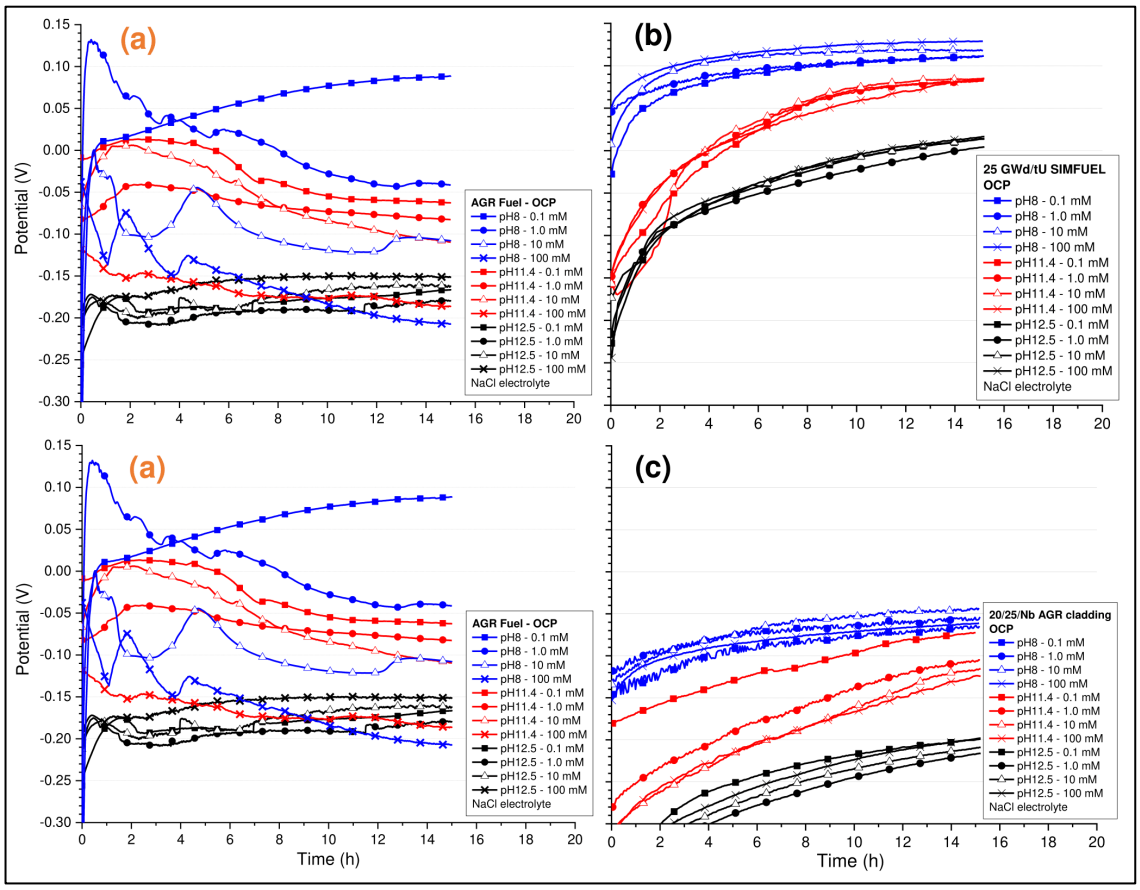

Figure 6-14: OCP measurements as a function of time comparing (a) AGR fuel, with (b) 25-SIMF and (c) AGR cladding. OCPs were recorded over 15 hours in 0.1, 1.0, 10, and 100 mM NaCl at pH 8, 11.4 and 12.5.

Figure 6-14(a) shows the measured OCP data for the real AGR fuel composite electrode, for a series of experiments recorded in 0.1, 1.0, 10, and 100 mmol/dm^3 NaCl at pH 8, 11.4 and 12.5. For comparison, Figure 6-14(b) and (c) presents the analogous OCP measurements conducted on standalone 25-SIMF and AGR cladding electrodes, respectively.

The dependence of the OCP on chloride concentration of the real AGR fuel electrode, Figure 6-14(a), is most closely matched with the analogous OCP data recorded from the unirradiated AGR cladding electrode, Figure 6-14(c). Although it can be seen that this correlation decreases with decreasing pH. A plausible explanation for this is as follows:

- It can be seen from the unirradiated cladding data that increasing chloride concentration produces only a marginal negative shift in the

equilibrium OCP. This is most likely due to the protection against corrosion afforded by the passive oxide layer that forms on the steel surface.

- This same effect is seen at pH 12.5 in the real AGR fuel data, where the OCP most closely matches that of the unirradiated cladding. This is again most likely attributed to the protection afforded by the passive oxide layer grown at this high pH.
- However, as pH decreases, the spread in OCP increases with increasing chloride concentration, as seen from the real AGR fuel data, i.e., the OCP starts to show a stronger dependence on the chloride concentration. This suggests that the cladding component of the real AGR fuel composite electrode is more susceptible to the effects of chloride, especially at lower pHs, and in particular when considered alongside the potential of RIS of the cladding component, as described above in Section 6.2.1.

Figure 6-15 shows the measured LSV data for the real AGR fuel composite electrode, for a series of experiments recorded in 0.1, 1.0, 10, and 100 mmol/dm^3 NaCl dosed to pHs 8, 11.4 and 12.5. For ease of comparison, Figure 6-15 also presents the analogous LSV plots recorded from the single component cladding and 25-SIMF electrode studies, originally presented in Chapter 4.

In Figure 6-15 the polarisation curves obtained from the real AGR fuel composite electrode have been surface-area-normalised with respect to the electrode component being compared with. Thus, Figure 6-15(a1)(b1)(c1) compares the real AGR fuel with the single-component AGR cladding data. All plots have been surface-area-normalised with respect to the cladding component and Figure 6-15(a2)(b2)(c2) compares the real AGR fuel with the single component 25-SIMF data; all plots have been surface-area-normalised with respect to the UO_2 component. This is indicated in the legend box of each graph.

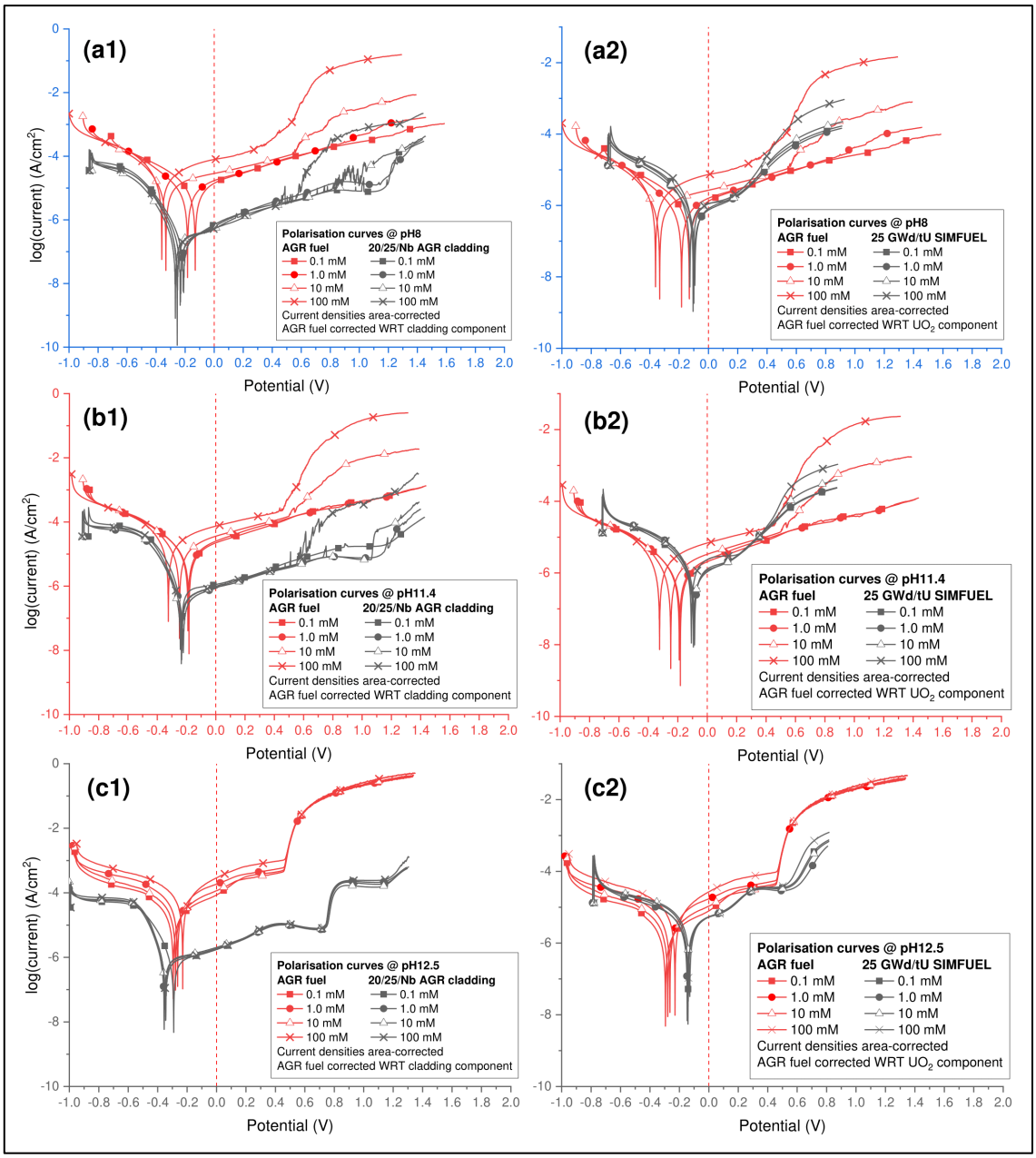

Figure 6-15: Polarisation curves obtained from LSV measurements recorded in 0.1, 1.0, 10, and 100 mM NaCl, at pH 8, 11.4 and 12.5, comparing AGR fuel with AGR cladding and 25-SIMF.

At the highest pH studied, pH 12.5, the polarisation curves of Figure 6-15(c1) exhibit virtually no change in form or magnitude as the chloride concentration is increased. As well, comparison of Figure 6-15(c1) with Figure 6-15(c2) suggests that at all chloride concentrations studied, the LSV data from the real AGR fuel is a better match for that derived from the 25-SIMF, than with the AGR cladding – both with respect to the, magnitude of the current densities observed and the general form of the polarisation curves obtained.

This is a similar observation to that seen in the real AGR fuel SSPW studies of the previous Section 6.2 and can be attributed to the high degree of passivation/corrosion protection of the cladding expected at this high pH. This passivation/protection both prevents the cladding component from dominating the AGR fuel response and mitigates against increasing chloride concentration affecting the form of the polarisation curves.

However, as the pH is decreased across the study, the form and magnitude of the polarisation curves and the current densities seen at any one chloride concentration, start to exhibit less preference for domination by either the cladding or UO_2 component of the real AGR fuel electrode.

Indeed, at pH 8 and 11.4 the plots recorded from the AGR electrode appear to gradually transition with increasing [Cl^-], from most closely resembling those derived from the 25-SIMF at low chloride, to most closely resembling those derived from the cladding component at high chloride. Consistent with this observation – and as might be expected – at lower [Cl^-], the LSV plots from the real AGR fuel electrode are similar to those presented in the SSPW studies in 30 µM NaCl, of Section 6.2.

Therefore, it would seem that, at these lower pHs of 8 and 11.4, the thinness of the passive layer formed at OCP allows for the corrosion processes occurring on the cladding to dominate the OCP. However, as the potential moves positive of the OCP in the LSV experiment, the passive layer on the cladding thickens and passivates the cladding, resulting in the preferential current path then being through the UO_2 component of the real AGR fuel composite electrode.

However, as the [Cl^-] is increased, the protection afforded by this electrochemically grown passivation layer is compromised, and the preferential current path is again through the cladding component. In contrast, at the higher pH 12.5 and as implied above, the combination of the thicker passive layer formed at the OCP and higher (passivating) hydroxide concentration, mitigating against chloride driven compromise of the passive layer as it further grows under the applied potential conditions of the LSV, means that the preferential current path remains through the UO_2 component at all potentials positive of the OCP – albeit not at the OCP itself. This is supported by real AGR fuel

polarisation curves shown in Figure 6-15(c2), which closely match that of the 25-SIMF polarisation curves.

Additionally, the data from EIS studies of the standalone 25-SIMF and AGR cladding single component electrodes, presented earlier in Chapter 4 Section 4.5 and Chapter 5 Section 5.2.1, have shown that the total resistance of the AGR cladding material is consistently much larger than that of the 25-SIMF material, across the same range of applied potentials as employed here in these LSV experiments.

In summary, the OCP and LSV studies of the legacy AGR SNF in 0.1, 1.0, 10 and 100 mmol/dm^3 NaCl at pH 8, 11.4 and 12.5 have shown that low chloride conditions are preferred when it comes to the prevention of corrosion of either the cladding or UO_2 component of the real AGR fuel composite electrode system.

Under the current UK AGR SNF pond storage strategy, this is already the case, as storage pond waters are currently dosed to pH 11.4 with chloride levels kept to a minimum. Should the scenario occur where the coupled cladding and UO_2 materials are exposed to the pond water, both components are expected to be passivated from the pond conditions and protected from corrosion.

Additionally, in the event that chloride concentrations in the storage pond increases beyond 0.1 mM NaCl and the corrosion potential increases above ~0.3 V, it is likely that the cladding component will switch on its electrochemistry and become the dominant current carrier, thus driving corrosion away from the UO_2 component, similar to a sacrificial anode.

6.4 Summary & Further Work

In this chapter we have presented novel data obtained from the electrochemical study of a sample of legacy UK AGR SNF. We have demonstrated the use of OCP and LSV voltammetric methods across two separate studies.

The first study was conducted in SSPW 30 μmol/dm^3 NaCl electrolyte solutions at pH 8, 11.4 and 12.5. The second study was conducted in NaCl electrolyte solutions containing 0.1, 1.0, 10 and 100 mmol/dm^3 NaCl, each at pH 8, 11.4 and 12.5.

The challenges and complexities associated with conducting experimental work with highly radioactive nuclear materials under hot-cell conditions were also discussed. This section provides a summary of the key findings.

1. Electrochemistry measurements conducted under hot-cell conditions required adjustments and adaptations to account for the constraints and limitations. The following challenges were encountered: (i) the impracticality of experimental setup including working with Master Slave Manipulators, (ii) the additional nuclear health and safety considerations for working with highly radioactive materials, (iii) the additional assumptions and adjustments made to the experimental measurement conditions due to the lack of control over external factors under hot-cell conditions, (iv) the time constraints imposed on the campaign of study due to access limitations on the research facility and nuclear materials used.
2. The novelty of this experimental campaign meant that no previous works were available for comparison. Thus, composite electrodes comprised of SIMFUELs and non-active AGR cladding simulants were used to obtain baseline data for comparison with the dataset from the real AGR fuel composite electrode. With this in mind, these studies have shown that the use of non-active 20/25/Nb AGR cladding and 25 GWd/tU AGR SIMFUELs are suitable for simulating the electrochemical behaviour of real AGR SNF.

SSPW Study

1. Data from the OCP measurements showed that the real AGR fuel composite electrode behaved similarly to the OCP data of AGR cladding – suggesting that the real AGR fuel composite electrode's exchange current path is dominated by the cladding component when under open circuit conditions. The following explanations were hypothesised: (i) different surface finishes that may be obtained on the real and surrogate composite systems, resulted in different passivating effects at the electrode surface which in turn affects the path of the mixed potential, and (ii) the more likely presence of Radiation Induced Segregation of the

alloy components present in the irradiated cladding of the real AGR fuel sample, the RIS of AGR cladding can alter the composition of the Fe-Ni-Cr alloy, leading to depletion of Cr and enrichment of Ni at the grain boundaries, which can cause increased localised corrosion susceptibility / suppressed passive film growth of the AGR cladding.

2. Data from the LSV measurements showed that the real AGR fuel composite electrode behaved similarly to the LSV data of Method-2 electrode – suggesting that the real AGR fuel behaviour is dominated by the UO_2 component when under LSV conditions. This behaviour was hypothesised as a result of the more favourable electrochemical processes taking place at the UO_2 surface and in combination with the greater overall resistance at the cladding component surface due to passivation.
3. The SSPW OCP and LSV studies have shown that the conditions of the current UK AGR SNF storage strategy provide sufficient corrosion protection for the AGR fuel composite electrode system.

NaCl Study

1. Data from the OCP measurements showed different behaviours across each pH. At pH 12.5, it was seen that the OCP behaviour most closely matched that of the unirradiated cladding, likely attributed to the protection afforded by the passive oxide layer grown on the cladding component. However, as pH decreases, the spread in OCP increased with increasing chloride concentration, showing a stronger dependence on $[Cl^-]$. This suggests that the cladding component of the real AGR fuel composite electrode is more susceptible to the effects of chloride, especially at lower pHs, and in particular when considered alongside the potential of RIS of the cladding component.
2. Data from the LSV measurements showed different behaviours in the polarisation curves across each pH. At pH 12.5, the polarisation curves exhibited behaviour similar to that of the 25-SIMF and showed virtually no change in form or magnitude as the chloride concentration was increased. This was attributed to the passivation/protection at the cladding component, thus preventing it from dominating the real AGR

fuel response. However, at lower pH, it was seen that AGR electrode behaviour appeared to gradually transition with increasing [Cl^-], from most closely resembling 25-SIMF at low chloride, to most closely resembling the cladding component at high chloride. This was attributed to the intricate balance between the competing corrosion process taking place at the surface of the cladding component and the UO_2 component, versus the degree of passivation at the surface of the cladding component, as a function of [Cl^-], and particularly more so when considered alongside the phenomenon of RIS on the AGR cladding – the RIS cladding is compromised and thus more susceptible to chloride attack, especially at high [Cl^-].

3. The NaCl OCP and LSV studies have shown that low chloride conditions are preferred when it comes to the prevention of corrosion of either the cladding or the UO_2 component of the real AGR fuel composite electrode system.

6.4.1 Further Work

Primarily, further work should aim to improve the practical aspects of the experimental work in order to increase reliability and repeatability. The experimental setup and procedures should be redeveloped to further improve usability and reliability for conducting future experiments under hot-cell conditions. Below are some recommendations:

- Improve cleaning procedure of all electrodes and improve repeatability of the polishing of the working electrode between measurements; this will ensure the surface of the working electrode is smooth, free from corrosion deposits and other debris to allow for consistency across measurement repeats.
- Improve storage and maintenance procedures for the reference electrodes so that the reference electrode systems remain calibrated; this will reduce error as a result of reference electrode values drifting.
- Develop a new 3-electrode cell to allow easier, accurate, and repeatable placement of electrodes into the measurement cell to eliminate points of

failure and improve ease of access and manoeuvrability for the Master Slave Manipulators.

Further studies can be carried out to supplement and build upon the findings from the work presented in this thesis. Below are some proposed further studies:

- Conduct a repeat of the measurements from the studies presented in this chapter, on electrodes of the separated components of irradiated cladding and UO_2 from a sample of real AGR fuel rod cross section. This would allow for detailed studies of the electrochemical behaviour of each individual component without interference from the other component, resulting in a more accurate electrochemical behaviour when compared to the mixed potential behaviours observed in this thesis. Results from these single component electrode studies would also be more suitable for direct comparison with their unirradiated/low activity surrogates and simulants.
- Conduct longer running OCP measurements on the real AGR fuel composite electrode over a period of 7 days, allowing time for the potential to stabilise and reach equilibrium to gain a better understanding of the OCP change over time.
- Increase the variety of LSV measurements by adjusting different measurement parameter variables, such as scan range and scan rate, to investigate the full range of LSV behaviours of the real AGR fuel composite electrode.
- Conduct CV measurements to investigate the currents associated with the forward oxidation and reverse reduction processes of the real AGR fuel composite electrode.

7 Electrochemical Oxidation of AGR SIMFUELs

7.1 Introduction, Objectives, & Methods

This chapter presents the preliminary results and discussions from the method development and initial trials of a new experimental setup, combining voltammetry and μ-Raman spectroscopy. The methodology aims to provide a combined method for surface analysis and monitoring of SIMFUEL electrode samples via in-situ μ-Raman spectroscopy paired with electrochemical oxidation measurements.

The primary objective of this chapter is to determine the effectiveness of combining these two techniques and whether such a combination of techniques could enable μ-Raman spectroscopy to be used in monitoring the degree of oxidation taking place at the surface of the SIMFUEL samples during an electrochemical experiment.

Electrochemical oxidation measurements were carried out on SIMFUEL electrodes, like those discussed in Chapter 3 Section 3.1.2, in a non-interfering background electrolyte containing 0.5 mol/dm^3 Na_2SO_4. Oxidation of the sample surface was achieved by application of an oxidation potential to the working electrode.

μ-Raman spectroscopy was used in-situ to record and monitor changes to the surface composition of the SIMFUEL samples. This was done by subsequent analysis of the acquired spectra by analysing the spectral changes within a broad band of peaks known as the “defect band”, situated approximately between 500 and 700 cm^{-1}, previously discussed in Chapter 2 Section 2.2.1 and Chapter 4 Section 4.4. Spectral analysis was conducted using peak fitting software Fityk [120], previously described in Chapter 3 Section 3.3.

As mentioned above, this new methodology was developed to enable electrochemical measurements in combination with Raman data acquisition. To facilitate this, a specially fabricated PTFE electrochemical cell was used, as shown in Figure 5-1. The unit consisted of the main electrochemical cell

compartment attached to an aluminium base plate, allowing it to be mounted onto the microscope stage of the μ-Raman instrument, as shown in Figure 7-2. The electrochemical cell compartment contained a port in the sidewall to allow the insertion of an Ag|AgCl reference electrode and a permanent Pt wire counter electrode attached through the sidewall of the cell, as shown in Figure 7-3.

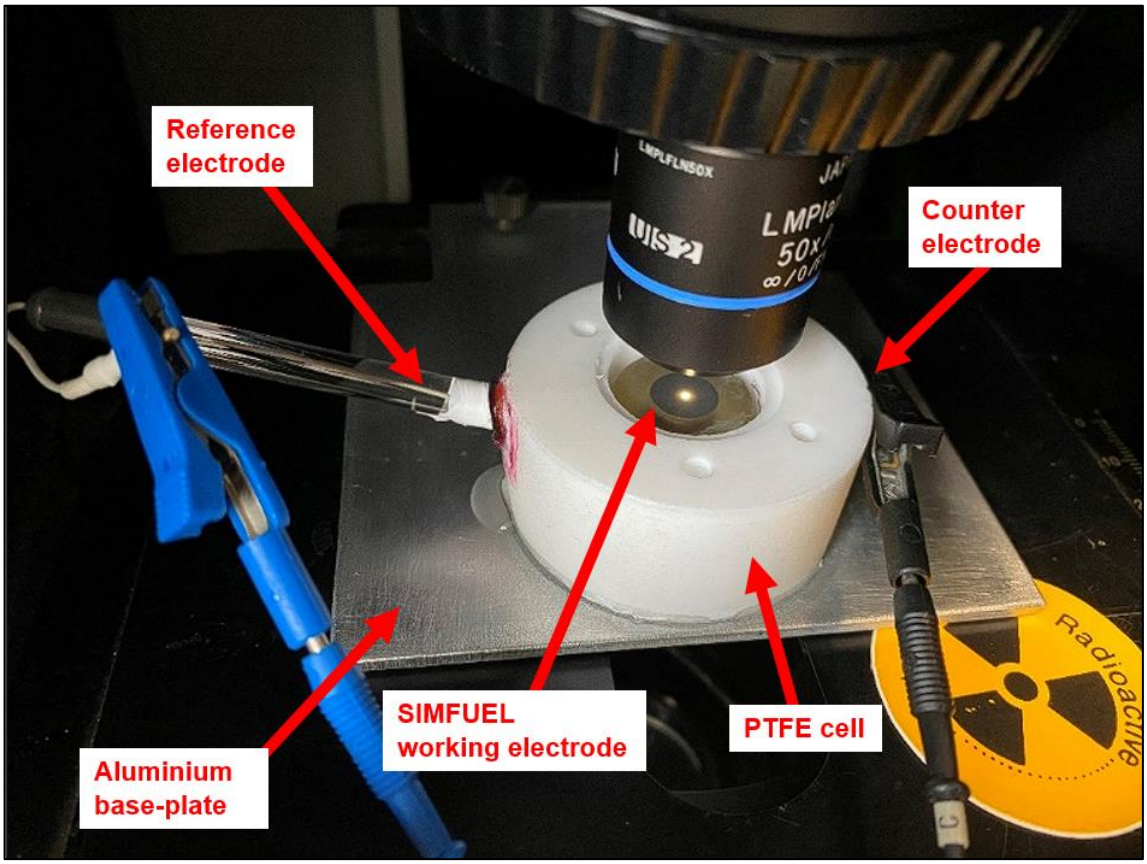

Figure 7-1: PTFE electrochemical cell with aluminium base for mounting to Raman microscope stage, shown here with a SIMFUEL electrode in the electrochemical cell cavity, along with the electrolyte solution.

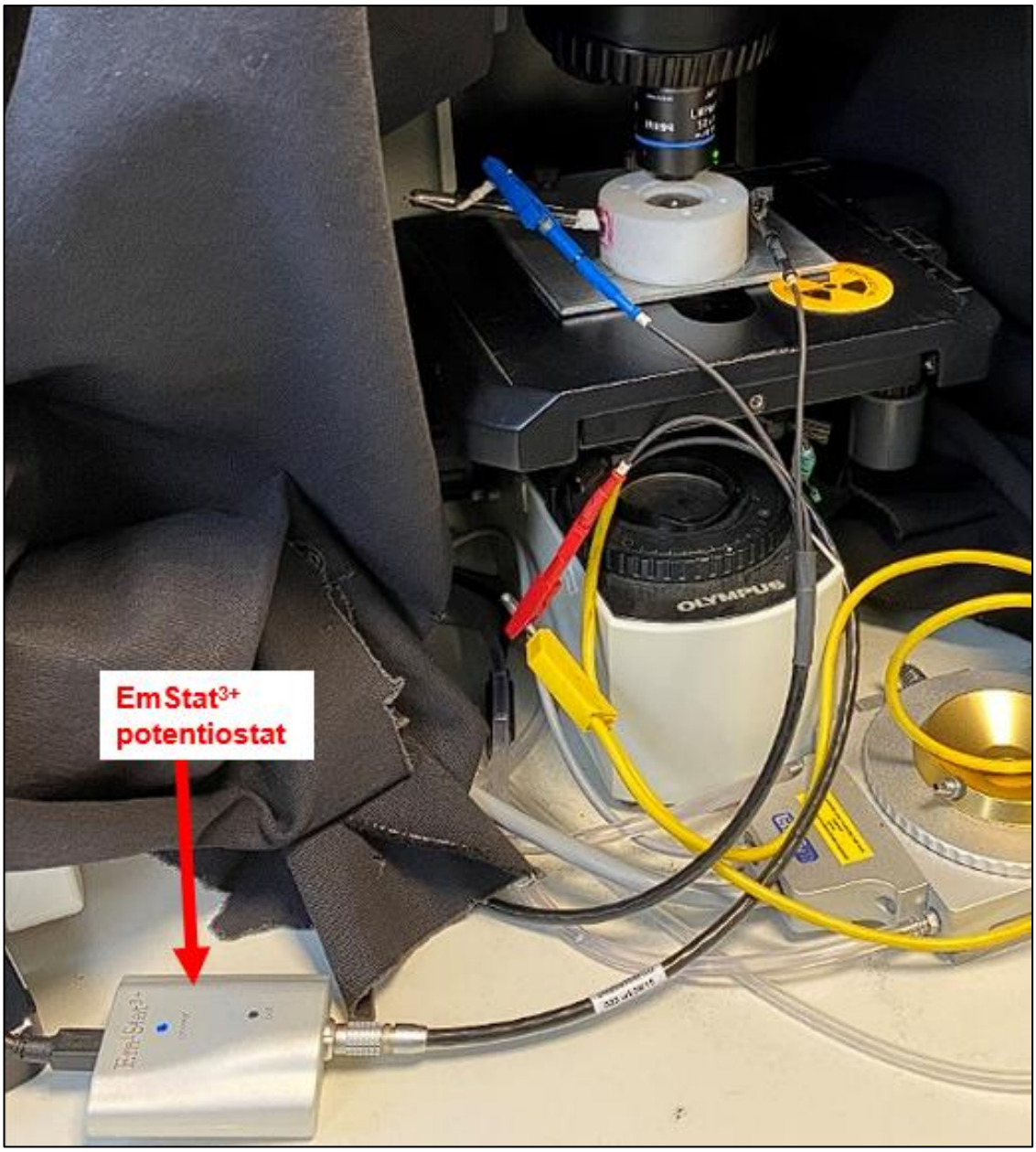

Figure 7-2: A wide view photo of Figure 5-1 showing PTFE electrochemical cell mounted to Raman microscope and connected to EmStat^{3+} potentiostat.

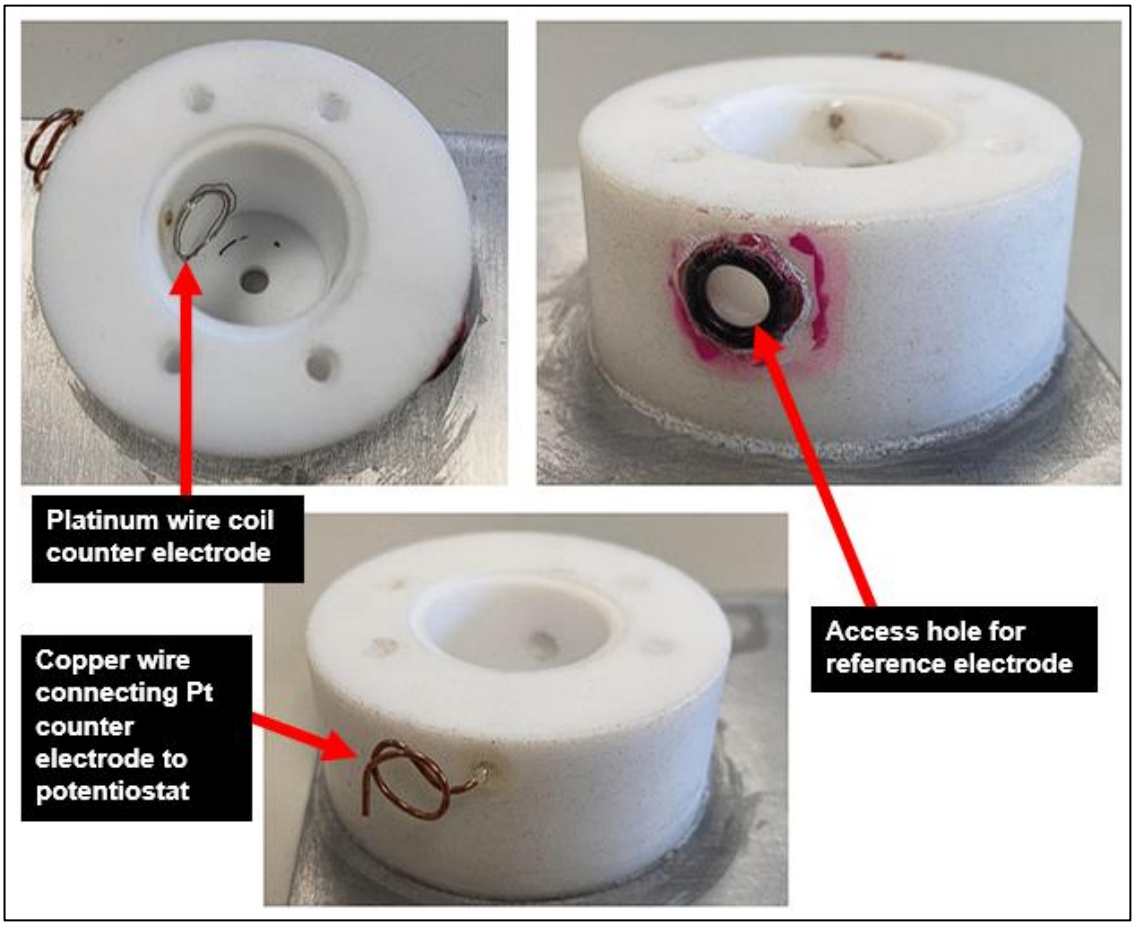

Figure 7-3: PTFE electrochemical cell showing the cell cavity compartment, an inner coiled platinum wire counter electrode connected through the cell wall via a copper wire, and a port in the sidewall for insertion of a reference electrode.

For each measurement, the SIMFUEL electrodes were first polarised at a reductive potential of -1.2 V (vs. Ag|AgCl reference electrode) for 15 – 30 minutes to electrochemically reduce and clean the surface of the electrode. At this reductive potential, the UO_2 typically undergoes reduction of higher oxides – as explained in Chapter 2 Section 2.2.3. This step was required to produce a consistent baseline starting position for the SIMFUEL surface, free from build-up of oxidised species.

The degree of oxidation at the surface and thus the degree of oxidised material formation/build-up at the SIMFUEL surface, is proportional to the magnitude and duration of the oxidation potential applied [174]. The typical oxidation potential range for UO_2 materials is between ~0.2 V and ~0.45 V (vs. Ag|AgCl reference electrode) – as explained in Chapter 2 Section 2.2.3. The SIMFUEL

samples were polarised by applying the desired oxidation potential to the working electrode for approximately 1.5 to 2 hours.

Following the anodic polarisation process, the electrode was left in the electrochemical cell and positioned beneath the microscope lens and laser path of the Raman microscope, as shown in Figure 5-1. Excess electrolyte solution (~1-2 mL) was then gently removed using a plastic pipette from the surface of the electrochemical cell compartment to expose the surface of the electrode. Raman scans were then recorded across the sample surface at multiple random locations to accumulate between ~5 to 30 scans – Raman acquisition was done according to the method described in Chapter 3 Section 3.3.

Post-processing of the spectra was carried out using Fityk peak fittings/deconvolutions. Peak positions, shape, and heights were extracted to calculate peak height ratios, according to the method described in Chapter 4 Section 4.4.1. Peak height ratios were calculated as ratios of the 'peak-of-interest' with respect to the 'fundamental U-O stretch'.

Peak heights were extracted from the signals of: (i) the ~444 cm^{-1} peak, assigned to the fundamental U-O stretch, (ii) the 535 cm^{-1} peak, associated with oxygen-vacancy-induced lattice distortions, (iii) the 575 cm^{-1} peak, associated with dopant/defect derived distortions to the cubic fluorite lattice, (iv) 625 cm^{-1} peak, associated with the measure of the degree of UO_2 hyperstoichiometry and thus level of oxidation. Discussions of the peak interpretations and assignments can be found in Chapter 4 Section 4.4.1 and further expanded upon in the following results and discussion sections.

The experiments in this chapter were divided into two studies, each using a different Raman excitation wavelength. Section 7.2 uses a 785 nm laser Raman microscope and Section 7.3 uses a 532 nm laser Raman microscope. The two different excitation wavelengths produced different spectra, which allowed the comparative study of the differences in spectral information. Further discussions on the chosen Raman excitation wavelength can be found in their respective results and discussion sections.

Figure 7-4, copied from Figure 4-16, shows the typical peak fitting deconvolutions for 25-SIMF and 43-SIMF spectra acquired using the 785 nm

laser Raman microscope. The fitting zone focuses on the wavenumber region of interest for this study, between ~350 to 700 cm^{-1}, highlighting the fundamental U-O stretch at ~444 cm^{-1} and the three signal contributions in the broad “defect band” between 500 and 700 cm^{-1}, previously described in Chapter 4 Section 4.4.1.

In comparison, Figure 7-5, copied from Figure 4-20, shows the typical fitting deconvolutions for 25-SIMF and 43-SIMF spectra acquired using the 532 nm laser Raman microscope, showing the same wavenumber region of interest, between ~350 to 700 cm^{-1}. However, the “defect band” signals have different relative intensities compared to those shown in Figure 7-4 due to the resonance-enhanced 575 cm^{-1} peak as a result of using the 532 nm excitation wavelength. This phenomenon has previously been described in Chapter 4 Section 4.4.2.

Examples of spectra fittings have not been shown for the 43-SIMF samples as the general observations between the two Raman excitation wavelengths are the same as for the 25-SIMF samples.

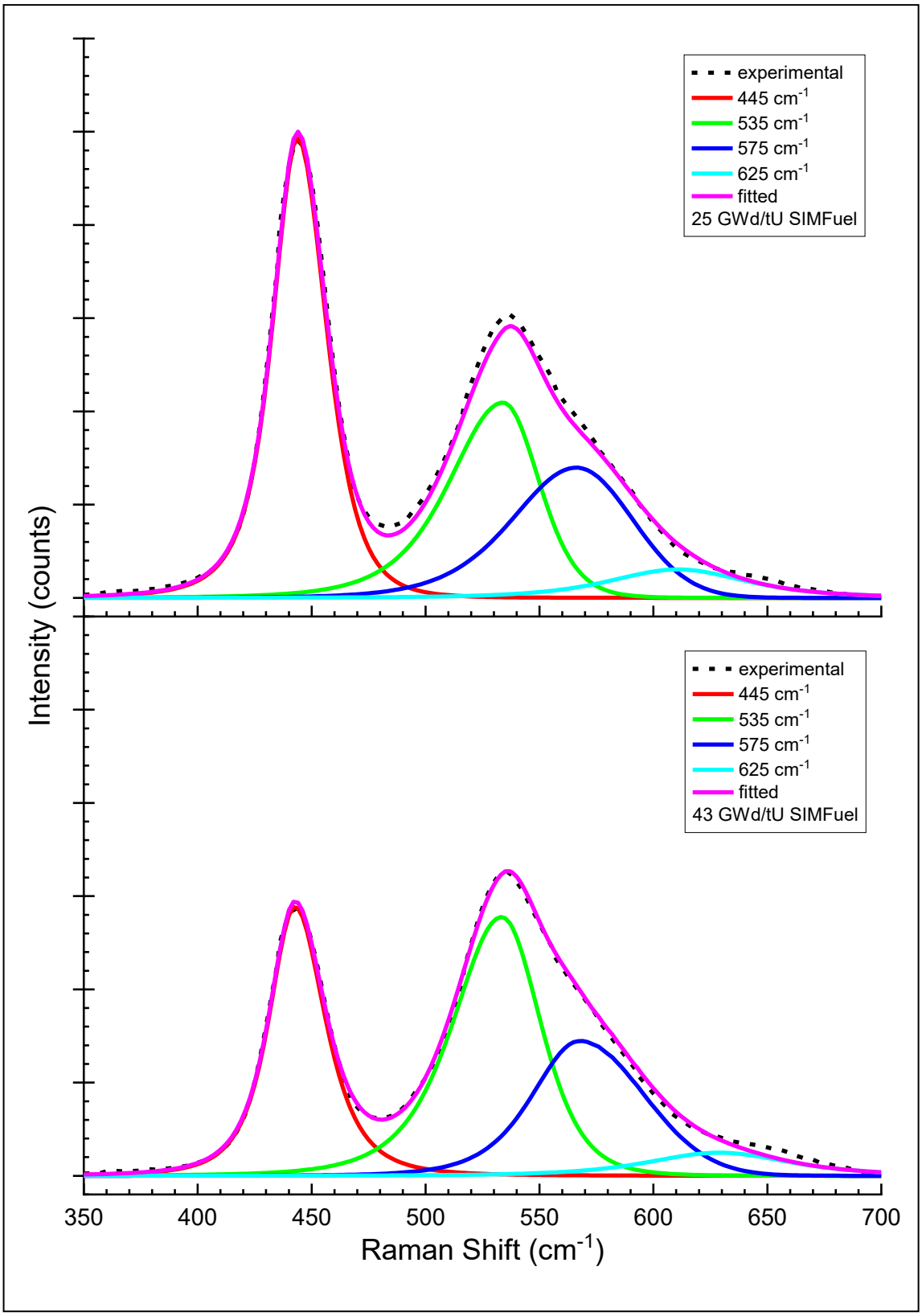

Figure 7-4: Spectra copied from Figure 4-16, showing a typical fit for 25-SIMF and 43-SIMF Raman spectra acquired on a 785 nm laser Raman microscope following the application of a reductive potential of -1.2 V in 0.5 M Na_2SO_4.

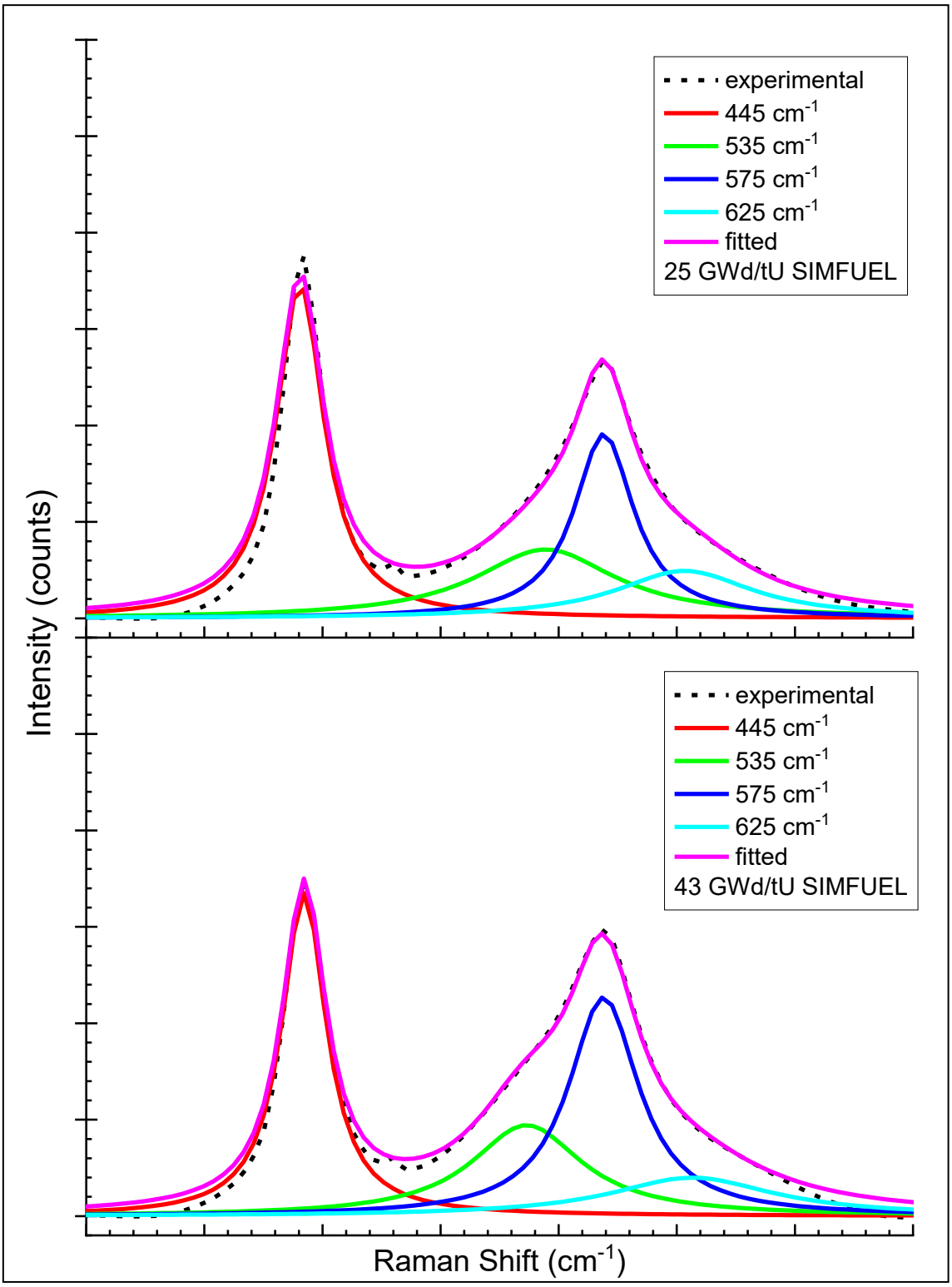

Figure 7-5: Spectra copied from Figure 4-20, showing a typical fit for 25-SIMF and 43-SIMF Raman spectra acquired on a 532 nm laser Raman microscope following the application of a reductive potential of -1.2 V in 0.5 M Na_2SO_4.

7.2 Measurements with 785 nm Raman Microscope

In this section, spectra were acquired using a 785 nm laser Raman microscope on samples of 25 GWd/tU AGR SIMFUEL and 43 GWd/tU AGR SIMFUEL. Interpretation of the spectra was focused on the deconvolution of the “defect band” situated between ~500 to ~700 cm^{-1} and the quantification of the changes in peak heights within this region. The 785 nm laser wavelength was chosen to avoid any spectral interferences, such as those caused by resonance effects between the laser and active Raman modes.

These measurements will enable us to study and compare the “defect band” behaviour under different applied oxidation potentials and will allow us to compare across the two different SIMFUEL burn-ups, 25-SIMF versus 43-SIMF.

The results presented here contain two datasets obtained from two separate experimental repeats. The two experimental repeats are labelled Run-1 and Run-2, and they differ slightly in measurement parameters. Minor changes to the methodology were made and incorporated into Run-2 following the results of Run-1 as part of the methodology development process. Differences between the Run-1 and Run-2 methodology are summarised below:

Run-1: The SIMFUELs were held at oxidation potentials of -1.2, 0.2, 0.35, 0.4 and 0.45 V for 1.5 hours and analysed using the 785 nm laser Raman microscope to acquire ~ 5 – 10 scans.

Run-2: The SIMFUELs were held at oxidation potentials of -1.2, 0.2, 0.25, 0.3, 0.35, 0.4 and 0.45 V for 2 hours and analysed using the 785 nm laser Raman microscope. Compared to Run-1, the SIMFUELs were polarised at a greater number of oxidation potentials to increase the number of data points, and the SIMFUELs were held longer at those potentials. The increased polarisation time was intended to increase the amount of oxidised species built-up at the electrode surface to improve Raman detection. The number of acquired scans was increased to ~10 – 20 scans.

7.2.1 Results & Discussion

Figure 7-6 shows a plot of current vs. time of the recorded current response during the application of the oxidation potentials employed to the 25-SIMF. The

plots show the expected trend of increasing current as a function of applied potential. The changes in current also agree well with the currents recorded from the forward anodic scans of 25-SIMF CV measurements, under similar conditions, as shown in Chapter 4 Section 4.3.1.

The oxidation potentials used here correspond to the oxidation reactions taking place at the surface of the SIMFUEL, previously discussed in Chapter 4 Section 4.3.1. At lower oxidation potentials below 0.4 V, the currents are typically associated with the in-grain oxidation of UO_2 to UO_{2+x} up to a maximum stoichiometry of $UO_{2.33}$, i.e., towards the formation of the higher oxide species of U_4O_9 and ultimately U_3O_7. Whereas at higher oxidation potentials above 0.4 V, the currents are typically associated with the onset of oxidation of UO_{2+x} to aqueous UO_2^{2+}, i.e., further growth of the $UO_{2.33}$ phase and towards the oxidative dissolution of UO_2^{2+} species [64].

Thus, it can be assumed that anodic polarisation of the 25-SIMF within this chosen range of oxidation potentials, should result in the formation and build-up of hyperstoichiometric UO_{2+x} species at the surface of the electrode [31, 174].

Furthermore, the presence of UO_2 surface oxidation under open air conditions has already been studied and shown in literature, in which the formation and build-up of oxides at the surface from air exposure is observed even without the need for electrochemical polarisation [175, 176].

These observations and interpretations can also be applied to the current vs. time plots of the similarly recorded polarisation measurements of the 43-SIMF, shown in Figure 7-7.

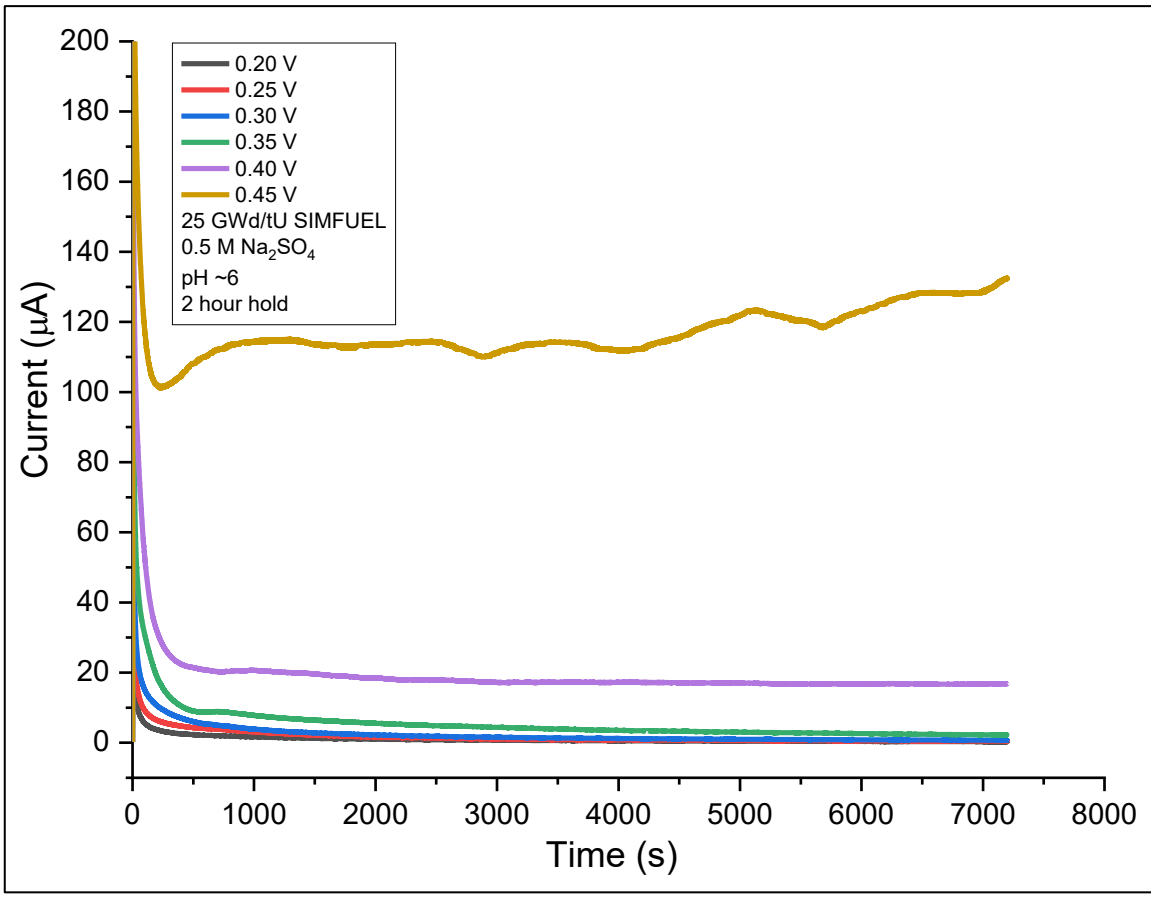

Figure 7-6: Plot showing the recorded current response as a function of time during the application of oxidation potential at each potential interval, recorded on a sample of 25 GWd/tU AGR SIMFUEL.

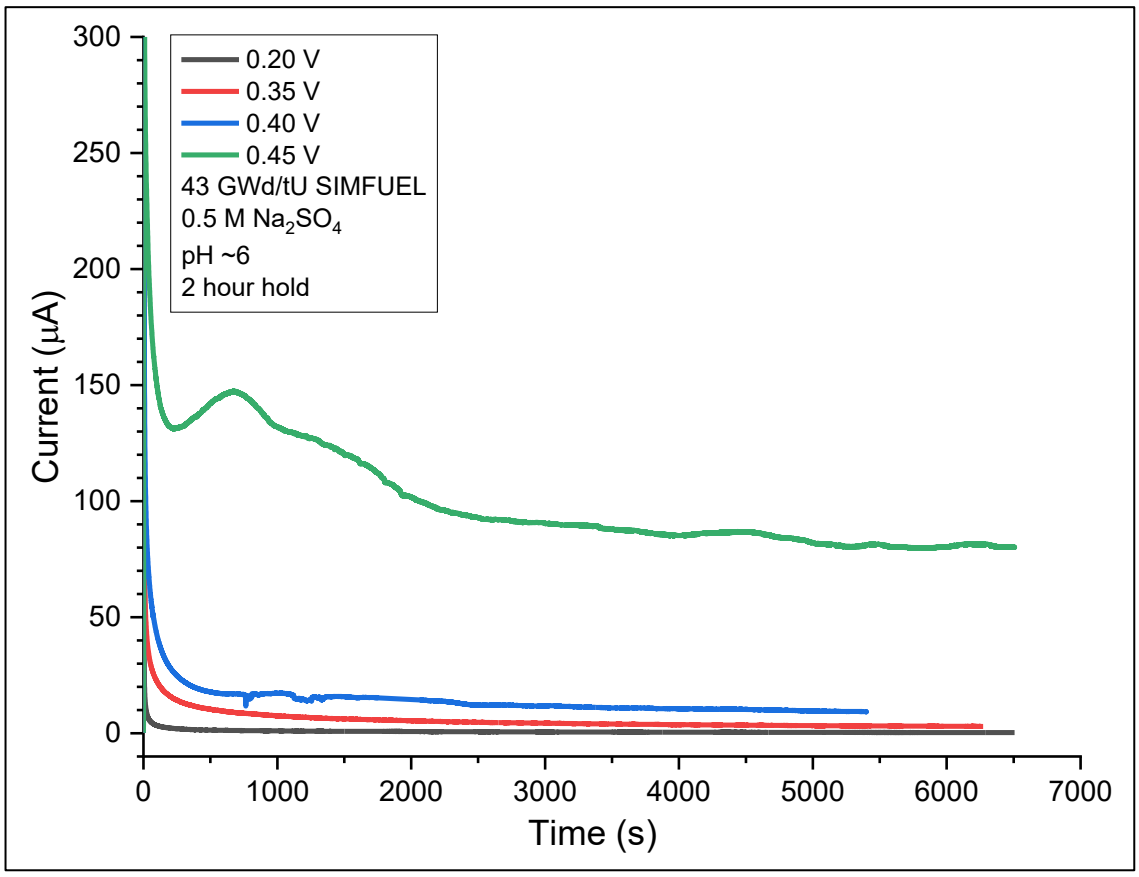

Figure 7-7: Plot showing the recorded current response as a function of time during the application of oxidation potential at each potential interval, recorded on a sample of 43 GWd/tU AGR SIMFUEL

The Raman spectra acquisition process involved capturing multiple scans at random locations across the sample surface; this process produced a diverse sample of spectra with varying signal intensities, representative of the whole surface composition. Therefore, extracted peak height ratios were plotted as averaged values, and the use of standard deviation error bars was necessary for highlighting the uncertainty in the average peak height ratios.

Expected changes and observations in the Raman spectra of the 25-SIIMF and 43-SIMF and the reported peak ratios may be as follows:

- Assignment of the 535, 575 and 625 cm^{-1} signals have previously been reported in literature on the same AGR SIMFUEL samples used in this study [38]. These peaks are associated with changes and/or the introduction of defects to the UO_2 lattice, as a result of either dopant incorporation or oxidation processes. Consequently, we should expect to see changes in the recorded Raman spectra and thus changes in the

calculated peak height ratios of the components within the “defect band”, as a function of applied oxidation potential, relative to their respective baseline unoxidised forms [138].

- **535 cm^{-1} peak**: It is generally agreed in the literature that this peak is associated with dopant effects and is specifically found to be increasing with the degree of lanthanide doping into the UO_2 matrix. This peak is assigned as a local phonon mode associated with oxygen-vacancy-induced lattice distortions, which are caused by the incorporation of lanthanide (III) dopants into the UO_2 matrix, resulting in the formation of oxygen vacancies to account for charge compensation. Thus, it is unlikely that the 535 cm^{-1} peak is responsible for indicating the process of UO_2 oxidation/hyperstoichiometry and we would not expect to see changes to the peak height ratios, as a function of applied oxidation potential [38, 86].
- **575 cm^{-1} peak**: Known in literature as the first overtone of the longitudinal optical (LO) phonon. This peak is typically not visible in pure undoped-UO_2 due to being Raman selection “forbidden” by symmetry conditions. However, the signal becomes visible in the case of defected UO_2 samples due to the breakdown of symmetry as the cubic fluorite lattice becomes distorted [38, 177]. The appearance of this peak in the SIMFUEL spectra can therefore be attributed to the distortion of the lattice symmetry due to the incorporation of dopants and introduction of vacancies into the UO_2 matrix. Additionally, distortions of the lattice may also arise from oxidation or hyperstoichiometry of the UO_2, which involves the introduction of oxygen interstitials to the lattice [53]. Thus, under anodic polarisation conditions, it may be possible to detect and observe changes to the 575 cm^{-1} peak intensity, due to further lattice distortion by UO_2 oxidation.
- **625 cm^{-1} peak**: Attributed to the clustering of interstitial oxygens to form cuboctahedrons; the formation of such higher oxidation state cuboctahedrons is considered equivalent to U_4O_9, which are likely to contain a mixture of U(IV) and U(V) oxides [176]. This process distorts the anion sublattice due to further incorporation of oxygen ions into the sublattice. Thus, the 625 cm^{-1} peak is likely indicative of the degree of

UO_2 oxidation and degree of hyperstoichiometry of the UO_{2+x} species, i.e., as degree of oxidation and/or hyperstoichiometry increases, the intensity of the 625 cm^{-1} peak also increases [53, 55]. Previously published Raman studies on hyperstoichiometric oxides of UO_{2+x} have already proven the capability of μ-Raman spectroscopy to detect and monitor the spectral changes associated with the ~625 cm^{-1} peak, as a function of increasing hyperstoichiometry [56, 178]. Thus, under the anodic polarisation conditions employed in this study, we would expect surface UO_2 oxidation and, thus, surface UO_{2+x} formation and observe an increase in peak height ratios.

Figure 7-8, Figure 7-9 and Figure 7-10 shows the average peak height ratios of the 535 to 444 cm^{-1} signal, 575 to 444 cm^{-1} signal and 625 to 444 cm^{-1} signal for the 25-SIMF, respectively. Figure 7-11, Figure 7-12 and Figure 7-13 shows the average peak height ratios of the 535 to 444 cm^{-1} signal, 575 to 444 cm^{-1} signal and 625 to 444 cm^{-1} signal for the 43-SIMF, respectively. Each figure is shown as a side-by-side comparison of the two measurement repeats, Run-1 and Run-2.

In the first instance, we compare the results between Run-1 and Run-2 across all the figures. The average peak height ratio values were similar and remained consistent between Run-1 and Run-2. In Run-2, the increase in the number of oxidation potentials at which the SIMFUELs were polarised at improved the data visualisation by increasing the number of data points available for predicting any trends.

It can be seen from Figure 7-8 to Figure 7-13 that the most noticeable difference between Run-1 and Run-2 was due to the increase in the number of scans acquired, which generally decreased the size of the standard deviation error bars of each measurement, implying the Run-2 measurements were more statistically robust than Run-1. Considering the above observations, all subsequent discussions in this section will therefore focus only on the Run-2 dataset/plots.

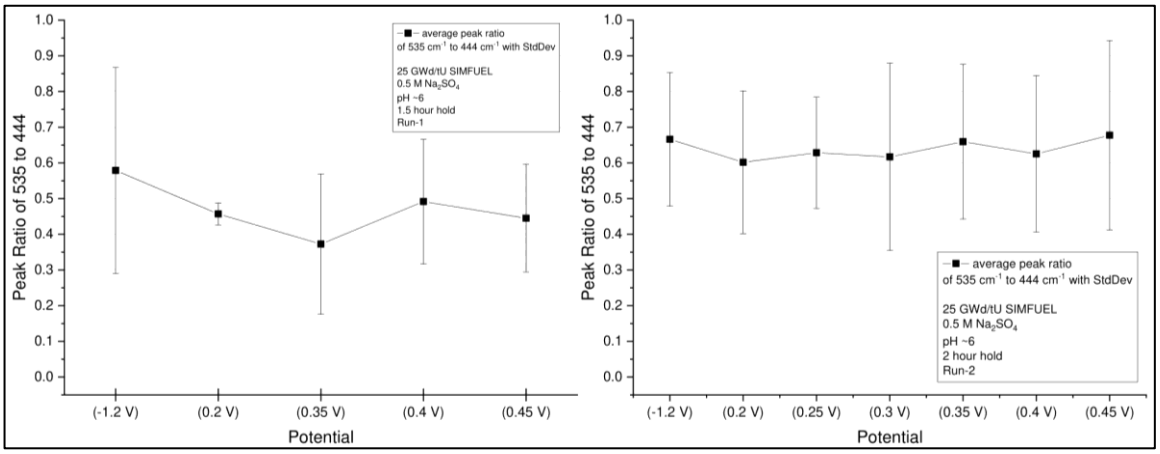

Figure 7-8: Plot of average peak height ratios of the 535 cm^{-1} to 444 cm^{-1} signal with standard deviation error bars, as a function of the applied oxidation potential, obtained from spectra acquired on the 785 nm Raman Microscope, from a sample of 25 GWd/tU SIMFUEL. The two graphs show results from two measurement repeats, Run-1 (left) and Run-2 (right).

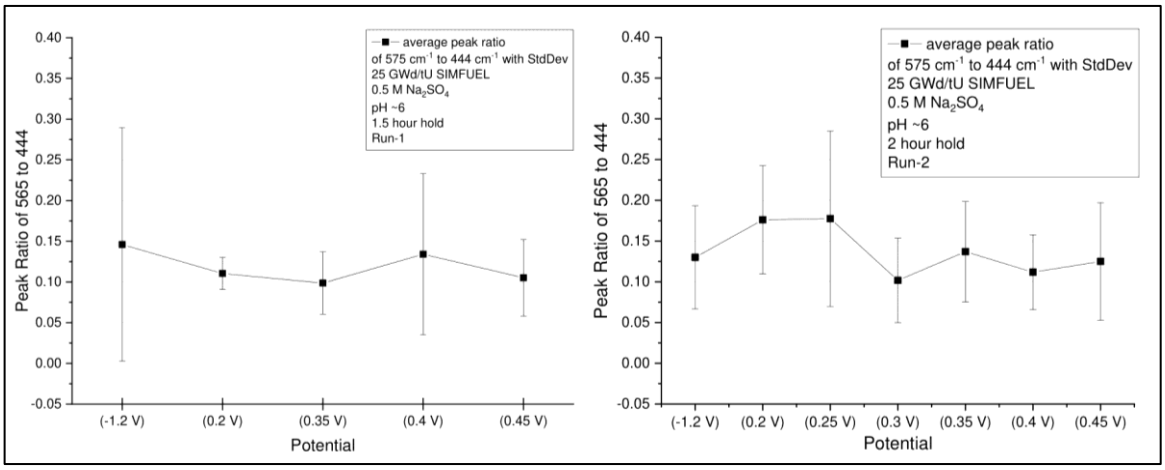

Figure 7-9: Plot of average peak height ratios of the 575 cm^{-1} to 444 cm^{-1} signal with standard deviation error bars, as a function of the applied oxidation potential, obtained from spectra acquired on the 785 nm Raman Microscope, from a sample of 25 GWd/tU SIMFUEL. The two graphs show results from two measurement repeats, Run-1 (left) and Run-2 (right).

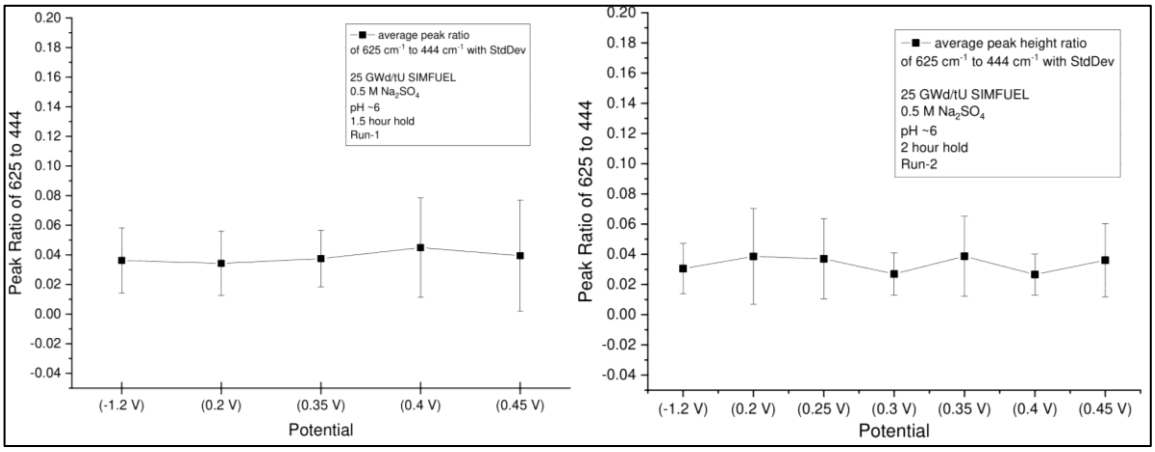

Figure 7-10: Plot of average peak height ratios of the 625 cm^{-1} to 444 cm^{-1} signal with standard deviation error bars, as a function of the applied oxidation potential, obtained from spectra acquired on the 785 nm Raman Microscope, from a sample of 25 GWd/tU SIMFUEL. The two graphs show results from two measurement repeats, Run-1 (left) and Run-2 (right).

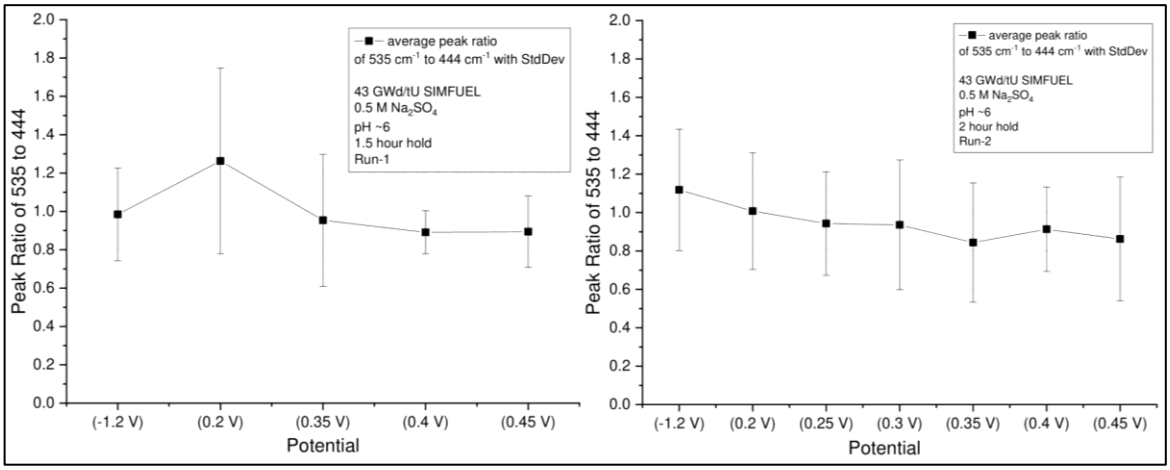

Figure 7-11: Plot of average peak height ratios of the 535 cm^{-1} to 444 cm^{-1} signal with standard deviation error bars, as a function of the applied oxidation potential, obtained from spectra acquired on the 785 nm Raman Microscope, from a sample of 43 GWd/tU SIMFUEL. The two graphs show results from two measurement repeats, Run-1 (left) and Run-2 (right).

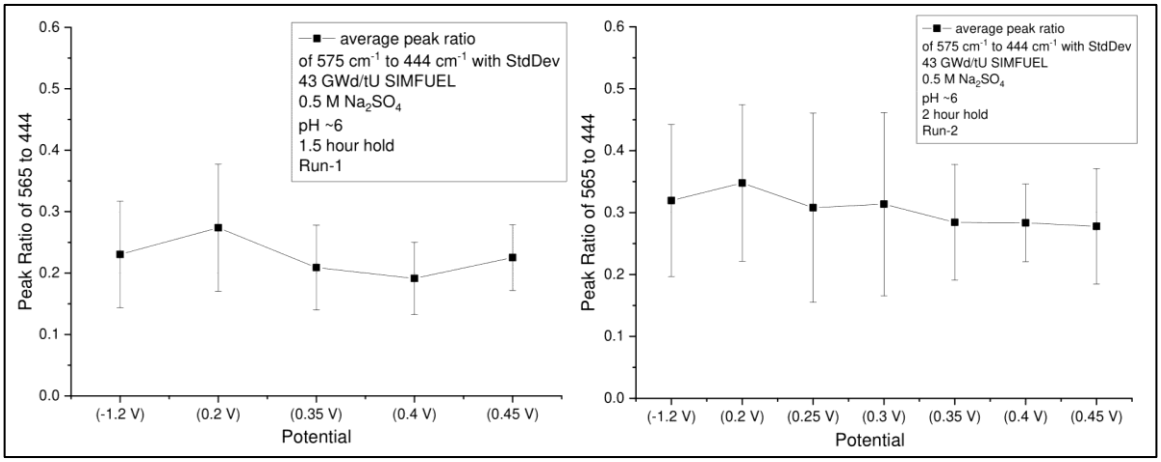

Figure 7-12: Plot of average peak height ratios of the 575 cm^{-1} to 444 cm^{-1} signal with standard deviation error bars, as a function of the applied oxidation potential, obtained from spectra acquired on the 785 nm Raman Microscope, from a sample of 43 GWd/tU SIMFUEL. The two graphs show results from two measurement repeats, Run-1 (left) and Run-2 (right).

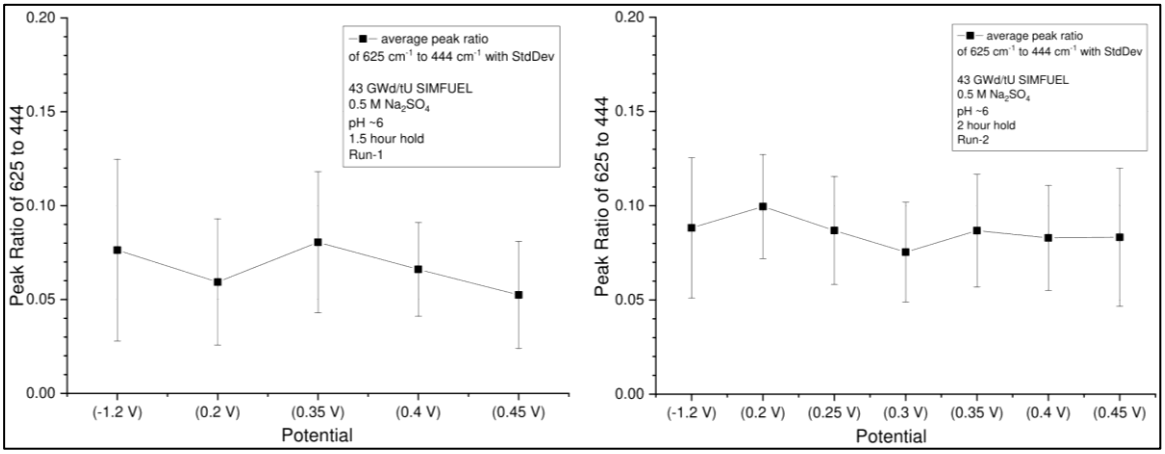

Figure 7-13: Plot of average peak height ratios of the 625 cm^{-1} to 444 cm^{-1} signal with standard deviation error bars, as a function of the applied oxidation potential, obtained from spectra acquired on the 785 nm Raman Microscope, from a sample of 43 GWd/tU SIMFUEL. The two graphs show results from two measurement repeats, Run-1 (left) and Run-2 (right).

Comparison of the results from the 25-SIMF and 43-SIMF electrodes, Figure 7-8 to Figure 7-10 and Figure 7-11 to Figure 7-13, respectively reveal a decrease in the intensity of the fundamental U-O stretch at 444 cm^{-1}, accompanied by an increase in the intensity of the broad “defect band”, relative to the 444 cm^{-1} signal [38].

This is consistent with the discussions of Chapter 4 Section 4.4.1 and can similarly be attributed to the larger number of dopants incorporated into the 43-SIMF matrix compared to that of the 25-SIMF. However, beyond this main difference, no other observations were present that were exclusively due to the anodic polarisations carried out in this study, as shown by a similar lack of changes in the spectral data with increasing oxidation potential across all the results from both the 25-SIMF and 43-SIMF studies.

Specifically, from the analysis of all the Run-2 plots, we can see that average peak height ratio values recorded at all applied potentials are within statistical error, the same as their respective baseline (recorded at -1.2 V) average peak height ratio values. Additionally, the average peak height ratios for each signal are also in agreement with the baseline 25-SIMF and 43-SIMF Raman data recorded in the absence of any applied potential, presented in Chapter 4 Section 4.4.1.

This lack of trend in peak height ratios as a function of the oxidation applied potential, suggests that no major changes in UO_2 oxidation state or hyperstoichiometry generation has occurred with increasing anodic polarisation. However, the inconclusive results did not necessarily suggest that the system undergoing anodic polarisation was not undergoing oxidation at the electrode surface but could instead indicate that such processes, under the conditions of this study, were undetectable by the μ-Raman spectroscopy.

Additionally, the large overlaps between the standard deviation error bars of the peak ratios indicated large statistical noise in the peak heights, which made observation and determination of trends or correlations difficult. The was likely error/noise introduced during the Raman acquisition process, which required the acquisition of multiple scans at random locations across the electrode

surface, resulting in a large spread of recorded spectra and with a wide range of peak heights.

In this section, the use of a 785 nm Raman microscope for in-situ spectra acquisition during anodic polarisations of 25-SIMF and 43-SIMF has been investigated. As part of the method development process, a new experimental setup was constructed and used for these studies; the initial results and discussions have shown no noticeable changes to the SIMFUEL samples. The average peak height ratio values from the deconvoluted “defect band” appear to show no trends with respect to the average peak height ratios of the 575 and 625 cm^{-1} peaks, as a function of applied oxidation potential. These results suggest the possibility of several explanatory scenarios:

1) No UO_2 oxidation is taking place and thus no build-up of oxidised species at the SIMFUEL surface and no detection by μ-Raman spectroscopy.
2) UO_2 oxidation and build-up of oxidised species is taking place at the SIMFUEL surface, however, the degree of surface oxidation or the amount of oxidised species formation at the surface is insufficient to be detectable by μ-Raman spectroscopy due to the obtained Raman signal being dominated by that of the unoxidised bulk, likely caused by the Raman sampling up to 1 μm or more into the sample.
3) UO_2 oxidation and build-up of oxidised species is taking place at the SIMFUEL surface and spectral changes due to UO_2 oxidation are being detected by μ-Raman spectroscopy. However, the spectra sample size is not large enough to reduce the statistical noise and is producing statistically insignificant results.
4) UO_2 oxidation and build-up of oxidised species is taking place at the SIMFUEL surface. However, the particular Raman microscope instrument used in this study is incapable of detecting the presence of surface UO_2 oxidised species.

We suspect that the likely scenario involves a combination of scenarios (2), (3) and (4) as we can eliminate the possibility of scenario (1) due to overwhelming voltammetry data and literature evidence to suggest that UO_2 oxidation does indeed occur under the applied oxidation potentials used in this study.

Scenarios (2) and (3) are likely as they are both concerned with the measurement processes within the experimental methodology. Both can be mitigated against by, for example (a) increasing the length of time at which the electrode sample is undergoing polarisation and thus maximising the layer thickness of the oxidised UO_2 surface build-up, or (b) increasing the Raman spectra sample size by increasing the number of scans acquired to improve the average and reduce the statistical noise.

However, even if scenarios (2) and (3) were addressed, scenario (4) could still be the main bottleneck in preventing Raman detection. We hypothesise that this is likely due to the non-complementary combination of the thin UO_2 oxidation surface layer formation, typically within the low nanometre range of approximately ~2 – 30 nm [27, 175, 176, 179, 180], and the larger depth resolution of a typical confocal Raman microscope, usually in the micrometre range of approximately > ~1 μm [181-183].

This discrepancy between the oxide layer thickness and Raman depth resolution is likely to cause difficulties in acquiring a signal from the surface, which is further exacerbated by the overwhelming signal of the sub-surface bulk UO_2 material. This would suggest that the particular Raman instrument used for this study is unsuitable for the requirements of this study. Therefore, further experimentation with different Raman instruments or setups would be necessary as part of the method development – this will be the subject of the next section.

7.3 Measurements with 532 nm Raman Microscope

In this section, Raman spectra were acquired using a 532 nm laser Raman microscope on samples of 25 GWd/tU AGR SIMFUEL and 43 GWd/tU AGR SIMFUEL, following similar processes as those described in Section 7.2. In contrast to the 785 nm excitation wavelength, the 532 nm excitation wavelength does induce a Raman resonance effect during the acquisition of spectra on the SIMFUEL samples and was specifically chosen to enhance the signal intensity of the LO phonon at 575 cm^{-1}, further discussions of this phenomenon can be found in Chapter 4 Section 4.4.2. The resonance effect artificially increases the

peak intensities in the “defect band” region, allowing for clearer deconvolution of the convoluted peaks and improves the ability to extract peak heights.

The measurement method used for the data acquisition has been adopted from that of the Run-2 experiments of Section 7.2. No changes were made to the Raman spectra acquisition process or the Raman spectra post-processing.

These measurements will enable us to further study and compare the “defect band” behaviour of the SIMFUELs under different oxidation applied potentials and will allow us to compare the differences between using the 532 nm versus the 785 nm excitation wavelength for μ-Raman spectroscopy studies of the 25-SIMF and 43-SIMF.

7.3.1 Results & Discussion

The SIMFUEL electrodes were polarised according to the same conditions and oxidation potentials as those of the Run-2 experiments of Section 7.2.2. Hence, plots of current vs. time of the recorded current response during the application of oxidation potentials have not been presented here, as they show similar results for both the 25-SIMF and 43-SIMF.

The 532 nm excitation wavelength used here, artificially enhances the signal strength of the first overtone of the longitudinal optical (LO) phonon at 575 cm^{-1} and also its accompanying 2LO phonon at 1150 cm^{-1}, spectra showing such features can be found in Chapter 4 Section 4.4.2. This phenomenon has been reported in literature under Raman studies of the same laser excitation wavelength [136-138].

Although the resonance effect does not specifically affect the signal strengths of the 535 and 625 cm^{-1} peaks within the “defect band”, they are somewhat enhanced due to their adjacent proximity to the enhanced 575 cm^{-1} peak. This minor enhancement of the 535 and 625 cm^{-1} peak signals allows them to be more prominent within the “defect band”, thus making it easier to peak fit and extract peak heights, in comparison with spectra acquired using the 785 nm Raman microscope. Figure 7-5 shows an example peak fitting of a Raman spectrum acquired using the 532 nm Raman microscope on a sample of 25-SIMF.

Figure 7-14, Figure 7-15, Figure 7-16 show the average peak height ratios of the 535 to 444 cm^{-1} signal, 575 to 444 cm^{-1} signal and 625 to 444 cm^{-1} signal for the 25-SIMF, respectively. Figure 7-17, Figure 7-18, Figure 7-19 shows the average peak height ratios of the 535 to 444 cm^{-1} signal, 575 to 444 cm^{-1} signal and 625 to 444 cm^{-1} signal for the 43-SIMF, respectively. The differences in spectra between the two SIMFUELs are the same as those reported in the 785 nm Raman results of Section 7.2.1. and were not affected by the use of the 532 nm Raman.

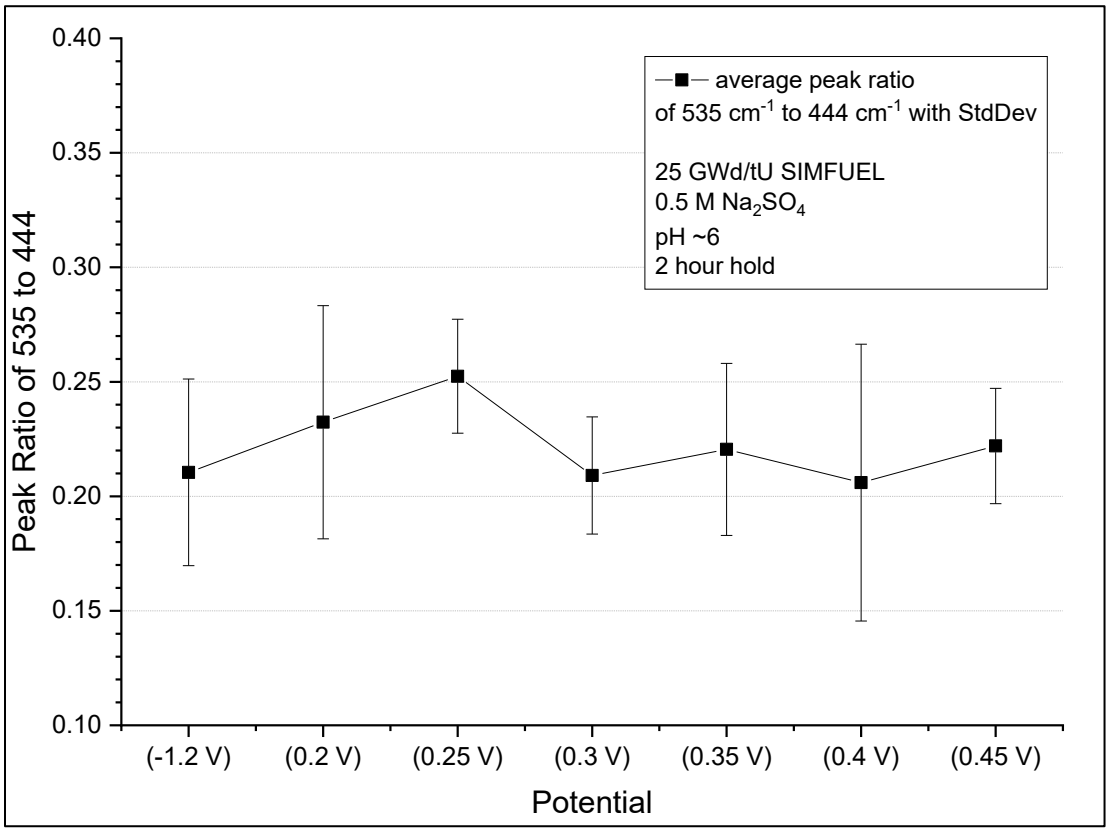

Figure 7-14: Plot of average peak height ratios of the 535 cm^{-1} to 444 cm^{-1} signal with standard deviation error bars, as a function of the applied oxidation potential, obtained from spectra acquired on the 532 nm Raman Microscope, from a sample of 25 GWd/tU SIMFUEL.

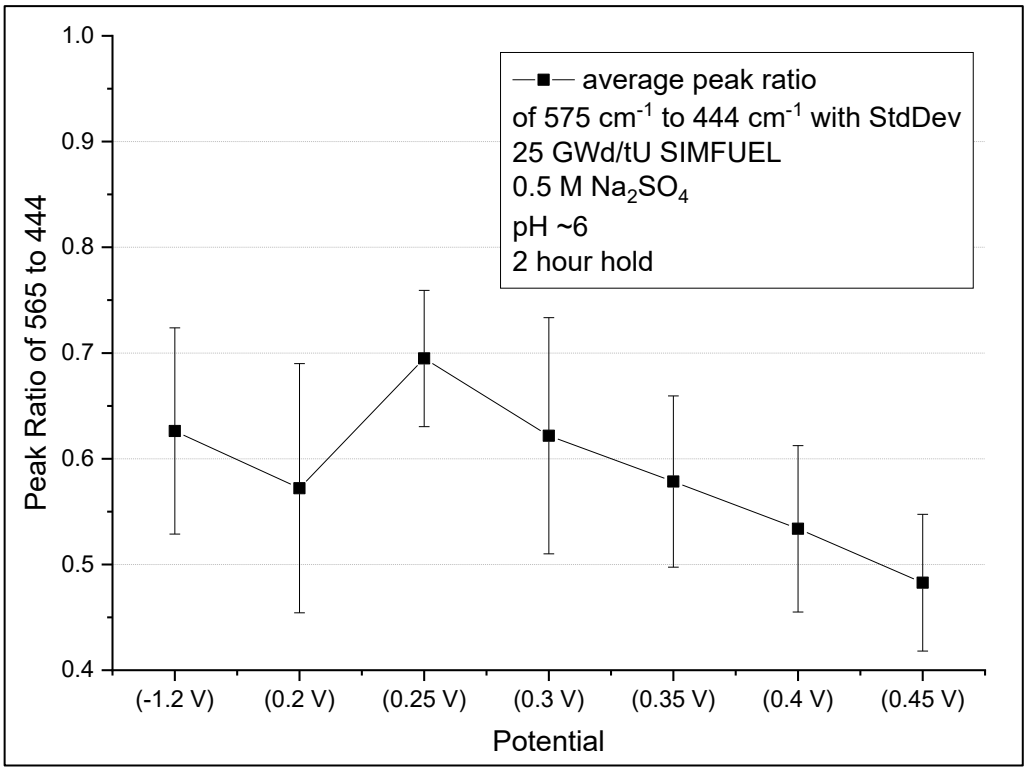

Figure 7-15: Plot of average peak height ratios of the 575 cm^{-1} to 444 cm^{-1} signal with standard deviation error bars, as a function of the applied oxidation potential, obtained from spectra acquired on the 532 nm Raman Microscope, from a sample of 25 GWd/tU SIMFUEL.

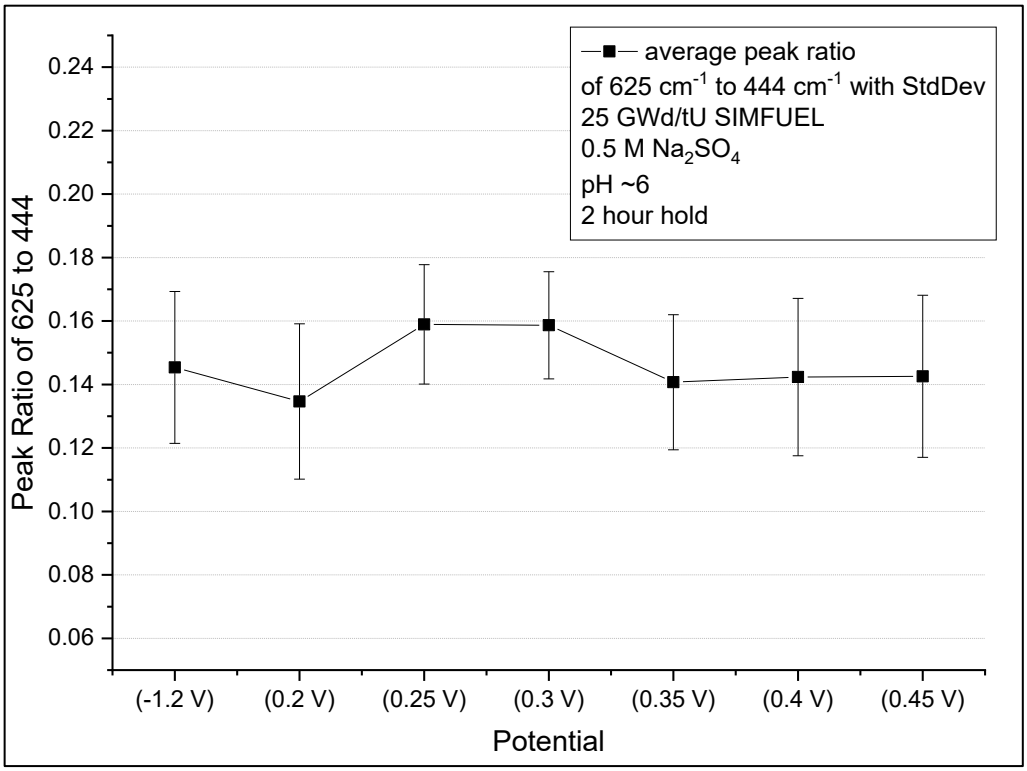

Figure 7-16: Plot of average peak height ratios of the 625 cm^{-1} to 444 cm^{-1} signal with standard deviation error bars, as a function of the applied oxidation potential, obtained from spectra acquired on the 532 nm Raman Microscope, from a sample of 25 GWd/tU SIMFUEL.

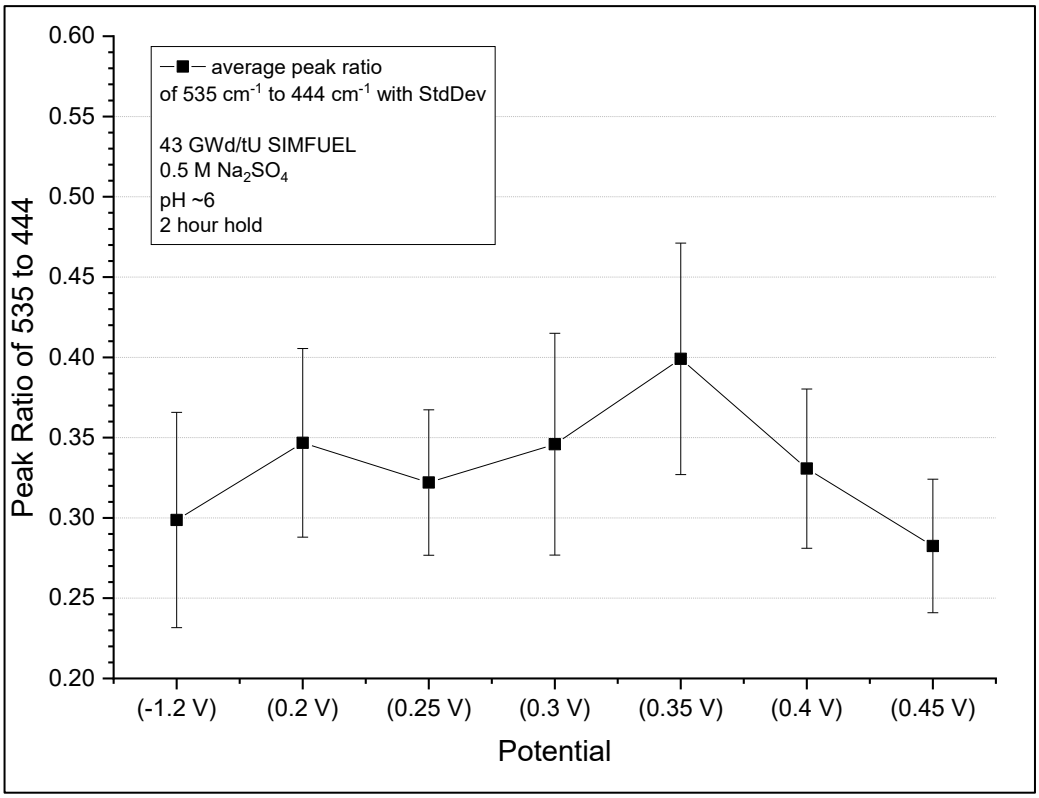

Figure 7-17: Plot of average peak height ratios of the 535 cm^{-1} to 444 cm^{-1} signal with standard deviation error bars, as a function of the applied oxidation potential, obtained from spectra acquired on the 532 nm Raman Microscope, from a sample of 43 GWd/tU SIMFUEL.

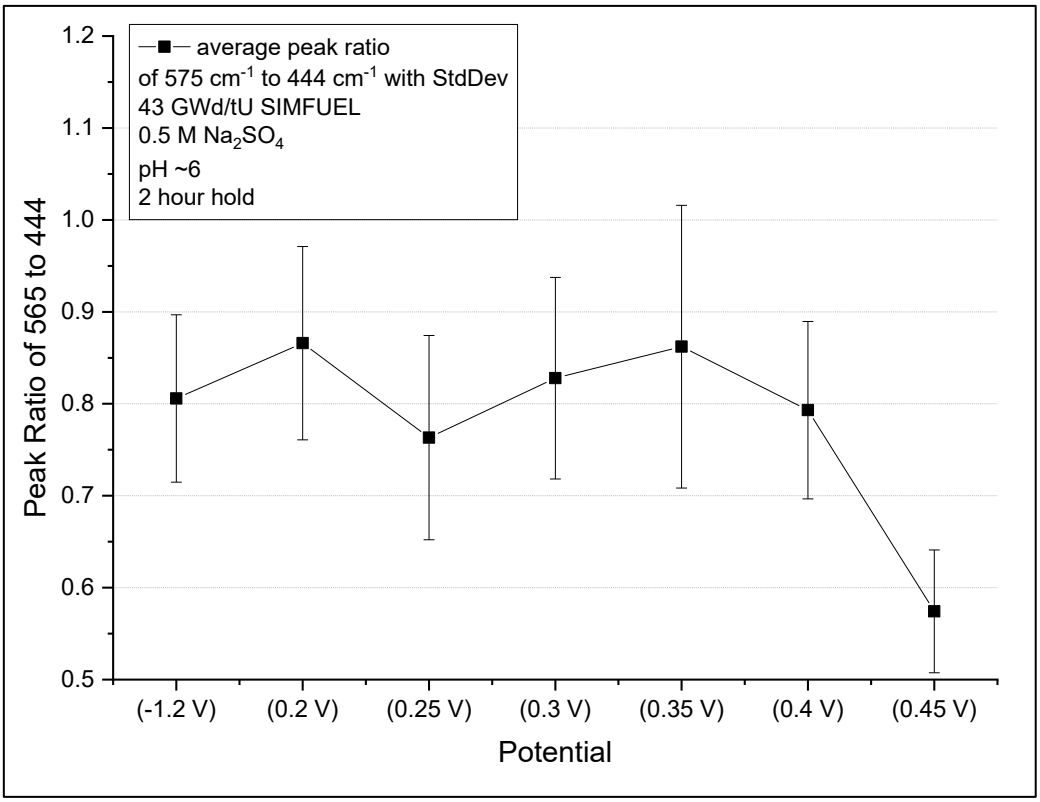

Figure 7-18: Plot of average peak height ratios of the 575 cm^{-1} to 444 cm^{-1} signal with standard deviation error bars, as a function of the applied oxidation potential, obtained from spectra acquired on the 532 nm Raman Microscope, from a sample of 43 GWd/tU SIMFUEL.

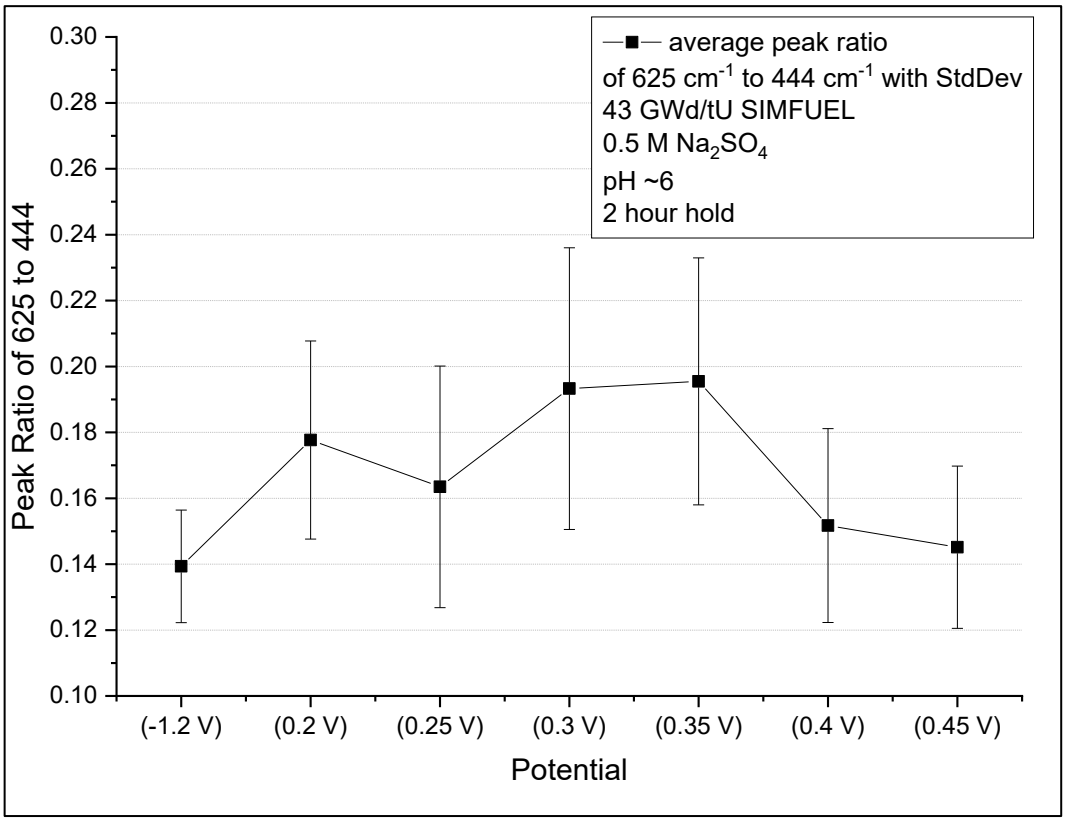

Figure 7-19: Plot of average peak height ratios of the 625 cm^{-1} to 444 cm^{-1} signal with standard deviation error bars, as a function of the applied oxidation potential, obtained from spectra acquired on the 532 nm Raman Microscope, from a sample of 43 GWd/tU SIMFUEL.

Comparison of the average peak height ratios as a function of applied potential versus their respective baseline average peak height ratios (recorded at -1.2 V), and versus those obtained in the absence of an applied potential (presented in Chapter 4 Section 4.4.2) reveal that, within a margin of error, all the average peak height ratios are the same at all applied potentials, indicating consistency across the results but also highlighting a lack of trends.

Furthermore, comparisons with the spectra acquired using the 785 nm excitation wavelength in Section 7.2.1, show a similar lack of trends, despite the resonance-enhanced signals of the “defect band”, i.e., the use of the 532 nm excitation wavelength did not reveal any additional trends associated with the average peak height ratios as a function of the applied oxidation potential.

Similarly to the results of Section 7.2.1, the plots of average peak height ratios presented here are shown with standard deviation error bars, which also show large deviation and overlap across the plotted averages, again making the said average peak height ratios reported here statistically insignificant.

The expected observations regarding the average peak height ratio plots, are the same as those discussed in Section 7.2.1. If UO_{2+x} species were to form at the surface of the electrodes as a result of oxidation and if the formation of such species were to be detected by Raman, then we would expect to see changes to the average peak height ratios of the 575 and 625 cm^{-1} peaks, as a function of the applied oxidation potential.

However, despite the enhanced intensity of the “defect band” peaks, from the use of the 532 nm Raman, the improvements to the peak fitting process and to the deconvolution of the “defect band”, did not generate any new results or observations that differed from the 785 nm Raman work presented in Section 7.2.1.

Based on the similarities of the results from both the 785 nm and 532 nm work, this scenario is more likely related to the discrepancy between the UO_2 oxidation surface layer thickness and the limitations imposed by the depth resolution of the Raman instrument used, rather than a matter related to signal visibility and spectra post-processing, similar to the conclusions discussed at the end of Section 7.2.1.

7.4 Summary & Conclusions

In this chapter, we presented the preliminary results and conclusions from the initial trials of a new combined experimental method for in-situ μ-Raman spectroscopy studies of SIMFUEL electrode samples during electrochemical oxidation measurements.

We demonstrated the use of μ-Raman spectroscopy for monitoring UO_2 electrochemical oxidation at the surface of the 25-SIMF and 43-SIMF electrodes using two different Raman excitation wavelengths, 785 nm and 532 nm.

We also demonstrated the use of a custom-made electrochemical cell that enabled voltammetry measurements to be carried out while integrated with a Raman microscope instrument to facilitate the in-situ Raman measurements.

Raman spectra of the SIMFUEL electrodes were acquired following anodic polarisation. The spectra were fitted in the wavenumber region between ~350 and 700 cm^{-1} to deconvolute the three main signal contributions within the

“defect band”. Peak height ratios were calculated as ratios of the ‘peak-of-interest’ with respect to the ‘fundamental U-O stretch’. Peak heights were obtained from the signals of:

- The ~444 cm^{-1} peak, assigned to the fundamental U-O stretch.
- The ~535 cm^{-1} peak, associated with oxygen-vacancy-induced lattice distortions.
- The ~575 cm^{-1} peak, associated with dopant density and distortions to the cubic fluorite lattice.
- The ~625 cm^{-1} peak, associated with the measure of the degree of UO_2 oxidation/hyperstoichiometry.

The primary objective was to determine the effectiveness of using μ-Raman spectroscopy for monitoring the degree of oxidation at the surface of AGR SIMFUEL electrodes during anodic polarisation and to determine whether the method and workflow being trialled could be improved and adopted for similar future studies.

The challenges encountered during the study were also discussed, along with suggestions for improvements and change, as part of the method development. This section provides a summary of the main findings and conclusions from this study.

Overall, the methodology and workflow were successful in obtaining results via the combination of μ-Raman spectroscopy and voltammetry; the experimental processes for the two techniques were successfully integrated to allow seamless measurements from the electrochemical oxidation of the sample to Raman acquisition.

However, the results from peak ratio vs. applied potential plots, obtained from the Raman spectra, were largely found showing no noticeable changes to the oxidation state of the SIMFUEL samples as a function of applied oxidation potential. Regardless of SIMFUEL dopant density, neither the 25-SIMF or 43-SIMF results showed any trends in the plotted average peak height ratios which could indicate the presence of UO_2 surface oxidation.

Results between the two Raman excitation wavelengths, 785 nm and 532 nm, also showed no differences between the average peak height ratios. Although the two sets of spectra acquired at the two excitation wavelengths, 785 nm and 532 nm, were different due to the artificially resonance-enhanced 575 cm^{-1} peak by the latter excitation wavelength, the improved peak intensities and peak separation within the “defect band” afforded by this phenomenon did not reveal any trends in the average peak height ratios.

We hypothesise that this is due to a combination of the incompatible choice of the Raman instrumentation used as part of this study, which lacked the capability to achieve a shallow depth resolution for near surface scanning, and the thin surface oxide layer formed during the SIMFUEL electrochemical oxidation process.

Further work would require continued development of this combined experimental method. Here we provide a summary of the main suggestions:

- A review of the possible changes and setups available to the Raman microscope instruments in order to facilitate a wider depth resolution range, i.e., to allow a shallower depth of penetration for scanning nanometre thick surface layer oxidation growths/deposits.
- Changes to the oxidation potential-hold process by increasing the length of time at which the electrodes undergo polarisation in order to promote thicker surface oxide layer build-up.
- Changes to the Raman acquisition process by further increasing the number of random scans of the SIMFUEL electrode surface in order to reduce statistical error.

8 Conclusions and Further Work

This chapter summarises the objectives and conclusion of the studies presented in this thesis and provides recommendations for further work.

8.1 Objectives

The main overarching objective of this research project was to study the corrosion behaviour of AGR SNF, under conditions relevant to AGR wet pond storage. The following materials were used for the studies conducted and discussed in this thesis:

- undoped-UO_2
- lower simulated burn-up 25 GWd/tU AGR SIMFUEL (25-SIMF)
- higher simulated burn-up 43 GWd/tU AGR SIMFUEL (43-SIMF)
- 43 GWd/tU AGR SIMFUEL with higher lanthanide doping (43-hiLn)
- 43 GWd/tU AGR SIMFUEL with higher lanthanide and chromium-doped (43-hiLnCr)
- as-received non-sensitised 20/25/Nb stainless steel AGR cladding
- legacy AGR SNF sample.

Chapter 4 and 5 presented the results of the baseline studies of AGR cladding, undoped-UO_2, and AGR SIMFUELs. The objective of these two chapters was to set the basis and baseline understanding of these surrogate AGR SNF materials in order to support the interpretation and understanding of the real legacy AGR SNF electrochemical studies presented in later chapters.

Chapter 4 presented the results from the single component electrode studies under AGR wet pond storage conditions, using electrochemical methods (LSV, OCP, EIS), SEM characterisation, and μ-Raman spectroscopy.

Chapter 5 presented the results from the studies of coupled-electrode systems comprising of both 20/25/Nb stainless steel AGR cladding and 25 GWd/tU AGR SIMFUEL using OCP and LSV electrochemical techniques.

Chapter 6 presented the results from the first-ever electrochemical study of a sample of legacy UK AGR SNF using electrochemical methods (LSV, OCP). The experimental campaign was conducted at the UK's NNL Windscale

Laboratory under hot-cell conditions. The main objective of this chapter was to report, analyse and interpret this novel dataset in order to derive information regarding the electrochemical behaviour of real AGR spent nuclear fuel under conditions relevant to pond storage. A key secondary objective was to explore and demonstrate the validity of using AGR-specific SIMFUELs as simulants for real AGR SNF. The results were analysed and compared with the baseline UO_2 and SIMFUEL studies of Chapter 4 and the cladding-SIMFUEL coupled electrode studies of Chapter 5.

Chapter 7 presented the preliminary results from an additional series of experimental work looking at the method development and initial trials of a new experimental setup, which combined voltammetry with μ-Raman spectroscopy. The main objective of this chapter was to determine the effectiveness of combining these two techniques and whether such a combination of techniques could enable μ-Raman spectroscopy to be used in monitoring the degree of oxidation taking place at the surface of the SIMFUEL samples during an electrochemical experiment.

Thus, the following Section 8.2 will discuss the achievement of the project objectives and summarise the key conclusions from each chapter of work.

8.2 Conclusions

This section summarises the key conclusions and findings from each chapter of work.

8.2.1 Baseline Studies of AGR Spent Fuel Simulants

Chapter 4 presented the baseline electrochemical, SEM, and μ-Raman spectroscopy studies of the following materials:

- undoped-UO_2.
- lower simulated burn-up 25 GWd/tU AGR SIMFUEL (25-SIMF).
- higher simulated burn-up 43 GWd/tU AGR SIMFUEL pellet (43-SIMF).
- 43 GWd/tU AGR SIMFUEL with higher lanthanide doping (43-hiLn).
- 43 GWd/tU AGR SIMFUEL with higher lanthanide and chromium-doped (43-hiLnCr).

- as-received non-sensitised 20/25/Nb stainless steel AGR cladding.

For each material, the baseline corrosion behaviour was studied using LSV and OCP in 0.5 mol/dm^3 Na_2SO_4 standard electrolyte and for μ-Raman spectroscopy studies, measurements were conducted using a 532 nm and a 785 nm laser excitation wavelength Raman microscope.

Additionally, each material the 25 GWd/tU SIMFUEL and 20/25/Nb AGR cladding samples were also studied under simulated AGR pond storage conditions.

The studies presented in Chapter 4 provided the baseline dataset upon which subsequent electrochemical and Raman studies of these materials and the legacy AGR SNF, were compared against. This enabled the comparison of the baseline electrochemical behaviour with the coupled-electrode studies of Chapter 5, the legacy AGR SNF electrode studies of Chapter 6, and the μ-Raman spectroscopy / electrochemical oxidation studies of Chapter 7.

The Chapter 4 objectives were successfully achieved and the full summary can be found in Chapter 4 Section 4.6. The following findings were reported and further summarised as follows:

1. SEM characterisation of the SIMFUELs showed that, broadly, the grain size decreases with Lanthanide (III) loading.
2. Voltammetry in Na_2SO_4 indicated that the electrochemical activity of the SIMFUELs increases with doping.
3. OCP measurements in Na_2SO_4 indicated that the Cr-free SIMFUELs exhibit OCP values which sit in the potential region more positive than that seen with undoped-UO_2 and associated with the onset of in-grain oxidation of UO_2 to UO_{2+x}.
4. Introduction of additional Ln(III) into the SIMFUEL matrix to give 43-hiLn, increases their electrochemical activity further compared to undoped-UO_2.
5. In Na_2SO_4, 20/25/Nb AGR cladding was observed to exhibit behaviour similar to that seen previously i.e., a wide region of passivity positive of -

0.6 V with onset of pre-transpassivity occurring at 0.2 V and onset of transpassivity occurring at voltages positive of 1.2 V. With OCP sitting at ~0.05 V i.e. in the passive region.

6. Raman analysis of the SIMFUELs revealed that, as expected from earlier studies, the SIMFUELs become more defected with increased fission product loading, mainly due to the addition of oxygen vacancies to compensate for the incorporation of Ln(III) dopants into the UO_2 matrix.
7. Under simulated AGR pond storage conditions, OCP, LSV and EIS measurements were conducted on 25-SIMF, and the following findings were reported:
    a. Polarisation curves from LSV measurements of 25-SIMF in SSPW showed a general trend associated with the increase in alkalinity of the electrolyte solutions. Similar to those recorded under baseline Na_2SO_4 electrolyte conditions.
    b. OCP measurements of the 25-SIMF in SSPW corroborated the pH effect seen in the polarisation curves. As pH increases, the open circuit potential becomes more negative. This suggests that increasing alkalinity shifts the equilibrium corrosion potential away from a region of potentials associated with active UO_2 dissolution.
    c. EIS measurements of 25-SIMF in SSPW showed a trend of increasing R(total) at the region of potentials between ~-0.3 to 0.2 V, which correlates with the onset of various UO_2 surface oxidation processes taking place at the SIMFUEL surface.
    d. Polarisation curves from LSV measurements of the 25-SIMF in alkaline chloride water showed that the presence of chloride from 0.1 to 100 mM NaCl in solution, does not appear to affect the electrochemical/oxidation processes.
    e. OCP measurements of the 25-SIMF in alkaline chloride water showed no dependence on the increase in chloride concentration of the electrolytes.

8. Under simulated AGR pond storage conditions, OCP, LSV and EIS measurements were conducted on 20/25/Nb AGR cladding, and the following findings were reported:

    a. Polarisation curves from LSV measurements of AGR cladding in SSPW showed that the AGR cladding becomes less susceptible to corrosion by chloride as pH increases from 8 to 12.5.
    b. OCP measurements of the AGR cladding in SSPW showed a trend of decreasing OCP with increasing pH, shifting the corrosion potential of the cladding further towards negative potentials and into a region of passivity.
    c. EIS measurements of the AGR cladding in SSPW showed that there is a correlation between the region of potentials associated with passive layer formation and the increase in R(total).
    d. Polarisation curves from LSV measurements of the AGR cladding in alkaline chloride electrolytes showed that there is a strong chloride effect at higher chloride concentrations. However, at pH 12.5 the effect of chloride is suppressed, up to concentrations of 100 mM NaCl.
    e. OCP measurements of the AGR cladding in alkaline chloride water showed no correlation between the OCP values and chloride concentration.

The findings from the Chapter 4 baseline studies showed that the materials under study behaved as expected under each measurement type and study condition. This provided the necessary reassurance for the electrochemical and Raman behaviour of the materials under a variety of measurement conditions, to give confidence when used in the comparison against the studies undertaken in Chapters 5 , 6, and 7.

8.2.2 Electrochemistry of Coupled 20/25/Nb AGR cladding and 25 GWd/tU AGR SIMFUEL

Chapter 5 presented the studies of coupled-electrode systems comprising of both 20/25/Nb stainless steel AGR cladding and 25 GWd/tU AGR SIMFUEL

using OCP and LSV electrochemical techniques. The two electrode coupling mechanisms developed for these studies are as follows:

a) Method-1 (M1) – consisting of two separate resin-cast “lollipop” electrodes of (i) a 25 GWd/tU SIMFUEL pellet, (ii) a cross-sectional piece of 20/25/Nb AGR cladding. These are coupled together via a conducting copper cable to form a single working electrode.

b) Method-2 (M2) – consisting of a single “lollipop” electrode containing both a 25 GWd/tU SIMFUEL pellet and a cross-sectional piece of 20/25/Nb AGR cladding, cast together in resin to form a single composite electrode wherein both components are physically as well as electrically coupled.

The studies presented in Chapter 5 demonstrated the use of simulant-based methods to replicate the electrochemical behaviour of a real AGR SNF electrode. This enabled the comparison of the simulant coupled-electrodes with the analogous composite electrode studies of the real legacy AGR SNF of Chapter 6.

The Chapter 5 objectives were successfully achieved and the full summary can be found in Chapter 5 Section 5.4. The following findings were reported and further summarised as follows:

1. Data from Method-2 experiments showed that the SIMFUEL component dominates the electrochemical behaviour over all experiment types conducted.

2. Data from Method-1 experiments showed a deviation in experiment-to-experiment variation. Neither component dominates the observed electrochemical behaviour with no preference towards the SIMFUEL or cladding-dominated behaviour during either OCP or LSV measurements.

3. Overall, Method-2 electrode system produced the most consistent and reproducible results. The fabrication method also results in a “lollipop” electrode that better resembles the physical composition of a real AGR fuel pin cross-section, as the SIMFUEL pellet is in direct contact with the AGR cladding.

4. Voltammetry data from both Method-1 and Method-2 was deconvoluted and simplified to being dominated by one or the other of its individual components. Therefore, it was more appropriate to use the single component voltammetry data of Chapter 4 Section 4.5 in conjunction with the Method-2 studies of Chapter 5, to support the real AGR SNF studies of Chapter 6.

The findings from the Chapter 5 coupled-electrode studies successfully demonstrated the use of simulant materials to simulate the coupling mechanism and electrochemical behaviour of a coupled-electrode/composite electrode. This provided the necessary electrochemical data and reassurance of the electrochemical behaviour under simulant AGR pond storage conditions, to assist in the analysis and interpretation of the electrochemical studies of real AGR SNF undertaken in Chapter 6.

8.2.3 Electrochemical Studies of Legacy AGR Spent Nuclear Fuel

Chapter 6 presented the results from the first-ever electrochemical study of a sample of legacy UK AGR SNF using electrochemical methods (LSV, OCP), carried out under hot-cell conditions. A cross-sectional sample of irradiated AGR spent fuel was fabricated into an electrode suitable for electrochemical measurements from a legacy AGR spent fuel rod.

This study, being the first of its kind, was faced with many challenges and complexities associated with the use of highly radioactive nuclear materials under hot-cell conditions. The electrochemistry measurements conducted under hot-cell conditions required adjustments and adaptations to account for the constraints and limitations.

This study was conducted in two parts. The first involved an investigation of the spent fuel electrode’s electrochemistry in a SSPW, at pH 8, 11.4 and 12.5 representative of, respectively, undosed pondwaters, pondwaters subject to the current caustic dosing strategy and pondwaters subject to a potential future dosing strategy.

The second part of the study looked at the effect of chloride ion concentration, at 0.1, 1.0, 10 and 100 mmol/dm^3 NaCl, on the electrochemical behaviour of the AGR SNF at pH 8, 11.4 and 12.5, again representative of, respectively, undosed pondwaters, pondwaters subject to the current caustic dosing strategy and pondwaters subject to a potential future dosing strategy.

The Chapter 6 objectives were successfully achieved and the full summary can be found in Chapter 6 Section 6.4. The following findings were reported and further summarised as follows:

1. The SSPW OCP and LSV studies showed that the conditions of the current UK AGR SNF storage strategy provide sufficient corrosion protection for the legacy AGR fuel composite electrode system.
    a. Data from the OCP measurements showed that the real AGR fuel composite electrode behaved similarly to the OCP data of AGR cladding – suggesting that the real AGR fuel composite electrode's exchange current path is dominated by the cladding component when under open circuit conditions.
    b. Data from the LSV measurements showed that the real AGR fuel composite electrode behaved similarly to the LSV data of Method-2 electrode – suggesting that the real AGR fuel behaviour is dominated by the UO_2 component when under LSV conditions.
2. The NaCl OCP and LSV studies have shown that low chloride conditions are preferred when it comes to the prevention of corrosion of either the cladding or the UO_2 component of the legacy AGR fuel composite electrode system.
    a. Data from the OCP measurements showed different behaviours across each pH. At high pH 12.5 there was likely corrosion protection afforded by the passive oxide layer grown on the cladding component. At lower pHs the cladding component of the real AGR fuel composite electrode was shown to be more susceptible to the effects of chloride, and in particular when considered alongside the potential of RIS of the cladding component.

b. Data from the LSV measurements showed different behaviours in the polarisation curves across each pH. At pH 12.5, the polarisation curves exhibited behaviour similar to that of the 25-SIMF with no correlation to $[Cl^-]$. However, as lower pH, it was seen that AGR electrode behaviour appeared to gradually transition with increasing $[Cl^-]$, from most closely resembling 25-SIMF at low chloride, to most closely resembling the cladding component at high chloride. This was attributed to the intricate balance between the competing corrosion process taking place at the surface of the cladding component and the UO_2 component, versus the degree of passivation at the surface of the cladding component, as a function of $[Cl^-]$, and including the considerations of cladding RIS.

3. The novelty of this experimental campaign meant that no previous works were available for comparison. Thus, the Chapter 6 studies were supported by the baseline UO_2 and SIMFUEL studies from Chapter 4 and the cladding-SIMFUEL coupled electrode studies from Chapter 5. These studies have shown that the use of non-active 20/25/Nb AGR cladding and 25 GWd/tU AGR SIMFUELs are suitable for simulating the electrochemical behaviour of real AGR SNF.

The findings from the Chapter 6 real AGR SNF studies highlighted the capabilities of using electrochemical measurements to study legacy AGR SNF and demonstrated the challenges associated with working under hot-cell conditions. The results from these studies revealed that the electrochemical behaviour of real AGR SNF closely resembles that of the AGR SIMFUELs. Showing us that, for the first time, AGR simulants are indeed suitable for simulating the electrochemical behaviour of real AGR SNF. But importantly, the results from these legacy AGR SNF studies revealed that the current wet storage conditions of AGR SNF are suitable for suppressing and preventing further corrosion of the AGR spent fuel materials during wet pond storage.

8.2.4 Electrochemical Oxidation of AGR SIMFUELs

Chapter 7 presented the preliminary results from an additional series of experimental work looking at the method development and initial trials of a new experimental setup, which combined voltammetry with μ-Raman spectroscopy.

Electrochemical oxidation measurements were carried out on SIMFUEL electrodes in a non-interfering background electrolyte containing 0.5 mol/dm^3 Na_2SO_4. Oxidation of the sample surface was achieved by application of an oxidation potential to the working electrode. μ-Raman spectroscopy was then used in-situ to record and monitor changes to the surface composition of the SIMFUEL samples, by analysing the spectral changes within a broad band of peaks known as the “defect band”, situated approximately between 500 and 700 cm^{-1}.

To facilitate this new methodology, a specially fabricated PTFE electrochemical cell was developed to enable electrochemical measurements in combination with Raman data acquisition, allowing the electrochemical cell compartment to be mounted onto the microscope stage of the μ-Raman instrument.

The Chapter 7 objectives were successfully achieved, such that the use of a new combined experimental method for in-situ μ-Raman spectroscopy with electrochemical oxidation was successfully demonstrated.

The use of a custom electrochemical cell that enabled voltammetry measurements to be carried out while integrated with a Raman microscope instrument to facilitate the in-situ Raman measurements, was demonstrated.

The use of μ-Raman spectroscopy for monitoring UO_2 electrochemical oxidation at the surface of the 25-SIMF and 43-SIMF electrodes using two different Raman excitation wavelengths, 785 nm and 532 nm, was demonstrated.

The full summary can be found in Chapter 7 Section 7.4. The following findings were reported and further summarised as follows:

- Overall, the methodology and workflow were successful in obtaining results via the combination of μ-Raman spectroscopy and voltammetry; the experimental processes for the two techniques were successfully

integrated to allow seamless measurements from the electrochemical oxidation of the sample to the Raman acquisition.

- However, the results were largely found to show no noticeable changes to the oxidation state of the SIMFUEL samples as a function of applied oxidation potential. Regardless of SIMFUEL dopant density, neither the 25-SIMF or 43-SIMF results showed any trends in the plotted average peak height ratios which could indicate the presence of UO_2 surface oxidation.
- It was hypothesised that this was likely due to a combination of the incompatible choice of the Raman instrumentation used as part of this study, which lacked the capability to achieve a shallow depth resolution for near-surface scanning, and the thin surface oxide layer formed during the SIMFUEL electrochemical oxidation process.

The findings from the Chapter 7 baseline studies showed that the methodology and workflow for combined μ-Raman spectroscopy and voltammetry studies were possible and practical. However, further testing and continued development would be required to improve this combined methodology and workflow, such that the experimental results yield the desired outcomes.

8.3 Recommendations for Further Work

The main focus of this thesis has been on the electrochemical corrosion behaviour studies of a legacy AGR SNF sample, supported by a series of analogous simulant studies. This real fuel experimental campaign was the first of its kind using a sample of legacy AGR spent fuel material for conducting electrochemistry studies in a hot-cell. These initial studies largely focused on the composite electrode studies of a cross-sectional segment of the legacy AGR spent fuel pin. Due to the unique system of the composite electrode, which is comprised of both the fuel pellet and cladding components in contact with one another, these studies were accompanied by a series of supporting electrochemical studies on analogous non-active and lower-activity simulant spent fuel materials, in order to support the analysis and interpretation of the legacy AGR SNF studies.

Detailed summaries of further work are already presented in each respective chapter of study with suggestions and considerations to further enhance the understanding of each study. Thus, this section provides a high-level summary of the key proposals and suggestions to further develop our understanding of the corrosion behaviour of legacy AGR SNF.

1. Further electrochemical studies of legacy AGR SNF should aim to improve the practical aspects of the experimental work in order to increase reliability and repeatability. The experimental setup and procedures should be redeveloped to further improve usability and reliability for conducting future experiments under hot-cell conditions. Further work should aim to supplement the findings from the work presented in this thesis.

   The primary proposal would be to repeat the studies of Chapter 6 but on electrodes of the separated components of irradiated cladding and UO_2 from a sample of legacy AGR spent fuel pin. This would allow for detailed studies of the electrochemical behaviour of each individual component without interference from the other components, resulting in a more accurate understanding of the electrochemistry of the different components in legacy AGR SNF.
2. Further electrochemical studies of simulant-based methods to replicate the electrochemical behaviour of a real AGR SNF electrode, should aim to repeat the coupled-electrode studies of Method-2 presented in Chapter 5, using different combinations of electrode coupling:
   a. Undoped-UO_2 + AGR cladding
   b. 43 GWd/tU SIMFUEL + AGR cladding
   c. 43 GWd/tU AGR SIMFUEL with higher lanthanide doping (43-hiLn + AGR cladding)
   d. 43 GWd/tU AGR SIMFUEL with higher lanthanide and chromium-doped (43-hiLnCr + AGR cladding)

   These further studies will help broaden the understanding of the electrochemical behaviour and coupling interaction between the different SIMFUEL materials with the AGR cladding and thus further support future electrochemical studies of legacy AGR SNF. Future studies should

also incorporate a variety of different electrochemical techniques, such as EIS and CV and explore a variety of measurement conditions to simulate future spent fuel storage and disposal scenarios, such as the presence of hydrogen peroxide and carbonate groundwaters.

9 References

1. UK Nuclear Decommissioning Authority, *2019 UK Radioactive Waste Detailed Data*. 2019, Nuclear Decommissioning Authority: https://ukinventory.nda.gov.uk.

2. UK Office for Nuclear Regulation, *Office for Nuclear Regulation Annual Report and Accounts 2019/20*. 2020, Office for Nuclear Regulation: https://www.onr.org.uk.

3. Howett, E., C. Boxall, and D. Hambley, *AGR Cladding Corrosion: Investigation of the Effect of Temperature on Unsensitized Stainless Steel.* MRS Advances, 2017. **2**(11): p. 615-620.

4. Hoffmann, K., *Otto Hahn: Achievement and Responsibility*. 2001: Springer New York.

5. Sime, R.L., *Lise Meitner: A Life in Physics*. 1996: University of California Press.

6. Byers, N., *Fermi and Szilard.* arXiv preprint physics/0207094, 2002.

7. World Nuclear Association. *Nuclear Power in the United Kingdom*. Available from: https://www.world-nuclear.org/information-library/country-profiles/countries-t-z/united-kingdom.aspx.

8. Westinghouse Electric Company LLC. *Westinghouse Springfields*. Available from: https://www.westinghousenuclear.com/springfields/products.

9. UK Department for Business, Energy and Industrial Strategy, *Implementing Geological Disposal*. 2018: https://www.gov.uk.

10. Standring, P.N., *The Long Term Storage of Advanced Gas-Cooled Reactor Fuel (IAEA-SM-352/28)*. 1998, IAEA: OSTI.gov.

11. Hambley, D., *Technical Basis for Extending Storage of the UK's Advanced Gas-Cooled Reactor Fuel*. 2013.

12. Nuclear Energy Authority, *The Safety of Long-Term Interim Storage Facilities in NEA Member Countries (NEA/CSNI/R(2017)4)*. 2017, NEA: https://www.oecd-nea.org/nsd/docs/2017/csni-r2017-4.pdf.

13. Nuclear Decommissioning Authority, *Oxide Fuels Preferred Option*. 2012, NDA: https://assets.publishing.service.gov.uk/government/uploads/system/uploads/attachment_data/file/457789/Oxide_fuels_-_preferred_options.pdf.

14. IAEA, *Further Analysis of Extended Storage of Spent Fuel (IAEA-TECDOC-944)*. 1997, IAEA: https://www-pub.iaea.org/MTCD/publications/PDF/te_0944_scr.pdf.

15. Howett, E.A., et al., *The behaviour of advanced gas reactor simulated spent nuclear fuels in wet interim storage conditions.* Progress in Nuclear Science and Technology, 2018. **5**(0): p. 140-143.

16. IAEA. *General Design and Principles of the Advanced Gas-Cooled Reactor (AGR)*. Available from: https://nucleus.iaea.org/sites/graphiteknowledgebase/wiki/Guide_to_Graphite/GeneralDesignandPrinciplesoftheAdvancedGas-CooledReactor(AGR).aspx.

17. Rossiter, G. and M.A. Mignanelli, *The Characteristics of LWR fuel at high burnup and their relevance to AGR spent fuel (NNL (10) 10930)*. 2011, National Nuclear Laboratory.

18. Fuels, B.N., *AGR Fuel Element*. 1982, Science Museum Group: Science Museum Group Collection Online.

19. Willis, B.T.M., *Structures of UO_2, UO_{2+x} and U_4O_9 by neutron diffraction.* Journal de Physique, 1964. **25**(5): p. 431-439.

20. LibreTexts, *Structure - Fluorite and Antifluorite*. LibreTexts: Chem.LibreTexts.Org.

21. Willis, B.T.M., *Positions of the Oxygen Atoms in $UO_{2.13}$.* Nature, 1963. **197**(4869): p. 755.

22. Willis, B.T.M., *The defect structure of hyper-stoichiometric uranium dioxide.* Acta Crystallographica Section A: Crystal Physics, Diffraction, Theoretical and General Crystallography, 1978. **34**(1): p. 88-90.

23. He, H. and D.W. Shoesmith, *Raman spectroscopic studies of defect structures and phase transition in hyper-stoichiometric UO_{2+x}.* Physical Chemistry Chemical Physics, 2010. **12**(28): p. 8109-8118.

24. Blackburn, P.E., J. Weissbart, and E.A. Gulbransen, *Oxidation of Uranium Dioxide.* The Journal of Physical Chemistry, 1958. **62**(8): p. 902-908.

25. Hoekstra, H.R., A. Santoro, and S. Siegel, *The low temperature oxidation of UO_2 and U_4O_9.* Journal of Inorganic and Nuclear Chemistry, 1961. **18**: p. 166-178.

26. Ohashi, H., E. Noda, and T. Morozumi, *Oxidation of Uranium Dioxide.* Journal of Nuclear Science and Technology, 1974. **11**(10): p. 445-451.

27. McEachern, R.J. and P. Taylor, *A review of the oxidation of uranium dioxide at temperatures below 400°C.* Journal of Nuclear Materials, 1998. **254**(2): p. 87-121.

28. Murty, K.L. and I. Charit, *An Introduction to Nuclear Materials: Fundamentals and Applications*. 2013: Wiley.

29. Michael V. Glazoff, I.J.v.R., Benjamin D. Coryell, Clemente J. Parga, *Comparison of Nuclear Fuels for TREAT:UO_2 vs U_3O_8 (INL/EXT-16-37972)*. 2016, Idaho National Laboratory: http://www.inl.gov/.

30. Shoesmith, D.W., S. Sunder, and J.C. Tait, *Validation of an electrochemical model for the oxidative dissolution of used CANDU fuel.* Journal of Nuclear Materials, 1998. **257**(2): p. 89-98.

31. Shoesmith, D.W., S. Sunder, and W.H. Hocking, *Electrochemistry of UO_2 Nuclear Fuel*, in *The Electrochemistry of Novel Materials*. 1994, VCH. p. 297-337.

32. Shoesmith, D.W., *Fuel corrosion processes under waste disposal conditions.* Journal of Nuclear Materials, 2000. **282**(1): p. 1-31.

33. Shoesmith, D.W., *Used fuel and uranium dioxide dissolution studies – A Review (NWMO TR-2007-03)*. 2007, Nuclear Waste Management Organization.

34. Shoesmith, D.W., et al., *Corrosion of Nuclear Fuel (UO2) Inside a Failed Nuclear Waste Container*. 2012. p. 79.

35. Johnson, L., et al., *Rapid aqueous release of fission products from high burn-up LWR fuel: Experimental results and correlations with fission gas release.* Journal of Nuclear Materials, 2012. **420**(1): p. 54-62.

36. Thomas, L.E., R.E. Einziger, and H.C. Buchanan, *Effect of fission products on air-oxidation of LWR spent fuel.* Journal of Nuclear Materials, 1993. **201**: p. 310-319.

37. Lucuta, P.G., et al., *Microstructural features of SIMFUEL — Simulated high-burnup UO2-based nuclear fuel.* Journal of Nuclear Materials, 1991. **178**(1): p. 48-60.

38. Wilbraham, R.J., et al., *Simulated advanced gas-cooled reactor spent nuclear fuels: Determination of the O/U ratio - an XRD, XPS and Raman study.* Journal of Nuclear Materials, 2022. **568**.

39. Howett, E., *The Behaviour of Spent Nuclear Fuel in Wet Interim Storage*, in *School of Engineering*. 2019, Lancaster University.

40. Thomas, R.N., et al., *Permeability of observed three dimensional fracture networks in spent fuel pins.* Journal of Nuclear Materials, 2018. **510**: p. 613-622.

41. Rauff-Nisthar, N., et al., *Corrosion Behaviour of AGR SIMFUELS.* ECS Transactions, 2015. **66**(17): p. 85-94.

42. Rauff-Nisthar, N., et al., *Corrosion Behavior of AGR Simulated Fuels – Evolution of the Fuel Surface.* ECS Transactions, 2013. **53**(21): p. 95-104.

43. Mignanelli, M.A. and T.L. Shaw, *Information on Phase Chemistry in UK Spent AGR Fuels (NNL (09) 9834)*. 2009, National Nuclear Laboratory.

44. Shoesmith, D.W., *Chapter 11: Chemistry/Electrochemistry of Spent Nuclear Fuel as a Wasteform*. 2013.

45. Razdan, M., *Electrochemical and Surface Compositional Studies on Uranium Dioxide*. 2013, The University of Western Ontario: Electronic Thesis and Dissertation Repository. 1740.

46. Hiezl, Z., et al., *Processing and microstructural characterisation of a UO_2-based ceramic for disposal studies on spent AGR fuel.* Journal of Nuclear Materials, 2015. **456**: p. 74-84.

47. Hiezl, Z., *Processing and Microstructural Characterisation of UO 2 - based Simulated Spent Nuclear Fuel Ceramics for the UK`s Advanced Gas-cooled Reactors*. 2015, Imperial College London.

48. Anwyl, C., et al., *Corrosion of AGR Fuel Pin Steel Under Conditions Relevant to Permanent Disposal.* Procedia Chemistry, 2016. **21**: p. 247-254.

49. Degueldre, C., et al., *Mechanical Properties of Advanced Gas-Cooled Reactor Stainless Steel Cladding After Irradiation.* Journal of Materials Engineering and Performance, 2018. **27**(5): p. 2081-2088.

50. Scholz, F., *Voltammetric techniques of analysis: the essentials.* ChemTexts, 2015. **1**(4): p. 17.

51. Stansbury, E.E. and R.A. Buchanan, *Fundamentals of Electrochemical Corrosion*. 2000: ASM International.

52. Kahlert, H., *Reference Electrodes*, in *Electroanalytical Methods*. 2010. p. 291-308.

53. He, H., Z. Qin, and D.W. Shoesmith, *Characterizing the relationship between hyperstoichiometry, defect structure and local corrosion kinetics of uranium dioxide.* Electrochimica Acta, 2010. **56**(1): p. 53-60.

54. Allen, G.C., I.S. Butler, and N.A. Tuan, *Characterisation of uranium oxides by micro-Raman spectroscopy.* Journal of Nuclear Materials, 1987. **144**(1): p. 17-19.

55. He, H., Z. Ding, and D.W. Shoesmith, *The determination of electrochemical reactivity and sustainability on individual hyper-stoichiometric UO_{2+x} grains by Raman microspectroscopy and scanning electrochemical microscopy.* Electrochemistry Communications, 2009. **11**(8): p. 1724-1727.

56. Elorrieta, J.M., et al., *A detailed Raman and X-ray study of UO_{2+x} oxides and related structure transitions.* Physical Chemistry Chemical Physics, 2016. **18**(40): p. 28209-28216.

57. Pourbaix, M., *Atlas of electrochemical equilibria in aqueous solutions*. 1974: National Association of Corrosion Engineers.

58. McCafferty, E., *Introduction to Corrosion Science* 1ed. 2010: Springer New York, NY.

59. Paquette, J. and R.J. Lemire, *A Description of the Chemistry of Aqueous Solutions of Uranium and Plutonium to 200°C Using Potential-pH Diagrams.* Nuclear Science and Engineering, 1981. **79**(1): p. 26-48.

60. Brookins, D.G., *Revised Eh-pH Diagrams (25°C, One Bar) for Uranium and Transuranic Elements: Application to Radioactive Waste Studies.* MRS Proceedings, 1988. **125**: p. 161.

61. Brookins, D.G., *Uranium*, in *Eh-pH Diagrams for Geochemistry*. 1988, Springer, Berlin, Heidelberg. p. 151-157.

62. Brown, M.A., et al., *A Novel Method for Molybdenum-99/Technetium-99m Recovery via Anodic Carbonate Dissolution of Irradiated Low-Enriched Uranium Metal Foil.* Industrial & Engineering Chemistry Research, 2015. **54**(2): p. 712-719.

63. Angus, J.C., B. Lu, and M.J. Zappia, *Potential-pH diagrams for complex systems.* Journal of Applied Electrochemistry, 1987. **17**(1): p. 1-21.

64. Seibert, A., et al., *The use of the electrochemical quartz crystal microbalance (EQCM) in corrosion studies of UO_2 thin film models.* Journal of Nuclear Materials, 2011. **419**(1-3): p. 112-121.

65. Hocking, W.H., J.S. Betteridge, and D.W. Shoesmith, *The cathodic reduction of dioxygen on uranium oxide in dilute alkaline aqueous solution*. 1991, Atomic Energy of Canada Ltd.

66. Torrero, M.E., et al., *Kinetics of corrosion and dissolution of uranium dioxide as a function of pH.* International Journal of Chemical Kinetics, 1997. **29**(4): p. 261-267.

67. Sattonnay, G., et al., *Alpha-radiolysis effects on UO_2 alteration in water.* Journal of Nuclear Materials, 2001. **288**(1): p. 11-19.

68. Broczkowski, M.E., D. Zagidulin, and D.W. Shoesmith, *The Role of Dissolved Hydrogen on the Corrosion/Dissolution of Spent Nuclear Fuel*, in *Nuclear Energy and the Environment*. 2010, American Chemical Society. p. 349-380.

69. Ekeroth, E. and M. Jonsson, *Oxidation of UO_2 by radiolytic oxidants.* Journal of Nuclear Materials, 2003. **322**(2): p. 242-248.

70. Razdan, M., et al., *Electrochemical reduction of hydrogen peroxide on SIMFUEL (UO_2) in acidic pH conditions.* Electrochimica Acta, 2012. **83**: p. 410-419.

71. Clarens, F., et al., *The oxidative dissolution of unirradiated UO_2 by hydrogen peroxide as a function of pH.* Journal of Nuclear Materials, 2005. **345**(2): p. 225-231.

72. James S. Betteridge, et al., *Effects of hyperstoichiometry and fission products on the electrochemical reactivity of UO_2 nuclear fuel (AECL-11647)*. 1997: Atomic Energy of Canada Ltd.

73. Goldik, J.S., J.J. Noël, and D.W. Shoesmith, *The Effects of Simulated Fission Products in the Reduction of Hydrogen Peroxide on Simulated Nuclear Fuel Electrodes.* Journal of The Electrochemical Society, 2006. **153**(9): p. E151-E159.

74. Broczkowski, M.E., J.J. Noël, and D.W. Shoesmith, *The inhibiting effects of hydrogen on the corrosion of uranium dioxide under nuclear waste disposal conditions.* Journal of Nuclear Materials, 2005. **346**(1): p. 16-23.

75. Trummer, M., O. Roth, and M. Jonsson, *H_2 inhibition of radiation induced dissolution of spent nuclear fuel.* Journal of Nuclear Materials, 2009. **383**(3): p. 226-230.

76. Broczkowski, M.E., et al., *Corrosion of Uranium Dioxide Containing Simulated Fission Products in Dilute Hydrogen Peroxide and Dissolved Hydrogen.* Journal of The Electrochemical Society, 2010. **157**(8): p. C275-C281.

77. Razdan, M. and D.W. Shoesmith, *The influence of hydrogen peroxide and hydrogen on the corrosion of simulated spent nuclear fuel.* Faraday Discussions, 2015. **180**(0): p. 283-299.

78. Kim, K.-W., et al., *Anodic Dissolution Characteristics of UO_2 Electrode in the Potential Ranges over Oxygen Evolution in Carbonate Solutions at*

Several pHs. Journal of The Electrochemical Society, 2010. **157**(10): p. D553-D558.

79. Keech, P.G., et al., *The anodic dissolution of SIMFUEL (UO_2) in slightly alkaline sodium carbonate/bicarbonate solutions.* Electrochimica Acta, 2011. **56**(23): p. 7923-7930.

80. Gaulard-Balandret, C., et al., *Kinetics of oxidation and dissolution of uranium dioxide in aqueous acid solutions.* Electrochimica Acta, 2012. **83**: p. 471-477.

81. Santos, B.G., J.J. Noël, and D.W. Shoesmith, *The influence of potential on the anodic dissolution of SIMFUEL (UO_2).* Electrochimica Acta, 2006. **51**(20): p. 4157-4166.

82. Sunder, S., et al., *The effect of ph on the corrosion of nuclear fuel (UO_2) in oxygenated solutions.* Corrosion Science, 1991. **32**(4): p. 373-386.

83. He, H., et al., *Characterization of the influence of fission product doping on the anodic reactivity of uranium dioxide.* Canadian Journal of Chemistry, 2007. **85**(10): p. 702-713.

84. Ding, H., et al., *Advanced Gas-cooled Reactor SIMFuel Fabricated by Hot Isostatic Pressing: a Feasibility Investigation.* IOP Conference Series: Materials Science and Engineering, 2020. **818**(1): p. 012011.

85. Rauff-Nisthar, N., *Corrosion Behaviour of AGR Simulated Fuels (SIMFUELs)*, in *Engineering*. 2021, Lancaster University.

86. Wilbraham, R.J., et al., *Raman studies of advanced gas-cooled reactor simulated spent nuclear fuels.* Progress in Nuclear Science and Technology, 2018. **5**: p. 4.

87. Davis, J.R., *Corrosion: Understanding the Basics*. 2000: ASM International.

88. Landolt, D., *Corrosion and Surface Chemistry of Metals*. 2007: EFPL Press.

89. Roberge, P.R., *Corrosion engineering : principles and practice.* 2008.

90. Ahmad, Z., *Principles of Corrosion Engineering and Corrosion Control*. 2006: Elsevier Science.

91. Wilbraham, R., *Surface Decontamination by Photocatalysis*. 2011, Lancaster University.

92. Williamson, R., *Mechanisms of Fixed Contamination of Commonly Engineered Surfaces*. 2018, Lancaster University.

93. Kamimura, T., et al., *The role of chloride ion on the atmospheric corrosion of steel and corrosion resistance of Sn-bearing steel.* Corrosion Science, 2012. **62**: p. 34-41.

94. Makjan, S., et al., *Effects of hydrogen peroxide on 304 stainless steel in high temperature water.* Journal of Physics: Conference Series, 2019. **1380**(1): p. 012087.

95. Wada, Y., et al., *Effects Of Hydrogen Peroxide On Intergranular Stress Corrosion Cracking Of Stainless Steel in High Temperature Water, (IV).* Journal of Nuclear Science and Technology, 2001. **38**(3): p. 183-192.

96. Miyazawa, T., et al., *Effects of Hydrogen Peroxide on Corrosion of Stainless Steel, (V) Characterization of Oxide Film with Multilateral Surface Analyses.* Journal of Nuclear Science and Technology, 2006. **43**(8): p. 884-895.

97. Uchida, S., et al., *Effects of Hydrogen Peroxide on Corrosion of Stainless Steel (VI).* Journal of Nuclear Science and Technology, 2007. **44**(5): p. 758-766.

98. Song, T.H. and I.S. Kim, *Effect of H_2O_2 on the Corrosion Behaviour od 304L Stainless Steel.* Journal of Korean Nuclear Society, 1995. **27**(4): p. 453-462.

99. Buck E.C., R.S.W., F.N. Skomurski, K.J. Cantrell, B.K. McNamara, and C.Z. Soderquist, *Radiolysis Process Model*. 2012, Pacific Northwest National Laboratory.

100. Fattah-Alhosseini, A. and N. Attarzadeh, *The Mechanism of Transpassive Dissolution of AISI 321 Stainless Steel in Sulphuric Acid Solution.* International Journal of Electrochemistry, 2011. **2011**: p. 521384.

101. Fattah-Alhosseini, A. and S. Vafaeian, *Effect of solution pH on the electrochemical behaviour of AISI 304 austenitic and AISI 430 ferritic stainless steels in concentrated acidic media.* Egyptian Journal of Petroleum, 2015. **24**(3): p. 333-341.

102. Prawoto, Y., K. Ibrahim, and w.s. wan nik, *Effect of ph and chloride concentration on the corrosion of duplex stainless steel.* Arabian Journal for Science and Engineering, 2009. **34**.

103. Schmutz, P. and D. Landolt, *In-situ microgravimetric studies of passive alloys: potential sweep and potential step experiments with Fe–25Cr and Fe–17Cr–33Mo in acid and alkaline solution.* Corrosion Science, 1999. **41**(11): p. 2143-2163.

104. Olsson, C.O.A. and D. Landolt, *Passive films on stainless steels—chemistry, structure and growth.* Electrochimica Acta, 2003. **48**(9): p. 1093-1104.

105. Jung, S.-H., J.-W. Yeon, and K. Song, *Effect of pH, temperature, and H2O2 on the electrochemical oxidation behavior of iron in perchlorate solutions.* Journal of Solid State Electrochemistry, 2014. **18**(2): p. 333-339.

106. Clark, R.N., et al., *The effect of sodium hydroxide on niobium carbide precipitates in thermally sensitised 20Cr-25Ni-Nb austenitic stainless steel.* Corrosion Science, 2020. **170**: p. 108596.

107. English, C.A., S.M. Murphy, and J.M. Perks, *Radiation-induced segregation in metals.* Journal of the Chemical Society, Faraday Transactions, 1990. **86**(8): p. 1263-1271.

108. Ashworth, M.A., D.I.R. Norris, and I.P. Jones, *Radiation-induced segregation in Fe-20Cr-25Ni-Nb based austenitic stainless steels.* Journal of Nuclear Materials, 1992. **189**(3): p. 289-302.

109. Goode, J.B., D. Harbottle, and B.C. Hanson, *Vacuum drying of advanced gas reactor fuel.* Progress in Nuclear Energy, 2018. **109**: p. 145-158.

110. Nonboel, E., *Description of the advanced gas cooled type of reactor (AGR)*. 1996: Denmark. p. 88.

111. Barcellini, C., et al., *Local chemical instabilities in 20Cr25Ni Nb-stabilised austenitic stainless steel induced by proton irradiation.* Journal of Nuclear Materials, 2019. **518**: p. 95-107.

112. Al-Shater, A., et al., *Characterization of the stress corrosion cracking behavior of thermally sensitized 20Cr-25Ni stainless steel in a simulated cooling pond environment.* Journal of Nuclear Science and Technology, 2017. **54**(7): p. 742-751.

113. Burstall, R.F., *FISPIN - a computer code for nuclide inventory calculations*. 1979: United Kingdom. p. 51.

114. Mendoza, S., et al., *Voltammetric Techniques*, in *Agricultural and Food Electroanalysis*. 2015. p. 21-48.

115. Elgrishi, N., et al., *A Practical Beginner's Guide to Cyclic Voltammetry.* Journal of Chemical Education, 2018. **95**(2): p. 197-206.

116. Biesheuvel, P., S. Porada, and J. Dykstra, *The difference between Faradaic and non-Faradaic electrode processes.* arXiv preprint arXiv:1809.02930, 2018.

117. Instruments, G. *Basics of Electrochemical Impedance Spectroscopy*. Available from: https://www.gamry.com/application-notes/EIS/basics-of-electrochemical-impedance-spectroscopy/.

118. Raman, C.V., *A new radiation [Reproduced from Indian J. Phys., 1928, 2, 387?398].* Current Science, 1998. **74**(4): p. 382-386.

119. Larkin, P.J., *Chapter 1 - Introduction: Infrared and Raman Spectroscopy*, in *Infrared and Raman Spectroscopy (Second Edition)*, P.J. Larkin, Editor. 2018, Elsevier. p. 1-5.

120. Wojdyr, M., *Fityk: a general-purpose peak fitting program.* Journal of Applied Crystallography, 2010. **43**(5 Part 1): p. 1126-1128.

121. Peres, V., L. Bourgeois, and P. Dehaudt, *Grain growth and Ostwald ripening in chromia-doped uranium dioxide.* J. Phys. IV France, 1993. **03**(C7): p. C7-1477-C7-1480.

122. Bourgeois, L., et al., *Factors governing microstructure development of Cr2O3-doped UO2 during sintering.* Journal of Nuclear Materials, 2001. **297**(3): p. 313-326.

123. Hossain, M.M. and M. Jonsson, *Effects of ionic strength on the kinetics for UO_2 oxidation.* Journal of Nuclear Materials, 2008. **373**(1): p. 190-193.

124. Kim, K.-W., et al., *Comparison of UO_2 and SIMFUEL Electrodes in Carbonate and NaCl Solutions at Several pHs.* Journal of The Electrochemical Society, 2012. **159**(5): p. D303.

125. Miserque, F., et al., *Use of UO2 films for electrochemical studies.* Journal of Nuclear Materials, 2001. **298**(3): p. 280-290.

126. Razdan, M. and D.W. Shoesmith, *Influence of Trivalent-Dopants on the Structural and Electrochemical Properties of Uranium Dioxide (UO2).* Journal of The Electrochemical Society, 2014. **161**(3): p. H105-H113.

127. Cardinaels, T., et al., *Chromia doped UO_2 fuel: Investigation of the lattice parameter.* Journal of Nuclear Materials, 2012. **424**(1): p. 252-260.

128. Kegler, P., et al., *Chromium Doped UO_2-Based Ceramics: Synthesis and Characterization of Model Materials for Modern Nuclear Fuels.* Materials, 2021. **14**(20): p. 6160.

129. Silva, C.M., R.D. Hunt, and K.S. Holliday, *An evaluation of tri-valent oxide (Cr_2O_3) as a grain enlarging dopant for UO_2 nuclear fuels fabricated under reducing environment.* Journal of Nuclear Materials, 2021. **553**: p. 153053.

130. Gao, S., et al., *Electrochemical Behavior and Nonlinear Mott-Schottky Characterization of a Stainless Steel Passive Film.* Analytical Letters, 2014. **47**(7): p. 1162-1181.

131. Saadawy, M., *Kinetics of Pitting Dissolution of Austenitic Stainless Steel 304 in Sodium Chloride Solution.* ISRN Corrosion, 2012. **2012**: p. 1-5.

132. Durán, A., et al., *Sol-Gel Protective Coatings for Metals*, in *Handbook of Sol-Gel Science and Technology: Processing, Characterization and Applications*, L. Klein, M. Aparicio, and A. Jitianu, Editors. 2018, Springer International Publishing: Cham. p. 2369-2433.

133. Corrosion Clinic. *Lecture 11: Electrochemical Techniques*. [cited 2022 20th Dec]; Available from: https://www.corrosionclinic.com/corrosion_online_lectures/ME303L11.HTM.

134. Betova, I., et al., *Transpassive Dissolution Mechanism of Ni-Based Alloys in a Simulated Bleaching Solution : Effect of Alloying Elements.* Journal of The Electrochemical Society, 2002. **149**(11): p. B499.

135. Betova, I., et al., *The transpassive dissolution mechanism of highly alloyed stainless steels: I. Experimental results and modelling procedure.* Corrosion Science, 2002. **44**(12): p. 2675-2697.

136. Karcher, S., et al., *Benefits of using multiple Raman laser wavelengths for characterizing defects in a UO2 matrix.* Journal of Raman Spectroscopy, 2022. **53**(5): p. 988-1002.

137. Livneh, T. and E. Sterer, *Effect of pressure on the resonant multiphonon Raman scattering in UO_2.* Physical Review B, 2006. **73**(8): p. 085118.

138. Rickert, K., et al., *Assessing UO2 sample quality with μ-Raman spectroscopy.* Journal of Nuclear Materials, 2019. **514**: p. 1-11.

139. Tian, G. and L. Rao, *Spectrophotometric and calorimetric studies of U(VI) complexation with sulfate at (25 to 70)°C.* The Journal of Chemical Thermodynamics, 2009. **41**(4): p. 569-574.

140. Antozzi, A.L., et al., *EIS study of the service life of activated cathodes for the hydrogen evolution reaction in the chlor–alkali membrane cell process.* Electrochimica Acta, 2008. **53**(25): p. 7410-7416.

141. Gore, C.M., et al., *Effect of composition and microstructure on electrical properties and CO2 stability of donor-doped, proton conducting BaCe1−(x+y)ZrxNbyO3.* Journal of Materials Chemistry A, 2014. **2**(7): p. 2363-2373.

142. Li, Q. and V. Thangadurai, *Synthesis, Structure and Electrical Properties of Mo-doped CeO2–Materials for SOFCs.* Fuel Cells, 2009. **9**(5): p. 684-698.

143. Chinarro, E., et al., *Bulk and grain boundary conductivity of Ca0.97Ti1−xFexO3−δ materials.* Solid State Ionics, 2003. **160**(1): p. 161-168.

144. Hjalmarsson, P., M. Søgaard, and M. Mogensen, *Electrochemical behaviour of (La1−xSrx)sCo1−yNiyO3−δ as porous SOFC cathodes.* Solid State Ionics, 2009. **180**(26): p. 1395-1405.

145. Li, Q. and V. Thangadurai, *A comparative 2 and 4-probe DC and 2-probe AC electrical conductivity of novel co-doped Ce0.9−xRExMo0.1O2.1–*

0.5x (RE = Y, Sm, Gd; x = 0.2, 0.3). Journal of Materials Chemistry, 2010. **20**(37): p. 7970-7983.

146. van Westing, E.P.M., G.M. Ferrari, and J.H.W. de Wit, *The determination of coating performance with impedance measurements-I. Coating polymer properties.* Corrosion Science, 1993. **34**(9): p. 1511-1530.

147. Hsu, C.H. and F. Mansfeld, *Technical Note: Concerning the Conversion of the Constant Phase Element Parameter Y0 into a Capacitance.* Corrosion, 2001. **57**(9): p. 747-748.

148. Chang, B.-Y., *Conversion of a Constant Phase Element to an Equivalent Capacitor.* J. Electrochem. Sci. Technol, 2020. **11**(3): p. 318-321.

149. Morrison, S.R., *Electrochemistry at semiconductor and oxidized metal electrodes*. 2nd printing ed. 1984, New York: Plenum.

150. Cruz-Manzo, S., R. Chen, and P. Greenwood, *Analysis of the Performance of an Open-Cathode Polymer Electrolyte Fuel Cell Stack Using Simultaneous Electrochemical Impedance Spectroscopy Measurements.* ECS Transactions, 2014. **48**(1): p. 47.

151. Armstrong, R.D. and M. Henderson, *Impedance plane display of a reaction with an adsorbed intermediate.* Journal of Electroanalytical Chemistry and Interfacial Electrochemistry, 1972. **39**(1): p. 81-90.

152. Bai, L., D.A. Harrington, and B.E. Conway, *Behavior of overpotential—deposited species in Faradaic reactions—II. ac Impedance measurements on H2 evolution kinetics at activated and unactivated Pt cathodes.* Electrochimica Acta, 1987. **32**(12): p. 1713-1731.

153. Thévenin, L., *Extension de la loi d'Ohm aux circuits électromoteurs complexes.* Ann. Tél, 1883. **10**: p. 222.

154. Terrell, D.L., *CHAPTER ONE - Basic Concepts of the Integrated Operational Amplifier*, in *Op Amps (Second Edition)*, D.L. Terrell, Editor. 1996, Newnes: Burlington. p. 1-35.

155. Dario Delgado, Manickam Minakshi, and D.-J. Kim, *Electrochemical Impedance Spectroscopy Studies on Hydrogen Evolution from Porous Raney Cobalt in Alkaline Solution.* International Journal of ELECTROCHEMICAL SCIENCE, 2015(10): p. 9379-9394.

156. Levinas, R., N. Tsyntsaru, and H. Cesiulis, *The Characterisation of Electrodeposited MoS2 Thin Films on a Foam-Based Electrode for Hydrogen Evolution.* Catalysts, 2020. **10**(10): p. 1182.

157. Bottomley, P.D.W., D.H. Wegen, and M. Coquerelle, *Construction of an electrode for irradiated U02 fuel and preliminary results concerning its use in aqueous solutions.* Journal of Nuclear Materials, 1996. **238**(1): p. 23-37.

158. Gaskova, O.L. and M.B. Bukaty, *Solubility of Uranium Dioxide during Underground Disposal of Radioactive Wastes and Spent Nuclear Fuel.* Chemistry for Sustainable Development, 2004. **6**: p. 649-655.

159. Ollila, K., *Work Report 2008-75: Solubility of UO_2 in the High pH Range in 0.01 to 0.1 M NaCl Solution Under Reducing Conditions*. 2008: POSIVA OY.

160. Elfström, B.O., *The effect of chloride ions on passive layers on stainless steels.* Materials Science and Engineering, 1980. **42**: p. 173-180.

161. Beverskog, B. and I. Puigdomenech, *Revised Pourbaix diagrams for nickel at 25–300 °C.* Corrosion Science, 1997. **39**(5): p. 969-980.

162. Beverskog, B. and I. Puigdomenech, *Revised pourbaix diagrams for chromium at 25–300 °C.* Corrosion Science, 1997. **39**(1): p. 43-57.

163. Revilla, R.I., et al., *EIS comparative study and critical Equivalent Electrical Circuit (EEC) analysis of the native oxide layer of additive manufactured and wrought 316L stainless steel.* Corrosion Science, 2020. **167**: p. 108480.

164. Boissy, C., C. Alemany-Dumont, and B. Normand, *EIS evaluation of steady-state characteristic of 316L stainless steel passive film grown in acidic solution.* Electrochemistry Communications, 2013. **26**: p. 10-12.

165. Rios, J.F., J.A. Calderón, and R.P. Nogueira, *Electrochemical Behavior of Metals Used in Drinking Water Distribution Systems: A Rotating Cylinder Electrode's Study.* Corrosion, 2013. **69**(9): p. 875-885.

166. Wu, S.L., et al., *EIS study of the surface film on the surface of carbon steel from supercritical carbon dioxide corrosion.* Applied Surface Science, 2004. **228**(1): p. 17-25.

167. Linardi, E.M., L.A. Lanzani, and J.R.C. Lacoste, *EIS studies of anodic aluminum oxide films.* MRS Online Proceedings Library, 2012. **1475**(1): p. 305-310.

168. Huang, Y., et al., *AGR fuel corrosion: SIMFUEL-based method development in preparation for electrochemical studies of real spent AGR nuclear fuel electrode.* MRS Advances, 2022.

169. Hughes, H. and R. Hargreaves, *AGR fuel pin pellet-clad interaction failure limits and activity release fractions*. 1985: International Atomic Energy Agency (IAEA). p. 189-200.

170. Stacey, R.D., P.M. Jones, and K.A. Bradshaw, *Mechanical interactions between fuel and cladding in Windscale AGR fuel pins.* Journal of the British Nuclear Energy Society, 1976. **15**(3): p. 237-246.

171. Santos, B.G., et al., *X-ray photoelectron spectroscopy study of anodically oxidized SIMFUEL surfaces.* Electrochimica Acta, 2004. **49**(11): p. 1863-1873.

172. Santos, B.G., J.J. Noël, and D.W. Shoesmith, *The effect of pH on the anodic dissolution of SIMFUEL (UO2).* Journal of Electroanalytical Chemistry, 2006. **586**(1): p. 1-11.

173. Ansuini, F.J. and J.R. Dimond, *Factors affecting the accuracy of reference electrodes*. 1994, United States: NACE International, Houston, TX (United States).

174. Sunder, S., et al., *Anodic oxidation of UO2: Part I. Electrochemical and X-ray photoelectron spectroscopic studies in neutral solutions.* Journal of Electroanalytical Chemistry and Interfacial Electrochemistry, 1981. **130**: p. 163-179.

175. Tracy, C.L., et al., *Measurement of UO2 surface oxidation using grazing-incidence x-ray diffraction: Implications for nuclear forensics.* Journal of Nuclear Materials, 2018. **502**: p. 68-75.

176. Desgranges, L., et al., *Raman spectrum of U4O9: a new interpretation of damage lines in UO2.* Journal of Raman Spectroscopy, 2012. **43**(3): p. 455-458.

177. Lv, J., et al., *Raman scattering from phonons and electronic excitations in UO2 with different oxygen isotopes.* Journal of Raman Spectroscopy, 2016. **47**(3): p. 345-349.

178. Elorrieta, J.M. and J.M.E. Baigorri, *Raman spectroscopy: a versatile tool in the multianalitycal characterisation of nuclear fuel*, in *Universidad Complutense de Madrid Facultad de Ciencias Químicas Departamento de Química Física*. 2019, Universidad Complutense de Madrid.

179. Stubbs, J.E., et al., *UO_2 Oxidative Corrosion by Nonclassical Diffusion.* Physical Review Letters, 2015. **114**(24): p. 246103.

180. Thomas, L.E. and R.E. Einziger, *Grain boundary oxidation of pressurized-water reactor spent fuel in air.* Materials Characterization, 1992. **28**(2): p. 149-156.

181. Everall, N.J., *Confocal Raman microscopy: performance, pitfalls, and best practice.* Appl Spectrosc, 2009. **63**(9): p. 245a-262a.

182. Opilik, L., T. Schmid, and R. Zenobi, *Modern Raman Imaging: Vibrational Spectroscopy on the Micrometer and Nanometer Scales.* Annual Review of Analytical Chemistry, 2013. **6**(1): p. 379-398.

183. Toporski, J., T. Dieing, and O. Hollricher, *Confocal Raman Microscopy*. 2018: Springer International Publishing.